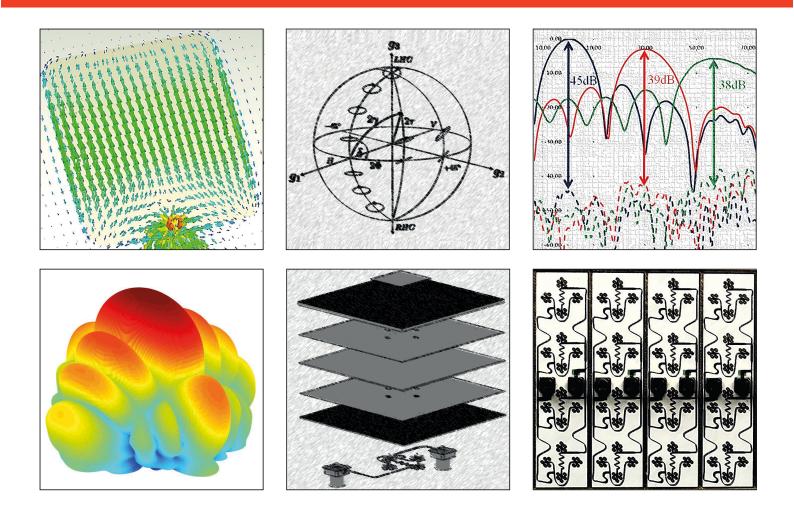


Fakultät für Elektrotechnik und Informationstechnik Professur Hochfrequenztechnik und Theoretische Elektrotechnik



### Dennis Vollbracht

Design and development of phasedarray antennas for dual-polarized weather radar applications Dennis Vollbracht

Design and development of phased-array antennas for dual-polarized weather radar applications

Dennis Vollbracht

Design and development of phased-array antennas for dual-polarized weather radar applications



TECHNISCHE UNIVERSITÄT CHEMNITZ

Universitätsverlag Chemnitz 2018

#### Impressum

#### Bibliografische Information der Deutschen Nationalbibliothek

Die Deutsche Nationalbibliothek verzeichnet diese Publikation in der Deutschen Nationalbibliografie; detaillierte bibliografische Angaben sind im Internet über http://www.dnb.de abrufbar.



Das Werk - ausgenommen Zitate, Cover, Logo TU Chemnitz und Bildmaterial im Text - steht unter der Creative-Commons-Lizenz Namensnennung 4.0 International (CC BY 4.0) http://creativecommons.org/licences/by/4.0/deed.de

Titelgrafik: Dennis Vollbracht Satz/Layout: Dennis Vollbracht

Technische Universität Chemnitz/Universitätsbibliothek Universitätsverlag Chemnitz 09107 Chemnitz https://www.tu-chemnitz.de/ub/univerlag

readbox unipress in der readbox publishing GmbH Am Hawerkamp 31 48155 Münster http://unipress.readbox.net

ISBN 978-3-96100-070-8

http://nbn-resolving.de/urn:nbn:de:bsz:ch1-qucosa2-320055

"Sometimes it takes a while, until the beauty of physics becomes visible to the human eye."

by Dennis Vollbracht



### Design and development of phased-array antennas for dual-polarized weather radar applications

Von der Fakultät für Elektrotechnik und Informationstechnik

der Technischen Universität Chemnitz

genehmigte

Dissertation

zur Erlangung des akademischen Grades

Doktoringenieur (Dr.-Ing.)

vorgelegt von

Dipl.-Ing. (FH) Dennis Vollbracht

geboren am 14. September 1980 in Haltern

eingereicht am: 27. Juni 2017

Gutachter: Prof. Dr. rer. nat. Madhukar Chandra Prof. Dr.-Ing. Dirk Fischer

Tag der Verleihung: 03. September 2018

## Abstract

Phased array weather radar antennas with beam steering capabilities are suitable alternatives to weather radars with mechanically scanning reflector antennas. Dual-polarized phased-array weather radar antennas, however, demand careful assessment of the x-polar characteristics.

The low x-pol radiation of polarimetric weather radar antennas is of significant importance for the proper classification and qualitative estimation of hydrometeors in illuminate volumes. Unfortunately, array antennas display changing x-pol contributions during the electronical beam steering process. Typically, the x-pol radiation will be substantially increased in the co-polar main beam direction but also in other angular directions. Consequently, it is a vital challenge to design arrays with low x-pol contribution during beam steering.

In this dissertation a new phased-array weather radar concept is developed. The phasedarray system configuration can be used to substitute state-of-the-art weather radars with reflector antennas. Furthermore, a dense network of these phased-array radars can be used to substitute a network of high power weather radars, which are used nowadays. The research focus of this work is the development of a dual-polarized microstrip patch antenna with phased-array capability and very high polarization purity. In this regard, new graphical techniques are developed to investigate the causes and the reduction of the x-pol radiation of isolated (stand-alone) microstrip patch antennas.

To further reduce the x-pol contribution of antennas, optimization methods have been investigated, evaluated and developed. For the first time in literature, differential-feed antenna arrays are compared to excitation optimized single-feed antenna arrays in their x-pol contribution in the boresight direction **and** during beam steering. In particular, two dual-polarized 4x8 antenna arrays have been developed and simulated by CST MWS, produced as multilayer PCB and verified at the compact antenna test range at RWTH Aachen. The results show that the x-pol contributions of arrays are significantly reduced for differentially-feed antenna arrays, even when beam steering is performed. During the azimuth scan of 120° a record setting x-pol suppression of -45 dB and -36 dB could be measured for the horizontal and vertical polarization channels, respectively.

#### Keywords:

Dual-polarized phased-array weather radars, phased-array antenna, beam steering, cross polarization, Cross polarization suppression, differential-feed antenna, limited field of view

# Kurzfassung

Wetterradarsysteme mit phasengesteuerten Antennen stellen eine echte Alternative zu Wetterradarsystemen mit mechanisch drehenden Reflektorantennen dar. Dual-polarisierte phasengesteuerte Antennen müssen jedoch sehr genau in ihrem Kreuzpolarisationsverhalten verifiziert werden, um für den Wetterradarbereich von Nutzen zu sein.

Die Unterdrückung der kreuzpolaren Anteile von Radarantennen ist von fundamentaler Bedeutung, um Hydrometeore mit Hilfe von polarimetrischen Wetterradarsystemen klassifizieren und qualitativ bestimmen zu können. Die hohe Anforderung an Polarisationsreinheit ist mit aktuell erhältlichen Arraydesigns nur schwierig zu realisieren, da sich die Kreuzpolarisationsunterdrückung während des elektronischen Schwenks der Hauptkeule signifikant verschlechtert.

Diese Dissertation stellt ein Wetterradar Systemkonzept mit phasengesteuerter Gruppenantenne vor, welches die aktuell genutzten Wetterradare mit Reflektorantennen ablösen könnte. Der Fokus der Arbeit wurde auf die Entwicklung einer Dual-polarimetrischen, polarisationsreinen und phasengesteuerten Mikrostreifenleiterantennen gelegt. Hierbei wurden neue grafische Verfahren entwickelt, die es ermöglichen, die Generierung der kreuzpolaren Anteile von isolierten Patchantennen (Einzelpatche) zu erklären und zu minimieren.

Um die kreuzpolaren Anteile weiter herabzusetzen wurden Optimierungsverfahren für Arrayantennen erforscht, bewertet und neu entwickelt. Zum ersten Mal wurden differentiell gespeiste mit einzel gespeisten Antennenarrays in ihrem Kreuzpolarisationsverhalten **während** des elektronischen Schwenks der Hauptkeule verglichen. Zwei Dual-polarimetrische 4x8 Antennenarrays (differentiell gespeist und mit optimierter Phasenansteuerung) wurden zu diesem Zweck mittels CST MWS entworfen, simuliert, als Multilagenplatine gefertigt und an der Antennentestanlage der RWTH Aachen vermessen. Die Resultate zeigen, dass die Kreuzpolarisationsanteile bei differentiell gespeisten Mikrostreifenleiterantennen in Gruppenkonfiguration, selbst beim elektronischen Schwenk der Hauptkeule, signifikant minimiert werden konnten. Für einen azimutalen Scanbereich von 120° konnte eine exzellente Kreuzpolarisationsunterdrückung zwischen -45 dB und -36 dB messtechnisch für den horizontalen und vertikalen Polarisationskanal nachgewiesen werden.

#### Schlagworte:

Dual-polarisiertes phasengesteuertes Wetterradar, phasengesteuerte Antennen, elektronischer Schwenk der Hauptkeule, Kreuzpolarisation, Kreuzpolarisationsunterdrückung, differentiell gespeiste Antennen, Antennengruppen mit eingeschränktem Scanbereich

## Introduction

Phased array radar systems have been in use for many years now. However, the investigation of phased-array weather radar systems for measuring and classifying hydrometeors has become ubiquitous in recent years.

When comparing the detection radars deployed in military sectors, the weather radar systems are profoundly accurate devices. A microwave engineer would describe the present weather radar systems as highly accurate vector network analyzers (VNA's). The two ports of the VNA correspond to the horizontal and vertical polarization channels of the dualpolarized radar antenna. For the classification of hydrometeors in different geometries, the accuracy requirement for dual-polarized weather radar systems is enormous.

According to international tender requirements for weather radar suppliers, the current accuracy measurement requirement (standard deviation) for the reflectivities (Z) is less than 0.5 dB and the other polarimeteric products such as differential reflectivity (ZDR) should be better than 0.1 dB [1]. However, this is quite difficult to achive given the physical behavior of the phased-array antenna. As soon as the main beam direction of the main lobe is changed by controlling the phase shift, most antenna arrays change their antenna radiation patterns. The variation in the antenna radiation pattern is shown by the reduction of main lobe antenna gain, broadening of the main lobe and an increase in the secondary lobes with a significant deterioration of the cross polar suppression. Through antenna modeling and estimation methods, the co-polar antenna parameters such as halfpower-beamwidth and antenna gain can be relatively and precisely estimated via the array factor calculation for different main beam positions. However, the x-polar component is difficult to predict by the classical estimation methods. Furthermore, the currently available phased-array antennas show increased cross polarization components when the main lobe is electronically scanned, which in turn is very disadvantageous for the polarimetric classification of hydrometeors.

The present dissertation addresses this issue; consequently a phase-controlled weather radar system is developed and presented in the beginning of the thesis. The central idea is to replace the currently available high-power weather radars with parabolic antennas which are operated by the weather services world-wide with small phased-array systems in a dense weather radar network. The detailed phased-array weather radar development has been carried out in advance to elaborate the influence on the antenna design, such that the phase controlled array is the most effective and plausible configuration for this application. The focus of this work was research and development of dual-polarized phased-array antennas with very low x-pol contribution. In this context, new graphical methods have been developed, which help explaining and minimizing the generation of the cross-polar distortions of isolated microstrip antennas.

Furthermore, optimization methods for array antennas have been researched, evaluated and newly developed to further reduce the cross-polar components. For the first time, differential-feed and single-feed antenna arrays were compared in terms of their crosspolarization behavior during the electronic scan of the main beam.

Two dual-polarized 4x8 antenna arrays (differential-feed and with optimized phase distribution) were designed, simulated and produced as a multilayer board using the CST MWS and measured at the compact antenna test range at the University RWTH Aachen.

Even for electronic tilt of the main lobe, the results show that the x-pol contributions in case of differential-feed array antennas could be substantially reduced. For an azimuth scan range of 120 *degree*, an excellent cross polarization suppression between -45 dB and -36 dB could be achieved for both the horizontal and vertical polarization channels.

This dissertation is divided into the *following chapters*:

**Chapter 1:** The radar basics are introduced. The reader is introduced to the function of a pulsed Doppler radar, the derivation of the point-target equation, the derivation of the volumetric-weather radar equation, as well as the development of the radar equation for weather radar with planar and phased-array antenna. After the introduction of the dual-polarized weather radar system, the basic dual-polarized weather radar parameters based on the scattering matrix and the covariance matrix are explained. The mathematical formulation of the implementation of pulse pair processing of I/Q- signals is detailed. Noise is a crucial topic in the weather radar domain. All the basic foundations are also made available to the reader in Chapter 1, which concludes with the bandwidth analysis of different radar types.

**Chapter 2:** For the detailed discussion of dual-polarized phased-array antennas and polarimetric weather radar systems, it is important to define the polarization state of electromagnetic waves. Consequently, the Maxwell's equations are introduced for the propagation of electromagnetic waves in vacuum (for the calculation of an antenna radiation pattern) or for propagation in a medium (for the description of electromagnetic waves in substrates of a microstrip antenna), and the applications will be found in the following chapters. Subsequently, the polarization state of EM waves is depicted with the help of the Jones vector, the polarization ellipse and the Poincaré sphere.

**Chapter 3:** The theoretical fundamentals of antennas are recapitulated, in order to understand the background of the dual-polarized phase array antennas, which are developed in the following chapters. For this reason, Chapter 3 provides an overview of all relevant antenna basics applicable in microwave technology. In particular, phased-array antennas are discussed and the relationship between the element factor of individual radiators and

the antenna array pattern is explained. The measurement definitions such as the far-field and Fresnel definition are also provided. From the literature presented to the reader, all relevant definitions about polarimetric antenna radiation patterns are summarized for the better interpretation. Particular attention is paid to the theoretical definitions, which deal with the cross polar contributions of antennas. After the introduction of the basic antenna principles, the architecture, the function (using the cavity model), the polarization control, the bandwidth definition and the feeding network design of microstrip antennas are discussed in great detail. In order to design antenna arrays on printed circuit boards (PCBs), equations are provided, which are the basis for the calculation of phase constants, group velocity and wave impedances on different dielectric substrates. Different types of substrates and their characteristic influences on the antenna parameters are also considered. In the last part of the third chapter, linear and planar phased-array antennas are considered. Illustrated further is how "Mutual Coupling" affects the function of phased-array antennas and which polarization effects are to be expected when the beam direction of the main lobe is varied and when it is useful to group individual radiators into subarrays.

**Chapter 4:** CST MWS Studio suite was chosen to design and simulate the dual-polarized multilayer antennas. This chapter explains the basic functionalities of the CST MWS program and graphically illustrates the numerical calculation method FIT (Finite Integration Technology). In particular, the "Time Domain Solver", which has provided all the simulation results within this dissertation is presented. The hardware environment and the duration of single radiator and antenna array simulations are also presented. The duration of the simulation strongly depends on the selected "Mesh" cells, i.e. the discretization of the 3D model. As a consequence, the mesh settings are also introduced. At the end of the fourth chapter, the optimization function of CST MWS is introduced, which addresses S-Parameters and polarimetric antenna measurement values. In order to quickly estimate the key antenna parameters of large array antennas with thousands of individual elements, the function of the "Far-Field Plot Monitor" is issued and explained in an application example.

**Chapter 5:** Chapter 5 gives reasons for the development of phased-array weather radar systems in a dense network. Additionally, a new phased-array weather radar system concept is presented, in order to design a suitable dual-polarized antenna array precisely for this application. Using CST MWS, the initial investigations are carried out with appropriate LFOV (Limited Field of View) antenna configurations for the weather radar application of an X-band radar with a restricted elevation range of about 30 °. Based on the weather radar equation, the output power that transmit and receive modules should provide for a 1x4 array is determined. A subarray configuration of 4x8 arrays with chip-based TRMs and a control FPGA is identified to ensure cost-effective PCB production. The system block diagram also describes the configuration of a large antenna array with complete analogue and digital transmission and reception paths. Solution concepts for highly accurate phase and amplitude calibrations of such a complex, phased-array weather radar system are provided. Given the small number of 50 I/Q- data channels, standard network components can be used by this system concept.

**Chapter 6:** Chapter 6 begins with summarizing and discussing literature references regarding the reduction methods of cross-polar radiation from single radiators. Concerning this, different feeding mechanisms for microstrip patch antennas are analyzed and evaluated. Probe-feed antennas are identified as suitable candidates for use within phased-array weather radar systems. For the first time, circular and square microstrip antennas are investigated and compared with respect to their cross polarization behavior. Furthermore, the effect of the x-polar reduction is discussed by increasing the antenna area and this in turn is evaluated by radiation pattern synthesis. The most promising technology considered for the reduction/suppression of x-polar radiation is the differential-feeding of microstrip antennas. In the case of the differential-feed, to feed an antenna two signals are used, which are phase-shifted by 180 degrees but have the same amplitude. The co-polar and x-polar antenna radiation patterns are then compared to those with the separately fed antennas (single-feed), so that the merits and demerits of these antenna types are apparent for use within the phased-array weather radars. In order to study the formation of x-polar radiation of all microstrip antennas, two new graphical approaches: the field line distribution below the patch and the current distribution on the patch, together with the theoretical cavity model of microstrip antennas, were developed. In this regard, the relevant reasons for the formation and generation of cross-polar radiation components of microstrip antennas have been identified.

**Chapter 7:** Chapter 7 begins by summarizing and discussing literature references regarding the reduction methods of cross-polar radiation in antenna arrays. Controlling the phase state of the individual radiators in antenna arrays, the x-polar radiation can be substantially reduced. Given this purpose, different phase distributions for 1x4 antenna arrays with CST MWS are simulated and then compared to a differential-feed 1x4 antenna array. The purpose of this study is to determine whether arrays with selected phase distributions provide cross polarization suppression results comparable with differential-feed antenna arrays, because the design of differential-feed antenna arrays with their feeding network is very complex and very difficult to implement in phase array radars with multilayer PCBs. Using the 3D field simulation program CST MWS, antenna arrays with 1x4 and 2x4 elements and optimized phase distributions are designed and qualified. After completion of the initial pre-analysis, the most promising phase distribution is applied to a 4x8 antenna array, which is then compared to a differential-feed 4x8 array.

**Chapter 8:** In chapter 8, all theoretical and practical experiences obtained from the previous chapters are used to design pure- and dual-polarized antenna arrays suitable for a weather radar application. Two different antenna types (first, 4x8 antenna array with optimized phase distribution and the second, a differential-feed 4x8 antenna array) are designed for this purpose by means of CST MWS simulation and are verified by the CATR (Compact Antenna Test Range) at the University of RWTH Aachen.Given the very low x-polar radiation contributions of the antennas developed in this chapter, the CATR of the RWTH Aachen University is initially qualified in its measuring accuracies (phase and amplitude) within the "QuietZone" for the co-polar and x-polar polarization patterns.

Furthermore, the sequence in which the different analysis and developments have taken place in order to finally obtain an antenna array with high cross-polar suppression is described in detail. For this reason, the development steps are described by a detailed sequential process. The antenna development is divided into two parts, the development of single radiators and the development of antenna arrays. The design of the dual-polarized individual radiators, which are fed either simply or differentially, is also discussed. The single-feed radiators are then used for phase optimized 4x8 arrays and the differential-feed radiators for the differential-feed 4x8 array. All antennas are measured in the CATR so that the simulation results can be compared with the real measurement data. The two antenna arrays are evaluated in terms of their cross-polarization behavior and, in particular, in phased-array operation over a scanning range of 120°. The phase optimized antenna array is used as an example to investigate the influence of amplitude taper on the cross-polar suppression. Chapter 8 concludes with a summary of all the results obtained.

The amplitude and phase distribution network is explained in detail in Appendix A, which was created under the author's supervision during the bachelor's thesis and was used to measure the antenna arrays in phased-array operation at the University of RWTH Aachen.

The dissertation concludes with a *summary and the conclusions*, and also with a detailed discussion of possible *future research topics* in the antenna and radar system technology.

### Einleitung

Phasengesteuerte Radarsysteme sind schon seit vielen Jahrzenten im Einsatz. Jedoch hat sich die Erforschung von phasengesteuerten Wetterradarsystemen für das Messen und Klassifizieren von Hydrometeoren erst in den letzten Jahren intensiviert.

Wetterradarsysteme sind, im Vergleich zu Detektionsradarsystemen aus dem Militärsektor, hochgenaue Messinstrumente. Ein Hochfrequenzingenieur würde die aktuell erhältlichen Wetterradarsysteme als hochgenaue vektorielle Netzwerkanalysatoren (VNA) bezeichnen. Hierbei entsprechen die zwei Ports des VNA dem horizontalen und vertikalen Polarisationskanal der dual-polarimetrischen Radarantenne. Um Hydrometeore in ihren Geometrien zu klassifizieren, sind die Genauigkeitsanforderungen an polarimetrische Wetterradarsysteme enorm hoch.

Die aktuelle Genauigkeitsanforderung an die Radarhersteller für die Messung der Reflektivitäten (Z) liegt bei unter 0.5 dB. Auch polarimetrische "Produkte" wie die differentielle Reflektivität (ZDR) müssen mit einer Genauigkeit, besser als 0.2 dB, gemessen werden. Diese Messgenauigkeit ist aufgrund des physikalischen Verhaltens einer phasengesteuerten Gruppenantenne nur sehr schwierig zu realisieren. Die meisten phasengesteuerten Antennengruppen verändern ihre Antennenrichtcharakteristik, sobald die Hauptabstrahlrichtung durch phasenverschobene Ansteuerung geändert wird. Die Veränderung der Abstrahlcharakteristik zeigt sich durch das Herabsetzen des Antennengewinns, eine Verbreiterung der Hauptkeule, eine Erhöhung der Nebenkeulen und durch eine signifikante Verschlechterung der Kreuzpolarisationsunterdrückung. Durch Antennenmodellierung und Abschätzverfahren können die co-polaren Antennenparameter wie Halbwertsbreite und Antennengewinn für unterschiedliche Hauptstrahlpositionen über Arrayfaktorkalkulation relativ genau geschätzt werden. Jedoch ist die x-polare Komponente durch klassische Abschätzverfahren nur schwer vorherzusagen. Weiterhin zeigen die aktuell erhältlichen phasengesteuerten Gruppenantennen erhöhte Kreuzpolarisationsanteile beim Schwenk der Hauptkeule, was wiederum sehr nachteilig für die polarimetrische Klassifizierung von Hydrometeoren ist. Genau an dieser Problematik setzt die vorliegende Dissertation an. In dieser Dissertation wird zunächst eine Wetterradarsystemvariante mit phasengesteuerter Gruppenantenne entwickelt und vorgestellt. Hierbei wird der Ansatz verfolgt, die aktuell auf dem Markt erhältlichen und von den Wetterdiensten weltweit betriebenen Hochleistungswetterradarsysteme mit Parabolantennen durch kleine Radare mit phasengesteuerten Gruppenantennen, angeordnet in einem dichten Radarnetzwerk, zu ersetzen. Die detaillierte Wetterradarsystementwicklung mit phasengesteuerter Gruppenantenne wurde durchgeführt, um den Einfluss auf das Antennendesign schon im Vorfeld auszuarbeiten, sodass die phasengesteuerten Mikrostreifenleiterantennen für die Verwendung innerhalb eines neuartigen Wetterradars die effektivste und plausibelste Antennengruppenkonfiguration erhält.

Der Fokus der vorliegenden Arbeit wurde auf die Erforschung und Entwicklung von sehr kreuzpolarisationsarmen, dual-polarimetrischen und phasengesteuerten Mikrostreifenleitergruppenantennen gelegt. In diesem Zusammenhang wurden neue grafische Verfahren entwickelt, die es ermöglichen, die Generierung der kreuzpolaren Anteile von isolierten Mikrostreifenleiterantennen (Einzelpatche) zu erklären und zu minimieren.

Um die kreuzpolaren Anteile weiter herabzusetzen, wurden Optimierungsverfahren für Arrayantennen erforscht, bewertet und neu entwickelt. Zum ersten Mal wurden differentiell gespeiste mit einzeln gespeisten Antennengruppen in ihrem Kreuzpolarisationsverhalten beim elektronischen Schwenk der Hauptkeule verglichen. Zwei dual-polarimetrische 4x8 Antennengruppen (differentiell gespeist und mit optimierter Phasenansteuerung) wurden zu diesem Zweck mittels CST MWS entworfen, simuliert, als Multilagenplatine gefertigt und an der Antennentestanlage der RWTH Aachen vermessen. Die Resultate zeigen, dass die Kreuzpolarisationsanteile bei differentiell gespeisten Mikrostreifenleiterantennen in Antennengruppenkonfiguration, selbst beim elektronischen Schwenk der Hauptkeule, signifikant minimiert werden konnten. Für einen azimutalen Scanbereich von 120° konnte eine exzellente Kreuzpolarisationsunterdrückung zwischen -45 dB und -36 dB messtechnisch für den horizontalen und vertikalen Polarisationskanal nachgewiesen werden.

Die vorliegende Dissertation ist in die *folgenden Kapitel* gegliedert:

Kapitel 1: Es werden die Radargrundlagen eingeführt. Der Leser wird über die Funktion eines gepulsten Dopplerradars, der Herleitung der Punktziel-Radargleichung, der Herleitung der Volumenziel-Wetterradargleichung sowie der Entwicklung der Radargleichung für ein Wetterradar mit planarer und phasengesteuerter Antenne informiert. Nach Einführung des Prinzips eines polarimetrischen Wetterradarsystems werden die grundlegenden polarimetrischen Wetterradarmessgrößen auf Basis der Streumatrix und Kovarianz Matrix erklärt. Die mathematische Implementierung im Wetterradarempfänger geschieht durch Puls-Paar-Prozessierung von I/Q-Signalen, welche nachfolgend detailliert beschrieben wird. Rauschen ist ein sehr wichtiges Thema, auch im Wetterradarbereich. Alle notwendigen Grundlagen diesbezüglich werden ebenfalls in Kapitel 1 dem Leser zur Verfügung gestellt. Das Kapitel 1 schließt mit der Bandbreitenbetrachtung für unterschiedliche Radarsystemvarianten ab.

**Kapitel 2:** Für die detaillierte Diskussion polarimetrischer Antennen und polarimetrischer Wetterradarsysteme ist es erforderlich den Polarisationszustand von elektromagentischen Wellen zu definieren. Konsequenterweise werden dazu die Maxwell'schen Gleichungen eingeführt, welche die Ausbreitung von elektromagnetischen Wellen im Vakuum (z. B. notwendig zur Berechnung eines Antennenrichtdiagramms) und in einem Medium (z. B. im Substrat einer Mikrostreifenleiterantenne) beschreiben. Der Polarisationsstatus von EM-

Wellen wird darauffolgend mit dem Jones Vektor, der Polarisationsellipse und der Poincaré Kugel veranschaulicht.

Kapitel 3: Um die Hintergründe von den in den Folgekapiteln entwickelten dual polarisiereten phasengesteuerten Antennenarrays zu verstehen, werden die theoretischen Grundlagen von Antennen bereitgestellt. Kapitel 3 liefert aus diesem Grund einen Überblick über alle relevanten Antennengrundlagen der Mikrowellentechnik. Speziell werden phasengesteuerte Antennen diskutiert und der Zusammenhang zwischen Elementfaktor von Einzelradiatoren und Antennenarrays erklärt. Aber auch Messdefinitionen wie die Fernfeldund Fresneldefinition werden bereitgestellt. Zum Deuten von polarimetrischen Antennenrichtcharakteristiken werden alle relevanten Definitionen aus der Literatur zusammengefügt dem Leser dargestellt. Besonders wird auf die theoretische Definition eingegangen, welche sich mit den kreuzpolaren Anteilen der Antenne beschäftigt. Nach Einführung der allgemein gültigen Grundlagen für alle Antennen wird sehr detailliert auf den Aufbau, die Funktion (mittels Hohlraumresonator-Modell), die Architektur, die Polarisationsteuerung, die Bandbreitendefinition und das Speisenetzwerkdesign von Mikrostreifenleiterantennen eingegangen. Um Antennenarrays auf Leiterplatten (PCBs) entwerfen zu können werden Gleichungen bereitgestellt, welche die Grundlage zur Berechnung von Phasenkonstanten, Phasengruppengeschwindigkeit und Wellenimpedanzen auf unterschiedlichen dielektrischen Substraten sind. Auch eine Reihe von unterschiedlichen Substratarten und der Einfluss von Substratkenngrößen auf die Antennenparameter werden diskutiert. Im letzten Teil des dritten Kapitels werden lineare und planare phasengesteuerte Antennenarrays betrachtet. Es wird beleuchtet, wie "Mutual Coupling" die Funktion von phasengesteuerten Antennen beeinflusst, mit welchen Polarisationseffekten zu rechnen ist, wenn die Strahlrichtung der Hauptkeule variiert wird und wann es sinnvoll ist, Radiatoren zu Subarrays zusammenzuschalten.

Kapitel 4: CST MWS wurde ausgewählt, um die polarimetrischen Multilagenantennen zu entwerfen und elektromagnetisch zu simulieren. In diesem Kapitel werden die Grundfunktionalitäten des Programms CST MWS erklärt und die numerische Berechnungsmethode FIT (Finite Integration Technik) grafisch beschrieben. Besonders wird auf den "Time Domain Solver" eingegangen, welcher alle Simulationsergebnisse der vorliegenden Dissertation geliefert hat. Auch die Hardwareumgebung und die Simulationszeiten von Einzelradiatoren und Gruppenantennen werden präsentiert. Die Simulationszeiten sind stark abhängig vom ausgewählten "Mesh", also der Diskretisierung des 3D Modells. Alle zu berücksichtigenden Einstellungen zu einem Mesh werden demzufolge ebenfalls eingeführt. Am Ende des vierten Kapitels wird die Optimierungsfunktion von CST MWS unter Berücksichtigung von S-Parameter Werten und auch Antennenmessgrößen gezeigt. Um Antennenschlüsselparameter von sehr großen Arrayantennen mit vielen Tausend Einzelelementen schnell abschätzen zu können, wird die Funktion des "Far-Field-Plot-Monitors" verwendet und an einem Applikationsbeispiel erklärt.

**Kapitel 5:** In Kapitel 5 werden Gründe genannt, die eine Entwicklung von phasengesteuerten Wetterradarsystemen in einem dichten Netzwerk, anstatt der Verwendung von Hochleistungswetterradarsystemen, rechtfertigen. Zudem wird ein neues Wetterradar-Systemkonzept mit phasengesteuerten Gruppenantenne vorgestellt, um in den Folgekapiteln ein geeignetes dual-pol. Antennenarray für genau diese Anwendung zu entwerfen. Mittels CST MWS finden diesbezüglich erste Untersuchungen statt, welche sich mit geeigneten LFOV (Limited Field of View) Antennenkonfigurationen für die Wetterradarapplikation eines X-Band Radars mit eingeschränktem Elevationsbereich von etwa 30° befassen. Anhand der Wetterradargleichung wird die Ausgangsleistung ermittelt, die ein Sende-Empfangsmodul für ein 1x4 Array bereitstellen sollte. Eine Subarray-Konfiguration von 4x8 Arrays mit chipbasierten TRMs und einem Kontroll-FPGA wird identifiziert, um eine kostengünstige Produktion der Leiterplatten zu gewährleisten. Das System-Blockdiagramm beschreibt zudem die Konfiguration einer großen Array Antenne mit komplettem analogen und digitalen Sende- und Empfangspfad. Lösungskonzepte für hochgenaue Phasen- und Amplitudenkalibrationen eines solch komplexen, phasengesteuerten Radarsystems werden bereitgestellt. Durch die geringe Anzahl von 50 I/Q-Datenkanälen können durch dieses Systemkonzept Standard Netzwerkkomponenten verwendet werden.

Kapitel 6: Das Kapitel 6 beginnt mit der Zusammenfassung und der Diskussion von Literaturquellen zu Reduktionsmethoden von kreuzpolarer Strahlung bei Einzelradiatoren. In diesem Zusammenhang werden unterschiedliche Speisemechanismen für Mikrostreifenleiterantennen analysiert und ausgewertet. Probe-Feed Antennen werden als geeignete Kandidaten für die Nutzung innerhalb von phasengesteuerten Wetterradarsystemen identifiziert. Zum ersten Mal werden kreisförmige und quadratische Mikrostreifenleiterantennen untersucht und in ihrem Kreuzpolarisationsverhalten verglichen. Zusätzlich wird der Effekt der kreuzpolaren Reduktion durch Vergrößerung der Antennenfläche diskutiert und anhand von Antennenrichtcharakteristiken ausgewertet. Die vielversprechendste Technologie zur Reduktion von x-polarer Strahlung, die differentielle Speisung von Mikrostreifenleiterantennen, wird genauestens betrachtet. Bei der differentiellen Speisung werden 2 Signale zur Speisung einer Antenne verwendet, welche um 180 Grad phasenverschoben sind, aber die gleiche Amplitude besitzen. Die co-polaren und kreuzpolaren Richtcharakteristiken werden daraufhin denen der separat gespeisten Antennen (single-feed) gegenüber gestellt, sodass die Vor- und Nachteile dieser Antennentypen für die Nutzung innerhalb eines phasengesteuerten Wetterradars ersichtlich wurden. Um die Entstehung von x-polarer Strahlung aller Mikrostreifenleiterantennen zu erforschen wurden zwei neue grafische Ansätze, die Feldlinienverteilung unterhalb des Patches und die Stromverteilung auf dem Patch zusammen mit dem theoretischen Kavitätsmodel von Mikrostreifenleiterantennen, betrachtet. Bei dieser Betrachtung konnten die maßgeblichen Gründe für die Entstehung von kreuzpolaren Strahlungsanteilen von Mikrostreifenleiterantennen identifiziert werden.

**Kapitel 7:** Das Kapitel 7 beginnt mit der Zusammenfassung und der Diskussion von Literaturquellen zu Reduktionsmethoden von kreuzpolarer Strahlung bei Antennengruppen. Durch geeignete Phasenansteuerung der Einzelradiatoren in Antennengruppen kann die x-polare Strahlung nachweislich herabgesetzt werden. Aus diesem Grund werden in diesem Kapitel unterschiedliche Phasenverteilungen für 1x4 Antennenarrays mit CST MWS simuliert und mit einem differentiell gespeisten 1x4 Antennenarray verglichen. Bei dieser Untersuchung soll herausgefunden werden, ob Arrays mit ausgewählten Phasenverteilungen eine vergleichbare Kreuzpolarisationsunterdrückung liefern wie differentiell gespeiste Antennenarrays. Denn das Design von differentiell gespeisten Antennenarrays mit ihren Speisenetzwerken ist sehr komplex und für die Anwendung in einem Radar mit phasengesteuerter Gruppenantenne sehr schwer umsetzbar. Mittels 3D Feldsimulationsprogramm CST MWS werden in Kapitel 7 Antennenarrays mit 1x4 und 2x4 Elementanordnung und optimierter Phasenverteilung entworfen und qualifiziert. Nach Beendigung der ersten Voranalyse wurde die vielversprechendste Phasenverteilung auf ein 4x8 Antennenarray angewandt, welches daraufhin mit einem differentiell gespeisten 4x8 Array verglichen wurde.

**Kapitel 8:** In Kapitel 8 werden alle theoretisch und praktisch erlangten Erfahrungen aus den vorherigen Kapiteln verwendet, um polarisationsreine und dual-polarimetrische Antennenarrays zu entwerfen, welche für eine Wetterradarapplikation geeignet sind. Zwei unterschiedliche Antennentypen (erstens, ein 4x8 Antennenarray mit optimierter Phasenverteilung und zweitens ein differentiell gespeistes 4x8 Antennenarray) werden zu diesem Zwecke entworfen, mittels CST MWS simuliert und messtechnisch in der CATR (Compact Antenna Test Range) der RWTH Aachen verifiziert.

Aufgrund der sehr geringen kreuzpolaren Strahlungseigenschaften der in diesem Kapitel entwickelten Antennen, wird die CATR der RWTH Aachen vor den Verifikationsmessungen in ihren Messeigenschaften qualifiziert und die Messgenauigkeiten innerhalb der "Quiet Zone" für die co-polaren und kreuzpolaren Messungen angegeben.

Weiterhin wird beschrieben, in welcher Reihenfolge die unterschiedlichen Analysen und Entwicklungen stattgefunden haben, um schließlich ein Antennenarray mit hoher Kreuzpolarisationsunterdrückung zu erhalten. Aus diesem Grund sind die Entwicklungsschritte durch einen detaillierten Prozessablauf beschrieben. Die Antennenentwicklung ist aufgeteilt in die Entwicklung von Einzelradiatoren und die Entwicklung von Antennenarrays. Dabei wird zunächst auf das Design der dual-polarimetrischen Einzelradiatoren eingegangen, welche entweder einfach oder differentiell gespeist sind. Die einfach gespeisten Radiatoren werden daraufhin für die phasenoptimierten 4x8 Arrays und die differentiell gespeisten Einzelradiatoren für das differentiell gespeiste 4x8 Array verwendet. Alle Antennen werden in der CATR vermessen, sodass die Simulationsergebnisse mit den realen Messdaten verglichen werden können. Die beiden Antennenarrays werden in ihrem Kreuzpolarisationsverhalten evaluiert und insbesondere bei phasenverschobener Ansteuerung über einen Scanbereich von 120° gegenübergestellt. Das phasenoptimierte Antennenarray wird exemplarisch verwendet, um auch den Einfluss von Amplituden-Taper auf die Kreuzpolarisationsunterdrückung zu untersuchen. Kapitel 8 schließt ab mit einer Zusammenfassung von allen erzielten Ergebnissen.

In **Anhang A** wird das Amplituden- und Phasenschiebernetzwerk beschrieben, welches während einer vom Autor angeleiteten Bachelorarbeit entstand und zur Verifikationsmessung an der RWTH Aachen benutzt wurde. Die Dissertation schließt ab mit einer **Zusammenfassung und den Schlussfolgerungen** sowie einer Diskussion zu möglichen **zukünftigen Forschungsthemen** aus der Antennen- und Radarsystemtechnik.

# Contents

| A  | bstra | ct       |  | 9  |
|----|-------|----------|--|----|
| A  | bstra | ct (Ge   | erman)   | 11 |
| In | trod  | uction   |  | 13 |
| In | trod  | uction   | (German)   | 19 |
| Li | st of | abbre    | viations and symbols   | 29 |
| 1  | Stat  | te-of-tl | he-art radar fundamentals                                      | 49 |
|    | 1.1   | Pulse    | Doppler radar principle  | 50 |
|    | 1.2   | Radar    | equation of a point target                                     | 56 |
|    | 1.3   |          | equation of a volume target                                    | 58 |
|    | 1.4   |          | equation of planar phased-array weather radar                  | 62 |
|    | 1.5   |          | ple of dual polarized weather radar                            | 63 |
|    |       | 1.5.1    | Scattering and Covariance Matrix                               | 64 |
|    |       | 1.5.2    | Polarimetric weather radar observables                         | 65 |
|    |       | 1.5.3    | Pulse pair processing of I/Q signals                           | 68 |
|    | 1.6   | Noise    | in radar systems   | 73 |
|    |       | 1.6.1    | Noise figure   | 74 |
|    |       | 1.6.2    | Antenna temperature  | 75 |
|    |       | 1.6.3    | Noise temperature of a cascaded radar system                   | 76 |
|    |       | 1.6.4    | Minimum detectable signal                                      | 78 |
|    |       | 1.6.5    | Noise signals for monitoring weather radar systems performance | 80 |
|    | 1.7   | Bandy    | vidth aspects in weather radar systems                         | 82 |
| 2  | Ger   | ieral to | erms and definitions in polarimetry                            | 85 |
|    | 2.1   | Descri   | ption and properties of plane waves                            | 85 |
|    | 2.2   | The J    | ones vector  | 88 |
|    | 2.3   | Comp     | lex polarization ratio   | 89 |
|    | 2.4   |          | sation ellipse and Poincaré sphere                             | 89 |
| 3  | Rel   | evant i  | microwave antenna fundamentals                                 | 93 |
|    | 3.1   | Gener    | al terms and definitions in microwave antennas                 | 93 |

|   | 3.2 | Relevant definitions for antenna pattern synthesis                           | 99  |
|---|-----|--|-----|
|   | 3.3 | Microstrip antennas  | 101 |
|   |     | 3.3.1 General design aspects for microstrip lines                            | 101 |
|   |     | 3.3.2 Substrates   | 104 |
|   |     | 3.3.3 Cavity model for microstrip antennas                                   | 106 |
|   |     | 3.3.4 Microstrip radiator shapes   | 112 |
|   |     | 3.3.5 Microstrip antenna architetures  | 114 |
|   |     | 3.3.6 Dual linear and circular polarized microstrip radiators                | 116 |
|   |     | 3.3.7 Microstrip antenna feeding networks                                    | 117 |
|   |     | 3.3.8 Bandwidth and efficiency of microstrip patch antennas                  | 120 |
|   | 3.4 | Phased array antenna theory  | 122 |
|   |     | 3.4.1 Linear phased-array antenna pattern                                    | 122 |
|   |     | 3.4.2 Planar phased-array antenna pattern                                    | 124 |
|   |     | 3.4.3 Properties of radiation pattern in antenna arrays                      | 125 |
|   |     | 3.4.4 Factors affecting mutual coupling in phased-array antennas             | 128 |
|   |     | 3.4.5 Polarization aspects for dual polarized planar phased-array antennas   | 130 |
|   |     | 3.4.6 Subarrays in phased-array antennas                                     | 132 |
| 4 | Des | ign and 3D EM field simulations using CST MWS                                | 135 |
|   | 4.1 | Hardware environment and experienced duration of simulation                  | 135 |
|   | 4.2 | Transient Solver using Finite Integral Technique                             | 136 |
|   | 4.3 | Meshing  | 136 |
|   | 4.4 | Boundary conditions for antenna design                                       | 138 |
|   | 4.5 | Simulation of antenna far field pattern                                      | 140 |
|   | 4.6 | Optimization functions   | 143 |
| 5 | Svs | tem design of polarimetric X-Band phased-array weather radar                 | 145 |
| Ŭ | 5.1 | Introduction   | 145 |
|   | 5.2 |  | 146 |
|   | 5.3 |  | 149 |
|   | 5.4 | Summary  | 157 |
| 6 | Un  | lerstanding and optimizing microstrip patch antenna cross polar-             |     |
| U |     |  | 159 |
|   | 6.1 | Introduction   | 160 |
|   | 6.2 | X-pol suppression techniques on element level, known from literature         | 161 |
|   | 6.3 | Feeding methods for low x-pol radiation in microstrip array design           | 161 |
|   | 6.4 | Thorough analysis of the differential feeding technique for phased-array     |     |
|   |     | weather radar applications   | 162 |
|   |     | 6.4.1 Analysis of potential x-pol sources in microstrip patch antenna design | 173 |
|   |     | 6.4.2 Probe-feed microstrip patches with plugged via holes                   | 173 |
|   |     | 6.4.3 Bended square patch antenna edges                                      | 174 |

|   |     | 6.4.4 CPS comparison of circular and square shaped microstrip patch an-   |
|---|-----|---|
|   |     | <ul><li>tenna elements</li></ul>  |
|   |     | <ul><li>shielding GND of the patch antenna</li><li>6.4.6 Analysis of antenna patch size</li></ul>   |
|   | 65  | v i   |
|   | 6.5 | Understanding the generation patch antenna x-pol radiation by using the new visual based field line and surface current distribution approach |
|   |     | 6.5.1 Discussion on patch antenna cavity model  |
|   |     | 6.5.2 Visual based field line distribution approach for x-pol explanation .   |
|   |     | 6.5.3 Visual based surface current distribution approach for x-pol expla-<br>nation   |
|   | 6.6 | Summary of observations   |
| 7 | -   | imum phase excitation in limited field of view antenna arrays to  |
|   |     | ace cross polarization radiation  |
|   | 7.1 | Introduction  |
|   | 7.2 | Literature research about radiator configurations in array antennas to reduce x-pol radiation   |
|   | 7.3 | Analysis of x-pol radiation patterns for different phase excitation distribu-<br>tions of mirrored radiators in 1x4 antenna arrays            |
|   | 7.4 | Analysis of x-pol radiation patterns for different phase excitation distribu-   |
|   |     | tions of mirrored radiators in 2x4 antenna arrays   |
|   | 7.5 | Comparison in x-pol performance of 4x8 arrays with single- and differential feeding   |
|   | 7.6 | Design considerations for single and differential-feed 4x8 antenna arrays with  |
|   | 1.0 | dual polarization capability  |
|   | 7.7 | Summary of observations   |
|   |     |   |
| 8 |     | relopment, design and verification of dual polarized antennas with<br>imized cross polarization pattern for phased-array weather radar        |
|   |     | lications   |
|   | 8.1 | Introduction  |
|   | 8.2 | Antenna verification at RWTH Aachen Compact Antenna Test Range  |
|   |     | 8.2.1 Quiet zone investigation  |
|   |     | 8.2.2 CATR set-up for phased-array antenna operation  |
|   | 8.3 | Discussion on antenna specification   |
|   | 8.4 | The phased-array antenna design process   |
|   | 8.5 | Development and design of a single probe-feed dual polarized microstrip   |
|   | 0.0 | patch antenna   |
|   |     | 8.5.1 Design overview of the single probe-feed dual polarized microstrip  |
|   |     |   |
|   |     | 8.5.2 Discussion of the results   |

|  | Development and design of a differential-feed and dual polarized microstrip   |   |
|--|---|---|
|  | patch antenna   | 2   |
|  | 8.6.1 Design overview of the single differential-feed dual polarized mi-  |   |
|  | crostrip patch antenna  | 2   |
|  | 8.6.2 Discussion of the results   | 2   |
| 8.7  | Development and design of a dual-polarized microstrip patch antenna array   |   |
|  | with optimum phase excitation   | 22  |
|  | 8.7.1 Design overview of a dual polarized microstrip patch antenna array  |   |
|  | with optimum phase excitation   | 22  |
|  | 8.7.2 Discussion of the results   | 22  |
| 8.8  | Development and design of a differential-feed and dual polarized microstrip   |   |
|  | patch antenna array   | 24  |
|  | 8.8.1 Design overview of a dual polarized microstrip patch antenna array  | _   |
|  | with differential-feeding   | 24  |
|  | 8.8.2 Discussion of the results   | 24  |
| 8.9  | Summary of observations   | $\frac{24}{26}$   |
| 0.9  |   |   |
| Summ   | ary and Conclusions   | <b>2</b>  |
|  |   |   |
|  |   |   |
| Summ   | ary and Conclusions (German)  | 2'  |
|  |   |   |
|  | ary and Conclusions (German)<br>e Outlook and Suggestions   |   |
| Future                                       | e Outlook and Suggestions   | 28  |
| Future<br>Appen                              | e Outlook and Suggestions<br>adix A   | 27<br>28<br>28  |
| Future<br>Appen                              | e Outlook and Suggestions<br>dix A<br>X-Band phase- and amplitude distribution network for phased-array antenna   | 28<br>28  |
| Future<br>Appen                              | e Outlook and Suggestions<br>dix A<br>X-Band phase- and amplitude distribution network for phased-array antenna<br>measurements   | 28<br>28<br>28  |
| Future<br>Appen                              | e Outlook and Suggestions<br>dix A<br>X-Band phase- and amplitude distribution network for phased-array antenna<br>measurements   | 28<br>28<br>28<br>28  |
| Future<br>Appen                              | e Outlook and Suggestions<br>dix A<br>X-Band phase- and amplitude distribution network for phased-array antenna<br>measurements   | 28<br>28<br>28<br>28<br>28  |
| Future<br>Appen                              | e Outlook and Suggestions<br>dix A<br>X-Band phase- and amplitude distribution network for phased-array antenna<br>measurements   | 28<br>28<br>28<br>28<br>28  |
| Future<br>Appen                              | e Outlook and Suggestions<br>dix A<br>X-Band phase- and amplitude distribution network for phased-array antenna<br>measurements   | 28<br>28<br>28  |
| Future<br>Appen                              | e Outlook and Suggestions<br>dix A<br>X-Band phase- and amplitude distribution network for phased-array antenna<br>measurements   | 28<br>28<br>28<br>28<br>28<br>28<br>28  |
| Future<br>Appen                              | <ul> <li>e Outlook and Suggestions</li> <li>adix A</li> <li>X-Band phase- and amplitude distribution network for phased-array antenna measurements</li> <li>A.1.1 Introduction</li> <li>A.1.1 Einleitung</li> <li>A.1.2 System set-up of phase- and amplitude distribution network to measure the antenna performance</li> <li>A.1.3 Labview graphical user interface for amplitude- and phase control</li> </ul>   | 288<br>288<br>288<br>288<br>288<br>288<br>288<br>288  |
| Future<br>Appen                              | <ul> <li>e Outlook and Suggestions</li> <li>adix A</li> <li>X-Band phase- and amplitude distribution network for phased-array antenna measurements</li> <li>A.1.1 Introduction</li> <li>A.1.1 Einleitung</li> <li>A.1.2 System set-up of phase- and amplitude distribution network to measure the antenna performance</li> <li>A.1.3 Labview graphical user interface for amplitude- and phase control</li> <li>A.1.4 Design overview of the phase- and amplitude distribution network analyzed</li> </ul>  | 28<br>28<br>28<br>28<br>28<br>28<br>28<br>28<br>28<br>28<br>28<br>28<br>28<br>2               |
| Future<br>Appen                              | <ul> <li>Outlook and Suggestions</li> <li>dix A</li> <li>X-Band phase- and amplitude distribution network for phased-array antenna measurements</li> <li>A.1.1 Introduction</li> <li>A.1.1 Einleitung</li> <li>A.1.2 System set-up of phase- and amplitude distribution network to measure the antenna performance</li> <li>A.1.3 Labview graphical user interface for amplitude- and phase control</li> <li>A.1.4 Design overview of the phase- and amplitude distribution network</li> <li>A.1.5 Absolute phase- and amplitude calibration using vector network analyze</li> <li>A.1.6 Hardware development experience gained for future TRM design</li> </ul>                                | 28<br>28<br>28<br>28<br>28<br>28<br>28<br>28<br>28<br>28<br>28<br>28<br>28<br>2               |
| Future<br>Appen                              | <ul> <li>e Outlook and Suggestions</li> <li>adix A</li> <li>X-Band phase- and amplitude distribution network for phased-array antenna measurements</li> <li>A.1.1 Introduction</li> <li>A.1.1 Einleitung</li> <li>A.1.2 System set-up of phase- and amplitude distribution network to measure the antenna performance</li> <li>A.1.3 Labview graphical user interface for amplitude- and phase control</li> <li>A.1.4 Design overview of the phase- and amplitude distribution network analyzed</li> </ul>  | 28<br>28<br>2<br>2<br>2<br>2<br>2<br>2<br>2<br>2<br>2<br>2<br>2<br>2<br>2<br>2<br>2<br>2<br>2 |
| Future<br>Appen<br>A.1                       | <ul> <li>Outlook and Suggestions</li> <li>dix A</li> <li>X-Band phase- and amplitude distribution network for phased-array antenna measurements</li> <li>A.1.1 Introduction</li> <li>A.1.1 Einleitung</li> <li>A.1.2 System set-up of phase- and amplitude distribution network to measure the antenna performance</li> <li>A.1.3 Labview graphical user interface for amplitude- and phase control</li> <li>A.1.4 Design overview of the phase- and amplitude distribution network</li> <li>A.1.5 Absolute phase- and amplitude calibration using vector network analyze</li> <li>A.1.6 Hardware development experience gained for future TRM design</li> </ul>                                | 2:<br>2<br>2<br>2<br>2<br>2<br>2<br>2<br>2<br>2<br>2<br>2<br>2<br>2<br>2<br>2<br>2<br>2<br>2  |
| Future<br>Appen<br>A.1                       | <ul> <li>Outlook and Suggestions</li> <li>dix A</li> <li>X-Band phase- and amplitude distribution network for phased-array antenna measurements</li> <li>A.1.1 Introduction</li> <li>A.1.1 Einleitung</li> <li>A.1.2 System set-up of phase- and amplitude distribution network to measure the antenna performance</li> <li>A.1.3 Labview graphical user interface for amplitude- and phase control</li> <li>A.1.4 Design overview of the phase- and amplitude distribution network</li> <li>A.1.5 Absolute phase- and amplitude calibration using vector network analyze</li> <li>A.1.6 Hardware development experience gained for future TRM design</li> <li>A.1.7 Summary</li> </ul>         | 28<br>28<br>2<br>2<br>2<br>2<br>2<br>2<br>2<br>2<br>2<br>2<br>2<br>2<br>2<br>2<br>2<br>2<br>2 |
| Future<br>Appen<br>A.1<br>List of<br>List of | <ul> <li>Outlook and Suggestions</li> <li>dix A</li> <li>X-Band phase- and amplitude distribution network for phased-array antenna measurements</li> <li>A.1.1 Introduction</li> <li>A.1.1 Einleitung</li> <li>A.1.2 System set-up of phase- and amplitude distribution network to measure the antenna performance</li> <li>A.1.3 Labview graphical user interface for amplitude- and phase control</li> <li>A.1.4 Design overview of the phase- and amplitude distribution network analyze</li> <li>A.1.5 Absolute phase- and amplitude calibration using vector network analyze</li> <li>A.1.6 Hardware development experience gained for future TRM design</li> <li>A.1.7 Summary</li> </ul> | 2<br>2<br>2<br>2<br>2<br>2<br>2<br>2<br>2<br>2<br>2<br>2<br>2<br>2<br>2<br>2<br>2<br>2<br>2   |

# List of Abbreviations and Symbols

### Abbreviations

| 3D        | Three dimensional  |
|-----------|--|
| ADC       | Analogue to Digital Converter  |
| AF        | Array Factor   |
| AMR       | Antenna-Mounted weather radar receiver   |
| ATAR      | Alternating Transmit and Alternating Receive                                     |
| ATSR      | Alternating Transmit and Simultaneous Receive                                    |
| AUT       | Antenna Under Test   |
| BITE      | Built- In Test Equipment   |
| BSA       | Backward Scattering Alignment  |
| CASA      | Engineering Research Center for Collaborative Adaptive Sensing of the Atmosphere |
| CATR      | Compact Antenna Test Range   |
| C-Band    | Frequency band 4 GHz to 8 GHz, IEEE Std. $321-2002$ (2003)                       |
| COTS      | Commercial off-the-shelf   |
| co - pol  | Copolar Polarization   |
| CPS       | Cross Polarization Suppression   |
| CPU       | Central Processing Unit  |
| CRC       | Central Radar Computer   |
| CST - MWS | CST- Microwave Studio  |

| DAC          | Digital to Analogue Converter  |
|--------------|--|
| dBi          | Decibel isotropic  |
| dBm          | Decibel milliwatts   |
| DC           | Direct current   |
| DLR          | Deutsches Zentrum für Luft- und Raumfahrt, engl. German Aerospace Center |
| DRAO         | Dominion Radio Astrophysical Observatory                                 |
| DRXCU        | Digital Receiver and Calibration Unit                                    |
| EBG          | Electric Band Gap  |
| E-Cut        | Electric field plane cut   |
| EF           | Element Factor   |
| EM           | Electromagnetic  |
| ENR          | Excess Noise Ratio   |
| EP           | Element Pattern  |
| e-scan       | Electronic scan  |
| FDTD         | Finite difference time domain  |
| Feed - V - 1 | First feed of vertical port  |
| Feed - V - 2 | Second feed of vertical port   |
| Feed - V - 1 | First feed of horizontal port  |
| Feed - V - 2 | Second feed of horizontal port   |
| FEM          | Finite element method  |
| FFT          | Fast Fourier Transformation  |
| FIT          | Finite Integration Technique   |
| FPGA         | Field Programmable Gate Array  |
| GND          | Ground   |
| GPS          | Global Positioning System  |

### LIST OF ABBREVIATIONS AND SYMBOLS

| GPU          | Graphical Processor Unit                          |
|--------------|---|
| H-Cut        | Magnetric field plane cut                         |
| HH           | Horizontal transmit and Horizontal receive        |
| H - Pol      | Horizontal Polarization                           |
| HV           | Horizontal transmit and Vertical receive          |
| Ι            | In phase  |
| ICPR         | Integrated Cross Polarization Ratio               |
| $ICPR_2$     | Two way Integrated Cross Polarization Ratio       |
| ICPS         | Integrated Cross Polarization Suppression         |
| IEEE         | Institute of Electrical and Electronics Engineers |
| IF           | Intermediate Frequency                            |
| Im           | Imaginary part                                    |
| L            | Length  |
| LNA          | Low Noise Amplifier                               |
| LFoV         | Limited Field of View                             |
| LHCP         | Left Hand Circular Polarization                   |
| LoPro        | Rogers substrate series with smoother copper      |
| LOU          | Local Oscillator Unit                             |
| MDS          | Minimum Detectable Signal                         |
| MMIC         | Monolithic Microwave Integrated Circuit           |
| MPL          | Microstrip Path Loss                              |
| MSL          | Microstrip line                                   |
| NVIDIA-Tesla | Type of graphic board (used here as GPU)          |
| RAM          | Random Access Memory                              |
| PAR          | Phased Array Radar                                |
| PAWR         | Phased Array Weather Radar                        |

| PBA           | Perfect Boundary Approximation  |
|---------------|---|
| PCB           | Printed Circuit Board   |
| PCG           | Pulse compression gain  |
| PJC           | Probert Jones Correction  |
| PN            | Pseudo Noise  |
| PPI           | Planar Position Indicator   |
| PRAWDCU       | Realtime RAW Control Unit   |
| PRT           | Pulse Repetition Time   |
| PTFE          | Polytetrafluoroethylene   |
| PW            | Pulse Width   |
| Q             | Quadrature phase  |
| RCS           | Radar Cross Section   |
| RCU           | Realtime Control Unit   |
| Re            | Real part of complex number   |
| RF            | Radio Frequency   |
| RHCP          | Right Hand Circular Polarization  |
| RHI           | Range Height Indicator  |
| RO4330B       | Rogers substrate RO4330   |
| RO4430F       | Rogers prepreg RO4430F  |
| 31HF          | ROHACELL 31HF foam material   |
| <i>RS</i> 232 | A standard for serial communication transmission of data in telecommunication |
| RWTH          | Rheinisch-Westfälische Technische Hochschule                                  |
| RX            | Receive   |
| SAR           | Synthetic Aperture Radar  |
| S-Band        | Frequency band 2 GHz to 4 GHz, IEEE Std. 321-2002 (2003)                      |

### LIST OF ABBREVIATIONS AND SYMBOLS

| SLS          | Sidelobe Suppression                                      |
|--------------|---|
| SMP          | Subminiature Push-On (connector)                          |
| SNR          | Signal to Noise Ratio                                     |
| SR           | Splitter ratio  |
| SSTX         | Solid state transmitter                                   |
| STALO        | Stable Local Oscillator                                   |
| STSR         | Simultaneous Transmit and Simultaneous Receive            |
| SW           | Switch  |
| TEM          | Transversal electromagnetic                               |
| TerraSAR - X | A radar earth observation satellite working on X-Band     |
| T-junction   | A type of power divider                                   |
| TL           | Transmission line   |
| TRM          | Transmit- Receive Module                                  |
| TST          | Thin Sheet Technique                                      |
| TX           | Transmit  |
| u            | Angular variable  |
| VH           | Vertical transmit and Horizontal receive                  |
| VNA          | Vector Network Analyzer                                   |
| V - Pol      | Vertical Polarization                                     |
| VSWR         | Voltage Standing Wave Ratio                               |
| VV           | Vertical transmit and Vertical receive                    |
| WLAN         | Wireless Local Area Network                               |
| X - Band     | Frequency band 8 GHz to 12 GHz, IEEE Std. 321-2002 (2003) |
| x - pol      | Cross Polarization  |

### Mathematical Symbols

| $\langle \rangle$      | Expectation values            |
|------------------------|-------------------------------|
| $\langle ab^* \rangle$ | Covariance between a and b    |
| a                      | Absolute                      |
|                        | Interior product              |
| ×                      | Outer product (Cross product) |
| $\bigtriangledown$     | Nabla the gradient operator   |
| $\bigtriangledown^2$   | Laplace operator              |
| *                      | Complex conjugate             |
| j                      | $\sqrt{-1}$                   |
| ln                     | $log_e$                       |
| $\Re$                  | Real part                     |
| $\Im$                  | Imaginary part                |

### Symbols

| α                | Angle between beam axis and the normal of the planar antenna array in section $1.4$ |
|------------------|---|
| $\alpha$         | Attenuation constant in chapter $3$   |
| $lpha_c$         | Conductor attenuation   |
| $lpha_d$         | Dielectric attenuation  |
| β                | Phase constant  |
| δ                | Phase difference  |
| $\Delta \Phi_x$  | Inter- element phase shift  |
| $\Delta R$       | Range resolution  |
| $\Delta R_{PCR}$ | Range resolution with pulse compression   |
| $\Delta t$       | Traveling time of pulse from antenna to target and back to the antenna              |

### LIST OF ABBREVIATIONS AND SYMBOLS

| $\Delta_t$         | Estimated time of flight                          |
|--------------------|---|
| $\delta_x$         | Zero phase of x- direction vector component       |
| $\delta_y$         | Zero phase of y- direction vector component       |
| $\Delta R$         | Minimum range resolution                          |
| $\Delta t$         | Time of flight                                    |
| $\epsilon$         | Permittivity (F/m)                                |
| $\epsilon'$        | Real part of the complex permittivity             |
| $\epsilon''$       | Imaginary part of the complex permittivity        |
| $\epsilon_0$       | Vacuum permittivity                               |
| $\epsilon_e$       | Effective dielectric constant                     |
| $\epsilon_L$       | Losses of the distribution network                |
| $\epsilon_m$       | Permittivity of the electric field modes m        |
| $\epsilon_n$       | Permittivity of the electric field modes <b>n</b> |
| $\epsilon_p$       | Constant for cavity eigenfunctions                |
| $\epsilon_r$       | Dielectric constant, relative permittivity        |
| $\epsilon_r^{eff}$ | Effective permittivity                            |
| $\epsilon_T$       | Efficiency of antenna taper function              |
| $\epsilon_x$       | X-component of anisotropic substrate matrix       |
| $\epsilon_y$       | Y-component of anisotropic substrate matrix       |
| $\epsilon_z$       | Z-component of anisotropic substrate matrix       |
| η                  | Antenna efficiency                                |
| $\eta_{min}$       | Minimum antenna efficiency                        |
| $\eta_R$           | Radiation efficiency of the antenna               |
| $\eta_{RR}$        | Effective radar reflectivity                      |
| Γ                  | Reflection coefficient                            |
| $\gamma$           | Propagation constant                              |
|                    |   |

| $ \Gamma $           | Absolute value of the complex reflection coefficient S11   |
|----------------------|--|
| κ                    | Electrical conductivity (S/m)  |
| λ                    | Wavelength   |
| $\mu$                | Permeability $(H/m)$   |
| $\mu_0$              | Vacuum permeability  |
| $\mu_r$              | Magnetic constant, relative permeability   |
| Ω                    | Beam solid angle   |
| $\omega_0$           | Angular frequency  |
| $\Phi$               | Orientation angle  |
| $\Phi_u$             | Element to element phase shift in u-plane  |
| $\Phi_v$             | Element to element phase shift in v-plane  |
| $\phi_0$             | Broadside 3 dB beamwidth in the $\phi$ plane   |
| $\phi_{DP}$          | Differential propagation phase   |
| $\phi_{DP}^{OFFSET}$ | Offset of differential propagation phase   |
| $\phi_{HH}$          | Cumulative phase from horizontal plane waves for the total<br>round trip between radar and the resolution volume |
| $\phi_{VV}$          | Cumulative phase from vertical plane waves for the total round<br>trip between radar and the resolution volume   |
| $\psi$               | Beam angle measured in y-z plane   |
| $\psi_{mn}$          | Eigenfunctions of the electric field modes (m,n)   |
| ho                   | Amplitude ration of complex polarization ratio   |
| ρ                    | Complex polarization ratio in section 2.2  |
| ρ                    | Electric charge density $(C/m^3)$ in section 2.1   |
| $ ho_{co}$           | Co-polar correlation coefficient   |
| σ                    | Radar cross section  |
| $\sigma_i$           | Radar cross section of the i-th backscattering hydrometeor   |
|                      |  |

36

| $\sigma(D)$               | Radar cross section of a backscattering hydrometeor with diameter D  |
|---------------------------|--|
| $\sigma^{HH}(D)$          | Radar cross section of a backscattering hydrometeor with di-<br>ameter D, illuminated with H-Pol and received with H-Pol               |
| $\sigma^{VV}(D)$          | Radar cross section of a backscattering hydrometeor with di-<br>ameter D, illuminated with V-Pol and received with V-Pol               |
| $\sigma^{HV}(D)$          | Corss polar radar cross section of a backscattering hydrometeor<br>with diameter D, illuminated with H-Pol and received with V-<br>Pol |
| $tan(\delta)$             | Loss tangent   |
| $tan(\gamma)$             | Amplitude ratio between two components of the Jones vector   |
| $ \tau $                  | Ellipticity angle  |
| $\Theta_0$                | Broadside 3 dB beamwidth in the principle plate at bore<br>sight direction   |
| $\Theta_H^\circ$          | 3dB antenna beamwidth in degree for one polarization plane in H- plane   |
| $\Theta_E^\circ$          | 3dB antenna beamwidth in degree for one polarization plane in E- plane   |
| $\theta$                  | Orientation angle $\theta$   |
| $\theta_0$                | Scan angle   |
| $	heta_{3dB}$             | 3 dB beamwidth of the main lobe  |
| $\theta_{3dB}(boresight)$ | 3 dB beamwidth in $\theta\text{-}$ cut   |
| $	heta_{boresight}$       | Broadside 3 dB beamwidth in $\theta\text{-}$ cut   |
| $	heta_E$                 | 3dB beamwidth in the E- plane of micorstrip antenna in section $3.3.3$   |
| $	heta_E$                 | 3dB antenna beamwidth in radians for one polarization plane in E- plane  |
| $	heta_{H}$               | 3dB beamwidth in the H- plane of micorstrip antenna in section $3.3.3$   |
| $	heta_H$                 | 3dB antenna beamwidth in radians for one polarization plane in H- plane  |

| ξ                     | Beam angle measured in x-z plane                           |
|-----------------------|--|
| A                     | Physical antenna area                                      |
| $A_{Cell}$            | Geometrical antenna area                                   |
| $A_E$                 | Effective antenna area                                     |
| $A_{mn}$              | The amplitude coefficients of cavity eigenfunctions        |
| $A_n$                 | Complex excitation coefficient                             |
| $A_Z$                 | Physical target cross section                              |
| Ant                   | Antenna  |
| AR                    | Axial Ratio  |
| $a_n$                 | Element weighting coefficient                              |
| $a_x$                 | X- direction vector component amplitude                    |
| $a'_x$                | Adjacent side in the polarization ellipse                  |
| $a_y$                 | Y- direction vector component amplitude                    |
| $a'_y$                | Cathetus side in the polarization ellipse                  |
| $\overline{B}$        | Magnetic flux density (Wb/m2)                              |
| В                     | Bandwidth  |
| $B_b$                 | Broadening factor  |
| $B_{MF}$              | Matched filter bandwidth                                   |
| $B_{pulse}$           | Pulse bandwidth  |
| C                     | Capacitor of Transmition line                              |
| CV                    | Corrected doppler velocity (m/s)                           |
| CW                    | Corrected spectral width (m/s)                             |
| CZ                    | Corrected Reflectivity                                     |
| <i>c</i> <sub>0</sub> | Speed of light in vacuum (2.99792458 x $10^8 \ {\rm m/s})$ |
| $c_{Athm}$            | Atmospheric attenuation constant                           |
| Cradar                | Radar constant   |

| $C_{SP}$             | A constant to transfer arbitrary power units to dBm                |
|----------------------|--|
| $\overline{D}$       | Electric flux density $(C/m2)$                                     |
| D                    | Backscattering drop diameter section $1.3$                         |
| D                    | Antenna directivity  |
| $D_{Cell}$           | Directivity of a single antenna element                            |
| $D_i$                | Diameter of the i-th hydrometeor                                   |
| $D_{max}$            | Maximum antenna directivity  |
| $D_{patch}$          | Directivity of the patch   |
| $D_x D_y$            | Patch antenna cross sectional area                                 |
| $D(	heta,\phi)$      | Directivity distribution of the antenna radiation pattern          |
| $d_{pol}$            | Degree of polarization   |
| $d_x$                | Inter-element-spacing in x-plane                                   |
| $d_y$                | Inter-element-spacing in y-plane                                   |
| $\angle E_{Co}$      | Phase value of copolar electric field                              |
| $\overline{E}$       | Electric field intensity $(V/m)$                                   |
| <u>E</u>             | Electric field vector at zero Time and space                       |
| $[E]^i$              | Incident electrical field vector                                   |
| $[E]^S$              | Backscattering electrical field vector                             |
| $E_{\Phi}$           | $\Phi$ electric field component in spherical coordinate system     |
| $E_{\phi}$           | $\phi$ electrical field component in spherical coordinate system   |
| $E_{\phi}(\Theta)$   | H- plane cut of the antenna radiation pattern derived by two slots |
| $E_{\Theta}$         | $\Theta$ electric field component in spherical coordinate system   |
| $E_{\Theta}(\Theta)$ | E- plane cut of the antenna radiation pattern derived by two slots |
| $E_{	heta}$          | $\theta$ electrical field component in spherical coordinate system |
| $E_0$                | Value of electric field component                                  |
|                      |  |

| 40                       | LIST OF ABBREVIATIONS AND SYMBOLS   |
|--------------------------|---|
| $ec{E_1}$                | Horizontal polarized field vector   |
| $ec{E_2}$                | Vertical polarized field vector   |
| $ec{E_a}$                | Electric field in a slot of length W and height H                               |
| $E_H$                    | Horizontal Electrical field component for Ludwig 3 transformation               |
| $\hat{e}_{ m H}$         | x-pol vector for visual explanation in section $6.5.2$                          |
| $\underline{E}_{R}(z,t)$ | Time and space-variant electric field vector                                    |
| $E_V$                    | Vertical Electrical field component for Ludwig 3 transformation                 |
| $E_x$                    | Electric field components in x-axis at zero time and space                      |
| $E_x(z,t)$               | Time- and space-variant electric field components in x-axis                     |
| $E_y$                    | Electric field components in y-axis at zero time and space                      |
| $E_y(z,t)$               | Time- and space-variant electric field components in y-axis                     |
| $EIRP_{Linear}$          | Equivalent Isotropic Radiated Power in linear units                             |
| $EIRP_{log}$             | Equivalent Isotropic Radiated Power in logarithmic units                        |
| $e_Z$                    | Z- unit vector for the direction of wave propagation                            |
| $eirp_{linear}$          | Equivalent isotropically radiated power   |
| F1                       | Array factor of slot 1  |
| F2                       | Array factor of slot 2  |
| $F3(\theta)$             | Array factor of 2 slots with correction factor (GND, Substrate) for the E plane |
| $F4(\theta)$             | Array factor of 2 slots with correction factor (GND, Substrate) for the H plane |
| $F_E(	heta)$             | Array factor of 2 slots for the E plane cut                                     |
| $F_H(	heta)$             | Array factor of 2 slots for the H plane cut                                     |
| $ar{f}$                  | Forward scattering amplitude  |
| f                        | Frequency   |
| $f_0$                    | Carrier Frequency   |

| $f_{copol}$    | Co-polarized antenna radiation to retrive $ICPR_2$              |
|----------------|---|
| $f_D$          | Doppler frequency   |
| $f_{dmax}$     | Maximum Doppler frequency                                       |
| $f_s$          | Sample frequency  |
| $f_{xpol}$     | X-polarized antenna radiation patterns to retrive $ICPR_2$      |
| F(u)           | 2D Radiation pattern of linear arrays                           |
| F(u, v)        | 3D Antenna radiation pattern for planar antenna arrays          |
| G              | Antenna gain  |
| $G_{\theta}$   | Antenna gain at angle position $\theta$                         |
| $G_{\theta_0}$ | Antenna gain at angle position $\theta_0$ , typically boresight |
| $g_0$          | Stoke vector element $g_0$ , wave intensity                     |
| $g_1$          | Stoke vector element $g_1$                                      |
| $g_2$          | Stoke vector element $g_2$                                      |
| $g_3$          | Stoke vector element $g_3$                                      |
| $G_{DUT}$      | Gain of Device Under Test                                       |
| $G_E$          | Antenna gain in receive   |
| $G_E^0$        | Broadside received antenna gain                                 |
| $G_{int}$      | Incoherent integration gain                                     |
| $G_{patch}$    | Gain of patch   |
| $G_{RX}$       | Received gain   |
| $G_S$          | Antenna gain in transmit  |
| $G^0_S$        | Broadside transmitted antenna gain                              |
| $G_Z$          | Gain or loss factor for irregular radar targets                 |
| Н              | Height in microstrip patch antenna                              |
| $\bar{H}$      | Magnetic field intensity (A/m)                                  |
| h              | Substrate height  |
|                |   |

| 42                       | LIST OF ABBREVIATIONS AND SYMBOLS   |
|--------------------------|---|
| h                        | Pulse length in space (pulse width multiplied with speed of light) in section $1.3$ |
| $\hat{h}$                | Horizontal polarization unit vector   |
| $\underline{H}_{R}(z,t)$ | Time and space-variant magnetic field vector  |
| i                        | Input   |
| $I_0$                    | Patch antenna excitation current  |
| $I_m$                    | The real part of the received echo voltage without considering clutter suppression  |
| $\bar{J}$                | Electric current density $(A/m2)$   |
| $J_b$                    | Current density below the patch   |
| $J_S$                    | Equivalent current density of side slots  |
| $J_t$                    | Equivalent current density moving on the top of the patch by excitation             |
| $J_z$                    | The excitation current density from coaxial or microstrip feed                      |
| K                        | Constant for antenna amplitude tapper   |
| $ K ^{2}$                | Complex refraction and absorption coefficient of a dielectric sphere (or drop)      |
| k                        | Boltzmann constant (1.38064832 $\cdot$ $10^{-23} \rm J/K)$                          |
| $k_0$                    | Wave number in free space   |
| $K_{DP}$                 | Specific differential phase   |
| $k_m$                    | Constant of eigenfunction depending on patch length                                 |
| $k_{mn}$                 | Constant of eigenfunction depending on patch length and width                       |
| $k_n$                    | Constant of eigenfunction depending on patch width                                  |
| L                        | Loss factor in section $1.6$  |
| L                        | Antenna length or slot distance in chapter $3$                                      |
| $L_{ m CPS}^{ m opt}$    | Length of a quadratic patch antenna element with optimized x-pol performance        |
| $L_{MF}$                 | Matched Filter Losses   |

| $L_T$             | Loss factor of transmission line   |
|-------------------|--|
| $L_{DR}$          | Linear depolarization ratio  |
| $L_{DR_{HV}}$     | Linear depolarization ratio (horizontal transmit and vertical receive in logarithmic units)                          |
| $L_{DR_{VH}}$     | Linear depolarization ratio (vertical transmit and horizontal receive in logarithmic units)                          |
| $L_{DR}^{OFFSET}$ | Offset due to imbalances for the transmission and reception<br>path for horizontal and vertical polarization channel |
| $ar{M}$           | Magnetic current density $(V/m2)$  |
| $ec{M_S}$         | Equivalent magnetic current density of side slots  |
| N                 | Number of patch antenna elements   |
| $\hat{n}$         | Direction of observed umit   |
| N(D)              | Particle size distribution   |
| $N_o^{Cascade}$   | Cascaded output noise power  |
| $N_G$             | Equivalent noise of the noise generator  |
| $N_i$             | Input noise power  |
| $N_P$             | Noise power  |
| $N_P^{RX_{out}}$  | Noise power output of a receiver   |
| NF                | Noise Figure   |
| $NF_{Cascade}$    | Cascaded Noise Figure  |
| $NF_{RX}$         | Received Noise Figure  |
| n                 | Number of elements   |
| $n_p$             | Number of pulses   |
| 0                 | Output   |
| $P_E$             | Received power   |
| $P_{in}$          | Antenna input power  |
| $P_M$             | Power input for one TRM  |
|                   |  |

| $P_N$                   | Detected noise level  |
|-------------------------|---|
| $P_N^H$                 | Detected noise level in horizontal channel  |
| $P_N^V$                 | Detected noise level in vertical channel  |
| $P_r$                   | Radiated power  |
| $P_{RX}$                | Received power  |
| $P_S$                   | Transmitted (radiated) power  |
| $P_{TRM}$               | TR- module output power   |
| $P_v$                   | Intrinsic power losses of the antenna   |
| PRF                     | Pulse repetition frequency  |
| $PRF_{Max}$             | Maximum pulse repetition frequency  |
| PRT                     | Pulse repetition time   |
| PW                      | Pulse width   |
| PW <sub>synthetic</sub> | Synthetic pulse width by using pulse compression                                    |
| q                       | Antenna area efficiency   |
| $Q_m$                   | Imaginary part of the received echo voltage without considering clutter suppression |
| R                       | Range of the target   |
| r                       | Radial distance   |
| r                       | The radius of a cylinder section $1.3$  |
| $R_0$                   | Autocorrelation value with clutter suppression                                      |
| $R_0^H$                 | Autocorrelation value with clutter suppression in horizontal channel                |
| $R_0^{HV}$              | Autocorrelation at Lag 0 between H and V pulse                                      |
| $R_0^V$                 | Autocorrelation value with clutter suppression in vertical chan-<br>nel             |
| $R_1^{HV1}$             | Co-polar correlation at Lag 1 between H2 and V1 pulses                              |
| $R_1^{HV2}$             | Co-polar correlation at Lag 1 between H1 and V2 pulses                              |
| 1                       |   |

44

| $R_1$   | Cross-correlation value with clutter suppression                                |
|---|---|
| $R_1$   | Radial distance of target 1 in section $1.1$                                    |
| $R_2$   | Cross-correlation value with clutter suppression                                |
| $R_2$   | Radial distance of target 2 in section $1.1$                                    |
| $R_L$   | Load resistance   |
| r <sub>min</sub>                                | Minimum distance between an antenna under test and a receiving antenna          |
| $R_{Rain}$                                      | Rain Rate   |
| $R_{UnA}$                                       | Unambiguous range   |
| RX  | Receiver  |
| [S]   | Backscattering matrix   |
| $S_1(R)$  | Transmitted power density   |
| $S_2(R)$  | Echo power density  |
| $\langle S_i\left(r,\theta,\phi\right) \rangle$ | Isotropic power density   |
| $(S_i/N_i)$                                     | Input signal to noise ratio   |
| $(S_o/N_o)$                                     | Output signal to noise ratio  |
| $(S_1/N_1)$                                     | Signal to noise ratio without pulse integration                                 |
| $S_{HH}$  | Component of scattering matrix while horizontal transmit and horizontal receive |
| $S_{HV}$  | Component of scattering matrix while horizontal transmit and vertical receive   |
| $S_{min}$                                       | Minimum signal strength   |
| $S_{max}(r, \theta, \phi)$                      | Maximum radiation density in the main beam direction                            |
| $S_{VH}$  | Component of scattering matrix while vertical transmit and horizontal receive   |
| $S_{VV}$  | Component of scattering matrix while vertical transmit and vertical receive     |
| str   | Steradian $sr = radian^2$   |

| SYS                     | System   |
|-------------------------|--|
| T                       | Temperature  |
| t                       | Time   |
| $T_0$                   | Room temperature   |
| $T_0$                   | Autocorrelation value without clutter suppression                        |
| $T_1$                   | Cross-correlation value without clutter suppression                      |
| $T_2$                   | Cross-correlation value without clutter suppression                      |
| $T_B(\theta,\phi)$      | Distributed background temperature                                       |
| $T^A_B nt(\theta,\phi)$ | Effective antenna brightness temperature                                 |
| $T_b$                   | Background temperature   |
| $T_e$                   | Equivalent temperature   |
| $T_e^{Ant}$             | Equivalent antenna temperature   |
| $T_e^{RX}$              | Equivalent temperature of the receiver                                   |
| $T_e^{SYS}$             | Equivalent system temperature of a cascaded system                       |
| $T_e^{TL}$              | Equivalent temperature of a transmission line                            |
| $T_e^{TL+RX}$           | Equivalent temperature of a transmission line and receiver               |
| $T_G$                   | Equivalent temperature of the noise generator                            |
| $T_p$                   | Physical Temperature   |
| $T_S^{Passive}$         | System temperature at the entrance of the receiver for a passive PAR     |
| u                       | Angular variable   |
| $U_m$                   | Received echo voltage without considering clutter suppression            |
| $U_{Mod}(t)$            | Modulation voltage for defining $pw$ and PRF                             |
| $U_{RX}(t)$             | Received RF signal   |
| $U_{RX}(r)$             | Received voltage of the backscattered signal after the target reflection |
| $U_{TX}(t)$             | Pulse modulated RF signal radiated from the antenna                      |

46

| $U_{TX}(r)$       | Transmission voltage with the TX pulse and the two targets prior the echo will be reflected                            |
|-------------------|--|
| UV                | Uncorrected Doppler velocity (m/s)   |
| UW                | Uncorrected spectral width (m/s)   |
| UZ                | Uncorrected Reflectivity (dBZ)   |
| $\hat{v}$         | Vertical polarization unit vector  |
| v                 | Angular variable   |
| $V_0$             | Voltage value across one slot  |
| $V_m$             | Signal time series after clutter correction  |
| $V_m^H$           | Horizontal signal time series after clutter correction   |
| $V_m^V$           | Vertical signal time series after clutter correction   |
| $V_{Max}$         | Maximum Doppler velocity   |
| $v_p$             | Phase velocity   |
| $V_{Pulse}$       | Pulse volume   |
| $V_{rad}$         | Radial velocity  |
| $V_{UnA}$         | Unambiguous Doppler velocity   |
| W                 | Width of the microstrip line or patch  |
| z                 | Space variable   |
| $Z_0$             | Field impedance  |
| $Z_1$             | Wave impedance   |
| $Z_{DR}$          | Differential reflectivity (dB)   |
| $Z_{DR}^{OFFSET}$ | Offset due to imbalances for the transmission and reception path for horizontal and vertical polarization channel (dB) |
| $Z_e$             | Effective Radar Reflectivity in dB scale (dBZ)   |
| $z_e$             | Radar Reflectivity $(mm^6/m^3)$  |
| $Z_H$             | Horizontal Co-polar reflectivity in dB scale   |
| $z_H$             | Horizontal Co-polar reflectivity   |

| $Z_{HV}$ | Cross-polar reflectivity                       |
|----------|--|
| Z - R    | Relationship between reflectivity and rainrate |
| $Z_V$    | Vertical Co-polar reflectivity in dB scale     |
| $z_V$    | Vertical Co-polar reflectivity                 |

# Chapter 1

## State-of-the-art radar fundamentals

In order to develop new system concepts and specific antenna configurations for phasedarray weather radar applications, it is essential to introduce the general radar fundamentals. To achieve this goal, the reader will be taken through the pulse Doppler radar principle and its most important performance parameters. Furthermore, graphical descriptions are presented in order to explain transmit and receive cycles of a pulsed Doppler radar.

The volume target weather radar equation will be used to point out the importance of the antenna parameters for weather radar observations, in particular when using phased-array antennas. The polarization state of the transmitted and received signal is significantly important for proper weather radar operation. This, in turn, requires the definition of polarization states of electromagnetic waves for understanding the dual-polarimetric observables, which are used to classify and quantify precipitation.

The principle of a dual polarized weather radar is explained in section 1.5. Starting with an overview about the state-of-the-art weather radars with dish antennas, the description of a backscattered EM-wave from hydrometeors is induced by the scattering matrix and the covariance matrix. The covariance matrix is further used to derive the polarimetric weather radar observables by pulse pair processing of I/Q signals.

Noise in radar systems is often unwanted, but it can also be used for identifying malfunctions of single units inside the radar system. This is especially relevant to the operation of a calibrated phased-array radars with numerous subarray units, (e.g. the developed system concept from [115] in section 5 incorporates 800 subarrays with 6400 TRMs) when it comes to the identification of subarray malfunction. If the impaired function of one transmit-receive module from any subarray is detected, the system controller can be informed about this circumstance. Consequently, different antenna parameters-, for instance the array taper must be adjusted; the antenna gain and the 3dB beamwidth values for the weather radar equation must be redefined for the new antenna characteristics.

The generation and the existence of noise are important topics for the discussion of radar systems. For this reason, the generation of noise in a cascaded-radar-system is considered in section 1.6. In this regard, the antenna temperature, one of the most important

properties of the radar system is discussed in detail. It will be shown that the antenna efficiency is strongly reflects on the minimum detectable signal of the radar system. To achieve this goal, the terms minimum detectable, minimum discernable signal as well as different definitions of the radar system bandwidth are addressed.

In each section, the reader will be provided with a detailed insight into state-of-the-art weather radars and their cross-connection to phased-array antennas.

## 1.1 Pulse Doppler radar principle

A state-of-the-art pulse Doppler radar consists of a trigger generator, modulator, transmitter, antenna, circulator/duplexer and a receiver. In most cases, the transmitter is based on a magnetron oscillator. But also solid state transmitters (SSTX) or klystron transmitters are very common due to their spectral purity, especially in Asian regions. Three dimensional (3D) scanning phased-array radars are typically equipped with multiple TRMs to enable transmission and reception for different elevation and azimuth scan angles. Most 2D Phased-Array Radars (PARs) rotate their antennas mechanically in azimuth while scanning the beam electronically in elevation to achieve 3D mapping of the environment. Frequency scanning antennas like [92] or [93] use a series of different frequencies to perform electronic-scans in azimuth and elevation planes.

The radar receiver is usually separated into analog and digital part. In weather radar systems with magnetron, klystron or SSTX, the analog receiver consists of one unit with a narrow band pass filter, a very sensitive low noise amplifier (LNA's) and a downconverter. The LNA's optimum mounting position is very close to the antenna port to keep the system noise figure as low as possible. In PARs the antenna has multiple radiators, which are either patch elements on a substrate, dipoles or waveguide slots. Most other radars employ reflector antennas with waveguide circuits.

For the sake of a better understanding, a simplified pulse Doppler radar is shown in the block diagram 1.1. The radar transmits the pulsed radio frequency (RF) signal generated by the trigger generator, the transmitter through the antenna into the atmosphere. The transmitted pulse is an amplitude modulated signal with the carrier frequency  $f_{TX}$ . As soon as the antenna has launched the transmission line-bounded electromagnetic wave into a free space EM-wave, the so transmitted wave will travel through atmosphere until it is reflected by a target at range R. The echo signal received by the antenna is filtered, amplified and down converted to intermediate frequency by the analog receiver.

Up-to-date heterodyne radar receivers use single or double down conversion. Single downconversion with only one mixer circuit is easier to design. The double frequency down conversion allows placing the image-frequency at larger offset from the carrier frequency. Consequently, the larger image to carrier offset relaxes the filter specification e.g. the inband ripple and slope requirements.

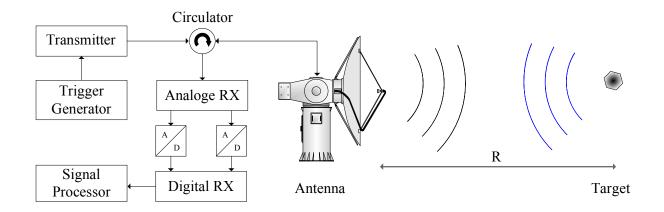


Figure 1.1: Pulse Doppler radar blockdiagram

The intermediate frequency is quantized/digitized by the A/D-converter (Analog to Digital-converter) to produce the digital I and Q (In phase and Quadrature phase) signals which are produced from the received echo voltages, depicted in figure 1.2a. The I and Q demodulation is used to retrieve the phase information from the echo signal in order to establish coherent radar operation, for instance, for obtaining the radial Doppler velocity of a moving target.

A typical transmit-receive pulse cycle is illustrated in figure 1.2a. The modulation voltage  $U_{Mod}(t)$  is generated by the trigger generator and defines the pulse repetition time *PRT* and the pulse width *PW*. To establish coherent radar operation necessary for Doppler estimations, the modulation voltage  $U_{Mod}(t)$  should be derived or governed from the radar master clock oscillator. In conventional pulsed radar systems there is no intra-pulse modulation applied. In pulse compression radars, on the other hand, the intra-pulse frequency or phase will be modulated. Pulse compression allows a radar to utilize a long pulse to achieve large radiated energy and yet simultaneously obtain the range resolution of a short pulse, [33]. Typical pulse compression radars use up- and down frequency chirps or phase codes on sub-pulse basis. These complex signal waveforms are used to increase the radar range resolution by increasing the signal bandwidth of the transmitted pulse.

The range of the target can be calculated by equation 1.1 [2], the estimated time of flight  $\Delta_t$  is shown in figure 1.2a and given by:

$$\Delta_t = \frac{2R}{c_0} \Rightarrow R = \frac{c_0 \cdot \Delta_t}{2} \tag{1.1}$$

The pulse modulated RF signal  $U_{TX}(t)$  radiated from the antenna in depicted in figure 1.2a. The received signal  $U_{RX}(t)$  is used in the signal processor for calculating the intensity of the reflected signal and the radial target Doppler velocity  $V_{rad}$ . Furthermore, the signal

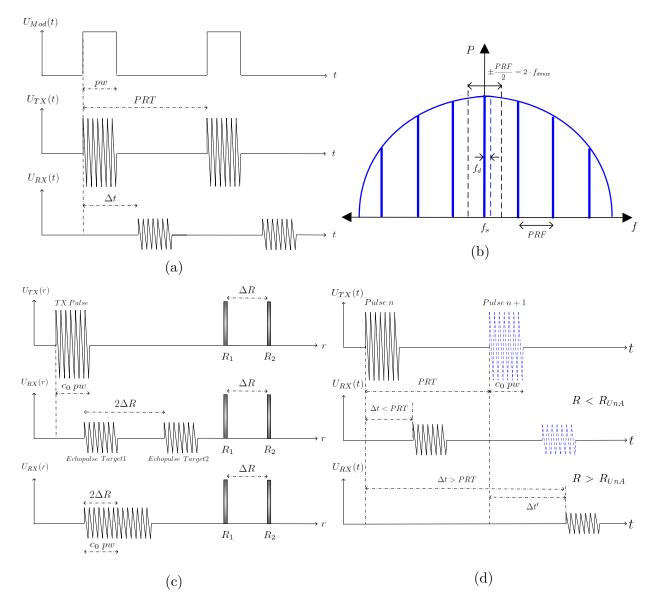


Figure 1.2: a) Pulsed radar transmit-receive cycle; b) Line spectrum for the explanation of unambiguous Doppler velocity; c) Graphical description of the range resolution; d) Graphical description of the unambiguous range

#### 1.1. PULSE DOPPLER RADAR PRINCIPLE

processor provides for different displays e.g. Plane Position Indicator (PPI), Range Height Indicator (RHI) in real time and user-products by applying special algorithms depending on the radar application. The signal processor for polarimetric weather radar applications provides polarimetric observables like  $Z_H$ ,  $Z_V$ ,  $Z_{DR}$ ,  $L_{DR}$ ,  $\phi_{DP}$ ,  $\rho_{co}$ ,  $K_{DP}$ . The derivation and discussion of polarimetric weather radar observables is detailed discussed later in section 1.5."Radars use Doppler frequency to extract target radial velocity (range rate), as well as to distinguish between moving and stationary targets or objects such as clutter. The radial target Doppler velocity is typically given by:

$$V_{rad} = \frac{R_{i+1} - R_i}{t_{i+1} - t_i} \approx \frac{\Delta R_i}{PRT} \approx \Delta R_i \cdot PRF$$
(1.2)

The Doppler phenomenon describes the shift in the center frequency of an incident waveform due to the target's motion, with respect to the source of radiation. Depending on the direction of the target's motion this frequency shift may be positive or negative. A waveform incident on a target has equiphase wave fronts separated by  $\lambda$ , the wavelength. A closing target will cause the reflected equiphase wave fronts to get closer to each other (smaller wavelength). Alternatively, a receding target (moving away from the radar) will cause the reflected equiphase wave fronts to expand (larger wavelength)" [32]. The Doppler effect can also be interpreted as a rescaling of the wavenumbers and their positions in the space between the target and the radar. We note that the wave backscattered from a moving target will display a different wavelength compared to the wave reflected from a stationary target.

The Doppler velocity of the target of interest can be estimated in both, time- and frequency domain. The time domain analysis is used for the Doppler velocity analysis, since this analysis can be realized without any Fast Fourier Transformation (FFT).

Closer examination shows that the radial velocity  $V_r \neq 0$  of a target can be observed by range or phase changes on a pulse-to-pulse basis. To retrieve the radial velocity  $V_{rad}$ , two successive range estimates of  $R_i$  and  $R_{i+1}$  are used [2] as shown in equation 1.2.

In frequency domain analysis, the radial Doppler velocity  $V_{rad}$  can be calculated from the Doppler frequency  $f_D$  due to the frequency shift of the echo-carrier signal frequency  $f_0$  [14] with

$$V_{rad} = \frac{f_D \cdot c_0}{2 \cdot f_0}.\tag{1.3}$$

The range resolution of the pulsed Doppler radar is now discussed by means of figure 1.2c. The range resolution  $\Delta R$  defines the minimum distinguishable radial distance between two targets, located along the antenna main beam axis. Therefore,  $\Delta R$  defines the case, when these two radial separated targets are still distinguishable. The two separate targets are detected as one target if radial distance falls below  $\Delta R$ . The limiting case for the range resolution definition is shown in figure 1.2c. The distance between the falling edge of echo pulse Target1 and the rising edge of echo pulse Target2 is exactly zero and establishes the definition of the range resolution from [2] with

$$\Delta R = \frac{PW \cdot c_0}{2} = \frac{c_0}{2 \cdot B_{pulse}}.$$
(1.4)

We note that the inverse value of PW is an estimate of the pulse bandwidth,  $B_{pulse}$ . As mentioned before, the radar range resolution can be improved by pulse compression methods. Naturally, pulse compression techniques are only applicable for amplifier based (e.g. SSTX and Klystron) radar transmitters. The frequency or phase intra-pulse modulation increases the signal bandwidth of the transmitted pulse. In figure 1.3, the well-known sinc function of a pulsed RF signal is shown. Pulse compression sets the nulls at  $f_s \pm \frac{n}{PW}$  for n integer values further apart, so that in consequence the signal bandwidth between the first nulls is enlarged. By increasing the pulse bandwidth  $B_{pulse}$ , the range resolution  $\Delta R$  will be improved (see equation 1.4). Other useful pulse compression binary phase and frequency codes are Barker codes, Frank codes and Costas codes [31]. The major disadvantages of pulse compression techniques are the resulting range side lobes (sometimes also called time sidelobes) and the increased dead time for TX/RX switching. The dead time occures due the transmission of long pulses. For the transmission of the signal the receiver is blind. The range side lobes are generated by the cross-correlation functions of the compression processor inside the receiver chain. "These sidelobes can be reduced by amplitude weighting of the received-signal spectrum, just as the spatial sidelobes of an antenna radiation pattern can be reduced by amplitude weighting the illumination across the antenna aperture; as it will be described later in table 3.4. The same illumination functions used in antenna design to reduce spatial sidelobes can also be applied to the frequency domain to reduce the range sidelobes from pulse compression" [33].

In regard of pulse compression, the term time-bandwidth-product can be derived via the pulse compression gain PCG from [34] as follows:

$$PCG = \frac{c_0 \cdot \frac{PW}{2}}{\frac{c_0}{2B_{pulse}}} = B_{pulse} \cdot PW = \frac{PW}{PW_{synthetic}}$$
(1.5)

PCG is a performance rating parameter of pulse compression radars with intra-pulse modulation compared to conventional pulsed radars with simple amplitude modulation.  $PW_{synthetic}$  represents the synthetic pulse length or width. This length is the inverse of the modulation bandwidth. For instance, if the pulse width PW is 10  $\mu s$  long and the intermodulation bandwidth occupies 20 MHz, then the synthetic pulse length  $PW_{synthetic}$  becomes 0.05  $\mu s$  and the PCG becomes 200.

Looking at the spectrum of the transmitted pulse signal in figure 1.3, the PW and the PRF can be identified. The distance between the spectral lines represents the PRF. For rectangular and unmodulated pulses of duration PW, the line spectrum creates an envelope of the sinc function. The zeros of order n represent the carrier frequency with the

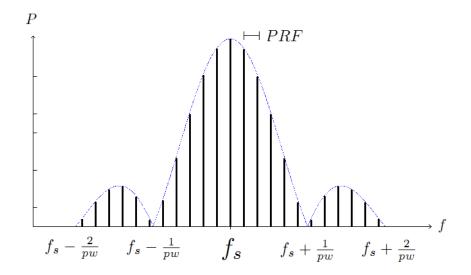


Figure 1.3: Chart description of the pulse spectrum to determine pulse width PW and pulse repetition frequency PRF

shift of the multiplicative inverse value of the pulse width. The inverse of PCG, namely the pulse compression ratio (PCR) describes the multiplication factor in equation 1.6 as an improvement factor of the range resolution achived with pulse compression radars.

$$\Delta R_{PCR} = c_0 \cdot \frac{PW_{synthetic}}{2} = PCR \cdot \frac{c_0}{2B_{pulse}} \tag{1.6}$$

The unambiguous range  $R_{UnA}$  is basically governed by the PRF. Figure 1.2d shows the conforming case  $R < R_{UnA}$  and the non-conforming case  $R > R_{UnA}$  of the unambiguous range definition. To receive the echo "unambiguously", the radar receiver requires the echo time delay  $\Delta t$  between the falling edge of the transmitted pulse (Pulse n) and the rising edge of the subsequent transmitted pulse (Pulse n+1) to be less than the PRT. During this time, the transmitted Pulse n has to travel from the antenna to the target and the echo pulse has to travel from the target back to the radar antenna. At  $\Delta t < PRT$ , the radar receiver allocates the echo signal to the correct transmitted pulse. Meanwhile at  $\Delta t > PRT = \Delta t'$ , a misinterpretation arises and the received pulse will be allocated to the subsequent transmitted pulse. This misinterpretation results in range mismeasurements of the illuminated target. Assuming that the pulse width is small in comparison to the PRT, the equation 1.7 from [14] can be used to calculate the unambiguous range.

$$R_{UnA} = \frac{c_0}{2PRF} \tag{1.7}$$

The origin of the term unambiguous range has its roots in operational radar engineering and is used in literature since the last decade. In reality, there are often reflections from previous

transmitted pulses in the unambiguous range interval, so that the word unambiguous is not exactly true. Theses back reflections are often weak, seldom identified as ghost targets or simply unperceived by the radar operators. However, with the second or third trip recovery algorithms, the radar operator is able to distinguish between consecutive echo pulses, so that target detection beyond the theoretical formulation in equation 1.7 becomes possible. Additionally, ghost target detection is prevented. For the second and the third trip recovery, the transmitted pulses are coded on pulse to pulse basis. Pulsed RF signals from magnetron transmitters are inherently useful for multiple trip recovery algorithms due to their randomly generated starting phase of the oscillator. Ambiguities can also arise for the radial target velocity. The maximum Doppler velocity  $V_{max}$  for a pulsed Doppler radar is defined by the Nyquist theorem. By using the line spectrum description from the figures 1.2b and 1.3 along with the equations 1.8 and 1.9 [14], the Doppler ambiguity as well as the corresponding Nyquist theorem violation can be explained. The spectral lines of the sinc function are separated by the PRF. As a consequence, the target Doppler frequency can only be measured unambiguously as long as the Doppler shift within  $\pm \frac{PRF}{2}$ . Is the target Doppler frequency higher than  $\pm \frac{PRF}{2}$ , aliasing occurs and the Doppler frequency will be misinterpreted.

$$\pm \frac{PRF}{2} = 2 \cdot f_{dmax} = \frac{2 \cdot V_{max}}{\lambda} \tag{1.8}$$

$$V_{max} = \pm \frac{PRF \cdot \lambda}{4} \tag{1.9}$$

To get the unambiguous Doppler velocity  $V_{UnA}$  for different scan configurations, the equations 1.8 and 1.7 are combined to equation 1.10.

$$V_{UnA} = \pm \frac{c_0 \cdot \lambda}{8 \cdot R_{UnA}} \tag{1.10}$$

It is clear that  $V_{max}$  in equation 1.9 will be enlarged when  $R_{UAR}$  in equation 1.7 will be reduced, when the PRF is increased. Vice versa the  $R_{UAR}$  will be increased and  $V_{max}$  will be reduced when the PRF becomes smaller. Modern weather radars use their transmitters in staggering mode to avoid this so called "Doppler dilemma" by employing different PRFs e.g. dual or triple PRF mode for the same range interval of interest.

## **1.2** Radar equation of a point target

The radar equation of a point target describes the propagation and reflection characteristics between the radar system and the point target in free space under perfect boundary conditions. It will be shown that the point target radar equation can be described by a fragmentation into three parts, as shown in figure 1.4. The first fragment is the transmitted power density  $S_1(R)$  and can be expressed as follows:

$$S_1(R) = \frac{P_S}{4\pi R^2} \cdot G_S \tag{1.11}$$

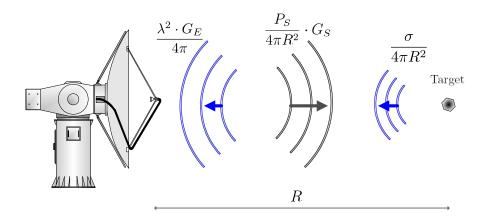


Figure 1.4: Visual explanation of the point target equation 1.15. The blue waves are representing the back propagation towards the radar.

The value  $P_S$  represents the transmitted power at the antenna reference point and  $G_S$  the antenna gain during transmission. Meanwhile represents  $\left(\frac{1}{4\pi R^2}\right)$  the surface of the spherical EM-wave, propagating into free space. In particular for digital beam forming and phased-array radars it is fundamentally important to consider the antenna gain for the transmission and reception case separately. In such systems the gain can be adjusted by amplitude and phase tapers, so that the gain values can differ for transmit and receive. The details are surveyed more precisely later in section 3.4.3. The second part of the radar point target equation is the echo power density  $S_2(R)$  of an isotropic radiating point target before the echo signal enters the effective area of the receiving antenna:

$$S_2(R) = \left(\frac{P_S}{4\pi R^2} \cdot G_S\right) \cdot \left(\frac{1}{4\pi R^2} \cdot A_Z \cdot G_Z\right)$$
(1.12)

The first bracket of equation 1.12 was already introduced with  $S_1(R)$  in equation 1.11.  $A_Z$  represents the physical target cross section and  $G_Z$  considers the gain/ loss factor for irregular radar targets with unknown backscatter coefficients and angles. The term  $\left(\frac{1}{4\pi R^2}\right)$ characterizes the free space propagation of the reflected spherical EM-wave. The product of  $A_Z$  and  $G_Z$  defines the well-known radar cross section  $\sigma$  with:

$$\sigma = G_Z \cdot A_Z \tag{1.13}$$

The forward wave propagation and the influence of the reflecting target can be constructed with  $S_1(R)$  from equation 1.11 and  $S_2(R)$  equation 1.12. To retrieve the complete radar equation of a point target, the effective antenna area should be introduced next. The effective antenna area  $A_E$  of the receiving antenna describes the third fragment of the radar point target equation as follows:

$$A_E = \frac{\lambda^2}{4\pi} \cdot G_E \tag{1.14}$$

Equation 1.14 is valid for every antenna shape and defines the strict correlation between antenna gain and effective antenna area, analytically proven in [12] with an Hertzian dipole antenna. The effective antenna area is an abstract area and can be interpreted as an area catching the electromagnetic energy incident on the antenna plane. This is not necessarily the geometrical area of the antenna.

Finally, the radar point target equation for a monostatic radar case can be constructed by combining the three fragments from equation 1.11, equation 1.12 and equation 1.14 into equation 1.15:

$$P_E = \frac{P_S \cdot G_S}{4\pi R^2} \cdot \frac{\sigma}{4\pi R^2} \cdot \frac{\lambda^2 \cdot G_E}{4\pi}$$
(1.15)

In figure 1.4, the three-part fragmentation of the radar point target equation is visualized and  $P_E$  represents the received power at the antenna reference point.

## **1.3** Radar equation of a volume target

The point target equation described in 1.15 needs to be modified for the operation of a weather radar. The weather radar makes measurements in a certain volume of space. Consequently, the following modification must be considered to derive the volume target weather radar equation from radar point target form:

$$P_E = \left[\frac{P_S \cdot G_S}{4\pi R^2} \cdot \frac{1}{4\pi R^2} \cdot \frac{\lambda^2 \cdot G_E}{4\pi}\right] \cdot V_{Pulse} \cdot PJC \cdot \sigma \tag{1.16}$$

The target in the weather radar equation contains distributed hydrometeors in the illuminated volume  $V_{Pulse}$  (see figure 1.5). The Probert-Jones correction factor PJC accounts for the beam width shape of narrow-beam antennas (i.e. high gain reflector antennas), as shown in figure 1.6.

$$V_{Pulse} = \pi \frac{R\theta}{2} \frac{R\phi}{2} \frac{h}{2}$$
(1.17)

The illuminated pulse volume will be defined by the horizontal cut of the antenna beamwidth  $\phi$ , the vertical cut antenna beamwidth  $\theta$ , the range R, and h the radiated pulse length in meters, under the assumption that the pulse volume corresponds to a cylindrical volume. The reason for using only the first half of the pulse illuminated volume is related to the range resolution explained in chapter 1. The pulse length h is the length in space analogous to the pulse width of the transmitter signal  $(h = c \cdot PW)$ . In figure 1.6 the side view of the pulse volume with distance R to the radar is shown. The letter r in figure 1.6 represents the radius of the cylinder and with the geometrical relation  $r = \frac{R\theta}{2}$  explains the terms appling in equation 1.17.

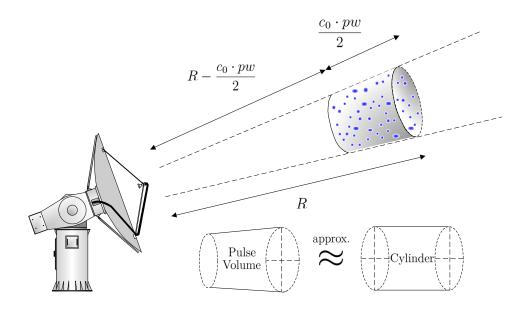


Figure 1.5: Pulse volume target for weather radar equation 1.27

 $\sigma$  in equation 1.18 accounts for hydrometeors distributed within the pulse volume; hence  $\sigma$  changes to a sum of  $\sigma_i$ , shown in equation 1.18, where  $\sigma_i$  represents the radar cross section of the i-th backscattering hydrometeor.

$$\sigma = \sum \sigma_i \tag{1.18}$$

$$PJC = \frac{1}{2\ln 2} \tag{1.19}$$

Probert Jones was the first one who recognized in 1962 [35], that the transmitted pulse in space contains only the energy of the half power beamwidths of the antenna. By using a Gaussian distribution as illustrated in figure 1.6, he introduced the correction factor PJC in terms of equation 1.19. By understanding the changes from point target to volume target illumination, we are now able to describe the volume target equation more precisely by inserting the equation 1.18, 1.17 and 1.19 in 1.16:

$$P_E = \left[\frac{P_S \cdot G_S \cdot G_E \cdot \lambda^{2} \cdot \theta \cdot \phi \cdot h}{1024 \cdot \ln 2 \cdot \pi^2 R^2}\right] \cdot \sum \sigma_i \tag{1.20}$$

The element in brackets from equation 1.20 represents the radar constant. By comparing the equations 1.20 and 1.15 it becomes clear, that the point target equation is a function of

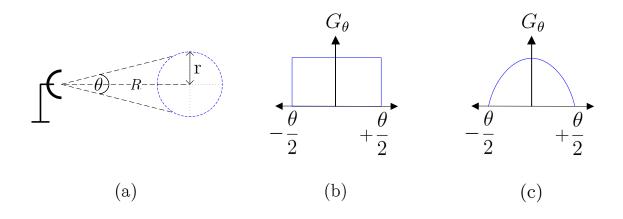


Figure 1.6: a) Side view of the pulse volume; b) Pulse volume homogeneously filled; c) Pulse volume weighted with 3dB antenna beamwidth for improved reflectivity estimates, discovered by Probert Jones.

 $R^4$  whereas is the volume target equation a function of  $R^2$ . Furthermore a new parameter named as "*Radar Reflectivity*" is introduced as follows:

$$\eta_{RR} = \sum_{Unit \ Volume} \sigma_i = \int_0^\infty \sigma(D) N(D) dD$$
(1.21)

with D the backscattering drop diameter and N(D) the particle size distribution. As hydrometeor backscattering cross section has units of  $m^2$ ,  $\eta_{RR}$  has the units of  $m^{-1}$ . Unfortunately the radar reflectivity  $\eta_{RR}$  depends on wavelength so that comparison between different radar systems becomes difficult. For this reason,  $\eta_{RR}$  is nowadays seldom directly used in the weather radar community and just shown here for completeness.

For most meteorological weather radars the wavelengths of 3cm (X-Band), 5cm (C-Band) to 10 cm (S-Band) can be considered to belarge in comparison to the scattering objects (assuming raindrops). Thus, the Rayleigh approximation [36] can be applied for the backscattering cross sectional area of the i-th dielectric sphere with:

$$\sigma_i = \frac{\pi^5 |K|^2 D_i^6}{\lambda^4} \tag{1.22}$$

Where  $D_i$  represents the diameter of the i-th hydrometeor,  $|K|^2$  is a complex material constant accounts for absorption within the sphere. In the common radar frequency bands  $|K|^2$  can be considered with 0.93 for water and 0.197 for ice.

#### 1.3. RADAR EQUATION OF A VOLUME TARGET

By inserting the equation 1.22 in equation 1.20 the received power in equation 1.23 is now the function of the sixth power of the drop diameter:

$$P_{E} = \left[\frac{\pi^{3} P_{S} \cdot G_{S} \cdot G_{E} \cdot \theta \phi h |K|^{2} \sum D_{i}^{6}}{1024 \ln 2\lambda \ ^{2}R^{2}}\right]$$
(1.23)

In reality the absolute drop diameter are unknown so a new parameter called "*Radar* Reflectivity" is used:

$$z_e = \sum_{Unit \ Volume} D_i^6 \tag{1.24}$$

The radar reflectivity factor  $z_e$  was mainly introduced for the reason of comparability of different weather radar data. The products of the radar systems of different wavelengths could be compared, since the radar cross-section is no longer a function of the radar wavelength. The relationship between radar reflectivity factor  $z_e$  also called "Effective Radar Reflectivity" and the radar reflectivity  $\eta_{RR}$  is shown next:

$$\eta_{RR} = \frac{\pi^5 \, |K|^2 \, z_e}{\lambda^4} \tag{1.25}$$

with

$$z_e \left[\frac{mm^6}{m^3}\right] = 10^{18} \frac{\lambda^4}{\pi^5 |K|^2} \int_0^\infty \sigma(D) N(D) dD$$
(1.26)

The factor  $10^{18}$  from equation 1.26 has its origin from the unit conversion from  $\left(\frac{m^6}{m^3}\right)$  to  $\left(\frac{mm^6}{m^3}\right)$ . Thus, the final radar equation for a volume target without considering the system losses (radome, waveguide, etc) for meteorological applications is:

$$P_{E} = \left[\frac{\pi^{3} P_{S} \cdot G_{S} \cdot G_{E} \cdot \theta \phi h |K|^{2} z_{e}}{1024 \ln(2) \lambda^{2} R^{2}}\right]$$
(1.27)

To extract the effective radar reflectivity in the dynamic range from very small targets close to thermal noise to very large targets as e.g. hail, a conversion to logarithmic values becomes reasonable. Accordingly, the logarithmic effective radar reflectivity  $Z_e$  can be expressed with

$$Z_e[dBZ] = 10 \log_{10} \left(\frac{z_e}{\frac{1mm^6}{m^3}}\right).$$
 (1.28)

Meteorologists are used to work with rain rates in units of  $\frac{mm}{hour}$ , so that a semi emperical relationship between rain rate  $R_{Rain}$  and the weather radar reflectivity factor  $z_e$  is introduced next with

$$z_e = 200 \cdot R_{Rain}^{1.6}.$$
 (1.29)

In the last decade, many scientists discussed this issue to find the best matching Z-R relation for different precipitation types and drop size distributions, so that only one classical example from [37] is shown in equation 1.29.

# 1.4 Radar equation of planar phased-array weather radar

As already introduced by the volume target weather radar equation 1.27, the weather radar system is calibrated, if the transmit power, the receiver gain, the antenna gain and beamwidth of the antenna are determined accurately. The knowledge of these variables is vitally important in order to evaluate the amplitude and phase of the received echo signals in both polarization channels with high accuracy. In phased-array weather radars, the main beam is electronically steered. The beam steering range is governed by the radiator element distance inside the antenna array as a function of wavelength. Within this beam steering range, the antenna gain varies (i.e. is decreased) and the beamwidth is increased by moving the main beam away from the boresight direction. The overall antenna gain is generally given by the multiplication of array factor and the element factor. All relationships between beam travelling range, array scan loss, element pattern, and array factor are detailed later in the phased-array antenna theory section 3.4.

However, to derive the PAWR equation 1.34 it is important to know the antenna gain, the beam solid angle and beamwidth, which are depending on the angular position of the electromagnetic beam in space. In [26] a weather radar equation modification for frequency agile phased-array radars is introduced. Here, the classical weather radar equation proposed by Probert Jones [35] was corrected with two terms. First, for the consideration of the antenna gain, beam solid angle and beamwidth variation as the function of the scan angle. And second, for the cross section density of precipitation in the Rayleigh region as the function of frequency. Assuming,  $G_S^0$  and  $G_E^0$  stand for the boresight antenna gains in transmit and receive cases.

$$G_S = G_S^0 \cdot \cos\left(\alpha\right) \tag{1.30}$$

$$G_E = G_E^0 \cdot \cos\left(\alpha\right) \tag{1.31}$$

$$\phi\Theta = \frac{\phi_0\theta_0}{\cos\left(\alpha\right)} \tag{1.32}$$

$$\alpha = \arctan\left[\sqrt{\left(\tan\xi\right)^2 + \left(\tan\psi\right)^2}\right]$$
(1.33)

According to [26], the term  $\alpha$  is the angle between beam axis and the normal of the planar antenna array. Meanwhile are  $\phi_0$  and  $\Theta_0$  the boresight 3 dB beamwidths in the principal planes at boresight direction. The terms  $\xi$  and  $\psi$  are the beam angles measured in the x-z plane and y-z plane, respectively. The Probert Jones equation requires the half power beamwidths  $\phi$  and  $\Theta$ . Equation 1.32 gives these beamwidths in terms of boresight beamwidth and the cosine of the angle  $\alpha$ . Furthermore, the relation between the beamwidth and the beam solid angle  $\Omega$ , will be given in section 3.1, for an arbitrary beam pointing direction.

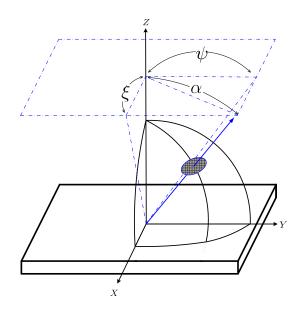


Figure 1.7: Planar antenna array with  $\alpha$ , the angle between the direction of main beam and the normal (Z-axis) of the array face.  $\xi$  and  $\psi$  are the beam angles between X-Z axis and Y-Z axis, respectively. In arbitrary direction, the antenna beam generates an ellipse on the surface of a sphere [26].

Now, the compression gain PCG and the synthetic pulse length  $PW_{synthetic}$ , as already introduced with equation 1.5 for pulse compression radars can be implemented in the weather radar equation. Therefore, the term h  $(h = PW \cdot c)$  must be substituted with  $h = PW_{synthetic} \cdot PCG \cdot c$ . Recalling, the classical Prober Jones weather radar equation introduced in 1.27, the new phased-array weather radar equation 1.34 with pulse compression capability and scan angle dependence can be derived with

$$P_E = \left[\frac{\pi^3 \cdot P_S \cdot PW_{synthetic} \cdot PCG \cdot c \cdot |K|^2 \cdot z_e}{1024 \cdot \ln\left(2\right) \cdot \lambda^2 \cdot R^2}\right] \cdot \left[G_S^0 \cdot G_E^0 \cdot \cos\left(\alpha\right) \cdot \phi_0 \cdot \Theta_0\right].$$
(1.34)

## 1.5 Principle of dual polarized weather radar

For the classification and assessment of hydrometeors in illuminated volumes, one should take advantage of polarization diversity radars. State-of-the-art radars from weather services in Europe are basically dual polarized. Most of these radars are working in hybrid mode, so that two electromagnetic field components, mostly horizontal and vertical polarizations are transmitted simultaneously. Ideally the transmitted polarization becomes then  $45^{\circ}$  linear. Rarely in use todayare weather radars in alternating mode. In alternating transmit mode, a pulse train with selectable polarization states for every pulse is generated. Typically, these pulses are alternating their polarization states, again between horizontal and vertical polarization. One exception in the European radars operating in dual polarization mode, is the fully polarimetric research weather radar at DLR (Deutsches Zentrum für Luft- und Raumfahrt, engl. German Aerospace Center). Here a ferromagnetic waveguide phaseshifter with a variable magnetic field is used to transmit and receive a set of desired polarizations in alternating mode. In 2010 it was the author's responsibility as project manager and systems engineer from Selex ES GmbH to upgrade this research radar with state-of-the-art analog and digital receiver technology. At the DLR radar, the receiver is mounted at the antenna (also called antenna mounted radar receiver system design) to reduce receive path losses, especially important for compensating the high insertion loss of the ferromagnetic switch [38]. Furthermore a new Waveguide Fiber Optic Rotary Joint (WG/FORJ) [39] has been developed to transfer the I/Q-data from the digital receiver, located at the antenna, over the rotating azimuth antenna axis to the signal processor in the cabinet room. An overview of the DLR radar and the antenna mounted receiver upgrade can be found in [40] and [41], respectively. Another note worthy example of antenna mounted receivers implemented in the operational Meteo Swiss C-Band radar network can be found in [42]. Advantages and disadvantages of the antenna mounted receiver system concept are addressed in [43]. We note especially that the absolute radar receiver calibration should be controlled for such system concepts as evidenced in [44]. All such radars with polarization diversity allow the measurement of hydrometeor characteristics. Especially the target classification is enabled by the size, shape and induced differential phase are made possible. The following section gives the theoretical background of the scattering matrix based description of radar observables for revealing meteorological properties.

#### **1.5.1** Scattering and Covariance Matrix

The complex 2 x 2 backscattering matrix [S] in equation 1.35 from [45] provides the relationship between the incident electrical field vector  $[E]^i$  and the backscattering field vector  $[E]^s$ , at the receive antenna plane, for a single particle illuminated by a plane wave. The incident wave transmitted by the radar antenna and backscattered wave from hydrometeors are travelling in opposite directions. In consequence, the backward scattering alignment (BSA) is mostly used from the weather radar community. The BSA uses the antenna as polarization reference.

$$\begin{bmatrix} E_H \\ E_V \end{bmatrix}^s = \begin{bmatrix} S_{HH} & S_{HV} \\ S_{VH} & S_{VV} \end{bmatrix} \begin{bmatrix} E_H \\ E_V \end{bmatrix}^i \frac{e^{-jkr}}{r}$$
(1.35)

The subscripts H and V are for the representations of horizontal and vertical polarizations during transmit (second subscript) and reception (first subscript). The [S] matrix elements on the main diagonal are the co-polarized (co-pol) components and the off diagonal elements are the cross-polarized (x-pol) components.

In the following we consider the covariance matrix concept. Here the asterisk \* sign denotes the complex conjugate.

In weather radars systems the signal voltages are sampled for investigating the characteristics of hydrometeors. The echo signal contains a superposition of voltages from an ensemble of scattering hydrometeors inside the illuminated volume. Consequently, the covariance elements are estimates for the complete pulse volume. The mean value of the phase terms would be canceled in terms of the summation over the multiple number of backscatters. "Thus, radar meteorologists use various second- order moments,  $\langle V_{ij}V_{kl}^*\rangle$  to characterize the polarized signals (the brackets  $\langle \rangle$  denote expectation values) and relate these to the properties of the hydrometeors"[14]. Further details about the relationship between second- order moments and the scattering coefficients can be found in [47]. The voltage covariance matrix is a scalar multiple of the backscattering covariance matrix as defined in equation 1.36 from [48].

#### **1.5.2** Polarimetric weather radar observables

The single polarization measurements of volume targets depend on the 6<sup>th</sup> power of hydrometeor drop size  $D_i$ , the number of raindrops N and the drop size distribution. A large number of small drops can produce the same radar reflectivity as a small number of large drops. For this reason, the estimation of attenuation and rain rate  $R_{Rain}$  leads to large errors. To solve this problem, dual polarized weather radars are used for measuring the raindrop oblateness in conjunction with the relationship to the equivalent drop diameter. The established relationship between drop size and drop oblateness is given in [49]. The drop diameter is known for its large variability.

#### Co-polar reflectivities $Z_H$ , $Z_V$ and differential reflectivity $Z_{DR}$

To retrieve the oblatness of raindrops the horizontal and vertical reflectivity factor  $Z_H$  and  $Z_V$  should be subtracted. The horizontal and vertical reflectivity factor can be expressed as:

$$z_{H} = \frac{4\lambda^{4}}{\pi^{4} |K|^{2}} \left\langle |S_{HH}|^{2} \right\rangle \tag{1.37}$$

$$z_V = \frac{4\lambda^4}{\pi^4 \left|K\right|^2} \left\langle \left|S_{VV}\right|^2 \right\rangle \tag{1.38}$$

$$\sigma^{HH}(D) = 4\pi |S_{HH}|^2 \tag{1.39}$$

$$\sigma^{VV}(D) = 4\pi \left| S_{VV} \right|^2 \tag{1.40}$$

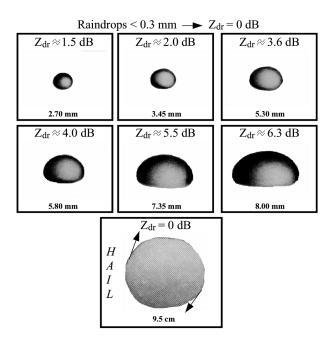


Figure 1.8: Typical  $Z_{DR}$  values of raindrops in various sizes and hail measured at S-Band. The black arrow on the hail particle represents the tumbling motions as it falls in a thunderstorm. Adapted from [50] and [51].

Furthermore, the reflectivity factors can be related to the first and last element of the covariance matrix in equation 1.36. The corresponding new polarimetric value is called the differential reflectivity  $Z_{DR}$  and can be defined by the subtraction of  $Z_H$  and  $Z_V$  in dB scale:

$$Z_{DR} = Z_H - Z_V = 10 \log_{10} \left(\frac{z_H}{z_V}\right) = 10 \log_{10} \left(\frac{\left\langle |S_{HH}|^2 \right\rangle}{\left\langle |S_{VV}|^2 \right\rangle}\right)$$
(1.41)

Typical values for  $Z_{DR}$  are shown in figure 1.8. "The measure of  $Z_{DR}$  enables the estimation of D, which is one of the key parameters describing the drop size distribution. It is more accurate at S-Band where Rayleigh scattering holds, as at C- and X-Band, where Mie scattering effects introducing more uncertainty." [51].

#### Cross-polar reflectivity $Z_{HV}$ and linear depolarization ratios $L_{DR_{HV}}$ , $L_{DR_{VH}}$

For  $Z_{DR}$ ,  $Z_H$  and  $Z_V$  calculations in equations 1.37, 1.38 and 1.41 the raindrops are assumed to be spheroids with zero canting angle. For the classification of hydrometeors with finite canting angle the so-called depolarization ratio, abbreviated to  $LDR_{HV}$  and  $LDR_{VH}$ , is used (recall the subscript "HV" stands for vertical transmit and horizontal receive and "VH" vice versa). Hydrometeors with tilted symmetry axis (canting angle) cause the incident wave to be depolarized during backscattering."The amount of depolarization will depend on a number of factors, namely, the hydrometeor size, the axis ratio, the degree of canting and the radar beam elevation. This will result in non-zero values for the magnitudes of  $S_{HV}$  and  $S_{VH}$  in the scattering matrix, defined in section 1.5.1"[51]. To retrieve the amount of depolarization induced by non-spherical raindrops the following formulations for cross polar reflectivity and linear depolarization ratio can be used:

$$z_{HV} = \frac{4\lambda^4}{\pi^4 |K|^2} \left< |S_{HV}|^2 \right>$$
(1.42)

$$\sigma^{HV}(D) = 4\pi \left| S_{HV} \right|^2 \tag{1.43}$$

In [52] it has been shown that:

$$z_{VH} = z_{HV} \tag{1.44}$$

The logarithmic depolarization ratio  $LDR_{HV}$  can be calculated with the cross polar reflectivity in equations 1.42 and the horizontal co-polar reflectivity from equation 1.37.

$$L_{DR_{HV}} = 10 \log_{10} \left(\frac{z_{HV}}{z_H}\right) = 10 \log_{10} \left(\frac{\left\langle \left|S_{HV}\right|^2\right\rangle}{\left\langle \left|S_{VV}\right|^2\right\rangle}\right)$$
(1.45)

The logarithmic depolarization ratio  $LDR_{VH}$  can be calculated with the cross polar reflectivity in equations 1.42 and the vertical co-polar reflectivity from equation 1.38.

$$L_{DR_{VH}} = 10 \log_{10} \left(\frac{z_{VH}}{z_V}\right) = 10 \log_{10} \left(\frac{\left\langle \left|S_{HV}\right|^2\right\rangle}{\left\langle \left|S_{HH}\right|^2\right\rangle}\right)$$
(1.46)

It is very challenging to retrieve the backscattered cross polar components of an illuminated volume. Especially the finite antenna cross polarization isolation of a weather radar limits the detection of intrinsic  $L_{DR}$ . Even more challenging is the development of a phased-array antenna with reasonable low cross polar contribution. In radar meteorology  $L_{DR}$  is mostly used for the classification of precipitation, e.g. for the detection of melting hydrometeors in the so called "melting layer".

#### Differential propagation phase $\phi_{DP}$ and specific differential phase $K_{DP}$

The horizontal and the vertical polarized EM-waves are differently affected by propagation through a volume of non-spherical raindrops (also called "forward scattering"). In particular the horizontal EM-wave is more strongly attenuated and suffers a higher phase lag relative to the vertically polarized EM-wave. Thus, attenuation correction in weather radar signal processing can be applied due to the relationship between the EM-wave attenuation and the differential propagation phase [53]. Furthermore, rain rate estimations are made possible with the evaluation of the differential propagation phase  $\phi_{DP}$  and it's range derivative, the specific differential phase,  $K_{DP}$ . Noting that:

$$\phi_{DP} = \phi_{HH} - \phi_{VV} \tag{1.47}$$

$$K_{DP} = \frac{1}{2} \frac{d}{dr} \phi_{DP} = \frac{2\pi}{k_0} \int \Re \left[ \hat{h} \cdot \bar{f} - \hat{v} \cdot \bar{f} \right] N(D) dD \tag{1.48}$$

Where  $\phi_{HH}$  and  $\phi_{VV}$  represent the cumulative phase from horizontal and vertical plane waves for the total round trip between radar and the resolution volume. The term  $\phi_{DP}$ is the differential phase shift generated by the backscatters inside the volume and the differential phase shift along the propagation path. The main problem is to distinguish between phase lags generated by propagation path and backscattering. The specific differential phase  $K_{DP}$  is expressed in degrees per kilometer,  $\bar{f}$  represents the forward scattering amplitude,  $k_0$  is the wave number in free space and  $\hat{h}$  and  $\hat{v}$  are the unit vectors for the horizontal and vertical polarization plane. For rain observations  $\phi_{DP}$  is constantly increasing along range. For uniform rain rates along the propagation path,  $K_{DP}$  becomes a constant.

#### The correlation coefficient $\rho_{co}$

Further precipitation information can be retrieved by the measure of the correlation coefficient  $\rho_{co}$ , which is the correlation between the horizontal and vertical polarized echo signals. The formulation in [54] is:

$$\rho_{co} = \frac{\langle S_{VV} S_{HH}^* \rangle}{\sqrt{\left(\left\langle \left|S_{HH}\right|^2 \right\rangle \left\langle \left|S_{VV}\right|^2 \right\rangle\right)}} \tag{1.49}$$

Again the expectation values from the covariance matrix in equation 1.36 are used for the evaluation of the polarimetric observable.  $\rho_{co}$  is mainly governed by non-rain hydrometeors. Bright band regions with rain/hail mixtures or irregular hydrometeor shapes produce  $\rho_{co}$  values around 0.9, as indicated in [55] and [56]. Whereas in rain, the values range from 0.98 to 0.995.

$$|\rho_{co}| = 1 - 2 \cdot 10^{0.1 L_{DR}} \tag{1.50}$$

By assuming randomly oriented particles in the polarization plane of interest, the relation 1.50 from [57] between  $L_{DR}$  and  $\rho_{co}$  can be used.

#### 1.5.3 Pulse pair processing of I/Q signals

In the previous section the theoretical background of the covariance matrix 1.36 and the scattering matrix 1.35 was given. The following section gives the mathematical implementation of the covariance matrix in the signal processing chain of the weather radar receiver. In particular, it will be shown how the auto and cross correlation functions from equations 1.52 to 1.57 are used to estimate the radar moments for specific range gates in the radial distance R. To treat this topic, the I/Q signals will be introduced first.

I (in-phase) and Q (quadrature-phase) data sets are generated to retrieve the phase- and amplitude values from echo signals. For generating the I/Q data series from the received echo pulse voltages, the signals are digitally multiplied with an coherent oscillator signal,

which is synchronized by the radar master clock. By assuming the coherent oscillator to be a sine signal, the I signal will be generated by the multiplication with sine-dependence and the Q signal by multiplication with cosine-dependence. Finally I and Q are the real and imaginary element of the received echo voltage:

$$U_m = I_m + jQ_m \tag{1.51}$$

Is the radar system not working in full coherent mode (e.g. in case of a magnetron transmitter), the transmitter phase needs to be considered. Modern weather radars with magnetron transmitters use numerical oscillators, which are synchronized by the transmitted phase, to work in coherent on receive radar mode. Phased array radars with multiple TRMs, Klystron radars or solid state radars are working in full coherent mode, so that the transmitter signal is already phase-synchronized by the radar master clock.

Pulse pair processing takes place in the radar signal processor. I/Q data sets are provided by the digital receiver and represent the down- and A/D-converted baseband information. The radar signal processor calculates for each range gate a pulse pair for estimating the auto (correlation considering the same polarization states for transmit and receive) and cross (correlation considering orthogonal polarization states for transmit and receive) correlation values at different time lags. I/Q data sets are typically synchronized (or tagged) by angle position to establish PPI visualization. The results from the auto and cross correlation are further used to calculate the radar moment data.  $V_m$  represents the signal time series after clutter correction, so that  $T_0$ ,  $T_1$ ,  $T_2$  stand for auto- and cross correlation values without clutter suppression and  $R_0$ ,  $R_1$  and  $R_2$  consider clutter suppression. The asterisk \* refers to a complex conjugated signal amplitude ( $U_m = I_m - jQ_m$ ).

$$T_0 = \frac{1}{N_S} \cdot \sum_{m=1}^{N_S} U_m \cdot U_m^*$$
(1.52)

$$R_0 = \frac{1}{N_S} \cdot \sum_{m=1}^{N_S} V_m \cdot V_m^*$$
(1.53)

$$T_1 = \frac{1}{N_S - 1} \cdot \sum_{m=2}^{N_S} U_m \cdot U_{m-1}^*$$
(1.54)

$$R_1 = \frac{1}{N_S - 1} \cdot \sum_{m=2}^{N_S} V_m \cdot V_{m-1}^*$$
(1.55)

$$T_2 = \frac{1}{N_S - 2} \cdot \sum_{m=3}^{N_S} U_m \cdot U_{m-2}^*$$
(1.56)

$$R_2 = \frac{1}{N_S - 2} \cdot \sum_{m=3}^{N_S} V_m \cdot V_{m-2}^*$$
(1.57)

The term "lag" can be understood as a time lag between consecutive echo pulses and describes the signal voltages that have been correlated to each other. E.g. represents Lag 0 the auto correlation from one pulse and represents the measure of signal power. Lag 1 serves the auto correlation of two voltages from consecutive echo pulses with time distance PRT. By assuming  $N_S$  complex samples for the calculation of one range gate, the auto and cross correlation values from [58] are given in equations 1.52 to 1.57.

#### Single- and dual-polarization moment calculation

The following single and dual polarization moments can be calculated by the auto and cross correlation results from the equations 1.52 to 1.57. In dual polarization mode the horizontal and vertical channels are processed separately.

$$UZ[dBZ] = 10\log_{10}(T_0 - P_N) + c_{SP} + c_{Radar} + 20\log_{10}(R) + c_{Athm}R + L_{MF}$$
(1.58)

$$CZ[dBZ] = 10\log_{10}(R_0 - P_N) + c_{SP} + c_{Radar} + 20\log_{10}(R) + c_{Athm}R + L_{MF}$$
(1.59)

Uncorrected reflectivity UZ and corrected reflectivity CZ can be calculated by pulse pair processing for horizontal and vertical polarized radar operation.  $T_0$ ,  $R_0$  are defined with equations 1.53, 1.52 and represent the uncorrected and clutter corrected signal powers detected in the signal processor.  $P_N$  stands for the detected noise level and is typically subtracted to visualize radar images free of system and background noise. How system and background noise is generated will be discussed in the following sections.  $c_{SP}$  is a constant to transfer arbitrary power units, generated by A/D conversion of the digital receiver, into dBm values during a receiver calibration procedure.  $c_{Radar}$  appears as the radar constant and takes all constants from the volume target equation 1.27 into account. Additionally the transmit and receive path waveguide losses and the radome losses are considered in  $c_{Radar}$ , as operational radars are working with this formulation. The matched filter losses  $L_{MF}$  need to be considered if the radar receiver is calibrated with a continuous wave signal. By using a gated noise signal as calibration reference source, the matched filter bandwidth needs to be adapted [59]. The atmospheric attenuation constant  $c_{Athm}$  of 0.016  $\frac{dB}{km}$  for S-Band, 0.019  $\frac{dB}{km}$  for C-Band and 0.024  $\frac{dB}{km}$  for X-Band frequencies from [14] and [58] should be used. An elevation dependence is not considered for  $c_{Athm}$ . Now we consider the measurement of Doppler velocities using the auto correlation of Lag 1:

$$UV\left[\frac{m}{s}\right] = \frac{V_{Max}}{\pi} \arg\left(T_1\right) \tag{1.60}$$

$$CV\left[\frac{m}{s}\right] = \frac{V_{Max}}{\pi} \arg\left(R_1\right)$$
 (1.61)

By recalling equation 1.9, the maximum Doppler velocity  $V_{Max}$  for a pulsed Doppler radar is defined by the Nyquist theorem.  $T_1$ ,  $R_1$  from equations 1.55 and 1.54 represent the auto correlation from lag 1, respectively for the uncorrected and the corrected data sets. Note the velocity sign is defined as negative, towards the radar [58].

$$UW\left[\frac{m}{s}\right] = \frac{V_{Max}}{\pi} \sqrt{\frac{2}{3} \ln\left(\frac{|T_1|}{|T_2|}\right)}$$
(1.62)

$$CW\left[\frac{m}{s}\right] = \frac{V_{Max}}{\pi} \sqrt{\frac{2}{3} \ln\left(\frac{|R_1|}{|R_2|}\right)}$$
(1.63)

The spectral width CW,UW can be calculated by considering the auto correlation results from lag 0 and lag 1, with  $T_0$ ,  $T_1$  for uncorrected case and  $R_0$ ,  $R_1$  for the corrected case. Mathematical represents the spectral width the standard deviation of a Gaussian distributed power spectrum of a weather signal. In meteorological regard, the spectral width is a measure of velocity dispersion generated by hydrometeor turbulences or shear in the sampled volume.

$$Z_{DR}[dB] = 10 \log_{10} \left( \frac{R_0^H - P_N^H}{R_0^V - P_N^V} \right) + Z_{DR}^{OFFSET}$$
(1.64)

The polarimetric observables as differential reflectivity  $Z_{DR}$ , the linear depolarization ratio  $L_{DR}$  and the differential phase  $\phi_{DP}$  are already introduced in the previous section. For sake of completeness the moment calculation from pulse pair processing are given in the equations 1.64, 1.65 and 1.66.

$$L_{DR}[dB] = 10 \log_{10} \left( \frac{R_0^H - P_N^H}{R_0^V - P_N^V} \right) + L_{DR}^{OFFSET}$$
(1.65)

Typically, weather services assume to transmit  $45^{\circ}$  linear and receive the echo signals simultaneously in H and V channel. Most likely, the transmitted electromagnetic wave is elliptically polarized due to the non-phase aligned H and V waveguide path. However, this mode is used for the calculation of  $Z_{DR}$  in equation 1.64. The  $L_{DR}$  measurements for equation 1.65 are established for horizontal transmission and H and V channel reception. In order to change from the 45° linear transmission mode to  $L_{DR}$  mode (typically full power established in horizontal transmission path), a high power waveguide switch is used. The microwave power during transmit reaches up to 100kW in X-Band, 600 kW in C-Band and 1 MW in S-Band, so that these switches need to handle a high amount of microwave power. The  $L_{DR}$  and  $Z_{DR}$  offsets are related to imbalances for the transmission and reception path for horizontal and vertical polarization channel. The offsets are incorporating the polarimetric imbalances from antenna gain, transmit path, receive path, radome attenuation (which is typically zero for pseudo random cut radomes), transmitted power and absolute radar calibration. Nowadays, weather radars are using the sun as a stable reference source to make absolute radar calibration in receive. Furthermore, the sun is providing un-polarized EM waves, so that the sun can also be used to evaluate the polarimetric system offset between horizontal and vertical channel. Indeed, the sun can only be used for calibration in reception. For calibration in transmit and receive fixed targets (e.g. metal sphere) might be used. Drawbacks of this two way calibration procedure are the TR limiter recovery times, the compliance to far field definition and the position stability of the sphere, commonly installed on an aerostat. For this reason the weather services are using other automatic calibration procedures. Either the sun [61] is evaluated in differential power or light rain at 90° elevation [62] is observed to calibrate  $Z_{DR}$ .

$$\phi_{DP} \left[^{\circ}\right] = \arg \left(R_0^{HV}\right) + \phi_{DP}^{OFFSET} \tag{1.66}$$

The specific differential phase  $K_{DP}$  can be calculated by the range derivate of  $\phi_{DP}$  as stated in equation 1.48.

$$R_0^{HV} = \frac{1}{N_S} \cdot \sum_{m=1}^{N_S} V_m^H \cdot V_m^{V^*}$$
(1.67)

$$R_1^{HV1} = \frac{1}{N_S - 1} \cdot \sum_{m=1}^{N_S - 1} V_m^H \cdot V_{m+1}^{V^*}$$
(1.68)

$$R_1^{HV2} = \frac{1}{N_S - 1} \cdot \sum_{m=1}^{N_S - 1} V_{m+1}^H \cdot V_m^{V^*}$$
(1.69)

$$\rho_{co}^{(0)} = \frac{\left|R_0^{HV}\right|}{\sqrt{\left|R_0^H - P_N^H\right| \cdot \left|R_0^V - P_N^V\right|}}$$
(1.70)

$$\rho_{co}^{(1)} = \frac{\left|R_1^{HV1}\right| + \left|R_1^{HV2}\right|}{2 \cdot \sqrt{|R_1^H| \cdot |R_1^V|}}$$
(1.71)

As shown in equations 1.70 and 1.71, the correlation coefficient  $\rho_{co}$  can be calculated for Lag 0 and Lag 1. The Lag 1 calculation of the correlation coefficient from [60] does not depend on noise power level.  $R_0^{HV}$  represents the auto correlation of Lag 0.  $R_1^{HV1}$  is the copolar correlation at Lag 1, with horizontal channel signal of pulse n and vertical channel signal of pulse n+1.  $R_1^{HV2}$  the copolar correlation at Lag 1, with horizontal channel signal of pulse n+1 and vertical signal of pulse n. The auto correlation at Lag 1 from horizontal and vertical channel  $R_1^H$  and  $R_1^V$  can be calculated with equation 1.55. All parameters for the calculation of  $\rho_{co}^{(1)}$  are visualized in figure 1.9.

All polarimetric observables can be estimated with the introduced auto and cross correlation functions for weather radars with hybrid and alternating transmission mode. Indeed, the Lag 0 can only be calculated in hybrid mode. Note that the decorrelation time becomes more critical for weather radars using the alternating mode. The hybrid mode allows the simultaneous reception of two voltages corresponding to the two polarization channels.

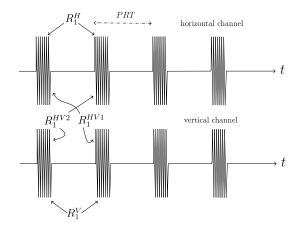


Figure 1.9: Graphical description of all parameters to retrieve  $\rho_{co}^{(1)}$  from equation 1.71. Pulse trains in the H and V channels and pulse pairs used in the calculations of the correlation functions in either channel and in both channels, adapted from [60].

## **1.6** Noise in radar systems

Noise levels detected by the radar receiver is a result of random processes such as the flow of charges in tube devices in the radar transmitter path, propagation through the atmosphere, the physical antenna noise contribution, the background noise received from the complete antenna radiation pattern and the intrinsic noise of the receiver chain. The noise level of the radar system sets the lower limit on the strength of a signal that can be detected in the presence of the noise. In particular phased-array radar systems with patch antennas are prone to contribute high noise levels due to lower antenna efficiency compared to radars with reflector antennas. On the contrary, the presence of noise has not only disadvantages. A lot of information can be derived by the analysis of noise signals, so that conclusions about the system stability, antenna performance and the status of the radar hardware can be established. For calibration purposes noise signals can be used as active reference signals. State-of-the-art weather radars incorporate automatic calibration procedures with active noise sources inside the receiver chain. These noise signals are used to calibrate the absolute and differential power levels at the receiver reference point. This section provides the theoretical background of noise in radar systems to determine the equivalent antenna temperature, the cascaded system temperature and the receiver noise figure. Furthermore, the minimum detectable and minimum discernable signal will be introduced as a figure of merit of a radar system and its sensitivity. Finally, it will be shown, how external and internal noise signals are used to retrieve information for the proper function of an operational weather radar system.

#### 1.6.1 Noise figure

The thermal noise power can be determined by the famous kTB relation derived in [29]:

$$N_P = k \cdot T \cdot B \tag{1.72}$$

with k the Boltzmann constant, T the temperature and B the bandwidth in Hz. If the noise power output of a DUT is required, the equivalent temperature of the DUT will be inserted.  $G_{DUT}$  represents the gain of the DUT in equation 1.73.

$$N_P = G_{DUT} \cdot k \cdot T_e \cdot B \tag{1.73}$$

The noise figure of a RF system is described by the quotient of the input signal to noise ratio  $(S_i/N_i)$  to the output signal to noise ratio  $(S_o/N_o)$ . Consequently, the definition for the noise figure NF in linear units can be described as follows:

$$NF = \frac{S_i/N_i}{S_o/N_o} \ge 1 \tag{1.74}$$

Equation 1.74 is only valid at defined  $T_0$  (e.g.  $T_0 = 290K$ ) for the input noise level  $N_i$ , with impedance matched input and output ports. Due to the fact that the output noise power is always higher than the input noise power, the linear noise figure is always greater than one. For receiver sensitivity considerations the noise figure will be expressed in logarithmic units:

$$NF[dB] = 10 \cdot \log_{10}(NF)$$
 (1.75)

For the impedance matched case the following relationship between equivalent temperature  $T_e$  and the linear noise figure of the device can be used:

$$T_e = (NF - 1) \cdot T_0 \tag{1.76}$$

A radar receiver can be considered as a cascade of individual stages. The cascade rule in equation 1.77 describes the accumulation of noise in a multi-stage receiver. It becomes clear, that the arrangement of the units has strong impact on the corresponding cascaded noise figure  $NF_{Cascade}$ . To establish a radar receiver chain with low noise contribution, the first unit of the receiver cascade becomes the most critical one. The noise figure values of consecutive units are reduced by the gain of the previous devices. As a consequence, the LNA (Low Noise Amplifier) is implemented as the first element in the receiver chain. Furthermore, the LNA should be implemented close to the antenna port to minimize losses and to keep the overall radar system noise figure low. A deep insight in the calculation of the system noise figure of a complete radar system is addressed in the next section. High gain LNAs are desirable, considering the optimization of the noise figure with higher noise figure values), according to Friis Noise Formula 1.77 derived in reference [22] in linear units as follows:

$$NF_{Cascade}] = NF_1 + \frac{NF_2 - 1}{G_1} + \frac{NF_3 - 1}{G_1G_2} \dots + \frac{NF_L - 1}{G_1G_2 \dots G_{L-1}}$$
(1.77)

#### 1.6. NOISE IN RADAR SYSTEMS

Or more generally:

$$NF_{Cascade}] = NF_1 + \sum_{m=2}^{L} \left( (NF_m - 1) / \left( \prod_{n=1}^{L-1} G_n \right) \right)$$
(1.78)

Common noise figure values for weather radar receivers in S-, C-, and X-Band are ranging from 1.5 dB to 3dB. Unfortunately the weather radar suppliers are indicating only the receiver noise figure and not the more important equivalent system temperature of the complete radar. The equivalent system temperature significantly depends on the radar system concept. In particular the receiver position, and, as a result, the distance between antenna feed and LNA are the most critical issues in this regard. But also the down converter and the digital receiver noise figure contribution to the cascaded noise figure are becoming more meaningful, since the LNA noise figure is almost pushed to the physical limit. E.g. an inadequate noise figure value of the A/D converter unit of the digital receiver (e.g. as second part of a cascade as shown in figure 1.1 with typical NF values ranging from 30dB to 36dB) can quickly degrade the overall receiver noise figure. In radio telescopes the LNAs are often actively cooled using Peltier elements or gas filled cavity with diaphragm to establish the Peltier-Effect or the Joule-Thomson-Effect, respectively. Compared to thermoelectric Peltier coolers with 240K end temperature [23], Joule- Thomson coolers are able to offer a lower cold end temperature, down to 115K, as experimentally shown with an LNA at 0.45 to 1.4GHz operating frequency band in [24]. As a result of such low temperatures, the corresponding equivalent system temperature can significantly be reduced. Weather radar receivers are not yet equipped with this active cooling technology. Reasons are the much greater expenses for the cooling environment and the comparatively small improvement factor of signal to noise ratio (tenth of a dB).

#### 1.6.2 Antenna temperature

The equivalent antenna temperature  $T_e^{Ant}$  is mainly effected by the background temperature  $T_b$ , the physical temperature  $T_p$  and the antenna efficiency  $\eta$ , as defined in reference [29]. Respectively, the equivalent antenna temperature can be calculated with:

$$T_e^{Ant} = \eta T_b + (1 - \eta) T_p$$
(1.79)

For instance, a phased-array antenna with typical antenna efficiency values ranging from  $\eta = 0.85$  to  $\eta = 0.70$ , an assumed background temperature of  $T_b = 100K$  at 5° elevation and a typical physical temperature  $T_p = 290K$  below radome provides an equivalent antenna temperature  $T_e^{Ant}$  of 128.5 K to 157 K. Reflector antennas with typical antenna efficiency values of  $\eta = 0.95$  are providing a much lower value of 109.5 K.

"When the antenna beamwidth is broad enough that the different parts of the antenna pattern see different background temperatures, the effective brightness temperature  $T_B^{Ant}(\theta, \phi)$  seen by the antenna can be found by weighting the spatial distribution of the background temperature by the pattern function of the antenna" [29].

$$T_B^{Ant}(\theta,\phi) = \frac{\int\limits_{\phi=0}^{2\pi} \int\limits_{\theta=0}^{\pi} T_B(\theta,\phi) D(\theta,\phi) \sin(\theta) d\theta d\phi}{\int\limits_{\phi=0}^{2\pi} \int\limits_{\theta=0}^{\pi} D(\theta,\phi) \sin(\theta) d\theta d\phi}$$
(1.80)

 $T_B(\theta, \phi)$  represents the distributed background temperature and  $D(\theta, \phi)$  is the directivity distribution of the antenna radiation pattern. As soon as the background temperature is not uniformly distributed, the background temperature  $T_b$  from equation 1.79 becomes the brightness temperature  $T_B^{Ant}(\theta, \phi)$  from equation 1.80. Background noise consists of all external radio sources and is strongly depending of the antenna elevation angle: cosmic microwave background radiation at 3-4K towards zenith, 50-100K toward horizon due to greater thickness of the atmosphere and 290-300K towards ground [29]. Is the noise power output of a receiver required and the receiver unit is directly connected to the antenna port, the simple relation from equation 1.73 can be modified to:

$$N_P^{RX_{out}} = G_{RX}k\left(T_e^{RX} + T_e^{Ant}\right)B \tag{1.81}$$

#### **1.6.3** Noise temperature of a cascaded radar system

Two special cases for system temperatures must be highlighted for phased-array radar systems and weather radars with dish antennas. A phased-array system is either working in active or in passive mode. Active phased-array radars are equipped with multiple TRMs installed behind each individual radiator. The passive phased-array system has typically one high power transmitter and one or multiple receiver units. For the distribution of RF power and for the connection between receiver and antenna, feeding networks (lossy lines) consisting of waveguides or microstrip lines are used. These lossy lines contribute noise, so that this fact must be considered in the noise characterization of passive phased-array systems and weather radars with dish antennas. For active phased-array radars equation 1.79 can be used to calculate the equivalent noise temperature of the antenna element "seen" by the receiver. The output power of the LNA located directly behind the antenna element of the active PAR can be calculated with equation 1.81.

Equation 1.82 provides the system temperature at the entrance of the receiver for a passive PAR with losses L in the receive path and the antenna efficiency  $\eta$  [29], as highlighted blue in figure 1.10. Note, that the following loss factors  $L_T, L$  must have values  $\geq 1$ .

$$T_{S}^{Passive} = \frac{1}{L} \left[ \eta T_{b} + (1 - \eta) T_{p} \right] + \frac{L - 1}{L} T_{p}$$
(1.82)

The system temperature for State-of-the-art weather radars with dish antennas can also be calculated with equation 1.82, since most of these radars are using waveguides as lossy

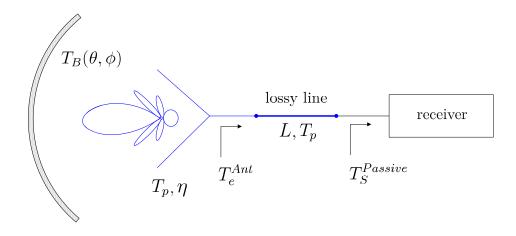


Figure 1.10: Radar receiver module connected through a lossy line to antenna, adapted from [29]. The units highlighted in blue are considered for the calculation of the equivalent system temperature in equation 1.82.

lines between the antenna reference port and the receiver input. Equation 1.82 is the simple expression for a cascade of two noisy components, without the consideration of the antenna mismatch factor and the receiver noise figure. The consideration of the antenna mismatch factor can be found in [29]. The radar antennas are typically impedance matched over the operating frequency band, so that this term can be neglected for noise estimates. Figure 1.10 shows the configuration of the antenna connected through a lossy line to the receiver to give an overview about the different equivalent temperatures in the cascaded system of two noisy elements.

For evaluating the noise power output of a cascaded radar system with three noisy elements, namely the antenna, the transmission line and the receiver unit, equation 1.84 can be used. In figure 1.11 the three noise contributors are highlighted in blue. The equivalent noise temperature of the receiver  $T_e^{RX}$  can be calculated with the linear noise figure of the receiver  $NF_{RX}$  and the physical temperature of the receiver  $T_0$  by using the relation from equation 1.76.

$$T_e^{RX} = (NF_{RX} - 1) \cdot T_0 \tag{1.83}$$

The equivalent noise temperature of the transmission line and receiver can be calculated with

$$T_e^{TL+RX} = T_e^{TL} + L_T \cdot T_e^{RX}.$$
 (1.84)

As introduced with equation 1.79, the effective antenna temperature  $T_e^{Ant}$  can be evaluated and inserted in equation 1.85. The exact received noise from radar antenna can be found by weighting the background noise with the complete antenna radiation pattern. The model can be simplified for narrow beam antennas (1°) with acceptable side lobe suppression. In this case, the measured background noise in main beam direction for the defined antenna elevation angle should be sufficient.

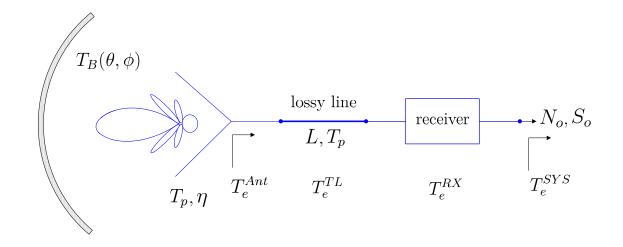


Figure 1.11: Noise output power analysis of a cascaded radar system, including the antenna, the lossy transmission line and the receiver performance [29]. The blue highlighted units are considered for the calculation of the equivalent system temperature  $T_e^{SYS}$  in equation 1.85 and the cascaded out noise power  $N_o^{Cascade}$  in equation 1.87.

The equivalent system temperature  $T_e^{SYS}$  of the cascaded system, as visualized in figure 1.11, can be found with:

$$T_e^{SYS} = T_e^{Ant} + T_e^{TL} + L_T \cdot T_e^{RX}$$

$$(1.85)$$

The cascaded input noise power  $N_i$  can be derived by the equivalent antenna temperature  $T_e^{Ant}$  and the KTB formula.

$$N_i = k \cdot T_e^{Ant} \cdot B = k \cdot (\eta T_b + (1 - \eta) T_p) \cdot B$$
(1.86)

$$N_o^{Cascade} = k \cdot B \cdot T_e^{SYS} \tag{1.87}$$

The cascaded output noise power  $N_o^{Cascade}$  is the function of the  $T_e^{SYS}$ . The system noise figure cannot easily be calculated with  $T_e^{SYS}$  and the relation in equation 1.76. The noise figure is defined with  $N_i = kT_0B$ , which is not the case for this cascaded system. In consequence, it is more convenient to work with equivalent temperatures and noise power in such cascaded systems.

#### 1.6.4 Minimum detectable signal

The minimum detectable signal (MDS) is a figure of merit of a radar receiver and value describes its sensitivity. Assuming a signal to noise ratio of 0 dB, the lowest signal strength that a radar receiver is able to detect can be estimated as follows:

$$S_{min}(dBm) = N_i(dBm) + NF_{RX}(dB) + B(dB) + L(dB)$$
(1.88)

With  $N_i$  the input noise power at 1 Hz (typically, the thermal noise of a matched 50 $\Omega$  resistor at  $T_0=290$ K, with  $kT_0$ B is used here),  $NF_{RX}$  the receiver noise figure, B the bandwidth (Typically defined by the matched filter bandwidth of the digital receiver part. E.g. 1 MHz for 1 $\mu$ s pulsewidth) and the losses in front of the receiver reference point. The calculated thermal noise power retrieved by equation 1.72 is -174dBm/Hz. The MDS is typically verified during acceptance tests of the radar receiver, so that a signal generator will be used for injecting a pulsed RF signal at the radar operating frequency, similar to the pulse signal of the radar transmitter. Finally, the strength of the injected signal will be reduced to verify  $S_{min}(dBm)$ . Note, the noise power  $N_i$  for this measurement setup will be dominated by the thermal noise of the signal generator, which is typically higher than the noise power of a high gain antenna pointing into free space. For this reason, the radar receiver in operational mode, with connected antenna port, shows better MDS results compared to the measurement setup previously explained.

In operational weather radar receivers multiple pulses are received, so that integrated over time can be used to increase the signal to noise ratio [7]. Through the integration of multiple pulses two cases of integration gains, namely the coherent and the incoherent integration gain, can be applied. The coherent integration gain is usually not used for the receiver verification measurement, but is indeed used for Doppler estimations in operational radar mode. Equation 1.89 describes the signal to noise ratio for a coherent integration of n pulses:

$$\left(\frac{S_n}{N_n}\right) = \frac{n_p^2 \cdot S_1}{n_p \cdot N_1} = n_p \left(\frac{S_1}{N_1}\right) \tag{1.89}$$

With  $n_p$  the number of pulses used for the integration and  $\left(\frac{S_1}{N_1}\right)$  the signal to noise ratio without pulse integration. Considering a coherent pulse sequence in equation 1.89 the voltages of successive pulses add and increase the signal powers by square. While are the noise voltages randomly distributed, so that the noise power values are only added together. This is the reason why the coherent integration gain is theoretical equal to the number of integrated pulses. For the more common incoherent integration gain  $G_{int}$  the empirical equation 1.90 [7] can be used.

$$G_{int} = \frac{n_p + \sqrt{n_p}}{2} \tag{1.90}$$

Typical minimum detectable signal values for weather radar receivers (e.g. 30 pulses of integration) are ranging from -114 dBm to -116 dBm, as a function of pulse width and the corresponding matched filter bandwidth.

#### **1.6.5** Noise signals for monitoring weather radar systems performance

As mentioned earlier, active noise sources are used for radar calibration. These noise sources consist typically of a noise diode followed by RF amplifier. In this way, strong noise signals are generated in the frequency band of interest. Noise sources are characterized by the measure of the output noise power, also called excess noise ratio (ENR):

$$ENR[dB] = 10 \cdot \log_{10}\left(\frac{N_G - N_P}{N_P}\right) = 10 \cdot \log_{10}\left(\frac{T_G - T_0}{T_0}\right)$$
(1.91)

 $N_G$  and  $T_G$  represent the noise and equivalent temperature of the noise generator. The values  $N_P$  and  $T_P$  are the noise power and temperature associated with a passive source at room temperature terminated by matched load (typically with 50 $\Omega$  wave impedance). Noise source ENRs are ranging from 15dB to 45dB. Noise sources (15dB ENR) without amplifiers are used to perform accurate noise figure measurements of RF devices. The amplified noise sources (45dB) are used as reference signals for calibration purposes. The high ENR values of 45dB are often necessary to overcome the insertion losses of couplers for injecting the noise signal in the receiver chain, without disturbing the in-line path of a radar echo signal. Drawbacks of active noise sources are the thermal dependence (0.015dB/K [44]) of the output signal. In [44] the temperature dependence and stability with focus on antenna-mounted weather radar receivers (AMR) and noise source generated reference signal is investigated. Finally a recommendation about temporal calibration cycles for AMR weather radar systems in European regions is given to assure a continuous accurate absolute radar calibration. In [59] the radar receiver configuration with noise source as reference signal is shown. Here the necessity of matched filter bandwidth definition for radar calibration with noise sources is investigated. By reason of the quasi white noise spectrum from the noise source reference signal, the matched filter bandwidth is different compared to the matched filter bandwidth for pulsed or continuous wave reference signals.

In 2011 Meteo Swiss started renewing and extending its operational C-Band weather radar network. The three already existing radar systems have been replaced by Selex-ES GmbH to state-of-the-art polarimetric Doppler radars with antenna-mounted receivers. The 4th and the 5th system have been installed in Wallis at 2970 m altitude in autumn 2013 and on Weißfluh Gipfel in autumn 2015. All five systems are based on antenna-mounted analog and digital receiver, to increase the system sensitivity. Weather radars are working 24/7 and should perform accurate measurements during all weather conditions. Unfortunately the radome insertion loss is significantly increased during a rain event above the radar. The water film on the radome surface induces additional insertion losses and disturbs the near field wave propagation from the antenna, so that the absolute gain value and the radome insertion loss used in the volume target weather radar equation 1.27 are biased. As reported in [76], [77] the calculated weather echoes are underestimated and the accuracy requirement of a weather radars is no longer established during such rain events directly above the radar. [78], [79] were the first who recognized that the degradation of radome

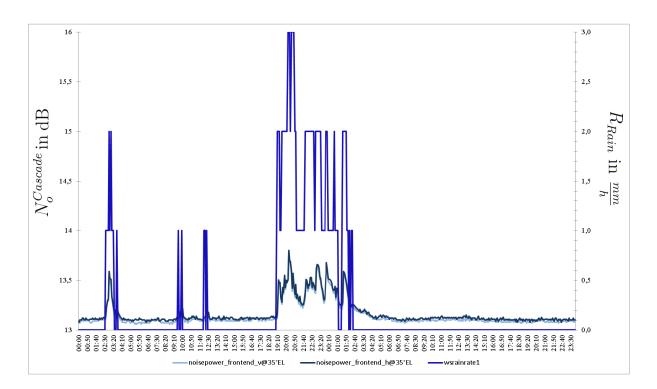


Figure 1.12: Noise signal observation for monitoring the weather radar system performance. The observation of the cascaded noise output power of a dual polarized weather radar system located in Switzerland on Albis for a 24 h time interval and a rain event above the radar. The data sets are acquired at 35° antenna elevation, so that the main beam is not filled with noise contributed by ground. The correlation between the rain rate  $R_{Rain}$  in  $\frac{mm}{h}$  (right y-axis) from external rain sensor, located at the radar tower and the detected noise power  $N_o^{Cascade}$  (left y-axis) from radar antenna system (radome + antenna), receiving waveguide path losses and analog- and digital radar receiver can be seen. The cascade of the receiving units are corresponding to the equivalent system noise temperature  $T_{SYS}$  in equation 1.84 and the cascaded output noise power  $N_o^{Cascade}$  from equation 1.87.

insertion loss during the rain event manifests itself as an increase of the measured system noise. Probably this effect is related to the rising equivalent antenna and radome temperature. The analysis of the cascaded noise power  $N_o^{Cascade}$  during a rain event above the radar system is shown in figure 1.12. Here the operational weather radar from Meteo Swiss on Albis (close to Zurich airport) was selected to give a showcase for noise observation and its usage.

From figure 1.12 it can be recognized, that the increase in detected system noise is strongly correlated to the rain rate intensity, sampled by an external rain sensor on radar site. This correlation can now be used to retrieve a correction factor for improving rain rate estimates during rain events above the radar. In theory, the increase of detected noise can be used to make estimates about the underestimation of a weather radar system during a rain event above the radar by using the equations 1.85 and 1.87. But it is ambiguous, if the increase of detected noise is related to the change in radome insertion loss and consequently related to the efficiency of the antenna system or due to an increase of the detected background noise produced by the antenna main beam pointing into a strong weather cell. This topic is still under investigation from the weather radar community.

Another external noise source for calibration purposes is the sun. The solar signal is a very good reference for ground based weather radar systems and can be used for several alignments. In [80] the antenna pointing accuracy was investigated, but also the stability of the receiver chain [81], in particular for dual polarized weather radars the  $Z_{DR}$  [82] can be monitored by using the sun as a stable reference signal. The signal to noise ratio for the radar measurement of the solar signal, at the receiver reference point, is typically 10 dB in S-Band, 8 dB in C-Band and 6 dB in X-Band. The solar signal is fluctuating due to the 11 year sun rotation cycle and solar flares. For this reason, the sun is monitored by observatories, for instance the Dominion Radio Astrophysical Observatory (DRAO) in Canada is monitoring the sun at S-Band frequency range. Meteo Swiss e.g. extrapolate the solar flux data from DRAO to their C-Band frequency, in order to calibrate the dual polarized weather radar in absolute  $(Z_H \text{ and } Z_V)$  and differential  $(Z_{DR})$  terms [83]. Selex-ES GmbH has developed a solar raster scan to retrieve the 2 dimensional antenna beamwidth from dual polarization weather radars [58]. Furthermore the gain offset in receive can be calculated with this solar raster scan to align the radar constant of an operational weather radar. In S-Band, the antenna sidelobes are also detectable by integrating the solar signal more intensively. But accurate sidelobe measurements as done on appropriate antenna test ranges (e.g. far-field, near-field) are not possible.

## **1.7** Bandwidth aspects in weather radar systems

Two different types of radar bandwidth can be distinguished, namely the signal bandwidth and the tunable bandwidth. Note, the tunable bandwidth has no information content. The signal bandwidth (can be interpreted as the information content) and its importance for the radar range resolution  $\Delta R$  was already discussed with equation 1.4 in section 1.1. Especially in pulse compression radars the signal bandwidth is increased by intra-pulse modulation for optimizing the range resolution  $\Delta R_{PCR}$ , introduced by equation 1.6.

The tunable radar bandwidth is defined by the change of the operational frequency the radar system allows. For instance, magnetron radars are changing their frequency via a tunable resonator. Klystron and SSTX are able to change their frequency with the frequency shift of the driving signal at intermediate frequency. Weather radars are typically operated in dedicated frequency bands, defined by the government regulating agencies. This is necessary to avoid mutual interference among nearby radio systems. The European frequency band for weather radar systems is also used by the WLAN (wireless local area network), so that the weather radar operating frequency should be selected very carefully. Before weather radars are installed, radio frequency site surveys are performed and the measurement results are taken for the decision of the final operating frequency.

Also for the system design of a new phased-array weather radar in a dense network, the radar system bandwidth must be evaluated carefully. In particular the antenna bandwidth must be designed sufficiently wide to operate the radar at different tunable frequencies in a dedicated frequency band with a wide signal bandwidth for the usage of pulse compression. In this work the operational center frequency is selected with 9395 MHz, the signal bandwidth of 10 MHz is chosen for pulse compression and a tunable frequency of 200 MHz, as used nowadays from state-of-the-art X-Band weather radars, is defined.

The bandwidth of phased arrays is dominated by two effects: the aperture effect and the feeding network effect as discussed in [25]. In both cases it is the difference in path length that influences the beam steering performance of a phased-array.

Beam steering of phased arrays is established by defined phase differences of the driving signal at the radiating elements, e.g. in planar antenna arrays. The phase front at the specific elements in such an array is therefore frequency dependent. This effect is the so-called aperture effect and should be considered, if the operational frequency of the phased-array radar is tuned. The aperture effect can be avoided by the accurate and frequency dependent phase shifter alignment.

The feeding network in phased-array antennas can be designed in different ways. The two main design classes are the series- and the parallel feeding networks. Series feeding networks are working with fixed distances between the feeding points allocated by microstrip lines. As a consequence, such designs are prone to contribute phase changes, when the operational frequency is changed. In frequency scanning antennas this effect is used to tilt the beam at desired point in space. As long as the same path lengths between feeding points and the multiple radiators are established, parallel fed antenna arrays are not contributing phase changes for different operating frequencies. A summary about state-of-the-art feeding networks will be introduced later in section 3.3.7.

# Chapter 2

# General terms and definitions in polarimetry

The development and the performance analysis of polarimetric microstrip patch antennas for weather radar applications require the theoretical foundations of electromagnetic theory. Also the propagation of electromagnetic waves through an illuminated volume of hydrometeors, the scattering process already introduced with the scattering matrix in equation 1.35, and the measurement of voltages by the weather radar signal processor using the covariance matrix in equation 1.36, requires the knowledge of electromagnetic theory.

For antenna and weather radar discussions in polarimetry, the polarization state must be clearly defined. Consequently, the Maxwell's equations are introduced first for the propagation of electromagnetic waves in vacuum (e.g. for the calculation of radiation pattern in far field) and isotropic media (e.g. for the wave propagation in substrates, used for the design of patch antennas). After introducing the free space field impedance, the polarization description are addressed by the Jones Vector and the complex polarization ratio. All introduced polarization descriptors are further used to describe the polarization state with the well-known geometrical representations in the polarization ellipse and the Poincare sphere.

# 2.1 Description and properties of plane waves

Electromagnetic waves at the macroscopic level are fully described by the Maxwell's equations [4] in their differential form, adapted by [28]:

$$\nabla \times \bar{E} = -\frac{\partial \bar{B}}{\partial t} - \bar{M} \tag{2.1}$$

$$\nabla \times \bar{H} = \frac{\partial \bar{D}}{\partial t} + \bar{J} \tag{2.2}$$

 $\nabla \cdot \bar{D} = \rho \tag{2.3}$ 

$$\nabla \cdot \bar{B} = 0 \tag{2.4}$$

with the vector quantities representing the time-varying vector fields:

- $\overline{E}$  the electric field intensity in (V/m),
- $\overline{J}$  the electric current density  $(A/m^2)$ ,
- $\overline{D}$  the electric flux density  $(C/m^2)$ ,
- $\overline{B}$  the magnetic flux density  $(Wb/m^2)$ ,
- $\overline{M}$  the magnetic current density  $(V/m^2)$ ,
- $\overline{H}$  the magnetic field intensity (A/m),
- $\rho$  the electric charge density  $(C/m^3)$ .

The source of the electromagnetic field can be explained by  $\overline{M}$ ,  $\overline{J}$  and  $\rho$ . The magnetic current density  $\overline{M}$  is a fictitious source and only considered for mathematical convenience. Magnetic monopole charges are not known to exist. The ultimate sources of the electromagnetic fields are the electric charges (charge density  $\rho$ ) and flow of charges in the form of electric current.

These four equations are complemented with the constitutive relations that are given for isotropic media as:

$$D = \epsilon E \tag{2.5}$$

$$\bar{B} = \mu \bar{H} \tag{2.6}$$

$$\bar{J} = \kappa \bar{E} \tag{2.7}$$

with the permittivity  $\epsilon$ ,  $\mu$  the permeability and  $\kappa$  the electrical conductivity. For the propagation of electromagnetic plane waves in source-free, linear, isotropic and homogeneous regions the Helmholtz equation can be derived as shown in reference [28]:

$$\nabla^2 \bar{E} + \omega_0^2 \mu \epsilon \bar{E} = 0 \tag{2.8}$$

The identical equation for  $\overline{H}$  is:

$$\nabla^2 \bar{H} + \omega_0^2 \mu \epsilon \bar{H} = 0 \tag{2.9}$$

Often the term in front of the electric field intensity  $\overline{E}$  is expressed with the constant  $k = \omega_0 \sqrt{\mu \epsilon}$ . Where, k is called the wavenumber or propagation constant of the medium with the unit 1/m.

In the following discussions, the electromagnetic waves are located in the far field region and are considered as homogeneous plane waves. In particular, the time variant homogeneous plane waves are investigated next for the description of electromagnetic waves. Figure 2.1 models the propagation of an electromagnetic(EM) wave through a medium. Here, the

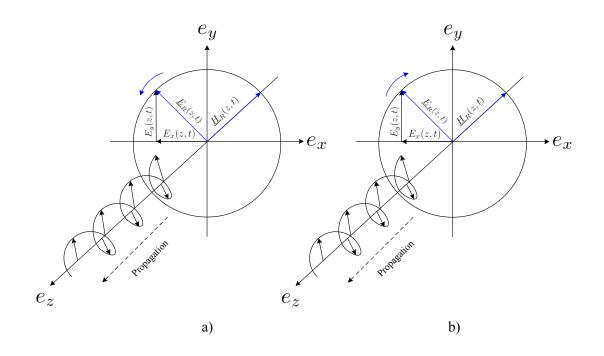


Figure 2.1: Propagation of electromagnetic plane wave, exemplary shown with a) right hand circular polarized (RHCP) and b) left hand circular polarized (LHCP) plane wave.

position of the time and space-variant electric field vector  $\underline{E}_R(z,t)$  and the magnetic field vector  $\underline{H}_R(z,t)$  are used for the description of homogeneous plane waves. At position z=0 and the time t=0 the vectors  $\underline{E}_R(z,t)$  and  $\underline{H}_R(z,t)$  are perpendicular to each other and perpendicular to the propagation direction vector  $e_Z$ .

$$\underline{H}_{R}(z,t) = \frac{(\pm e_{Z} \times \underline{E}_{R}(z,t))}{Z_{0}}$$
(2.10)

Equation 2.10 from reference [21] expresses the relationship of the electric and the magnetic field intensity. The magnetic field intensity is the vector product of electrical field intensity and the propagation direction vector  $e_Z$ , divided by the field impedance  $Z_0$ . As shown in figure 2.1 the field intensities  $\underline{E}_R(z,t)$  and  $\underline{H}_R(z,t)$  are perpendicular to each other. The sign of  $e_Z$  determines the direction of wave propagation. In this regard, the definition of the field impedance in vacuum from [21] can be derived with

$$Z_0 = \sqrt{\frac{L}{C}} = \sqrt{\frac{\mu_0}{\epsilon_0}} = 120\pi\Omega = 377\Omega.$$
 (2.11)

 $\mu_0$  represents the magnetic field constant and  $\epsilon_0$  the electric field constant. Another interpretation of equation 2.10 can be established by the use of Ohm's law. In this regard represents  $\underline{H}_R(z,t)$  the electric current,  $\underline{E}_R(z,t)$  the electric voltage and  $Z_0$  the resistor.

Due to the fact that the magnetic field vector can always be calculated by considering

equation 2.10, only the electrical field vector is used for the following polarization descriptions.

To describe plane waves in lossy materials as is necessary for microwave antenna substrates or hydrometeors forming a distributed target for weather radar observation, the complex propagation constant  $\gamma$  for the medium must be considered with:

$$\gamma = \alpha + j\beta = j\omega_0 \sqrt{\mu\epsilon'(1 - j\tan(\delta))}.$$
(2.12)

Here,  $\alpha$  represents the attenuation constant and  $\beta$  the phase constant. The loss can also be treated through the use of complex permittivity with

$$\epsilon = \epsilon' - j\epsilon'' = \epsilon'(1 - j\tan(\delta)) = \epsilon_r \epsilon_0 (1 - j\tan(\delta)).$$
(2.13)

The imaginary part of  $\epsilon$  accounts the losses inside the medium generated by heat. Microwave substrates are characterized by the real part of the complex permittivity with  $\epsilon' = \epsilon_r \epsilon_0$  and the loss tangent  $\tan(\delta)$ .

## 2.2 The Jones vector

The following derivation of the Jones vector description is adapted from reference [21]. The electrical field vector  $E_R(z,t)$  can be expressed by two orthogonal electric field components  $E_x(z,t)$  and  $E_y(z,t)$ . Both vectors are time- and space-variant and expressed as follows:

$$\underline{E}_{R}(z,t) = \begin{pmatrix} E_{x}(z,t) \\ E_{y}(z,t) \end{pmatrix} = \begin{pmatrix} a_{x}\cos(\omega_{0}t \pm \frac{2\pi}{\lambda}z + \delta_{x}) \\ a_{y}\cos(\omega_{0}t \pm \frac{2\pi}{\lambda}z + \delta_{y}) \end{pmatrix}$$
(2.14)

 $a_x$  and  $a_y$  characterize the vector component amplitude,  $\omega_0$  the angular frequency,  $\pm \frac{2\pi}{\lambda}$  the wave number and  $\delta_x$  and  $\delta_y$  are the zero phases of the vector components. A negative sign of the wave number describes a positive propagation direction. t and z are the time and space variables. For mathematical simplicity, the following complex representation described by equation 2.15 will be used for  $\underline{E}_R(z,t) = \Re \{\underline{E}(z,t)\}$ .

$$\underline{E}(z,t) = \begin{pmatrix} a_x e^{j\delta_x} \\ a_y e^{j\delta_y} \end{pmatrix} \cdot e^{j\omega_0 t} \cdot e^{j\left(\pm\frac{2\pi}{\lambda}z\right)}$$
(2.15)

At t=0 and z=0 we retrieve the complex Jones Vector in equation 2.16.

$$\underline{E} = \begin{pmatrix} E_x \\ E_y \end{pmatrix} = \begin{pmatrix} a_x e^{j\delta_x} \\ a_y e^{j\delta_y} \end{pmatrix}$$
(2.16)

The 2-component complex vector of equation 2.16 is called Jones vector [11] and it can be used to describe the polarization state of monochromatic transversal EM waves.

## 2.3 Complex polarization ratio

Based on the components of the complex Jones Vector, the complex polarization ratio will be introduced next. The complex polarization ratio is another polarization description and can also be used to visualize the polarization state of an electromagnetic wave in the polarization ellipse and on the surface of the Poincaré sphere, later introduced in subsection 2.4.

$$\rho = \frac{E_y}{E_x} = \frac{a_y}{a_x} \cdot e^{j(\delta_y - \delta_x)} = |\rho| \cdot e^{j\delta} = \tan(\gamma) \cdot e^{j\delta}$$
(2.17)

$$|\rho| = \frac{a_y}{a_x} \quad ; \quad \delta = \delta_y - \delta_x \tag{2.18}$$

The amplitude ratio is represented by  $\tan(\gamma)$ . Here,  $\delta$  expresses the phase difference between the two electric field vector components.

# 2.4 Polarisation ellipse and Poincaré sphere

All introduced variables from the Jones vector description are now used to describe the polarization states of full polarized plane waves by the well-known geometrical ellipse representation in figure 2.2.

The tip of the time variant field vector, observed with increasing time, at a fixed point z passes the ellipse contour, which is determined by the complex vector amplitude. Depending on  $a_x$ ,  $a_y$ ,  $\delta_x$  and  $\delta_y$  the geometry and the electrical field vector rotation direction of the polarization ellipse changes. For the presentation of full polarized plane waves by using the polarization ellipse, additional variables are introduced next to describe the geometry of the ellipse in figure 2.2 accurately.

The orientation angle  $\Phi \in (0 \le \Phi \le \pi)$  characterizes the angle between the positive x-axis and the ellipse main axis. The ellipticity angle  $|\tau| \in (0 \le |\tau| \le \frac{\pi}{4})$  is defined by the ratio of cathetus and adjacent side:

$$\tan(|\tau|) = \frac{\dot{a_y}}{\dot{a_x}} \tag{2.19}$$

The rotation direction is characterized by the sign of  $|\tau|$ . The ellipse size is a function of the wave amplitude  $a = \sqrt{\dot{a_y}^2 + \dot{a_x}^2}$ , which forms the hypotenuse of the triangle in the polarization ellipse.

The position of the tip of the electric field vector on the ellipse contour at t=0 represents the wave zero phase  $\alpha$ . Where the angle  $\alpha$  corresponds to the complex vector amplitude zero phase  $\delta_x$ . The following definition for left-handed polarization holds: "A circularly or an elliptically polarized electromagnetic wave for which the electric field vector, when viewed with the wave approaching the observer, rotates clockwise in space. Notes: 1. This definition is consistent with observing a counterclockwise rotation when the electric field vector is viewed in the direction of propagation. 2. A left-handed helical antenna radiates a left-hand polarized wave" [124].

Two electromagnetic plane waves with the same parameters  $\Phi$  and  $\tau$  and different wave amplitudes *a* and wave zero phases  $\alpha$  have the same polarization. Between the parameters of the complex Jones Vector and the geometrical parameters of the ellipse, the following geometrical relationships are introduced:

$$\tan(2\Phi) = \tan(2\gamma)\cos(\delta) \tag{2.20}$$

$$\sin(2\tau) = \sin(2\gamma)\sin(2\delta) \tag{2.21}$$

These auxiliary variables are called Deschamps [18] parameters and are used for polarization state visualization on the Poincaré sphere, as shown in figure 2.3. Another representation of a polarization state is the Stokes vector, which will be introduced next.

Originally, the Stokes vector was introduced to describe polarization states in physical optics. The Stokes vector is a time-averaging polarization description. Due to the fact that the stokes vector do not consider the wave zero phase, it is an incoherent description and therefore not a complete polarization description.

The stokes vector can be characterized by the geometrical parameters of the ellipse and the Poincaré sphere as follows:

$$g = g_0 \begin{pmatrix} 1\\ \cos(2\tau)\cos(2\Phi)\\ \cos(2\tau)\sin(2\Phi)\\ \sin(2\tau) \end{pmatrix}$$
(2.22)

The elements  $g_1$ ,  $g_2$  and  $g_3$  create the three main axis in the Poincaré sphere in figure 2.3. The wave intensity  $g_0 = a^2$  will be represented by a pointing vector through the point p. To address a polarization state by a point on the surface of the Poincaré sphere the elements of the Stokes vector  $g_1$ ,  $g_2$  and  $g_3$ , the polarization ellipse parameters  $2\tau$  and  $2\Phi$ , or the Deschamps parameters  $2\gamma$  and  $\delta$  can be used.

The stokes elements  $g_0$ ,  $g_1$ ,  $g_2$  and  $g_3$  can also be used to evaluate the degree of polarization  $d_{pol}$ . The definition of  $d_{pol}$  is formulated in [124] as follows: "The fraction of the total power in a wave that is completely polarized. Note: Sometimes the definition is further restricted to a given polarization state, as in degree of linear polarization".

$$d_{pol} = \frac{\sqrt{g_1^2 + g_2^2 + g_3^2}}{g_0} \tag{2.23}$$

 $d_{pol}$  becomes zero for un-polarized and one for fully polarized waves.

The Poincaré sphere is defined by [124] as follows: "A tool for graphically displaying

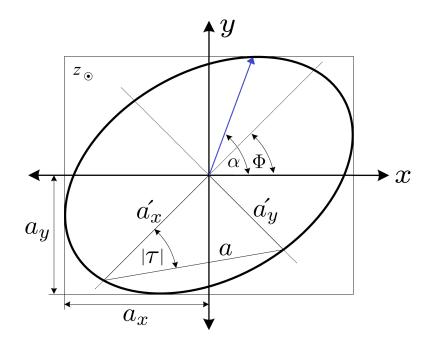


Figure 2.2: The polarization ellipse and its parameters adapted by [21] with the orientation angle  $\Phi$ , the ellipticity angle  $|\tau|$ , wave zero phase  $\alpha$  and wave amplitude a.

the polarization state of a monochromatic wave. For a fully polarized wave, each point on the sphere's surface defines a unique polarization state, with axial ratio and tilt angle mapping into latitude and longitude, respectively". On the North Pole the left hand circular polarization is located. The right hand circular polarization is located at the South Pole. Orthogonal states of polarizations are represented on the Poincaré sphere by antipodal points, as shown for instance in figure 2.3 for horizontal H and vertical V polarization, the circular polarization states and the  $\pm 45^{\circ}$  polarization states. Linear polarization states are located exclusively at the equator of the sphere. Everything in north and south direction between the equator and the poles is elliptically polarized. The northern hemisphere of the Poincaré sphere shows left-handed and the southern hemisphere shows right-handed elliptically polarized states.

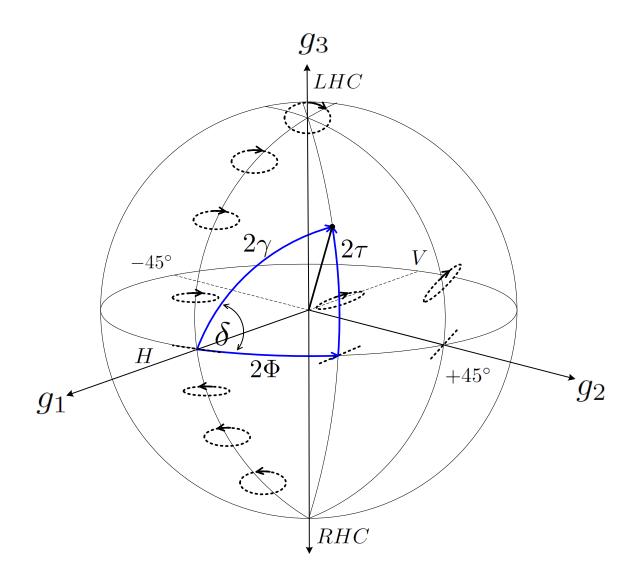


Figure 2.3: The Poincaré sphere. To describe a point on the surface of the Poincaré sphere, the polarization descriptors of the Stokes vector  $g_1$ ,  $g_2$  and  $g_3$ , the polarization ellipse parameters  $2\tau$  and  $2\Phi$ , or the Deschamps parameters  $2\gamma$  and  $\delta$  can be used.

92

# Chapter 3

# Relevant microwave antenna fundamentals

In order to develop dual polarized phased-array antennas, it is essential to treat the theoretical background of antennas. This chapter gives an overview of the general terms and definitions in microwave antennas. In particular, phased-array antennas are addressed. The sum pattern calculation of an antenna array, formed by single radiating elements is given. The general definition of the antenna multiplication law is shown by considering the array- and the element factor. Furthermore, the main attention will be drawn on microstrip antennas. The microstrip antenna principle will be explained by the well-known cavity model and different microstrip antenna architectures are summarized. One class of microstrip antennas, namely the pin feed microstrip antennas are investigated in detail. Also general microwave PCB design aspects are discussed. In this context, available feeding network structures from literature are shown and the equations for the calculation of line impedance and phase constant for microstrip lines on substrates are given.

Finally, an overview of the antenna-pattern definitions relevant for the discussions on polarimetric phased-array antenna radiation pattern are given in the following chapters. In particular the theoretical definitions for cross-polarization isolation, cross-polarization discrimination and cross polarization suppression are addressed.

# 3.1 General terms and definitions in microwave antennas

An isotropic radiator at a distance R produces, depending on the direction in space and the radiated power  $P_s$ , a spherical phase front with the following power density as introduced in [12]:

$$\langle S_i \left( r, \theta, \phi \right) \rangle = \frac{P_s}{4\pi r^2} \tag{3.1}$$

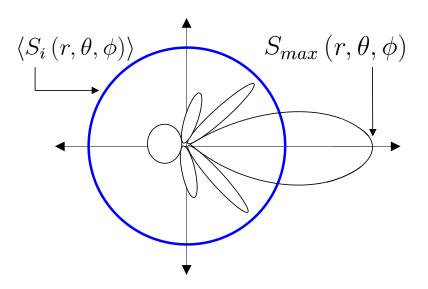


Figure 3.1: Grapical explanation of the antenna directivity [12]. The maximum radiation density in the main beam direction  $S_{max}(r, \theta, \phi)$  will be referred to isotropic radiation  $\langle S_i(r, \theta, \phi) \rangle$ . The ideal isotropic radiator is radiating the same amount of field intensity in all angular directions.

An ideal isotropic radiator radiates electromagnetic fields with the same amount of energy in all angular directions, as indicated with a blue circle in figure 3.1. For this reason, the antenna directivity is often expressed in dBi indicating the reference to the isotropic radiator in logarithmic units.

The directivity D in equation 3.2 can be understood as the maximum radiation density in the main beam direction of the antenna, divided by the radiance of a isotropic radiator at the same point in space [12].

$$D = \frac{S_{max}(r,\theta,\phi)}{\langle S_i(r,\theta,\phi) \rangle} = 4\pi r^2 \frac{S_{max}(r,\theta,\phi)}{P_s}$$
(3.2)

The radiated power  $P_s$  in free space differs from the antenna input power  $P_{in}$  by intrinsic power losses  $P_v$  of the antenna  $P_{in} = P_s + P_v$ . As a consequence, the antenna efficiency can be introduced as follows:

$$\eta = \frac{P_s}{P_{in}} = \frac{P_s}{P_s + P_v} \le 1 \tag{3.3}$$

In conventional weather radars with reflector antennas the intrinsic losses are created by the waveguides. The waveguide losses are a function of the operational frequency and the waveguide types. In S-Band, C-Band and X- Band the losses can be broadly estimated with 0.025dB/m, 0.05dB/m and 0.1dB/m, respectively. Such reflector antennas with center feed horns establish antenna efficiencies higher than 95 percent. Phased array microstrip antennas contribute losses due to their feeding networks and the lossy excitation process due to the substrate below the radiating patch. Here the insertion loss depends on the loss tangent from the substrate and the architecture of the patch antenna. Typically phased-array antennas are providing lower efficiency values of around 80 to 90 percent.

With the knowledge of the antenna efficiency  $\eta$  the gain of an antenna can be calculated as follows:

$$G = \eta \cdot D = \frac{P_s}{P_{in}} \cdot 4\pi r^2 \frac{S_{max}(r, \theta, \phi)}{P_s} = 4\pi r^2 \frac{S_{max}(r, \theta, \phi)}{P_{in}}$$
(3.4)

The antenna gain can be interpreted as a comparison of the maximum radiation density of an considered antenna with a radiation density of an isotropic radiator with same input power. For lossless antennas ( $\eta = 1$ ) the gain G and directivity D is equal. For real antennas G is always smaller than D (G < D).

The EIRP (equivalent isotropically radiated power) is usually based on a logarithmic scale in watts and can be expressed with:

$$eirp_{Linear} = G \cdot P_{in} \tag{3.5}$$

$$EIRP\left[dBW\right] = 10 \cdot \log_{10}\left(\frac{eirp_{Linear}}{1W}\right) = 10 \cdot \log_{10}\left(\frac{G \cdot P_{in}}{1W}\right)$$
(3.6)

The EIRP describes the equivalent radiated power of an isotropic radiator for the considered antenna gain G and the antenna input power  $P_{in}$ .

To get a raw estimation of the antenna directivity D in the desired polarization plane, the co-polar beamwidth in the H and E cut (in degree) together with the corresponding amplitude distribution factor K (also called amplitude taper factor) for different antenna shapes can be used. The table 3.1 from [21] provides examples of K for different antenna shapes and the corresponding amplitude tapers.

$$D \approx \frac{K}{\Theta_H \Theta_E} \tag{3.7}$$

Every receiving antenna removes from an incident wave a certain amount of energy. This energy will be transformed from free space EM wave into a guided EM wave and corresponds to the receiving power  $P_{RX}$ . The power density S of an incident wave together with the received power  $P_{RX}$  has the following relationship [12]:

$$P_{RX} = A_E \cdot S \tag{3.8}$$

In equation 3.8 the effective antenna area  $A_E$  is introduces. The antenna extracts received power from the amount of wave density, which passes through the effective area of the antenna. This effective area differs from the physical antenna area.

| Antenna shape | Amplitude distribution                | Κ     |
|---------------|---------------------------------------|-------|
| Circular      | homogeneous                           | 34240 |
| Rectangular   | homogeneous                           | 32685 |
| Circular      | parabolic with edge decay of 15 dB $$ | 39248 |
| Rectangular   | parabolic with edge decay of 15 dB $$ | 36191 |
| Circular      | parabolic with edge decay of 12 dB    | 26000 |

Table 3.1: K factors for different antenna shapes and amplitude distributions [16]

To receive the maximum amount of antenna energy, the antenna impedance should be conjugate complex to the receiver impedance or vice versa.

When the impedance of the receiver is perfectly matched to the antenna impedance, the effective antenna area  $A_E$  can be considered as a stand-alone antenna parameter, independent from antenna design or type. The relation between effective antenna area and the antenna gain from [12] is given by equation 3.9. This relation is already known from the point and volume target weather radar equations 1.15 and 1.27. There  $A_E$  was introduced as the receive effective antenna area in equation 1.14. Equation 3.9 is more generally expressed and valid for both, a receiving and a transmitting antenna.

$$A_E = G \cdot \frac{\lambda^2}{4\pi} \tag{3.9}$$

A further important antenna parameter is the equivalent beam solid angle  $\Omega$ . The equivalent beam solid angle is related to the antenna directivity in equation 3.2 and the entire radiation density  $P_s$  with

$$P_s = \int_{\phi=0}^{2\pi} \int_{\theta=0}^{\pi} S_r(r,\theta,\phi) r^2 \sin(\theta) \,\mathrm{d}\theta \,\mathrm{d}\phi.$$
(3.10)

By implementing equation 3.10 in the dominator of equation 3.2 as done by [12], the equivalent beam solid angle  $\Omega$  can be derived.

$$D = \frac{4\pi}{\int\limits_{\phi=0}^{2\pi} \int\limits_{\theta=0}^{\pi} \frac{S_r(r,\theta,\phi)}{S_{max}(r,\theta,\phi)} \sin(\theta) \, \mathrm{d}\theta \, \mathrm{d}\phi} = \frac{4\pi}{\int\limits_{\phi=0}^{2\pi} \int\limits_{\theta=0}^{\pi} C^2(\theta,\phi) \sin(\theta) \, \mathrm{d}\theta \, \mathrm{d}\phi}$$
(3.11)  
$$\Omega = \int\limits_{\phi=0}^{2\pi} \int\limits_{\theta=0}^{\pi} C^2(\theta,\phi) \sin(\theta) \, \mathrm{d}\theta \, \mathrm{d}\phi \le 4\pi$$
(3.12)

For C=1 an isotropic radiator would illuminate a full sphere with  $\Omega = 4\pi$ . The equivalent beam solid angle can further be used to evaluate the antenna directivity with equation 3.13.

$$D = \frac{4\pi}{\Omega} \approx \frac{4\pi}{\theta_E \theta_H} \tag{3.13}$$

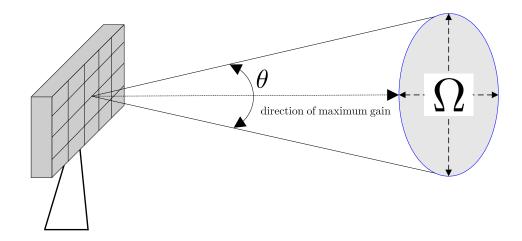


Figure 3.2: Equivalent beam solid angle

 $\theta_E$  and  $\theta_H$  are representing the 3dB antenna beamwidths in radians, for one polarization plane. The multiplication of both corresponds to the angle  $\Omega$ . Is the antenna beamwidth with 1° in both cuts assumed and the transformation from radians to degree with  $(180/\pi)^2$ is considered, an antenna directivity of approximately 46.1dBi, with  $K = 4\pi (180/\pi)^2 =$ 41253 by equation 3.7, can be calculated. The equivalent beam solid angle  $\Omega$  can be interpreted as an abstract and theoretical beam angle, in which the antenna is radiating the entire power. All other solid angle coordinates are assumed to be free of radiation, so that no sidelobes, grating lobes or any other pattern parts are considered. The entire radiated power from the complete antenna radiation pattern is contained in the equivalent beam solid angle. Also, the main beam of  $\Omega$  is not Gaussian distributed, as known from the regular antenna beamwidth. The main lobe filled with maximum radiation density, namely the equivalent beam solid angle  $\Omega$ , can be assumed to be homogeneously distributed. Additionally,  $\Omega$  is used as a figure of merit for the focusing ability of antennas and is defined in steradian  $sr = radian^2$ . For scanning phased-array radars, the main beam of a high gain antenna at arbitrary point in space would form an ellipse on the surface of a sphere, as shown in the figures 1.7 and 3.2. For measuring the antenna radiation pattern of any antenna type accurately, the following far field definition for the minimum distance  $r_{min}$  between an antenna under test (AUT) and a receiving antenna must be established:

$$r_{min} \ge \frac{2D^2}{\lambda} \tag{3.14}$$

Equation 3.14 is only valid for homogeneous phase and amplitude distributed antennas. As soon as the antenna taper differs or high gain antennas are used, equation 3.15 should be used to measure the antenna radiation pattern in far field accurately:

$$r_{min} \ge G \cdot \lambda \tag{3.15}$$

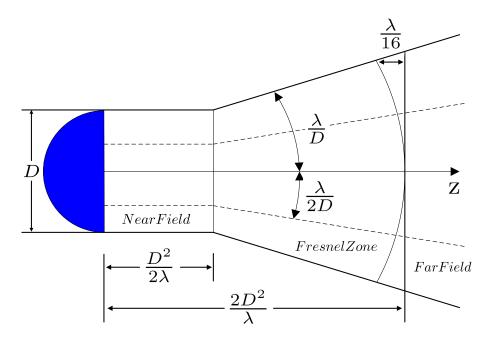


Figure 3.3: Definition of near field, fresnel zone and far field, adapted by [12]

In particular high gain antennas are operated with taper functions to retrieve low sidelobes. Here the efficiency of the effective antenna area defines the beginning of the far field zone.

"In figure 3.3 a parabolic antenna aperture with diameter  $D \ge \lambda$  is visualized. The antenna generates the radiation with homogeneous phase and amplitude distribution. The maximum radiation density follows the direction of the z-axis. At the angle  $\lambda/2D$  radian, the radiation density decrease to half of the maximum radiation density, while at  $\lambda/D$  radian the first null of the antenna radiation pattern occurs.

The near field area extends to the Rayleigh distance  $D^2/2\lambda$ . In this region the main radiation density is propagating almost parallel in a cylindrical geometry with the diameter D. Starting from the Rayleigh distance the radiation reams up in a conical area with an opening angle of  $\lambda/D$ . The phase difference between the center path travelling on zaxis and the endpoint of near field is  $\lambda/4$ . After passing through the Fresnel zone with  $D^2/2\lambda < r < 2D^2/\lambda$ , the phase difference is smaller than  $\lambda/16$  and the far field zone is reached. In far field area the wave has practically a plane phase front and the electricaland magnetic field vector propagates in phase"[12].

If the antenna radiation pattern would not be measured in the dedicated far field, the spherical phase front (with its phase differences) would produce misinterpretations of the measured power values. Consequently, the antenna key parameters, like the sidelobe suppression or the absolute gain values, would be determined erroneously.

# **3.2** Relevant definitions for antenna pattern synthesis

This section gives the reader an overview of the antenna pattern definitions, relevant for the discussions on polarimetric phased-array antenna radiation pattern in the following chapters. Unless otherwise indicated, the definitions are approved by the IEEE Standards Board and are derived by the IEEE Standard Definitions of Terms for Radio Wave Propagation [124] and the IEEE Standard Definitions of Terms for Antennas [125].

- Directivity, partial (of an antenna for a given polarization): In a given direction, that part of the radiation intensity corresponding to a given polarization divided by the total radiation intensity averaged over all directions. NOTE: The (total) directivity of an antenna, in a specified direction, is the sum of the partial directivities for any two orthogonal polarizations.
- Gain, partial (of an antenna for a given polarization): In a given direction, that part of the radiation intensity corresponding to a given polarization divided by the radiation intensity that would be obtained if the power accepted by the antenna were radiated isotropically.
- Realized gain, partial (of an antenna for a given polarization). The partial gain of an antenna for a given polarization reduced by the loss due to the mismatch of the antenna input impedance to a specified impedance.
- **Major lobe** also called main lobe or main beam: The radiation lobe containing the direction of maximum radiation.
- Front-to-back ratio: The ratio of the maximum directivity of an antenna to its directivity in a specified rearward direction.
- Half-power beamwidth also called (3dB beamwidth): In a radiation pattern cut containing the direction of the maximum of a lobe, the angle between the two directions in which the radiation intensity is one-half the maximum value. See: principal half-power beamwidths.
- **Principal half-power beamwidths**: For a pattern whose major lobe has a halfpower contour that is essentially elliptical, the half-power beamwidths in the two pattern cuts that contain the major and minor axes of the ellipse, respectively.
- Side lobe level, maximum relative: The maximum relative directivity of the highest side lobe with respect to the maximum directivity of the antenna.
- **H-plane**, **principal**: For a linearly polarized antenna, the plane containing the magnetic field vector and the direction of maximum radiation.
- **E-plane**, **principal**: For a linearly polarized antenna, the plane containing the electric field vector and the direction of maximum radiation.

#### CHAPTER 3. RELEVANT MICROWAVE ANTENNA FUNDAMENTALS

- Orthogonal polarization: For a given wave, the unique polarization state containing no components of the given wave's polarization. Notes: 1. For linear polarization, the (linear) polarization perpendicular to the reference (linear) polarization. 2. For circular polarization, the (circular) polarization with the opposite sense of rotation. 3. For elliptical polarization, the polarization with the same axial ratio, opposite rotation sense and major axis perpendicular to that of the reference polarization.
- **Co-polarization**: That polarization that the antenna is intended to radiate or receive. Synonym: co-pol
- **Cross-polarization**: The polarization orthogonal to a reference polarization. Synonym: x-pol
- Cross-polarization discrimination: The ratio of the power level at the output of a receiving antenna, nominally co-polarized with the transmitting antenna, to the output of a receiving antenna of the same gain but nominally orthogonally polarized to the transmitting antenna.
- **Cross-polarization isolation**: The ratio of the wanted power to the unwanted power in the same receiver channel when the transmitting antenna is radiating nominally orthogonally polarized signals at the same frequency and power level.
- Cross-polarization suppression: The cross polarization suppression is not specified in [124], [125]. For this reason, the following definition is used as cross-polarization suppression in this work: The ratio of maximum realized gain in the main lobe, for a given reference polarization (co-pol) and at desired scan angle, to the realized gain of the orthogonal polarization (x-pol) at exactly the same scan angle. The term cross polarization suppression will be used to describe the suppression of undesired field components in the angular region of interest. If not explicitly stated, the cross polarization suppression is referred to the maximum intensity of the main lobe. Synonym: CPS
- Integrated (two-way) cross polarization ratio: The integrated (two-way) cross polarization ratio is not specified in [124], [125]. In [126] the  $ICPR_2$  is induced as figure of merit of dual-polarized antennas. The  $ICPR_2$  takes the complete co- and x-polarized antenna radiation pattern into account. The  $ICPR_2$  is defined in reference [126] with

$$ICPR_{2} = 10 \log_{10} \left| \frac{\int f_{copol} f_{xpol} \sin(\theta) d\theta}{\int f_{copol}^{2} \sin(\theta) d\theta} \right|.$$
 (3.16)

Where  $f_{copol}$  and  $f_{xpol}$  are representing the copolarized and cross polarized antenna radiation patterns, respectively.

• Scan angle also called beam angle: The angle between the direction of the maximum of the major lobe or a directional null and a reference direction. Notes: 1. The term

beam angle applies to the case of a pencil beam antenna. 2. The reference boresight is usually chosen as the reference direction. 3. Not specified in [124], [125]: In a spherical coordinate system two angles are used to define a point in space on a given sphere. Consequently,  $\theta$  and  $\phi$  are used in this work to describe the azimuth and elevation scan angle of a pencil beam.

• Electrical boresight: The tracking axis as determined by an electrical indication, such as the null direction of a conical-scanning or monopulse antenna system, or the beam-maximum direction of a highly directive antenna.

# 3.3 Microstrip antennas

#### 3.3.1 General design aspects for microstrip lines

Microstrip lines are belonging to the class of planar transmission lines. Other popular types of transmission lines are striplines and ground coplanar microstrip lines. All such transmission lines are fabricated comparable easily with a photolithographic process by fabrication labs. The geometry of a microstrip line (MSL) is shown in figure 3.4. The copper around the microstrip line is removed by the galvanic process, so that a conductor with the width W is generated. The substrate supplier are providing different substrate height H and relative permittivity  $\epsilon_r$ , in order to match the PCB design with the specification. The microstrip lines in this work are designed and simulated with CST MWS. However, a set of formulas are given to find reasonable starting values for the hardware design of microstrip lines. For the evaluation of all necessary PCB design parameters, the formulas 3.17 to 3.28 from [29] are introduced. In particular the formulas for the effective permittivity  $\epsilon_e$ , the wave impedance  $Z_0$ , the effective wavelength  $\lambda_e$  and  $\alpha$  the microstrip line attenuation coefficient are addressed. The region above the microstrip lines is assumed to be air with  $\epsilon_r = 1$ . The antenna feeding network for the final phased-array weather radar application is designed in MSL and implemented on the backside of the antenna, so that the assumption of air becomes reasonable. The field lines of microstrip lines are concentrated mostly below the conductor. But a fraction of the field lines are also located above the conductor, as shown in figure 3.5. Consequently, the EM wave (assumed to be quasi-TEM for H  $\ll \lambda$ ) travels mainly through the dielectric substrate and partly through air. The phase velocity  $v_p$  and the propagation constant  $\beta$  for microstrip lines are expressed in the equations 3.17 and 3.18, with  $k_0 = \frac{2\pi f}{c_0}$  the wave number and  $c_0$  for the speed of light.

$$v_p = \frac{c_0}{\sqrt{\epsilon_e}} \tag{3.17}$$

$$\beta = k_0 \sqrt{\epsilon_e} \tag{3.18}$$

As already stated, the majority of the field lines are located in the dielectric substrate region. For this reason, the relation  $1 < \epsilon_e < \epsilon_r$  becomes valid. The effective dielectric constant  $\epsilon_e$  can be approximated with

$$\epsilon_e = \frac{\epsilon_r + 1}{2} + \frac{\epsilon_r + 1}{2} \frac{1}{\sqrt{1 + 12\frac{H}{W}}}$$
(3.19)

and interpreted as a homogeneously distributed dielectric medium around the microstrip line, substituting the air and dielectric regions from figure 3.5.

The characteristic wave impedance  $Z_0$  can be calculated for different W/H ratios as follows: for  $\frac{W}{H} \leq 1$ 

$$Z_0 = \frac{60}{\sqrt{\epsilon_e}} \ln\left(\frac{8H}{W} + \frac{W}{4H}\right) \tag{3.20}$$

for 
$$\frac{W}{H} \ge 1$$
  
$$Z_0 = \frac{120\pi}{\sqrt{\epsilon_e} \left[\frac{W}{H} + 1.393 + 0.667 \ln\left(\frac{W}{H} + 1.444\right)\right]}$$
(3.21)

for  $\frac{W}{H} < 2$ 

$$\frac{W}{H} = \frac{8e^A}{e^{2A} - 2}$$
(3.22)

for  $\frac{W}{H} > 2$ 

$$\frac{W}{H} = \frac{2}{\pi} \left[ B - 1 - \ln\left(2B - 1\right) + \frac{\epsilon_r - 1}{2\epsilon_r} \left( \ln\left(B - 1\right) + 0.39 - \frac{0.61}{\epsilon_r} \right) \right]$$
(3.23)

and the coefficients A and B:

$$A = \frac{Z_0}{60} \sqrt{\frac{\epsilon_r + 1}{2}} + \frac{\epsilon_r - 1}{\epsilon_r + 1} \left( 0.23 + \frac{0.11}{\epsilon_r} \right), \qquad (3.24)$$

$$B = \frac{377\pi}{2Z_0\sqrt{\epsilon_r}} \tag{3.25}$$

After the successful evaluation of the characteristic impedance governed by the corresponding microstrip line width, the microstrip line length depending on the phase velocity inside the dielectric substrate, the calculation of the effective dielectric constant, the attenuation of an microstrip line can be investigated. The attenuation  $\alpha$  can be separated into attenuation due to the dielectric loss ( $\alpha_d$  in equation 3.26) and the attenuation related to the conductor ( $\alpha_c$  in equation 3.27).

$$\alpha_d = \frac{k_0 \epsilon_r (\epsilon_e - 1) \tan(\delta)}{2\sqrt{\epsilon_e} (\epsilon_r - 1)} \frac{Np}{m}$$
(3.26)

$$\alpha_c = \frac{R_S}{2\sqrt{Z_0 W}} \frac{Np}{m} \tag{3.27}$$

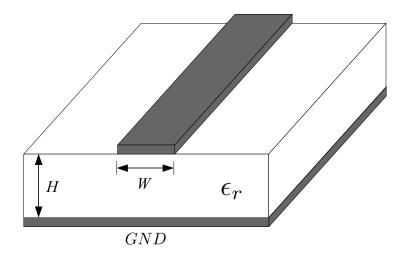


Figure 3.4: Microstrip transmission line geometry with substrate height H, the dielectric constant  $\epsilon_r$  of the substrate and W the width of the microstrip line. Above the microstrip line  $\epsilon_r = 1$  for air is assumed.

$$\alpha = \alpha_d + \alpha_c \tag{3.28}$$

$$\frac{\alpha}{dB} = \frac{20}{\ln(10)} \cdot \frac{\alpha}{Np} = 8.6859 \cdot \frac{\alpha}{Np} \tag{3.29}$$

The attenuation values are given in Neper. It my be noted, Nepers are often used for voltage ratios. The fixed relation between dB and Neper is given in equation 3.29 from [30].  $R_S$  represents the surface resistivity of the conductor with  $R_S = \sqrt{\frac{\omega_0 \mu_0}{2\sigma}}$ .

A special microstrip line is the quarter wave transformer. The quarter wave transformer is used for matching a load resistance  $R_L$  with a piece of MSL with the length  $\frac{\lambda}{4}$  and characteristic wave impedance  $Z_1$  to the MSL wave impedance  $Z_0$ . The antenna feeding network uses MSL wave impedances with 50 $\Omega$  or 100 $\Omega$ . By considering the wave impedance to be  $Z_0 = 50\Omega$  and  $R_L = 100\Omega$  (e.g. given by an antenna port impedance  $R_L$ ) the  $\frac{\lambda}{4}$  MSL transformer should be designed with  $Z_1 = 70.7\Omega$ , as given by equation 3.30.

$$Z_1 = \sqrt{Z_0 \cdot R_L} \tag{3.30}$$

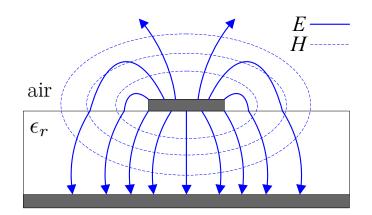


Figure 3.5: Electric (solid blue) and magnetic (dashed blue) field line distribution around the microstrip line. Above the microstrip line  $\epsilon_r = 1$  for air is assumed.

#### 3.3.2 Substrates

Antenna designers should pay maximum attention on the selection of suitable substrates. Several material properties need to be considered. There are hundreds of different substrates available on the market. Unfortunately, not every substrate can be handled by the PCB manufacturers. Depending of the specific PCB design, the production process can quickly exceed the maximum predefined costs of the PCB board. It is also possible that the intended design is not suitable for production. As a consequence, the antenna designer should communicate the choice of microstrip substrate, the choice of prepreg (a diectric layer for cementing different layers) and the complete development draft prior the antenna design should be established.

There are several microwave substrates with different material properties available. The main material properties are namely the dissipation factor  $\tan(\delta)$  and the dielectric constant  $\epsilon_r$  and their variation with temperature and frequency, homogeneity, degree of the isotropic nature, thermal coefficient and operating temperature range, humidity, aging and thickness uniformity. The large range of PTFE, polystyrene, polyolefin, polypheenylene, alumina, sapphire, quartz, ferromagnetic, rutile and semiconductor substrates available permits considerable flexibility in the choice of substrate for particular applications [110]. Conformal antennas require flexible substrates. Low-frequency applications require higher dielectric constants to keep the antenna size small in regard to the free space wavelength. The synthetic substrates of PTFE or Teflon, polystyrene, polyolefin and polypheenylene provide low loss and low permittivity values. From the electromagnetic perspective these substrates are suitable for the design of microstrip patch antennas. Unfortunately, these substrates are soft and unstable with temperature. As a consequence, the substrate man-

| Substrate Type                | $\epsilon_r$    | Design $\epsilon_r$ | $\tan(\delta)$ | MCF |
|-------------------------------|-----------------|---------------------|----------------|-----|
| RO4350 (17/250/17)            | $3.48 \pm 0.05$ | 3.66                | 0.0037         | 1   |
| RO4003 (17/250/17)            | $3.38 \pm 0.05$ | 3.55                | 0.0027         | 1   |
| RO3003 (17/250/17)            | $3.00 \pm 0.04$ | 3.00                | 0.0010         | 2   |
| RO3006 (17/250/17)            | $6.15 \pm 0.15$ | 6.5                 | 0.0020         | 3   |
| RO6002 (17/250/17)            | $2.94 \pm 0.04$ | 2.94                | 0.0012         | 8.5 |
| TMM4 (17/380/17)              | $4.50 \pm 0.05$ | 4.70                | 0.0020         | 9.3 |
| Ultralam 2000 (17 / 260 / 17) | 2.4 - 2.6       | n.a.                | 0.0022         | 6.5 |

Table 3.2: Properties for relevant microwave substrates with material cost factor (MCF), using RO4350 as reference.  $tan(\delta)$  was measured at 10 GHz.

ufactures are producing composite materials to combine for instance the electromagnetic benefits of Teflon with the stability of ceramics. A very wide variety of composite substrates is available on the market, with relative permittivity range from 2 to 10 and  $\tan(\delta)$ values from 0.0005 to 0.0020. One example is the RO4000 substrate series. Here a hydrocarbon ceramic composite was created, in order to offer low loss dissipation factors and low dielectric constants with adequate material robustness. The established material robustness allows the standard production process by PCB manufacturers at acceptable prices. Other microwave materials from the RO3000 Roger series are very soft and flexible. The 3200 series is more robust due to the higher amount of fiber glass in it. The RO6000 series is providing excellent dissipation factor values, but is again mechanically unstable. Generally, microwave substrates are very robust against aging. The dielectric constant  $\epsilon_r$  varies only a few percentage (1- 2.5 percent) within 10 years [19]. The saturation of dielectric constant change is typically reached after 6 years [19]. Another important factor of the substrate is the roughness of the copper below the microstrip line. The roughness has significant influence on the attenuation of an EM wave travelling through and above the substrate. Consequently, Rogers recently provides the "LoPro" series with smoother copper plane to reduce the insertion loss on microstrip lines.

In stripline technology the implementation of resistors in antenna feeding networks are very complicated. For this reason, thin film resistor foils are used to define planar resistors between copper structures. One natural example for the thin film resistor foil application is the implementation of Wilkinson power dividers in stripline technology. In a 50 $\Omega$  stripline impedance network the 100 $\Omega$  resistor can be modeled by a thin film resistor foil.

Especially for microwave applications, the substrate costs can vary considerably. Using RO4350 laminate (with  $17\mu m$  copper on top and bottom and  $250\mu m$  substrate height), as the material cost reference, a list for the relevant microwave substrates can be given. As shown in table 3.2, the choice of substrate material can readily vary the final PCB price in the range from 1 to almost 10. It should be noted that this cost list was provided by PCB manufacturer for the specific antenna microwave application between 9 GHz and 10 GHz. Different cost factors should be used for other design frequencies and applications.

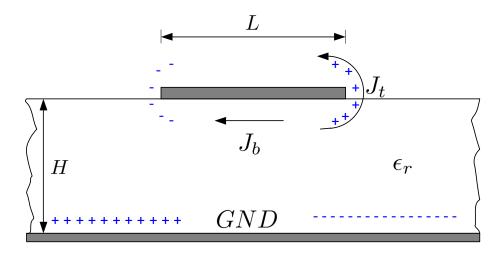


Figure 3.6: Current and charge distribution of microstrip patch antenna

A further cost driver is the multilayer PCB design with multiple layers and a high number of vias. Depending of the multilayer structure, several production processes are necessary, so that the production costs are increased significantly.

Substrate suppliers are providing often two permittivity values in the datasheet. One is related to the material permittivity and the other represents the design permittivity. The design permittivity is an average number from several different tested substrate lots. The difference between the two permittivity values can partly be explained by the anisotropy of the composite material. Is the dielectric anisotropy and the design permittivity not accounted for, the antenna designer can expect serious resonance frequency shifts between simulations and measurements [110].

The substrate anisotropy is defined as the dependence of substrate dielectric constant on the orientation of the applied electrical field. For a biaxial and anisotropic substrate the permittivity is expressed in reference [110] with

$$\epsilon = \begin{pmatrix} \epsilon_x & 0 & 0\\ 0 & \epsilon_y & 0\\ 0 & 0 & \epsilon_z \end{pmatrix}.$$
(3.31)

#### 3.3.3 Cavity model for microstrip antennas

In several antenna literature references e.g.[103] or [110], the microstrip patch antenna radiation process is explained by the well-known cavity model. The approach presented in this subsection is adapted by [110] and is valid for a substrate height  $H \ll \lambda_0$ . The current and charge distribution of microstrip patch antennas is presented in figure 3.6. The most of the charges concentration is below the patch with corresponding current density  $J_b$ , but a fraction of current density  $J_t$  moves also to the top surface of the patch antenna. This weak current flow generates a weak magnetic field tangential to the edges. By assuming the tangential magnetic fields to be zero, for instance by implementing four perfect magnetic walls surrounding the volume and two electric walls on top and ground, the patch can be modeled as a cavity. Appling the Huygens field equivalence principle, the patch antenna can be interpreted as an equivalent current density  $J_t$  on the top surface with four side slots of equivalent current densities  $J_S$  and  $M_S$ . The ground plane can be considered by the image theory. As a consequence, the equivalent current density will be doubled to

$$\vec{M}_S = -2\hat{n} \times \vec{E_a}.\tag{3.32}$$

The slot of length W and height H is defined as electric field  $\vec{E_a}$  with

$$\vec{E_a} = \hat{z}E_0 \tag{3.33}$$

and shown in figure 3.7. The other two slots along the length L and height H can be defined with  $\pi \pi$ 

$$\vec{E_a} = -\hat{z}E_0\sin(\frac{\pi x}{L}) \tag{3.34}$$

Using the equivalent principle each slot can be interpreted as a magnetic dipole with magnetic current density  $\vec{M_s}$ . The radiation along the length L is low and neglected in the cavity model. Also the fringing fields from the sine distribution along the length L are not considered by the cavity model, due to the assumption of perfect magnetic walls surrounding the volume. Consequently, the cavity model only considers the two vertical slots separated by the length L. The vertical slots are further replaced by planar slots in order to calculate the radiation pattern. The field distribution below the patch, as illustrated in figure 3.7 generates the co- and x-pol pattern by assuming two radiating slots with distance L separating them. The uniform field distribution over the width W and the sine distribution over the length L for the dominant TM010 mode can be recognized. The field distribution of a patch antenna can be separated into two regions, namely the interior and exterior region. The exterior fields are interpreted as the sum antenna radiation pattern generated by two slots separated by the length L. The interior fields can be describes as TM modes inside the cavity. The electric field must satisfy the wave equation 3.35.

$$\nabla \times \nabla \times \bar{E} - k^2 \bar{E} = -j\omega_0 \mu_0 \bar{J} \tag{3.35}$$

or

$$\frac{\partial^2 E_z}{\partial x^2} + \frac{\partial^2 E_z}{\partial y^2} + k^2 E_z = j\omega_0 \mu_0 J_z \tag{3.36}$$

with  $k^2 = \omega_0^2 \mu_0 \epsilon_0 \epsilon_r$  and  $J_z$  the excitation electric current density from coaxial or microstrip feed. The electric field inside the cavity can be expressed as follows:

$$E_z(x,y) = \sum_m \sum_n A_{mn} \psi_{mn}(x,y)$$
 (3.37)

The amplitude coefficients  $A_{mn}$  and the eigenfunctions  $\psi_{mn}$  are depending of the electric field modes (m,n). The eigenfunctions are considered with

$$\psi_{mn}(x,y) = \sqrt{\frac{\epsilon_m \epsilon_n}{LW}} \cos(k_m x) \cos(k_n y) \quad m, n = 0, 1, 2, p, \dots$$
(3.38)

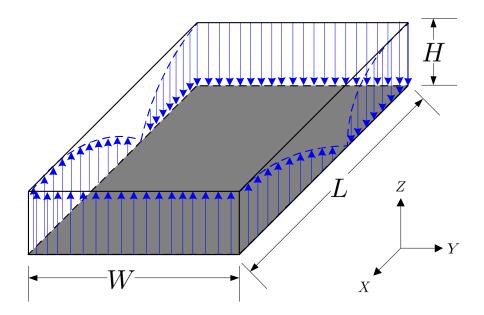


Figure 3.7: Electrical field distribution below microstrip patch antenna with surrounding, perfect magnetic walls

with  $\epsilon_p = 1$  for p=0 and  $\epsilon_p = 2$  for p=0 and

$$k_m = \frac{m\pi}{L}, \quad k_n = \frac{n\pi}{W}, \quad k_{mn}^2 = k_m^2 + k_n^2$$
 (3.39)

The coefficients  $A_{mn}$  are depending of the excitation currents, which are generated by the coaxial feed.

$$A_{mn} = \frac{j\omega_0\mu_0}{k^2 - k_{mn}^2} \int_{feed} \int \psi_{mn}^*(x,y) J_z \, dxdy \tag{3.40}$$

The coaxial feed can be interpreted as a rectangular current source with cross sectional area  $(D_x D_y)$ . The feed is located at  $(x_0, y_0)$  on the surface of the patch. The amplitude coefficients  $A_{mn}$  can be calculated with  $J_z = \frac{I_0}{D_x D_y}$ .

$$A_{mn} = \frac{1}{D_x D_y} \frac{j\omega_0 \mu_0}{k^2 - k_{mn}^2} \int_{feed} \int I_0 \psi_{mn}^*(x, y) \, dx dy$$

$$= \frac{j\omega_0 \mu_0 I_0}{k^2 - k_{mn}^2} \sqrt{\frac{\epsilon_m \epsilon_n}{LW}} \cos(k_m x_0) \cos(k_n y_0) G_{mn}$$
(3.41)

with

$$G_{mn} = sinc\left(\frac{n\pi D_x}{2L}\right)sinc\left(\frac{m\pi D_y}{2W}\right),\tag{3.42}$$

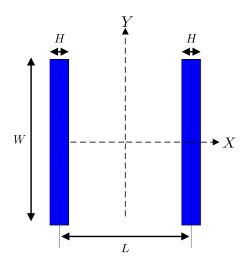


Figure 3.8: Two- slot model of rectangular patch antenna for determining the radiation patterns, adapted by [110].

by assuming  $D_x = 0$  and  $D_y$  equal to a microstrip line feed. The final expression of the electric fields in the cavity with  $E_z(x, y)$  in [110] can be derived with

$$E_z(x,y) = j\omega_0\mu_0 I_0 \sum_{m}^{\infty} \sum_{n=0}^{\infty} \frac{\psi_{mn}(x,y)\psi_{mn}(x_0,y_0)}{k^2 - k_{mn}^2} G_{mn}.$$
(3.43)

With equation 3.43 the electric fields inside the cavity are fully derived, but also the exterior fields generated by the cavity should be investigated. For this reason the radiation pattern based on a two-slot model are derived next. The approach introduced next is adapted from [110] and considers the  $TM_{10}$  mode from figure 3.7 for the calculation of the antenna radiation pattern of 2 slots with length W, spaced with distance L. The geometrical configuration of the two slots representing the patch antenna are shown in figure 3.8. By assuming a voltage  $V_0$  across one slot, the radiation pattern can be evaluated by multiplication of slot radiation pattern with array factor  $F_2$ . The spherical angles  $\phi$  and  $\theta$  are shown in figure 3.9, together with the microstrip patch antenna and its parameters.

$$E_{\theta} = -jk_0 V_0 W \frac{e^{-jk_0 r_i}}{4\pi r_i} \cos(\phi) F_1 F_2$$
(3.44)

$$E_{\phi} = jk_0 V_0 W \frac{e^{-jk_0 r_i}}{4\pi r_i} \cos(\theta) \sin(\phi) F_1 F_2$$
(3.45)

with

$$F_1 = sinc\left(k_0 H \sin(\theta) \cos\left(\frac{\phi}{2}\right)\right) \ sinc\left(k_0 W \sin(\theta) \sin\left(\frac{\phi}{2}\right)\right)$$
(3.46)

$$F_2 = 2\cos\left(k_0 L\sin(\theta)\cos\left(\frac{\phi}{2}\right)\right) \tag{3.47}$$

For the expression of the antenna radiation pattern in the principal planes the following equations 3.48 and 3.50 can be used. The E plane cut can be calculated with  $E_{\phi}(\theta) = 0$  for  $\phi = 0^{\circ}$  and the H plane cut with  $E_{\theta}(\theta) = 0$  and  $\phi = 90^{\circ}$ .

$$E_{\theta}(\theta) = -jk_0 V_0 W \frac{e^{-jk_0 r_i}}{2\pi r_i} F_E(\theta)$$
(3.48)

with

$$F_E(\theta) = sinc\left(k_0 H \sin\left(\frac{\theta}{2}\right) \cos\left(k_0 L \sin\left(\frac{\phi}{2}\right)\right)\right)$$
(3.49)

$$E_{\phi}(\theta) = jk_0 V_0 W \frac{e^{-jk_0 r_i}}{2\pi r_i} F_H(\theta)$$
(3.50)

$$F_H(\theta) = sinc\left(k_0 W \sin\left(\frac{\theta}{2}\right)\right) \cos(\theta)$$
 (3.51)

It should be noted that the antenna radiation patterns are calculated for slots in free space. The effect of ground plane and substrate are considered with the following corrections factors, with  $F_3(\theta)$  for the E plane and  $F_4(\theta)$  for the H plane cuts.

$$F_3(\theta) = \frac{2\cos(\theta)\sqrt{\epsilon_r - \sin^2(\theta)}}{\sqrt{\epsilon_r - \sin^2(\theta)} - j\epsilon_r\cos(\theta)\cot\left(k_0H\sqrt{\epsilon_r - \sin^2(\theta)}\right)}$$
(3.52)

$$F_4(\theta) = \frac{2\cos(\theta)}{\cos(\theta) - j\sqrt{\epsilon_r - \sin^2(\theta)}\cot\left(k_0H\sqrt{\epsilon_r - \sin^2(\theta)}\right)}$$
(3.53)

The final antenna radiation pattern for E and H cut are expressed in equation 3.54 and 3.55, respectively. The consideration of ground and substrate is multiplied by correction factors.

$$E_{\theta}(\theta) = -jk_0 V_0 W \frac{e^{-jk_0 r_i}}{2\pi r_i} F_E(\theta) F_3(\theta)$$
(3.54)

$$E_{\phi}(\theta) = jk_0 V_0 W \frac{e^{-jk_0 r_i}}{2\pi r_i} F_H(\theta) F_4(\theta)$$
(3.55)

Other important design parameters are the beamwidth and the gain of a single microstrip antenna. The 3dB beamwidth in the principle planes can be approximated with:

$$\theta_H = 2\sin^{-1} \left(\frac{1}{2+k_0 W}\right)^{\frac{1}{2}} \tag{3.56}$$

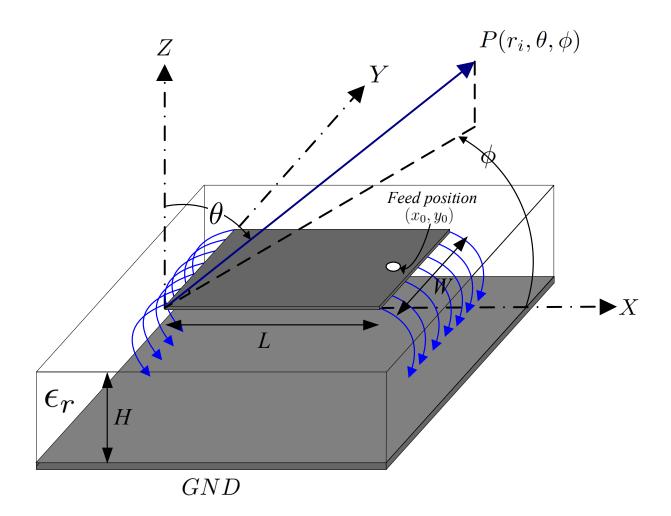


Figure 3.9: Geometry of rectangular microstrip patch antenna with spherical angles  $\theta$  and  $\phi$ , the feed location at  $(x_0, y_0)$ , the patch width W and length L, the substrate height H and  $\epsilon_r$  the relative permeability of the substrate.

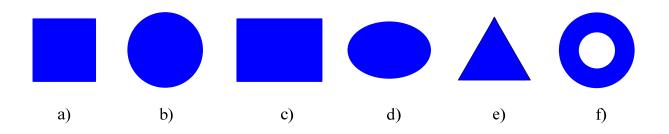


Figure 3.10: Basic microstrip patch antenna shapes commonly used in practice, adapted by [110]

$$\theta_E = 2\sin^{-1} \left( \frac{7.03}{3k_0^2 L^2 + k_0^2 H} \right)^{\frac{1}{2}}$$
(3.57)

By investigating the approximation formulas for the beamwidths it becomes clear that the beamwidth can be increased by reducing the antenna edge length W and L. As a consequence, the antenna gain and directivity decreases, as the beamwidth is increased. The antenna gain of a microstrip patch antenna can be calculated with:

$$G_{Patch} = \eta_R D_{Patch} \tag{3.58}$$

with  $\eta_R$  the radiation efficiency of the antenna  $D_{Patch}$  the antenna directivity.

$$D_{Patch} = \frac{\frac{r_i^2}{2Z_0} \left( |E_\theta|^2 + |E_\phi|^2 \right)|_{\theta=0}}{P_r/4\pi}$$
(3.59)

 $Z_0 = 120\pi\Omega$  represents the free space field impedance,  $P_r$  the radiated power and  $E_{\phi}$  and  $E_{\theta}$  the electrical fields. The antenna directivity increases when the substrate thickness H and the patch width W are increased. The beamwidth can be expected to decrease for higher H and W values.

#### 3.3.4 Microstrip radiator shapes

The microstrip patch definition is given in [15] as follows: "The generic microstrip patch is an area of metallization supported above a ground plane and fed against the ground at an appropriate point or points". Several microstrip patch antenna shapes are available in literature. Figure 3.10 shows the basic geometrical shapes, used nowadays. Generally, the resonator length  $L \approx \lambda_e/2$  determines the resonance frequency of the microstrip patch antenna. Due to the fringing fields at the radiating edges (figure 3.9), the microstrip patch radiator becomes electrically larger than its physical dimension. Reasons are the height

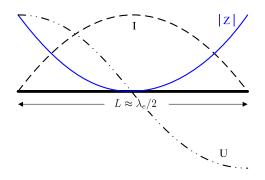


Figure 3.11: The impedance |Z|, voltage U and current I distribution along the patch resonator length  $L \approx \lambda_e/2$ .

and the dielectric constant of the substrate between radiating patch and the ground. The impedance of the microstrip patch antenna is low at the patch center and increases along the the length L. Accordingly, the maximum impedance can be found near the two radiating edges. The current, voltage and impedance distribution along the patch resonator length L is shown in figure 3.11.

Table 3.3 gives typical performance parameters of rectangular, circular, equitriangular and annular-ring patch antenna shapes for comparison. It should also be noted that only the basic microstrip patch antenna shapes are discussed in this section. In literature, numerous shapes are developed and investigated. Other shapes are for instance H-shapes, U-shapes, Hexagonal-shapes and Pentagon-shapes. Every microstrip patch antenna in fundamental mode behaves like a dipole antenna and can be modeled with two radiating slots. Except for the angular-ring patch antenna, operated in  $TM_{12}$  mode, all basic antenna shapes from table 3.3 are providing comparable antenna performances. The angular-ring gives increased bandwidth, directivity and gain. Unfortunately, the angular-ring becomes physically large, which is often undesired. The polarization purity and the bandwidth can widely vary for different geometrical microstrip patch antenna shapes.

For weather radar applications, only the square and the circular disk can be chosen from the basic antenna shapes in figure 3.10. Both shapes are rotation symmetric and equal in the H- and in E-Cut beamwidths. Furthermore, the antenna radiation patterns in both polarization planes (H+V polarization) would be similar. As a consequence, a phased-array antenna consisting of multiple dual polarized microstrip patch elements would form two antenna radiation sum patterns with coincident, symmetrical pencil beams. The scan loss (defined by the patch antenna element patterns for both polarizations) of the phased-array antenna pattern would be equal for azimuth and elevation scanning. Every difference in scan loss for the two polarization planes would produce a mismatch in dual-polarimetric weather radar observation.

| Characteristics | Rec-                 | Circular             | Equi-                | Angular              | Angular               |
|-----------------|----------------------|----------------------|----------------------|----------------------|-----------------------|
|                 | tangular             | $\mathbf{Disk}$      | triangular           | Ring                 | Ring                  |
| Mode            | $TM_{10}$            | $TM_{11}$            | $TM_{10}$            | $TM_{11}$            | $TM_{12}$             |
| 3dB Beamwidth   | 102°                 | 100°                 | 100°                 | 103°                 | 30°                   |
| E-Plane         |                      |                      |                      |                      |                       |
| 3dB Beamwidth   | 85°                  | 80°                  | 88°                  | 81°                  | 47°                   |
| H-Plane         |                      |                      |                      |                      |                       |
| Directivity     | 7.0 dB               | 7.1 dB               | 7.1 dB               | 7.1 dB               | 10.9 dB               |
| Efficiency      | 87%                  | 94%                  | 87%                  | 86%                  | 97%                   |
| Gain            | 6.1 dB               | 6.8 dB               | 6.2 dB               | 6.1 dB               | 10.6 dB               |
| Bandwidth (2:1  | 0.7%                 | 1.1%                 | 0.78%                | 0.70%                | 3.8%                  |
| VSWR)           |                      |                      |                      |                      |                       |
| Physical        | a=4.92cm             | a=4.92cm             | a=6.57cm             | a=0.92cm             | a=4.45cm              |
| Dimension       | b=3.82cm             |                      |                      | b=1.82cm             | b=8.9cm               |
| Area            | $16.1 \mathrm{cm}^2$ | $24.3 \mathrm{cm}^2$ | $18.1 \mathrm{cm}^2$ | $10.6 \mathrm{cm}^2$ | $186.6 \mathrm{cm}^2$ |

Table 3.3: Performance parameters of rectangular, circular, equitriangular and annularring patch antenna shapes for comparison, adapted by [15]. The parameters are retrieved for  $\epsilon_r$ =2.32, substrate height H=1.59mm and a frequency of 2 GHz.

#### 3.3.5 Microstrip antenna architetures

A selection of microstrip patch antenna architectures is given in figure 3.12. The architectures differ in the feeding mechanism. Most prominent feeding techniques are coaxial feeding, coupled resonator feeding, probe-feeding, proximity (electromagnetically) coupled feeding and the aperture-coupled feeding. The choice for a specific feeding method is governed by numerous factors. In this regard, the most important factors for phased-array weather radar applications are the efficiency of the power transfer from the feeding line to the radiating patch, the adequate usage in dual-polarization array configurations and the high requirement for minimum x-pol radiation. A deep analysis of the polarimetric properties of feeding structures is addressed in section 6.3. The coaxial feed in figure 3.12a is mechanically complicated to establish. The ground cylinder from the coaxial feed must be connected properly to the GND layer of the microstrip antenna. Additionally, the coaxial line is equipped with dielectric material, so that this material property needs to be considered for impedance matching in the electromagnetic simulations.

The coplanar feed microstrip patch antenna in figure 3.12b is usefull for antenna arrays with low requirements regarding x-pol. One advantage of this architecture is the inexpensive implementation on only one PCB layer. Typically, the series or in coplanar feeding networks are located on the same layer. In reference[75]the main disadvantages are stated: "The use of coplanar microstrip feed networks for microstrip patch arrays allows simple construction, but incurs both gain loss and degradation in sidelobe and cross polarisation due to resistive loss and feed radiation". A special design of the coplanar feed microstrip

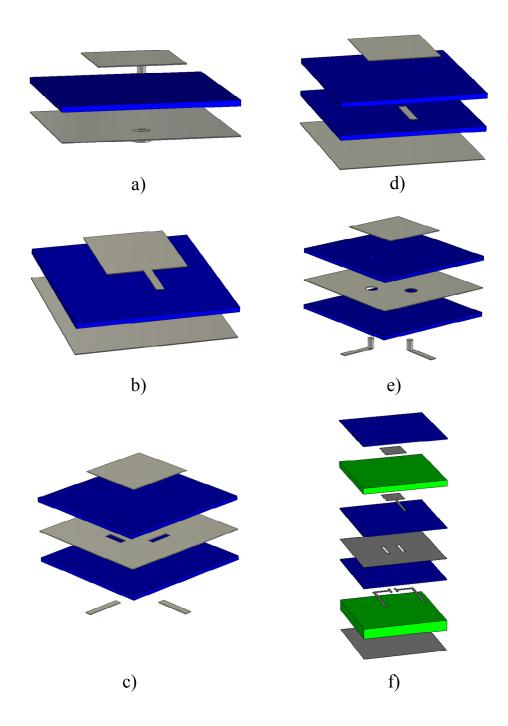


Figure 3.12: Patch antennas with different feeding structures with a) Coaxial feeding, b) Coplanar feed, c) Aperture-coupled feeds for dual linear or circular polarization mode, d) Proximity (Electromagnetically) coupled microstrip feed, e) probe-feed microstrip patch antenna with two feeds for dual linear or circular polarization capability, f) A combination of different feeding structures are given within one dual polarization microstrip patch antenna design, adapted from [112]. The grey layers represent copper structures for patch microstrip lines and ground, the substrate layers are indicated with blue color and the green layers are spacers, made by foam material.

patch antenna is the insert-feed microstrip patch. Here, the impedance matching is established by gap structures on the patch antenna surface near the feeding point. Furthermore, a more centered feeding point can be used for matching the patch antenna impedance to the microstrip line wave impedance. In this way, external matching networks are avoided.

In figure 3.12c, a aperture-coupled microstrip patch antenna is shown. The aperturecoupled feeds are excited by microstrip lines. Often, the microstrip lines are designed with open stubs for impedance matching. The aperture is defined by the hole in the ground plane. Several aperture geometries are reported in the literature. The aperture geometry in [112] is designed in bone structure, to enhance the impedance bandwidth of the antenna. Another advantage of this patch antenna architecture is the lower radiation of the feeding network, located below the ground layer.

The proximity (Electromagnetically) coupled microstrip feed is given in figure 3.12d. The patch edge is here excited by an open microstrip line.

The probe-feed microstrip patch antenna with two feeds for dual linear or circular polarization capability is given in figure 3.12e. Dual linear polarization is generated, if the two feeds are excited with equal phases. By adjusting the signal phases with 90° phase difference, circular polarization can be established. The probe-feed microstrip patch antenna is a very elegant feeding structure in regard of suppressing x-pol radiation. The small holes in the ground plane are contributing only marginally to the x-pol radiation and the probe-vias are very easy to establish.

Figure 3.12f accommodates several feeding techniques within one antenna design. There are two feeding lines below the first substrate shown. These feeding lines are excited with 180° phase difference to excite the centered patch by aperture-coupled slots. The aperture slots are defined with bone geometry, to enhance the impedance bandwidth for this polarization channel. The green spacers in figure 3.12f are representing foam material with very low  $\epsilon_r$ . These foam material is used as spacer between the lower ground plane and the aperture-slots and as spacer between the two patches. The height of the lower foam spacer is specifically defined with  $\lambda/2$  to use the ground as a reflector. The orthogonal polarization will be generated by the centered coplanar feed microstrip patch antenna. Is the centered patch excited for horizontal (from the slots) or vertical (from the coplar microstrip line) polarization, the upper patch is excited, as coupled resonance feed, to radiate. Such patch antenna configurations are used to enhance the impedance bandwidth. Both patch antenna sizes differ in length L. As a consequence, two different resonance frequencies are established to broader the impedance bandwidth for both polarization channels.

#### 3.3.6 Dual linear and circular polarized microstrip radiators

There are several techiques available to establish circular or dual polarization capability from microstrip patch antennas. Generally, the polarization capability can be provided by the radiator shape or by the phase relations of the driving signals governed by the feeding network. In figure 3.14a and 3.14b are patch antennas with feeding networks shown. The

#### 3.3. MICROSTRIP ANTENNAS

two driving signals are  $90^{\circ}$  out of phase and exciting the horizontal and vertical radiating edges. Due to the  $90^{\circ}$  phase difference the two electrical fields are added to circular polarization.

Figure 3.14c and 3.14d shows a realization of microstrip patch shapes with intrinsic capability for circular polarization. Here, only one feed is necessary to excite the patch crosswise. One electric field vector is generated by the non-truncated edges of the patch. The orthogonal field vector is generated by the excitation of the truncated corners, with 90° out of phase. The 90° phase difference will be determined by the truncation. In far field, the two field vectors are summarized to a plane wave with circular polarization. Depending on the geometrical order of the truncations LHCP and RHCP can be established.

Figure 3.14e shows the excitation of a squared microstrip patch antenna with 4 feeds. The opposite sided feeds are working together and are excited with  $180^{\circ}$  phase difference to radiate the desired polarization. Typically, this configuration is used to generate horizontal and vertical polarization in alternating radiation mode or linear polarization in simultaneous radiation mode. This feeding configuration is called "differential feeding" and is very useful for the reduction of unwanted cross-polarization levels. The advantages and disadvantages of the differential feeding technique are briefly discussed in section 6.4. Circular polarization can be generated from the configuration in figure 3.14e, when the two driving input signals are defined with  $90^{\circ}$  out of phase.

#### 3.3.7 Microstrip antenna feeding networks

The relevant feeding networks discussed here are either one or two dimensional copper structures realized in micostrip line technology. Typically, the feeding networks either are parallel or series fed systems.

In figure 3.14a, 3.14b and 3.14c the parallel feeding networks are shown. In figure 3.14a, given is a simple one dimensional, coplanar, and parallel feeding network. To establish a desired amplitude antenna taper, the power division ratios can be selected along the antenna array. Often the power dividers are design as T-Junction or Wilkinson power dividers. For uniform amplitude taper distribution the ratios should be set equal. When the distance between the antenna input ports (shown with dots in figure 3.14) and the microstrip line length between feeding network input port and antenna port is chosen to be equal, the antenna beam is directed to boresight. As already introduced in section 1.7. the antenna main lobe direction is independent of the frequency in regular parallel feeding networks. Figure 3.14b shows an exceptional case of a regular parallel feeding network. Here, the line length is progressively extended along the linear array. As a consequence, the main beam will be shifted in off-boresight direction. Furthermore, this parallel feeding network can now be used as a frequency scanning antenna. The line length is a function of wavelength and frequency. If the frequency is changed, the resulting antenna main beam direction is changed. Figure 3.14c illustrates a schematic layout of a two dimensional parallel feeding network as 4x8 corporate feeding structure. Are the distances between

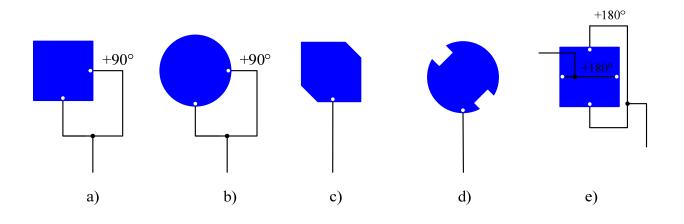


Figure 3.13: Circular and differential feed microstrip patches. a) and b) shows a square and circular microstrip patch with feeding network, providing two excitation signals 90° out of phase. After the equal power split, the 90° phase difference will be established by microstrip line with  $\frac{\lambda}{4}$  difference in length. c) and d) are typical configurations for radiating circular polarization by the excitation of only one feed. The shape geometry establishes the simultaneous radiation of two vector components, exactly 90° out of phase. The square and circular patch in c) and d) are excited at the edges, crosswise. e) shows the excitation of a square microstrip patch with 4 feeds. The opposite sided feeds are excited with 180° phase difference to radiate either horizontal or vertical polarization. This configuration is used for the reduction of cross-polarization levels, briefly discussed in the later chapters.

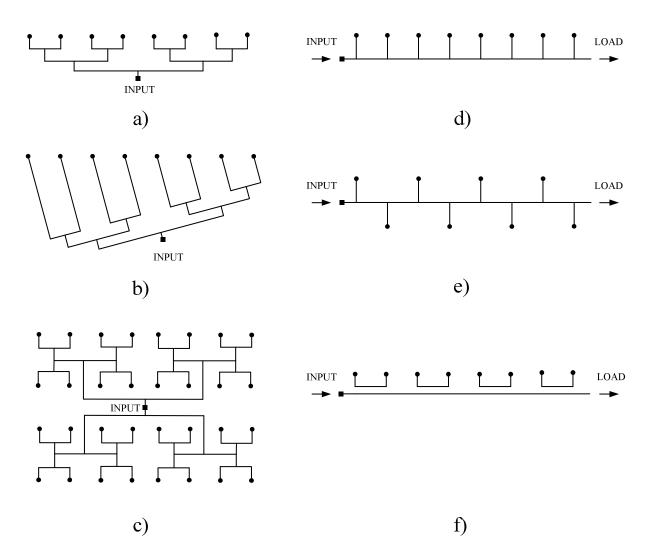


Figure 3.14: Feeding networks

the antenna elements set equally in x- and y-axis, the antenna beam is again pointed in boresight direction. This concept is suitable for array antennas with multiple antenna radiators without the requirement of beam steering. Adequate beam steering capability becomes only possible, if phase shifters or time delay units are implemented in front of every antenna input port. If the phase shifters are implemented at other points inside the feeding structure, limited field of view antenna arrays can be established. This special case of subarray configuration is discussed in details in section 3.4.6.

Figure 3.14d and 3.14e show two schematic layouts of simple series feeding network. This network works as a travelling wave feed and is typically used to set the main lobe at a desired inclination angle. The inclination of the main beam angle can be either generated by frequency scanning or by selection of phase differences between the consecutive antenna input ports, induced by the path length. If the signal path length to each antenna input

port is set equal to a multiple of the design wavelength, the beam will be set to the boresight direction. The amplitude distribution of the antenna array can be set by the strength of the coupling to each element. For instance, the proximity coupling from figure 3.12d can be seleted to achive this goal. As shown in figure 3.14f, the coupling can also be established by microstrip directional couplers as a part of the feeding network. In this case, every antenna architecture from figure 3.12a to 3.12d can be connected to the feeding network. A matched load serves as the termination of the series feeding structure. Alternatively, the matched load can be replaced with a radiating element in order to increase the overall array efficiency of the antenna complex. If the radiating elements are spaced with multiples of  $\lambda$  or  $\lambda/2$ , the unwanted reflections by each element are combined in-phase. As a consequence, the input port of the series feed antenna array would show large VSWR values.

There are many more feeding networks described in literature, including, the combination of series and parallel feeds. The interested reader can find a good overview of different feeding network designs in [15].

#### 3.3.8 Bandwidth and efficiency of microstrip patch antennas

One of the most important parameters of patch antennas is the realized bandwidth. Several requirements and definitions addressing the topic of weather radar system bandwidth have already been introduced in section 1.7. For the discussion of bandwidth aspects in the field of microstrip patch antennas, it must be noted that several bandwidth definitions are available in literature. Accordingly, the definitions for impedance bandwidth, polarization bandwidth, efficiency bandwidth and gain bandwidth are introduced next. Typically, only the impedance bandwidth is given in antenna datasheets.

The impedance bandwidth (also called VSWR bandwidth) is defined by the value of the return loss (or VSWR) at the antenna input port, related to the given wave impedance. Classical S11 values for bandwidth definitions are -10dB and -20dB. Commonly, the wave impedance of  $50\Omega$  is used, but also other reference impedances are frequently used. The microstrip patch antennas developed in this work are designed with  $100\Omega$  wave impedance at the input port of the single patch antenna element. The 1x4 arrays are fed by connectors with  $50\Omega$  wave impedances. Consequently, the bandwidth is discussed with S11 either at  $100\Omega$  or  $50\Omega$ . For a lot of applications other bandwidth requirements should be used. For instance, frequency scanning antennas are prone to change their polarization, efficiency and gain capability. The gain bandwidth is defined within a certain frequency range and with predefined gain flatness value. The efficiency bandwidth defines the frequency range wherein the antenna provides certain efficiency. The polarization bandwidth expresses the frequency range wherein the antenna maintains its polarization.

Figure 3.15a shows the bandwidth performance of patch antennas with circular or squared radiator shape, as a function of  $\frac{H}{\lambda\epsilon_r}$ . In detail, three different dielectric constants are investigated in their bandwidth characteristics. On x-axis the ratio of substrate height and effective wavelength is given. The y-axis shows the impedance bandwidth of the

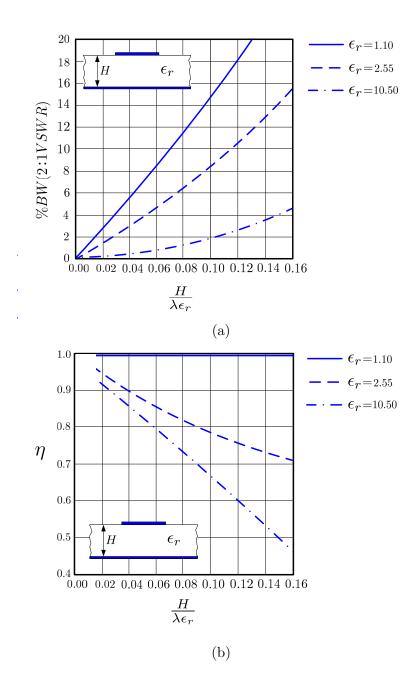


Figure 3.15: (a) Antenna bandwidth characteristics as a function of  $\frac{H}{\lambda\epsilon_r}$ . (b) Antenna efficiency  $\eta$  characteristics as a function of  $\frac{H}{\lambda\epsilon_r}$ . Both graph are adapted by [20].

microstrip patch antenna with VSWR limit of 2:1. The VSWR of 2:1 represents S11 $\approx$ -10 dB. It is clear visible that the bandwidth can be enlarged when the substrate height will be increased. Additionally, the bandwidth can be changed by the proper choice of the substrate. Substrates with lower dielectric constants are providing higher antenna impedance bandwidth values compared to substrates with higher dielectric constant. For antenna applications with strong space requirements higher dielectric constants are used. Therefore, the antenna designer should be aware of the limited bandwidth. To increase the bandwidth, several approaches are available in literature. One approach was already introduced by the antenna architecture with two stacked patch antenna elements, shown in figure 3.12f. The slightly different resonance of both patches enlarges the overall antenna impedance bandwidth. Other methods to increase the bandwidth are the implementation of gap structures in the antenna ground plane, different geometries of excitation apertures or different patch antenna shapes. In order to establish an extended bandwidth in aperture-coupled antennas, spacers with low dielectric constant are used.

In Figure 3.15b the relation of antenna efficiency and the ratio  $\frac{H}{\lambda \epsilon_r}$  is given. The antenna efficiency will significantly be decrease with higher substrate height and a chosen substrate with higher relative permittivity values.

## **3.4** Phased array antenna theory

#### 3.4.1 Linear phased-array antenna pattern

In the following linear antenna array discussions the amplitude excitation coefficients are assumed to be homogeneously distributed. Only the inter-element phase values are changed in order to establish beam scanning. The far field radiation pattern can be interpreted as the discrete Fourier transformation of the array excitation coefficients. Furthermore, the antenna array pattern is the product of the element pattern from single radiator and the array factor. The following section provides the necessary equations for the calculation and analysis of uniformly excited linear antenna array radiation pattern. To express the radiation pattern of linear arrays, the following equations 3.60 to 3.64 adapted by [9] can be used.

$$F(u) = \sum A_n e^{jkd_x u(n-1)}$$
(3.60)

 $A_n$  represents the complex excitation coefficient, which is assumed to be constant for the array discussions in this section. The value n is the number of elements in the linear array and u is the angular variable with  $u = \sin(\theta) - \sin(\theta_0)$  with  $\theta_0$  the scan angle. For equation 3.60 the inter-element spacing is assumed to be equal to  $d_x$ . k represents again the wavenumber with  $k = 2\pi/\lambda$ . For uniform excitation the array pattern becomes

$$F(u) = e^{j\pi u(n-1)} \left( \frac{\sin\left(\frac{nkd_x u}{2}\right)}{n\sin\left(\frac{kd_x u}{2}\right)} \right), \qquad (3.61)$$

122

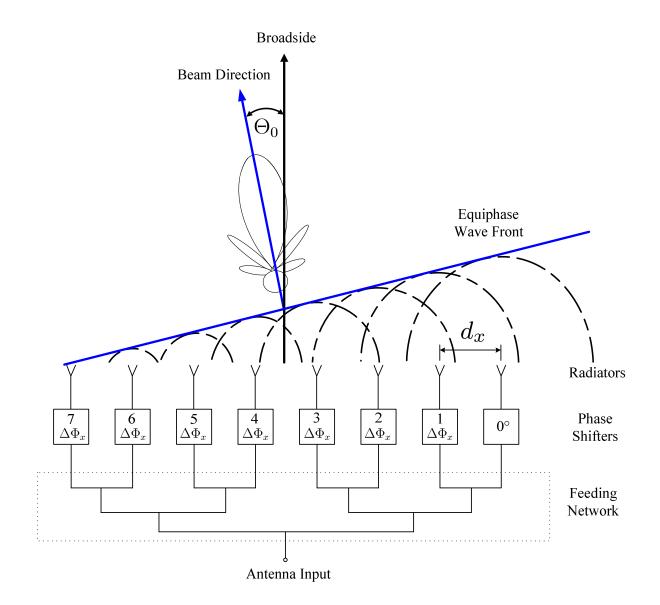


Figure 3.16: Linear antenna array geometry with equiphase wave front, generating the far field antenna radiation pattern at scan angle  $\theta_0$ . The first phase shifter, on the right, defines the reference phase. The consecutive phase shifters are excited with a phase increment of  $n\Delta\Phi_x$ .

with inter- element phase shift of  $kd_x \sin(\theta_0)$ . The beam position can be scanned to  $\theta_0$  by varying the inter element phase  $\Delta \Phi_x$ , as shown in figure 3.16. The relation between the beam pointing angle  $\Theta_0$  and inter element phase shift  $\Delta \Phi_x$  can be described with

$$\Delta \Phi_x = \frac{2\pi}{\lambda} d_x \sin(\Theta_0). \tag{3.62}$$

The half power points of linear antenna arrays can be evaluated by

$$\frac{\sin\left(\frac{nkd_xu}{2}\right)}{n\sin\left(\frac{kd_xu}{2}\right)} = \sqrt{0.5}.$$
(3.63)

For large arrays with N>4, equation 3.63 can be simplified to  $nkd_xu/2 = \pm 0.4429$  so that the beamwidth can be approximated with

$$\theta_{3dB} \approx \frac{0.8858\lambda}{nd_x \cos(\theta_0)}.$$
(3.64)

#### 3.4.2 Planar phased-array antenna pattern

The following section provides the necessary equations for the calculation and analysis of the antenna radiation patterns in planar array of elements on a rectangular lattice with even numbers of radiators along the x-axis and also along the y-axis. To express the antenna radiation pattern generally for planar antenna arrays, equation 3.65 adapted by [9] can be used.

$$F(u,v) = \sum_{n=1}^{n/2} \sum_{m=1}^{m/2} A_{nm} \cos\left[\left(n - \frac{1}{2}\right) k d_x u\right] \cos\left[\left(m - \frac{1}{2}\right) k d_y v\right]$$
(3.65)

Please note, the array excitation coefficients are assumed to be symmetrical, so that the pattern can by established by summing over the half elements along each axis. As shown in figure 3.17,  $d_x$  and  $d_y$  are representing the element spacing in x- and y-axis. The direction cosine plane variables are represented by

$$u = \sin(\theta)\cos(\phi) - \sin(\theta_0)\cos(\phi_0) \tag{3.66}$$

and

$$v = \sin(\theta)\sin(\phi) - \sin(\theta_0)\sin(\phi_0). \tag{3.67}$$

The angles  $\theta_0$  and  $\phi_0$  are the beam pointing angles. The inter element phase shifts are forming the main beam at desired point in space and can be calculated with

$$\Phi_u = k_0 d_x u_0 = k_0 d_x \sin(\theta_0) \cos(\phi_0) \tag{3.68}$$

and

$$\Phi_v = k_0 d_y v_0 = k_0 d_y \sin(\theta_0) \sin(\phi_0). \tag{3.69}$$

The values  $\Phi_u$  and  $\Phi_v$  are the element to element phase shifts in x- and y-direction, respectively. For better understanding the mathematical expressions of the antenna radiation pattern, figure 3.17 with the geometry of a planar array, can be used.

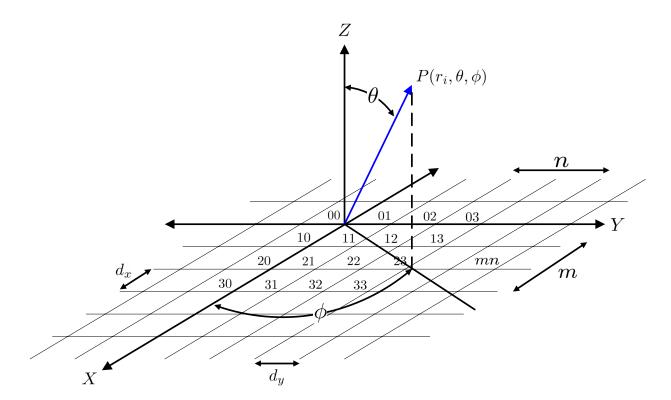


Figure 3.17: Geometry of planar phased-array antenna

#### 3.4.3 Properties of radiation pattern in antenna arrays

In radar systems with phased-array antennas the antenna key parameter beamwidth, gain and directivity play a special role. All antenna parameter change for different scan positions of the main lobe. The maximum scan area of a 2D array antenna depends on the design of a single element with its polar pattern and the inter element spacing. Is the inter element spacing selected with  $d > \frac{\lambda}{2}$  the grating lobes enters the visible space. The following subsection will deal with all scan-angle-dependent parameters from the antenna radiation pattern and gives design advises for developing phased-array antennas for specific applications.

One of the most important antenna design law is the pattern multiplication law for array antennas. Here, the sum antenna radiation pattern can be evaluated with the multiplication of the element pattern and the antenna array factor. By steering the antenna off-boresight direction it becomes clear that the antenna gain of the main lobe is decreasing, while the 3dB antenna beamwidth broadens. In this case, the propability for a grating lobe entering the visible space increases, so that energy will be radiated into undesired angular direction

The decay of the element pattern has not only cons. The decay of the element pattern can be used to suppress the grating lobes, which are usually present at the edge of the antenna array factor. The following equation 3.70 expresses the relationship of the element spacing  $d_x$  and the maximum scan angle  $\theta_0$ , when the grating lobe is still outside the visible space:

$$\frac{d}{\lambda} \le \frac{1}{1 + |\sin(\theta_0)|} \tag{3.70}$$

The definition of a grating lobe in [125] is given as follows: "A lobe, other than the main lobe, produced by an array antenna when the inter element spacing is sufficiently large to permit the in-phase addition of radiated fields in more than one direction". Grating lobes can be interpreted as periodic occurrence of the main beam, when the inter element spacing is chosen greater than  $\lambda/2$ . Generally grating lobes should be avoided, because grating lobes in visible space radiate power which would be actually used in the main lobe. As soon as a grating lobe enters the visible space the antenna gain of the main lobe will be decreased significantly.

The beamwidth, the side lobe level decay and the side lobe suppression of an antenna array are affected by the aperture taper distribution. In general, the half-power beamwidth  $\theta_{3dB}$  of the radiation pattern for the principal planes of a rectangular array **at boresight** can be approximated as follows:

$$\theta_{3dB}(boresight) = 0.886B_b \frac{\lambda}{L} \tag{3.71}$$

 $B_b$  represents the broadening factor, which depends on the array aperture taper and has unity value for a homogeneous distributed taper. The value 0.886 is explained with  $nkd_xu/2 = \pm 0.4429$ . L is the length of the antenna by considering a linear antenna array with n elements  $L = nd_x$ .

The table 3.4 partly adapted by [8] provides a selection of taper functions with different gain, beamwidth and side lobe suppression performances. If a very narrow beamwidth is required, degradation in side lobe suppression performance can be expected. On the other hand, clever amplitude tapers provide good side lobe suppression performance, but an expanded 3 dB beamwidth and a decreased antenna gain factor. Equation 3.72 gives a raw estimate of the 3dB beamwidth at defined scan angle  $\Theta_0$  and shows the  $\frac{1}{\cos(\Theta_0)}$  dependence. The cosine distribution is responsible for the expanding beamwidth of the main lobe when the beam will be steered off-boresight direction.

$$\theta_{3dB} = \frac{\theta_{3dB}(boresight)}{\cos(\theta_0)} \tag{3.72}$$

The gain factor shown in table 3.4 can be calculated with the corresponding formula for taper efficiency [8]:

$$\epsilon_T = \frac{1}{n} \frac{\left|\sum a_n\right|^2}{\sum |a_n|^2} \tag{3.73}$$

 $a_n$  represents the element weighting coefficient and n the number of elements in a linear array or in principal planes of a rectangular array.

Recalling equation 3.7, the antenna directivity can be estimated with the constant K

126

| Taper function   | Beam-<br>width           | Distance<br>to First<br>Zero | Sidelobe<br>Suppres-<br>sion | Gain<br>factor |
|--|--------------------------|------------------------------|------------------------------|----------------|
| -1  0  +1  | $50.8 \frac{\lambda}{L}$ | $57.3 \frac{\lambda}{L}$     | 13.2                         | 1              |
|  | $50.8\frac{\lambda}{L}$  | $57.3 \frac{\lambda}{L}$     | 13.2                         | 1              |
| $\Delta$ 0.8   | $52.7 \frac{\lambda}{L}$ | $60.7 \frac{\lambda}{L}$     | 15.8                         | 0.994          |
| $\begin{vmatrix} -1 & 0 & +1 \end{vmatrix} = 0.5$              | $55.6 \frac{\lambda}{L}$ | $65.3 \frac{\lambda}{L}$     | 17.1                         | 0.970          |
| $f_{(x)} = 1 - (1 - \Delta)x^2$ 0                              | $65.9 \frac{\lambda}{L}$ | $81.9rac{\lambda}{L}$       | 20.6                         | 0.833          |
| $-1 \underset{f(x) = \cos\left(\frac{\pi x}{2}\right)}{0} + 1$ | $68.8\frac{\lambda}{L}$  | $85.9 \frac{\lambda}{L}$     | 23.0                         | 0.810          |
| $-1 \underbrace{0}_{f(x)} + 1$                                 | $83.2\frac{\lambda}{L}$  | $114.6 \frac{\lambda}{L}$    | 32.0                         | 0.667          |

Table 3.4: Taper functions

and the principal plane beamwidths  $\Theta_H$  and  $\Theta_E$ . This equation can now be adapted for scanning phased-array antennas by implementing the cosine dependence  $cos(\Theta_0)$ .

$$D \approx \frac{K \cos(\Theta_0)}{\Theta_H^\circ \Theta_E^\circ} \tag{3.74}$$

K represents again the amplitude distribution factor and is defined with 32400 in [8]. As one can see the table 3.1 shows a very similar amplitude distribution factor with 32685. For this directivity calculation the principal beamwidths are expressed in degrees. The maximum antenna directivity without any efficiency consideration can be computed with the knowledge of the geometrical antenna area  $A_{Cell}$  of one cell, the wavelength  $\lambda$  and the number of radiating elements n with

$$D_{max} = \frac{4\pi n A_{Cell}}{\lambda^2}.$$
(3.75)

The expected directivity at arbitrary scan angle, for a chosen taper in tabel 3.4, can be estimated by expression 3.76. To retrieve the scan dependent antenna gain, equation 3.77 can be used. Expression 3.77 includes several efficiency considerations for the calculation of the antenna gain. D includes, as shown in equation 3.76, the scan loss with  $cos(\Theta_0)$  and the taper efficiency  $\epsilon_T$ .  $\epsilon_L$  represents the losses of the distribution network.

$$D = D_{max} \epsilon_T cos(\Theta_0) \tag{3.76}$$

$$G = \epsilon_L (1 - |\Gamma|^2) D \tag{3.77}$$

 $\Gamma$  represents the reflection coefficient as function of the scan angle. Consequently, the antenna ports are not impedance matched and mutual coupling between the radiating elements can be generated.

#### 3.4.4 Factors affecting mutual coupling in phased-array antennas

The mutual coupling effect of antennas is defined in [125] as follows:

a)"On the radiation pattern of an array antenna: For array antennas, the change in antenna pattern from the case when a particular feeding structure is attached to the array and mutual impedances among elements are ignored in deducing the excitation to the case when the same feeding structure is attached to the array and mutual impedances among elements are included in deducing the excitation".

b)"On input impedance of an array element: For array antennas, the change in input impedance of an array element from the case when all other elements are present but open-circuited to the case when all other elements are present and excited".

The review article from reference [46] gives a good overview about the factors generating the mutual coupling in phased-array antenna systems. Furthermore, techniques are explained to mitigate mutual coupling effects in phased arrays. In particular, the mutual coupling effects are explained there by "the electromagnetic characteristic of a particular antenna element influenced by the elements in their proximity. This inter-element influence or mutual coupling between the antennas is dependent on various factors, namely, number and type of antenna elements, inter-element spacing, relative orientation of elements, radiation characteristics of the radiators, scan angle, bandwidth, direction of arrival (DOA) of the incident signals, and the components of the feed network, that is, phase shifters and couplers " [46]. Scan blindness at specific angles can occur, when the mutual coupling effects are neglected. These radiation blind directions are highly undesirable and should be avoided in any case, to operate the phased-array antenna with predictable radiation characteristics.

3D field simulation software packages take the mutual coupling into account and give the antenna designer more freedom to mitigate/consider the mutual coupling effects at very early stage of the array antenna design process. In such simulation environments, the main mutual coupling factors are considered. These factors are surface waves (typically generated by thicker substrates for wideband applications), the geometrical position of the single radiator in the array (typically, the inner elements are showing different impedances and radiation characteristics compared to the edge located radiators), the finite isolation between the different feeding networks (for instance the finite isolation of polarization channels in dual polarization feeding networks), the finite isolation and impedance inbalances between radiators which are sharing the same feeding network and finally the change of mutual impedances during beam steering.

The antenna design in this work only considers the mutual coupling aspects in the 3D full wave simulations from CST MWS. The array factor function of CST MWS works with simple pattern multiplication, by assuming equal element patterns and the numerical array factor. The geometrical position and its influence on the sum pattern is not considered for the simple pattern multiplication function.

The mutual coupling from surface waves can be reduced by electromagnetic band gap structures or by the choice of suitable substrates. The change in element radiation pattern and port impedance can be optimized in 3D full wave simulations. Here, the proximity of the "single antenna element under test" can be considered. The same is true for the simulation of the feeding network. For instance, the differential feed 4x8 patch antenna array for weather radar application is equipped with via fences between the 8 feeding networks. As a consequence, the polarization and channel isolation was increased and strong mutual coupling effects are avoided. Judicious design of phase relations inside the feeding network, based on integral multiples of  $\frac{\lambda}{2}$ , can also be used for mitigating the mutual coupling effect between adjacent radiators. This fact will be shown later, in the design description of the differential feed 4x8 patch antenna array for weather radar applications.

# 3.4.5 Polarization aspects for dual polarized planar phased-array antennas

Planar phased-array antennas are prone to increase the x-pol fields as soon as the antenna main lobe is steered off the boresight direction. One reason is the misprojection of the co-polar and x-polar fields onto the local horizontal and vertical directions of the main lobe [64]. Even if the antenna array would be equipped with perfectly polarized radiators, the misprojection induces polarization errors, compared to mechanically steered antennas. This misprojection is investigated in details with orthogonal current sheets forming a dual polarized phased-array in [63]. In this reference, an adaptive compensation method is derived by the control of amplitudes and phases, to mitigate the intrinsic polarization distortion by misprojection. In [64] the induced biases on the measurement of polarimetric observables in the two radar operation modes, namely the ATSR (Alternating Transmit and Simultaneous Receive) mode and the STSR (Simultaneous Transmit and Simultaneous Receive) mode, are investigated. In [64] it is stated, that the observation of polarimetric variables with electronically steered antenna can cause measurement biases that are comparable or even larger than the intrinsic polarimetric characteristics of hydrometeors. As a consequence, the polarimetric scattering matrix is multiplied with the inverse of the projection matrix, to remove the biases from the dual-polarized planar phased-array weather radar measurements. To avoid the misprojection during azimuthal beam steering a cylindrical phased-array weather radar is proposed in the references [65], [92], [93]. This cylindrical antenna configuration maintains the antenna main lobe shape during the azimuth beam scanning. As a result, the gain and beamwidth in both polarization planes are kept constant. But for the elevation scanning the misprojection is still present. Furthermore, the elevation beam steering will be performed by frequency shift of the operating radar frequency, which is highly undesired for operational use in dense network with narrow bandwidth regulations.

In [66] the concept for interleaved sparse arrays in proposed. The authors from [67] adapted this concept for remote sensing applications to mitigate the x-pol contribution from misprojection or intrinsic characteristics of dual polarized planar phased-array antennas. Here, the transmitted polarization is changed by a clever choice of a subset of elements in the antenna array. This subset of elements radiates the orthogonal polarization state. More precisely, two orthogonal array factors ( $AF_1$  for the desired polarization from the majority of antenna elements, and  $AF_2$  for the orthogonal polarization from the minority of antenna elements) are generated and multiplied in order " to (1): synthesis a polarization that is rotated in order to minimize the misprojection of co-polar and x-polar fields onto the horizontal and vertical directions of the radiated beam, and (2): enables the cancellation of cross polarization components of antenna elements at array level"[66]. The co-polar antenna gain in large antenna arrays is only slightly decreased by the interleaved sparse arrays concept. The impact on the co-pol antenna parameters by this thinning factor method is a function of the number of elements-, used to radiate the orthogonal polarization states. For instance, the simulation of an antenna array of 32x32 elements has shown,

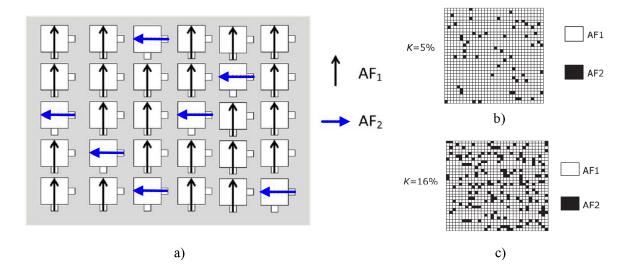


Figure 3.18: a) Illustration of sparse array concept for polarization control. A set of elements are excited with orthogonal polarization to mitigate the x-pol contribution from phased-array misprojection and the intrinsic array characteristic. b) 32x32 antenna array with thinning factor K=5%. c) 32x32 antenna array with thinning factor K=16%. All three figures are adapted by [67].

that a thinning factor of 5%, results in a co-polar gain loss of only 0.5 dB. On the other hand, the ICPR could be improved from 24.4 dB to 45.2dB. The CPS has been improved from 24.4dB to 48.8dB. The second simulation example investigates the interleaved sparse array concept during beam steering. In this case the main lobe was steered to the azimuth position of 45° and the thinning factor of 16% was selected. The ICPR could be improved from 14.5 dB to 29.8 dB and the CPS from 14.4 dB to 40.5 dB.

In [68] a case study of a panelized polarimetric phased-array antenna is investigated. Here, cross talk between horizontal and vertical antenna ports, the gain mismatched among T/R-modules, the individual polarimetric element patterns and the polarimetric array factors are considered in a calibration and correction method to mitigate these effects.

The research article published by [69] treats four factors of polarization distortion from planar phased-array antennas, operated in ATSR and STSR mode. These four factors are the intrinsic limitation of a single dual polarized antenna element, the antenna pattern measurement error, the entire array pattern and the imperfections in the T/R-module design of horizontal and vertical channels. Here, it was shown that the channel imbalances (complex gain and phase imbalances between H and V channel) should be below 0.05 dB and the channel isolation (cross-coupling between H and V channel) over 40 dB, to establish an  $Z_{DR}$  bias below 0.1 dB.

The misprojection problem was addressed in [70] with a new polarization basis approach, using the Huygens source element model. Here, two orthogonal co-polar fields are pro-

jected to the new polarization basis, so that the measurement error is only influenced by the x-polar fields. The influence on x-pol contribution in planar phased-array antennas will be further investigated later in the design chapter of the single and differential feed antenna arrays with 4x8 elements. In order to provide antenna beam steering in planar antenna arrays the phase of adjacent elements must be changed. The advantage of optimum phase excitation of mirrored elements inside the antenna array only exists, if the phase relation of  $\frac{\lambda}{2}$  between adjected elements are kept. Consequently, the benefit of x-pol suppression is degraded as soon as beam steering will be performed. By comparing the differential- and single-feed antenna arrays it can be recognized that the single-feed arrays are only comparable in boresight direction. The discoved quintessence is that the CPS can be kept constant during beam steering, if every antenna element of the planar array is fed differentially.

#### 3.4.6 Subarrays in phased-array antennas

In phased-array antenna systems, it can be very helpful to combine individual radiators to a group of radiators. This group of radiators is called a subarray. Typically, the antenna array can consist of a large number of subarrays. The system concept developed in chapter 5 is equipped with 800 subarrays. 32 elements are used to create one subarray. Generally, two types of subarrays exist. First, subarrays using the same phase on every radiator port and the second, subarrays equipped with phase shifters or real time delays in front of every radiator port. The following discussion is focused on subarrays using the same phase at the antenna ports. Correspondingly, the subarray defines a new element pattern, which the pencil beam of the complete array has to follow, in terms of scan loss and angular scan range. This new element pattern is also called subarray pattern.

In reference [71] the main advantages and disadvantages of subarrays are addressed. There it is stated, that "the subarrays are very advantageous, particularly for an active array antenna because of the following reasons:

• (a) It requires a smaller number of excitation sources than that of a normal array of equal number of radiating elements.

• (b) For active array applications, the number of phase shifters and amplifiers are reduced by the same factor as the number of elements in a subarray.

• (c) The interelement spacing in a subarray can be kept small; thus the aperture efficiency can be very close to 100%.

Some of the disadvantages are as follows:

• (a) Each subarray requires a power divider circuit in order to excite the elements of the subarray with desired taper.

• (b) The scan loss (gain loss due to off bore-sight scan) is higher as compared to an array of individually excited elements.

• (c) A large cell size limits the scanning range because unwanted grating lobe and scan blindness problems may occur".

132

#### 3.4. PHASED ARRAY ANTENNA THEORY

As the list of advantages and disadvantages above account for many antenna array performance parameters, it is vital to find a suitable subarray concept for the specific application. For phased-array weather radars in dense networks [99], as discussed in [115] the angular scan of interest is defined with only 30° in elevation scanning. For this reason, it is instructive to group a number of individual radiating elements into a subarray with its associated field of view that is limited with respect to the ungrouped full array. Such subarrays are also called limited filed of view arrays. At the same time, it should be avoided that grating lobes or nulls from the new subarray pattern become visible in angular region of interest. Additionally, the increase in scan loss during beam steering should be comparably low.

A good overview of methods for the construction of limited field of view arrays is given in reference [74]. Here, design methods are provided for optimizing the array gain in a given limited scanning sector. "The methods considered include the use of passive multiport networks, coupled dual-mode waveguides, protruding dielectric elements, corrugated structures, and quasi-optical networks that provide excitation of the necessary over-lapped subarrays". Another focus is the shaping of the flat-topped sector-element patterns.

Another disadvantage, not induced in the table of subarray disadvantages above, is the effect of quantization lobes. Quantization lobes can arise when an antenna array composed of subarrays is built with finite adjusted-distance between the edges of the adjacent subarrays. In this regard, it is possible that the inter-element spacing is violated at the location where the subarrays are connected to each other. As a consequence, the fragmentation of the complete array into a number of subarrays becomes visible in the sum antenna radiation pattern. For this reason, the quantization lobes can arise, as a function of fragmentation on different positions. Is the antenna array uniformly discretized into subarrays, the lattice of the quantization becomes symmetrical over the 3D antenna pattern. In [72] and [73] arrays with irregular polyomino subarrays are investigated in order to eliminate the quantization lobes in large phased-array antennas.

# Chapter 4

# Design and 3D EM field simulations using CST MWS

The design- and EM simulation tool CST MICROWAVE STUDIO (CST MWS) was selected, in order to establish a polarimetric phased-array antenna in PCB multilayer structure. In particular, the transient time domain solver was chosen for investigating different microstrip patch antenna structures and their polarimetric radiation characteristics. The transient time domain solver is based on the Finite Integration Technique (FIT) [84], [85] and is using hexahedral mesh grids. Furthermore, CST MWS incorporates some very advanced numerical techniques like the Perfect Boundary Approximation (PBA) and the Thin Sheet Technique (TST) for the memory efficient computation of surface currents and the propagating electromagnetic fields on curved structures. In this chapter, the main functionalities of CST MWS are explained and the FIT is graphically introduced. Additionally, the computer hardware environment and the required simulation duration for single radiators and antenna arrays are presented. For antenna radiation pattern discussions the boundary conditions for antenna field simulations are defined and the derivation from spherical electric field vectors to horizontal and vertical field components expressed with Ludwig's third definition are mathematically introduced. For fast approximation of the antenna array performances, the CST MWS far field plot functions are shown. Exemplarily, the optimization functions for S-Parameters and the antenna co- and x-pol radiation pattern are graphically given.

# 4.1 Hardware environment and experienced duration of simulation

The CST MWS software package has been implemented on a TAROX workstation computer, together with an operational software using 64 Bit WINDOWS 7 Professional. The maximum possible random access memory (RAM) of 32 GB was allocated and the Intel(R) Core(TM) i5-2500 CPU @ 3.3 GHz quad core was used. To decrease the simulation duration the NVIDIA Tesla C2075 graphical processor unit (GPU) was installed. This GPU generates internally up to 448 CPUs for fast parallel computing. The NVIDIA Tesla C2075 is able to perform parallel computing with up to 70 million mesh cells and accelerates the simulation duration with factor 5 to 6. This high amount of mesh cells becomes necessary for the accurate electromagnetic field calculation of antenna arrays with multiple radiators, within the predefined level of simulation accuracy. The evaluation run of an antenna array with 4x4 radiators and 68 million mesh cells for instance, can take up to 8 hours. For the optimization of complex antenna array designs, the range of the optimization variable must be selected very carefully. Such an optimization process requires up to 25 runs. A dual polarized patch antenna with 16 million mesh cells took 30 minutes for one evaluation run. By starting the antenna design in single polarization mode, without 3D connectors, the antenna was established with 4 to 5 million mesh cells. Is the antenna showing symmetry planes, the number of mesh cells and consequently the simulation duration can further be reduced.

## 4.2 Transient Solver using Finite Integral Technique

All electromagnetic simulations in this work are carried out with the transient time domain solver in CST MWS. The transient time domain solver uses the before mentioned FIT. FIT is a general purpose 3D EM simulation method, applicable in both time and frequency domains. Unlike other numerical methods like finite difference time domain (FDTD) or finite element method (FEM), FIT solves the Maxwell's equations in integral form rather the differential ones earlier introduced in equations 2.1 to 2.4. The Maxwell equations in interval form are applied for finite calculation domains, so that multiple small grid cells in a hexahedral grid system are generated during the mesh process. A single grid cell as one of multiple cells in the finite calculation domain is shown in figure 4.1. The electric grid voltages e and magnetic facet fluxes b are visualized on the grid. On a second calculation domain grid, the material properties like dielectric facet fluxes as well as the magnetic grid voltages are defined. The Maxwell's equations are solved for each cell facets separately. "Considering Faraday's Law, the closed integral on the equation's left side can be rewritten as a sum of four grid voltages without introducing any supplementary errors. Consequently, the time derivative of the magnetic flux defined on the enclosed primary cell facet represents the right-hand side of the equation, as illustrated in the figure 4.1 below. Repeating this procedure for all available cell facets summarizes the calculation rule in a matrix formulation, introducing the topological matrix as the discrete equivalent of the analytical curl operator" [86].

# 4.3 Meshing

Tetrahedral meshing in FEM improves the geometrical accuracy, but increases the numerical effort, meanwhile provides staircase meshing from FDTD fast solutions with lower accuracies for curved objects. The FIT provides an advanced volume discretization method

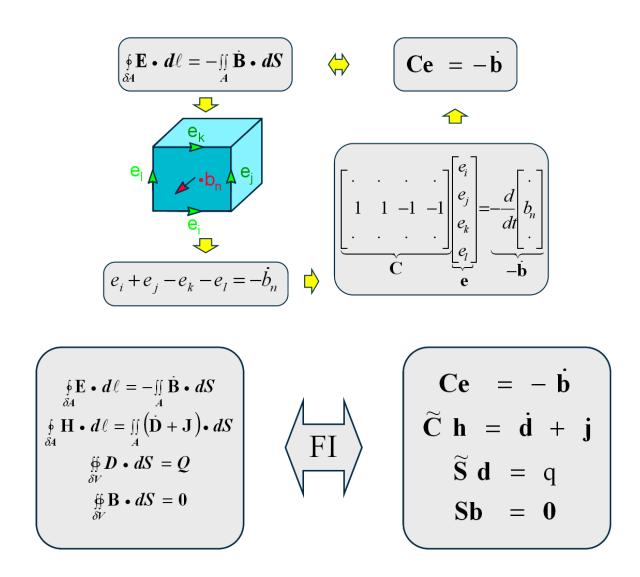


Figure 4.1: Allocation of field components of one grid cell with the discretization of Maxwell's equations to Maxwell's Grid Equations, adapted from [87].

with its Perfect Boundary Approximation (PBA) and the Thin Sheet Technique (TST). TST provides the solution of the Maxwell equations for 3 different material types within one cubic mesh cell. The mesh has strong influence on the accuracy of the performed simulation. The automatic mesh generation function from CST MWS provides a suitable mesh for antenna structure. The Adaptive Mesh Refinement (Energy Based or Expert System Based) finds the most suitable mesh automatically by recognizing the regions of field concentration or field gradients to refine the mesh step wise. The required accuracy e.g. from the S-Parameters can be selected by the designer. But also other goals, for instance the antenna gain at desired angular region of radiation pattern can be defined. The mesh of the X-Band patch antenna designs in this work was ranging from 4 to 16 million mesh cells. The value of mesh cells depends on the number of layers and connectors, which are also fully implemented as 3D model in the antenna design. The final dual polarized 4x8 antenna array was not simulated in 3D full wave, due to the fact that more that 120 million mesh cells would have been required. The NVIDIA Tesla C2075 GPU provides only resources for the calculation of 70 million mesh cells at most. As a consequence, only 4x4 antenna arrays have been solved in 3D full wave. The numerical results of the full wave simulations are further used from the CST MWS array factor calculator to calculate the sum antenna radiation pattern of the final 4x8 antenna array. Exemplarily, a mesh of a 4x4 antenna array with differential feeding network is shown in figure 4.2.

## 4.4 Boundary conditions for antenna design

CST MWS is able to calculate electromagnetic problems only in finite geometrical expansion. For this reason, the boundary conditions must be defined and limited in space for the specific application. Different boundary conditions are available and highlighted by the color of the surrounding box. Figure 4.3 shows the boundary conditions of a 4x4patch antenna array. The recommended boundary condition for antenna problems is the open boundary with added space [86]. The open boundary condition simulates free space boundary, with minimal reflections, in all directions. The added space is necessary for the accurate calculation of the far fields. Another important boundary condition is the periodic boundary. Here, phased-array antenna elements in large arrays can be investigated and the influence of mutual coupling by near field disturbances among antenna individual elements can be simulated. Due to the fact that this work is not investigating the behavior of large antenna arrays, the periodic boundary condition was not used. Another property of the boundary condition is the selection of symmetry planes for the reduction of simulation duration. Is the 3D antenna model symmetric in one plane, the calculation time can be reduced by a factor of 2. During the development of single and dual polarized microstrip patch antennas, this elegant way was often used to half the duration of the simulation. Especially in the beginning of antenna design, many variables (up to 40) are used for optimization procedures, so that this symmetry plane property becomes necessary to provide reasonable simulation duration.

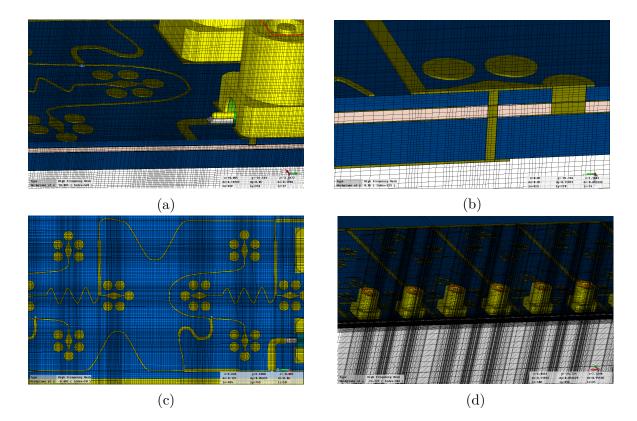


Figure 4.2: Mesh examples of 4x4 antenna array with 68 million mesh cells. On, below and above the radiating patches, a very high mesh density is selected. Also the 3D connectors and the patch antenna probe-feeds (vias for exciting the patch edges) are meshed with very high resolution. In these areas the field concentration and gradients are very strong, so that higher mesh resolution is applied.

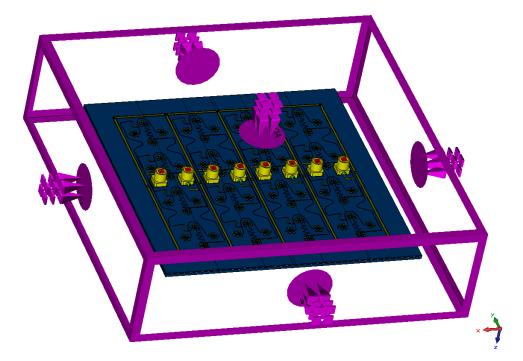


Figure 4.3: Selected open boundary conditions with add space, for 3D full wave simulations of antennas and proper calculation of the far field.

# 4.5 Simulation of antenna far field pattern

CST MWS calculates the far field of the radiated EM waves of the finite antenna structure by assuming spherical waves and neglecting the higher order terms in predefined distance to the structure. Consequently, the transversal field components are considered in the far field calculations from a spherical coordinate system with two corresponding angles  $\theta$ and  $\phi$ . In detail, the far field vectors are calculated from the electromagnetic fields on the boundary box of the calculation domain, as introduced in figure 4.3. The calculation results are displayed in polar and Cartesian plots. 2D and 3D visualizations are also available. Especially the visualization of directivity, gain, realized gain and phase of the electrical field components are used in this work for the description of the antenna radiation characteristics. The phase values are shown on the surfaces of the corresponding 3D far field pattern. These phases are calculated with the real (Re) and imaginary (Im) parts of the co- and x-polar field components from CST MWS, as described in reference [86].

$$\angle E_{Co} = \arctan\left(\frac{Im_{E_{Co}}}{Re_{E_{Co}}}\right) \tag{4.1}$$

The cut of a plane is defined by the polar field vector, e.g. the vertical co-polar component is defined by the y-axis and z-axis also called E-Plane. The other plane cut is perpendicular to the E-Plane and defined by the x-axis and z-axis, also called H-Plane. "A far field vector is composed of two tangential and one radial field component. These components are always ordered such that they form a right-handed coordinate system" [86]. The electric field components in spherical coordinate system are composed of  $E_{\Theta}$  and  $E_{\Phi}$ . These theta and phi components are further transformed to the Ludwig 3 [113] representation. The transformation is done for the main lobe alignment within this work. The vertical and horizontal field components are calculated with:

$$E_H = E_\Theta \cos\left(\Phi\right) - E_\Phi \sin\left(\Phi\right) \tag{4.2}$$

$$E_V = E_\Theta \sin\left(\Phi\right) + E_\Phi \cos\left(\Phi\right) \tag{4.3}$$

The calculated directivity and gain values in CST MWS are related to the standard definitions as already introduced in section 3.1. It should be mentioned that the antenna gain is calculated with the accepted power. Respectively, the impedance mismatch losses are not considered. In order to compare the simulation results to real antenna measurements, the realized gain is used for all pattern synthesis within this work. The realized gain value considers also the impedance mismatch losses of the structure. The antenna efficiency can also be distinguished between radiation and total antenna efficiency. The radiation efficiency is derived by the standard gain definition with accepted power. The total antenna efficiency examines also the mismatch impedance losses of the structure. Are the antenna ports well impedance matched, the difference between the radiation and total efficiency becomes very small.

The CST MWS far field plot function (Farfield Plot/ Plot properties/ Farfield Array) is used to estimate the total gain of antenna arrays with identical elements. Here, the element pattern multiplication with the array factor will be performed to retrieve a sum pattern as theoretically introduced in section 3.4. This function is only a array performance estimate, since the antenna array mutual coupling and array edge effects are not considered for the calculation of the sum antenna pattern. Also the total array efficiency is not calculated with this function. Better results for antenna arrays with identical elements can be retrieved by the periodic boundary condition, already explained earlier in section 4.4. However, the phased-array performance can be investigated very easy with this function. For every antenna element the phase and amplitude coefficients are set separately. Furthermore, the sum pattern can be calculated with selectable the element spacing, as shown in figure 4.4a. Reasonable scan angles for different antenna array designs, the scan losses and the performance for different amplitude- and phase tapers can be evaluated. As an example, the array sum pattern of a 4x8 antenna array generated by the CST MWS far field plot function, is shown in figure 4.4. In 3D simulation and in the CST MWS far field plot function, the phase center of the antenna can be evaluated. The phase center is defined in [125] as follows: "The location of a point associated with an antenna such that, if it is taken as the center of a sphere whose radius extends into the far field, the phase of a given field component over the surface of the radiation sphere is essentially constant, at least over that portion of the surface where the radiation is significant. Note: Some antennas do not have a unique phase center".

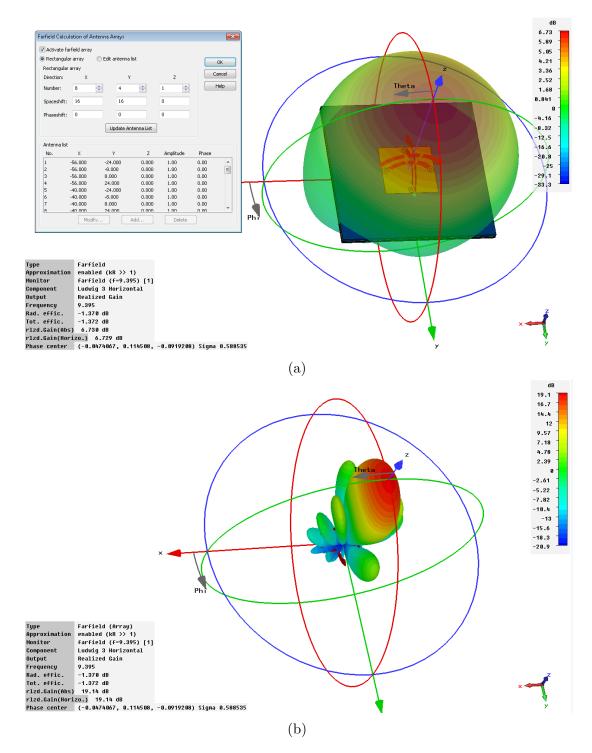
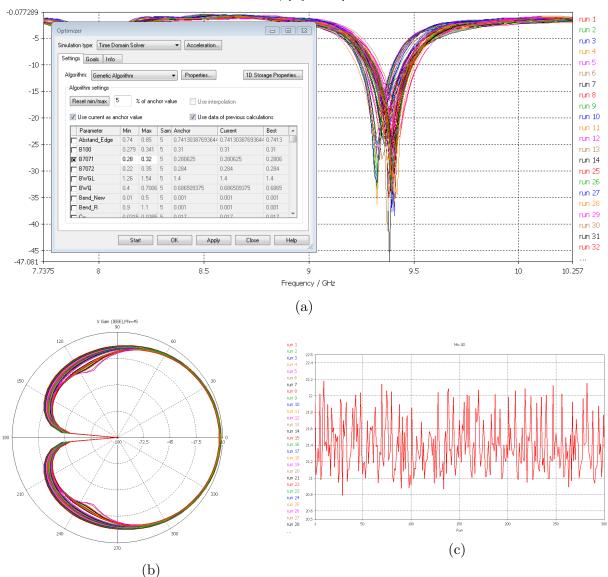


Figure 4.4: The CST MWS far field calculator was used to evaluate the antenna array performance. From single patch antenna element pattern, the array sum pattern will be calculated, without the consideration of mutual coupling and edge effects. In (a) the single antenna with the far field calculator is visualized. An element spacing of 16 mm is selected and corresponds to half free space wavelength at X-Band frequency. In (b) the 3D co-planar antenna radiation pattern result for a 4x8 antenna array is shown.

## 4.6 **Optimization functions**

CST MWS provides several algorithm types for the optimization procedure. The different algorithm types are briefly explained in [86]. The feeding network and the antenna radiation characteristic have been optimized with different algorithms in CST MWS. In particular the trust region framework and the genetic algorithm have been used. In the optimization frontend different goals are selectable. S-Parameters, co-polar antenna gain and x-pol suppression were mainly used for the optimization of the antenna radiation pattern and impedance matching of the antenna ports. For the optimization of the microstrip patch antenna elements, up to 60 variables were defined. Some variables are fixed from the 3-D design procedure and not very often changed. E.g. the substrate height has been defined in the very beginning of the antenna design. After antenna bandwidth investigation, this value was changed only ones to greater substrate height available from substrate suppliers. On the other hand are several variables intensively optimized to retrieve reasonable S11 results for impedance matching of the antenna ports. The CST MWS optimizer uses the predefined variables from the parameter list to find the best parameter configuration. The numbers of possible parameter configurations are becoming easily too high. For this reason, the optimization procedure was performed with only up to 4 variables and narrow variable ranges. The antenna designer should select the range of the variables very carefully. Wide variable ranges are resulting in multiple and time consuming optimization procedures. Often parameter sweeps of single variables are performed previously to localize the area of optimum. The parameter sweep function is a very good choice to start the optimization of a complex problem. In figure 4.5a the S-Parameter results for a optimizer run with genetic algorithm is visualized. The optimizer stops as soon as the predefined goal is reached. In this case the goal of the S11 was set to -40 dB and three variables for optimization are selected. Due to the 16 million mesh cells in this specific antenna design, the optimizer performed 45 evaluation runs in 30 hours to reach this goal. Figure 4.5b and figure 4.5care showing results from another antenna using the optimization run. Here, the envelope of the antenna gain and cross polarization suppression is examplary shown.



S1,1 [Magnitude in dB]

Figure 4.5: (a)Example of S-Parameter results from optimizer using the genetic algorithm. The goal was set to S11= -35dB at resoance frequency of 9395 MHz. (b) Examplary, the evolution of antenna gain with increasing numbers of optimization runs. (c) Evolution of cross polarization suppression with increasing number of optimization runs.

# Chapter 5

# System design of polarimetric X-Band phased-array weather radar

Almost all weather service radars are using parabolic dish antennas together with high power magnetron or klystron transmitters. Meanwhile solid state low power phased-array weather radars in dense networks are under discussion that are promising even faster 3D scans and more precise near-ground rain rate estimations.

This chapter describes the determination of the key characteristics for developing such a new low power Phased-Array Weather Radar (PAWR) from the system engineering point of view. Furthermore, an innovative system concept with a planar active phased-array antenna with optimized Limited Field of View (LFoV) subarrays for the reduction of phase/amplitude control units (in TRMs) and a unique PN-Gating calibration method adapted from the TerraSAR-X instrument will be presented.

## 5.1 Introduction

The requirements of national meteorological weather services are constantly increasing. Weather services are calling for weather radar systems that allow three-dimensional mapping of the environment with refresh rates of less than 1 minute [88]. Commercially available weather radar systems with 2-axis mechanical antenna drives allow refresh rates of about 5 to 10 minutes [89]. During this 5 to 10 min period, extreme weather situations can change significantly.

Another limitation of today's weather radar networks are widely spaced radar sites at distances of about 200-300 km, where near-ground precipitation data beyond a distance of 40 km cannot be acquired due to the Earth's curvature, which leads to considerable weather radar measurement errors [90]. In addition, short-term weather forecasting for urban regions [91] is changing from precipitation estimates with low resolution to accurate rain rate estimations on street level in order to provide flood warnings and accurate precipitation forecasts to the end users for the next hours, especially on mobile devices. In alpine regions like Switzerland or southern Bavaria, the terrain blockage becomes another reason for investigating dense radar network strategies and new radar system concepts as gap-fillers in order to retrieve weather radar data with high spatial-and range resolution at short scan times.

Phased array radar systems are well known from military applications since several decades. They promise to meet a lot of the demands of the weather radar community. However, military phased-array radars were developed for target detection, cross section measurement for classification and tracking. These applications do not require a high accuracy of the received signal level. On the contrary, PAWRs should establish measurement accuracies to the order of tenths of dBs to be comparable to the state-of-the-art weather radars with reflector antennas.

PAWRs promise to be a viable solution and easy to install, especially for dense radar networks, similar to the cell networks for telecommunication. In Japan, comparably dense weather radar networks but with small rotating antennas were successfully tested by CASA [91]. One of the first mobile phased-array weather radar demonstrators with frequency scanning antenna array is under investigation at the University of Oklahoma and the National Severe Storms Laboratory in the U.S.[92],[93].

## 5.2 PAWR system key characteristics

The calculated key characteristics of the new PAWR are listed in table 5.1. The equations and text references are provided and explained thereafter.

For defining the correct frequency band in European regions, the German frequency regulation [94] was used. The frequency band of 9.3 GHz to 9.5 GHz seems to be reasonable, since this band is allocated for civil and military weather radar applications. The individual radars in future dense networks will have a coverage radius of about 50 km. A frequency offset of about 30 MHz between adjacent radars provides sufficient bandwidth margin for pulse compression techniques. The center frequency of the radar demonstrator presented in this paper is selected with 9395 MHz.

There are several geometrical antenna shapes under investigation for PAWR. The most promising antenna shapes are cylindrical [92], [93] or planar structures like for instance the AN/SPY-1 array of the weather radar test bed in Norman, Oklahoma. Although cylindrical antennas have advantages like beam shape consistency over azimuth scanning, planar arrays are more common and have been investigated over a longer period for military and weather radar applications.

For the present analysis, it is assumed that the key system parameters are determined by a planar antenna structure. Moreover, a PAWR in an envisaged theoretical dense network should be composed of at least three 2-dimensional planar antennas with 120° azimuth and at least 30° elevation scanning range for retrieving a full 3D image of the surrounding area without mechanical scanning. The symmetrical 3dB antenna beamwidth in E-cut  $\theta_{3dB}$  and the 3dB antenna beamwidth in H-cut  $\phi_{3dB}$  should be less than 2° for each beam position to afford the same spatial resolution as the state-of-the-art X-Band Radars [95] with reflector antennas.

This first requirement of the maximum allowed beamwidth of  $\Theta_{3dB}=2^{\circ}$ , together with the maximum scan angles of  $\theta_0=\pm60^{\circ}$  produce the associated boresight beamwidth  $\theta_{Broadside}$  of 1° by recalling equation 3.72. Concerning grating lobes, we recall the relation in equation 3.70, which tell us how to avoid the occurrence of grating lobes in visible space, with  $\theta_0$  as the maximum scan angle,  $\lambda$  being the wavelength in free space and d as the element-to-element distance.

To further avoid scan blindness and undefined gain loss of the main beam caused by the occurrence of grating lobes in observed space, a maximum scan angle of 90° will be used here for defining the patch element spacing of  $d = \lambda/2 = 0.0166$  m at X-Band frequency. At  $\theta_0 = +90^\circ$  the grating lobe occurs at -90° and vice versa. Since the maximum scan angle used is defined with  $\pm 60^\circ$ , no grating lobe will appear in the visible space of the antenna radiation pattern. As a consequence, the required boresight beamwidth should fulfill the relation from equation 3.71.

The geometrical antenna dimensions can be calculated from equation 3.71 with L=2.7 m. The number of patch elements can be determined by the necessary patch element spacing d=  $\lambda/2=0.016$  m in equation 3.70. Here 0.886  $B_b$  represents the broadening factor of the beamwidth, which depends on the array amplitude taper. For the  $\cos(\theta_0)^2$  amplitude distribution, mandatory for a sidelobe suppression (SLS) of -32 dB in boresight beam direction, the factor 0.886  $B_b$  becomes 83.2, as shown in taper table 3.4.

With L from equation 3.71 divided by d from equation 3.70, the number of antenna rows and columns  $(\frac{L}{d}=160)$  and the number of antenna elements (N=160\*160=25600) of the complete array can be obtained. By dividing with 32 antenna elements for one subarray, we get the final number of 800 subarrays for a two dimensional planar phased-array antenna, as graphically illustrated in figure 5.1.

Equation 5.1 introduced next, gives the relationship between the antenna gain  $G_{\Theta_0}$ , the physical antenna area A, and the antenna area efficiency q.

$$G_{\Theta_0} = \left[10\log\left(\frac{4\pi}{\lambda^2}qA\cos(\Theta_0)\right)\right]$$
(5.1)

The squared bracket in equation 5.1 from [97] is valid for all antenna types and must be multiplied with  $\cos(\Theta_0)$  to be useful for calculating the antenna gain on different main lobe positions  $\Theta_0$  for phased-array antennas. The cosine function is a common assumption for the consideration of the single element pattern. For the mentioned  $\cos(\Theta_0)^2$  amplitude distribution, q becomes 0.44.  $G_{\Theta_0}=45.8$  dBi can be computed for  $A=(2.7 \text{ m})^2$  and  $\Theta_0=0^\circ$ .For maximum scan angle direction at  $\Theta_0=60^\circ$  we get  $G_{\Theta_0}=42.6$  dBi.

For radar sensitivity considerations, the weather radar equation 1.27 can be applied to a state-of-the-art X-Band weather radar [95], in order to determine the received power

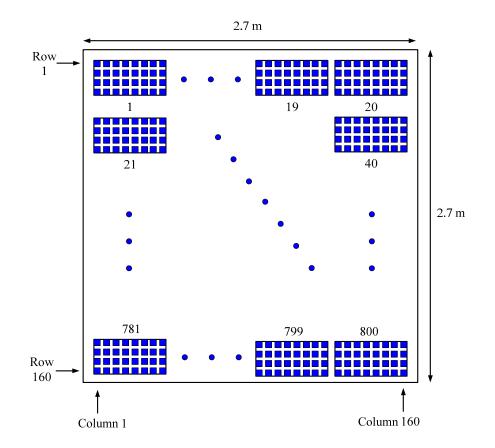


Figure 5.1: Two dimensional planar phased-array antenna. The PAWR should be composed of three 2-dimensional planar antennas with  $120^{\circ}$  azimuth and  $30^{\circ}$  elevation scanning range in order to provide  $360^{\circ}$  weather radar observation.

 $P_R$  for a given volume target of light rain with Z=100  $\frac{mm^6}{m^3}$ =20 dBZ. The following system parameters from [95] were used to estimate received power: transmitted peak power  $P_T$ =75 kW, reflector antenna gain G=45 dBi, beamwidth in E- and H-cut  $\Theta = \Phi = 1^{\circ}$ , typical radar operating range of R=100 km, pulse length in space h=ct=c\*3,  $3\mu s=990$  m and magnitude of complex index of refraction from water  $|K|^2=0.93$ . The resulting estimated received power is  $P_R$ =-80.5 dBm.

By assuming that the new PAWR should deliver the same echo signal of  $P_R$ =-80,5 dBm for the same volume target of Z=20 dBZ at an operating radar range of R=50 km, we are now able to calculate the transmitted power  $P_T$ =14,3 kW by considering the array antenna gain  $G_{\Theta_{60^\circ}}$ =42.6 dBi, the 3dB beamwidths in E- and H-cut  $\Theta$ = $\Phi$ =2°, the same h,  $|K|^2$ .

To evaluate the amount of power at the antenna element reference input port  $P_{Element}=560$  mW, the overall transmitted power of  $P_T=14,3$  kW should be divided by the number of antenna elements N=25600.

$$P_{TRM} = P_{Element} + SR + MPL = 27.5dBm + 6dB + 0.5dB = 34dBm = 2.5W$$
(5.2)

Depending on the subarray concept, (in this case the LFoV concept with 4 connected antenna patches will be considered, as shown in figure 5.2) the transmitter output port of one TR-module should provide sufficiently high power to overcome the splitter-ratio (SR) with 6 dB and microstrip line path losses (MPL) of around 0.5 dB from the feeding network. If all values are accounted for, the TR-module output power of  $P_{TRM}=2.5$  W can be estimated. The TR-module output power can be decreased by evaluating this example by considering the pulse compression gain, as introduced in the phased-array weather radar equation 1.34. Another alternative is to enlarge the operating range of the radar system. However, pulse compression has several disadvantages. One drawback is the receiver blindness at the time when longer pulses are transmitted. As a consequence, the blind zone of the radar will be significantly increased. To avoid these blind zones, pulse length switching is typically performed. But this leads to dramatic sensitivity transitions generated by switching from long to short pulses. For this reason the system performance was evaluated without the usage of pulse compression.

### 5.3 Detailed concept description

The new PAWR system is composed of 3 planar phased-array antennas with 120° azimuth scan capability, a local oscillator unit (LOU) and a central radar computer (CRC). In figure 5.2, the system block diagram is shown with the main building blocks and routing of the signals. For a detailed treatment of the analysis of 3 or more planar antenna arrays for dense radar networks, one may refer to [99].

A 2D planar phased-array antenna compliant to the requirements outlined above with the dimensions of 2.7m x 2.7m comprises 800 subarrays and 25 Digital Receiver- and Calibration Units (DRXCU).

| Attribute                          | Value                           | Status           |  |  |
|------------------------------------|---------------------------------|------------------|--|--|
| System frequency:                  | 9.3 to 9.5 GHz $f_c$ +/- 15 MHz | defined with [6] |  |  |
| Demonstrator frequency:            | 9395 MHz +/- 15 MHz             | defined with [6] |  |  |
| System architecture:               | 2D Phased-Array with TRMs       | defined in 5.3   |  |  |
| Broadside Antenna Gain:            | 45.8 dBi                        | using eqn 5.1    |  |  |
| Antenna Gain at $\pm 60^{\circ}$ : | 42.6 dBi                        | using eqn 5.1    |  |  |
| PRF:                               | 350 Hz- 5 kHz                   | defined in 5.2   |  |  |
| Broadside Beamwidth:               | 1°                              | using eqn $3.72$ |  |  |
| Beamwidth at $\pm 60^{\circ}$ :    | 2°                              | defined in $5.2$ |  |  |
| Azimuth Travelling Range           | 120°                            | defined in $5.2$ |  |  |
| for 2D planar antenna:             |                                 |                  |  |  |
| Elevation Travelling Range         | 30°                             | defined in $5.2$ |  |  |
| for 2D planar antenna:             |                                 | Simulated        |  |  |
|                                    |                                 | in 5.3           |  |  |
| Sidelobe Suppression:              | <-32dB                          | defined in $5.2$ |  |  |
| Antenna Dimentions:                | 2.7 m x 2.7 m                   | using eqn $3.71$ |  |  |
| Subarray concept:                  | Rectangular. 4x8 Elements       | defined in 5.2   |  |  |
|                                    | with LFoV                       |                  |  |  |
| Transmitted Peak Power:            | 14.3 kW                         | using eqn $1.27$ |  |  |
| Max. Antenna Element In-           | 560  mW                         | calculated       |  |  |
| put Power:                         |                                 | in 5.2           |  |  |
| TR-module output power:            | 2.5 W                           | calculated       |  |  |
|                                    |                                 | in 5.2           |  |  |
| Typ. Operating Range:              | 50 km                           | Open             |  |  |

Table 5.1: PAWR System Parameter

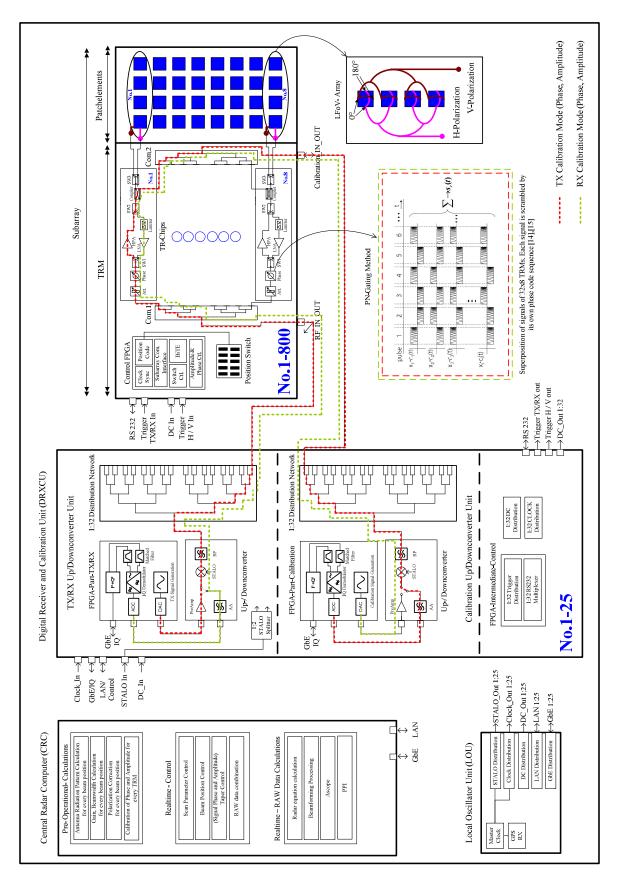


Figure 5.2: PAWR System Blockdiagram with PN Gating sequence from [100], [101], [102]

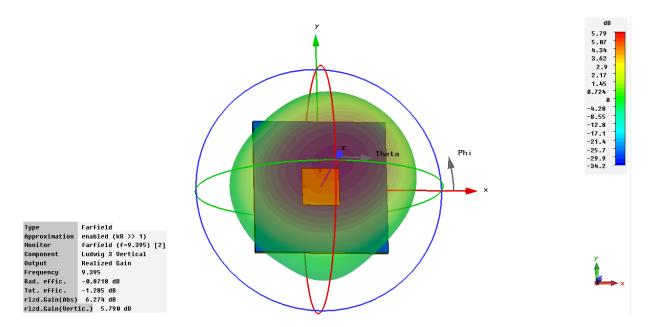


Figure 5.3: 3D pattern of single-feed and dual-polarized patch antenna, as an example used to establish the LFoV analysis

A single subarray accommodates 32 patch antenna elements, two 1:8 combiner networks, 8 microwave MMIC or hybrid circuit TRMs and one control FPGA. All devices are located on the subarray backplane in tile structure. The 8 TRMs are fed by the same RF signal source provided from the DRXCU. The 1:8 divider/combiner Com.1 distributes the RF signal simultaneously to the 8 TRMs.

One TRM chip allocates 6 bit phase shifting and amplitude tapering control, low noise and high power amplification, duplexing, RX protection, TX/RX switches SW1 and SW2 and the polarization switch SW3 for horizontal and vertical polarization pulse alternating mode. The coupler between SW2 and SW3 is necessary for the TX/RX amplitude and phase calibration. Currently 6 Bit (360°) phase shifting is typically used in TRM chip sets. It should just be mentioned here that the finite phase resolution of  $5.6^{\circ}$  leads to non-covered regions at larger azimuth scan angles and should be considered in the final system design.

The patch antennas are ordered in 4x8 lattices and are designed as a LFoV array to minimize the amount of amplitude and phased control units. The LFoV subarray with 1x4 elements is very economical and only possible because of the specified narrow elevation scan range of 30°. The azimuth scan range will not be influenced by the vertical combination of patch antenna elements. Figure 5.4 shows the element and subarray pattern analysis from CST MWS. The element pattern of a simple probe-feed microstrip patch antenna was simulated with 3D full wave Time Domain Solver and the CST Microwave Far Field Calculator was used to calculate the array antenna patterns with the theoretical array factor, without considering mutual coupling. In figure 5.3 the 3D coplanar element pattern

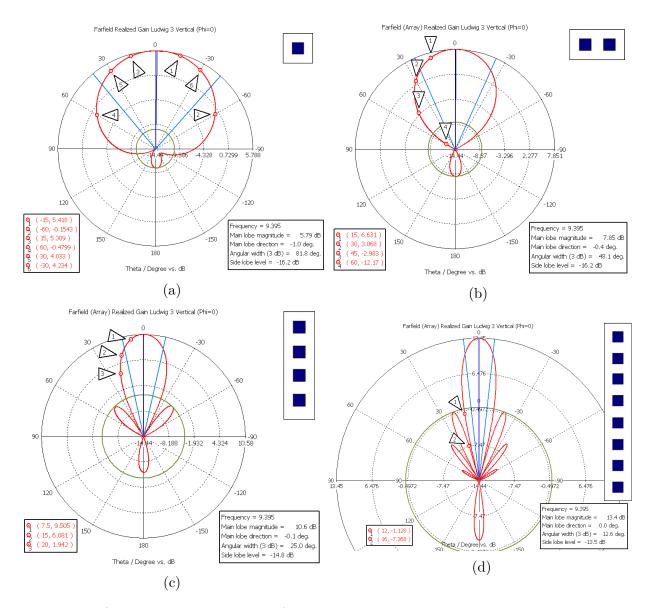


Figure 5.4: a) single element pattern; b) LFoV pattern with 2 horizontal grouped elements, limits the azimuth scan range; c) LFoV pattern with 4 vertical grouped elements, limits the elevation scan range; d) LFoV pattern with 8 vertical grouped elements, limits the elevation scan range dramatically, due to the first null.

from the microstrip patch antenna under test is shown. This pattern will be used as an example to analyze the LFoV-characteristics for the elevation and azimuth scan travelling range of the phased-array antenna main lobe. Figure 5.4a represents the  $\theta$ -cut at  $\phi = 0$  from figure 5.3. The markers are set to the most important beam angles, which are  $\pm 15^{\circ}$  for elevation scanning and  $\pm 60^{\circ}$  for azimuth scanning.

If every antenna element would be equipped with a separate phase shifting capability the phased-array antenna main beam would be able to scan  $\pm 60^{\circ}$  in azimuth and elevation with only 6 dB scan loss. Should the two radiators be combined horizontally in the array lattice, the azimuth scan is limited to approximately  $\pm 45^{\circ}$  by 11 dB scan loss, as illustrated in figure 5.4b. The scan loss would be dramatically increased to 20dB, if the scan travelling range of  $\pm 60^{\circ}$  is needed. Due to the specifications in table 5.1, a horizontal grouping of two elements cannot be applied. The combination of two horizontally grouped elements would be attractive from the cost-benefit point of view, when the scan travelling range in the specification will be decreased to  $\pm 45^{\circ}$ . The number of control units (TRMs) would be reduced by 50%.

If four elements (figure 5.4c) are fed with the same phase; the elevation scan travelling range of the complete array would be reduced to  $\pm 15^{\circ}$  with a gain loss of 4.6dB. Within this, even up to  $\pm 20^{\circ}$ , the main lobe can be steered. Consequently, the scan loss would be further increased to 8.5 dB.

If six elements are combined (not shown graphically), a scan loss of up to 12 dB for  $\pm 15.0^{\circ}$  can be expected. A combination of eight elements (figure 5.4d) limits the elevation scan range dramatically. A first null is produced at approximately  $\pm 15^{\circ}$ . Is the complete antenna array established by 1x8 subarrays, unwanted blind spots in the sum antenna radiation pattern are generated. As a consequence, a combination of 8 elements is not recommended for the weather radar application, discussed here.

To fulfill the requirements of the azimuth and elevation travelling ranges for 2D planar antenna in table 5.1, an LFoV-subarray with 4 vertically grouped elements should be used. The simulation results have shown that two combined patch elements would result in a scan loss of up to 20dB at  $\pm 60.0^{\circ}$ . To minimize the phase control elements for azimuth scanning, two elements may be combined, but only if the azimuth scanning range of  $\pm 45^{\circ}$ and 11 dB scan loss can be accepted. For reducing the cross polarization levels, the final dual polarized patch element design should be optimized by the so-called differential feeding techniques (LFoV-Array of 1x4 elements excited with 0° and 180°), as suggested in figure 5.2. Ingenious combinations of mirrored single-feed dual polarized patch antennas is another alternative to provide reasonable x-pol levels, as shown in the references [118], [119]. A detailed analysis about mirrored elements in subarrays is established in chapter 7. The advantages of differential-feed patch antenna elements are investigated in chapter 6.

Since the CRC in figure 5.2 needs to identify the geometrical housing position of every subarray in the complete antenna array, the position will be hard coded by a position switch and read via the control FPGA. The control FPGA receives the commanded antenna main beam position (azimuth and elevation angle) and the amplitude taper function via RS232 from the CRC. Taking this information and the subarray housing position into account, the eight phase- and amplitude values are calculated by the FPGA and transferred via bit streams to the eight TRM chips by serial data lines. For temperature, power supply voltages, communication and other monitoring tasks a BiTE (Built-in-Test-Equipment) function is implemented on the control FPGA. The trigger signals for transmit/receive mode and polarization selection will be applied from the DRXCU to the eight TRMs.

The TX/RX and the Calibration Up/Down converter units are grouped into one DRXCU. 25 DRXCUs are used for driving 800 subarrays. Both units are using the functionality of one high performance processing FPGA and the RF circuits are identically constructed for simplicity and cost considerations. The up and down conversion is designed to be reciprocal to further reduce costs. From the local oscillator unit (LOU) the stable local oscillator (STALO), DC voltages, Master Clock and Ethernet for control and I/Q data transmission will be routed to the DRXCU. The Master Clock will be disciplined by a GPS receiver to synchronize the three planar antenna arrays building one PAWR. Even multiple PAWRs in a dense radar network can be synchronized by GPS to establish bistatic weather radar observations.

The TX intermediate frequency signal will be generated by the TX/RX FPGA Part and will be routed through the up converter and the 1:32 distribution network to the subarrays. One DRXCU is able to feed 32 subarrays. The RX signals from 32 subarrays are received by the other port of the processing FPGA. Taking into account that the phase shifting and amplitude tapering will be done in the subarrays, the FPGA always receives the signals in correct amplitude and phase relation. The generation of the transmission signal has a high degree of freedom so that pulse width modulation and frequency modulation for pulse compression techniques are implementable.

The red and green signal lines in figure 5.2 demonstrate the calibration process for the transmission (red) and reception (green) case, which was adapted from [100], [101], [102]. The so called "pseudo-noise gating method" (PN-Gating) is operationally in use for the TerraSAR-X instrument and has shown very valuable results with respect to calibration accuracies.

The PN-Gating method works in the following way: The steering of the antenna main beam, the antenna gain and the amplitude taper are determined by the excitation coefficients of every single TRM. To retrieve these coefficients, special calibration pulse sequences with orthogonal codes are injected. The phase shifter on every individual TRM chip will be controlled with different pulse sequence codes of  $+-90^{\circ}$  phase shifts. The superposition of (in this case 32x8=256) TRM signals will be recorded by the Calibration FPGA part for the transmission case (red lines), where the cross correlation function with the corresponding code sequence will be applied to extract the phase and amplitude information of any individual TRM channel. The same procedure will be carried out for the reception case (green lines); meanwhile the calibration signal will be generated here on the Calibration FPGA part and recorded by the TX/RX FPGA part.

The CRC is the brain of the PAWR and is separated in the 3 main units; Pre-Operational-Calculation Unit, Realtime-Control Unit and Realtime-RAW Data Calculation Unit.

The main task of the Pre-Operational-Calculation Unit is the antenna radiation pattern calculation for every desired antenna main beam position in space by considering the actual amplitude and phase coefficients acquired with the PN-Gating processing. The calculation of the required array antenna gain and the beamwidth is a multistage process. At first, the antenna radiation pattern of one isolated subarray will be simulated and measured in an anechoic chamber. The simulated and measured subarray radiation pattern will be stored and considered as being the same for all subarrays. Afterwards the housing position of the subarray inside the complete antenna array will be simulated and another matrix coefficient created. To retrieve the mutual coupling between subarrays, the complete planar array needs to be simulated. Since mutual coupling depends on the steering angle of the array antenna, every possible angle needs to be considered and recorded in another additional mutual coupling coefficient. By multiplying the housing position coefficient matrix, the actual amplitude and phase coefficients from the individual TRMs and the mutual coupling coefficients, the final sum antenna radiation pattern can be calculated for every beam steering position.

Once the antenna radiation pattern is calculated, the beamwidth and antenna gain for every beam position in space are made available for the real time processing of the weather radar equation. The polarization correction needs to be done because of the non-spherical surface of the phased-array antenna. The planar phased-array antenna influences the polarization by pointing the antenna main beam away from the boresight direction, as detailed explained in section 3.4.5.

The Realtime Control Unit is the radar system controller. All scan parameters like, pulse width mode (long, medium, short), pulse repetition frequency (PRF), start and stop range, range step width,  $1/R^2$  range correction, polarization mode (H, V), antenna main beam angle in space, processing filters (time and frequency domain), amplitude antenna taper functions, pulse compression codes or a complete scan scheduler (RHI-Scan, PPI-Scan) are adjustable.

Finally, the central radar computer (CRC) will receive the I/Q data streams from the 25 DRXCUs to calculate all commonly known weather radar observables, introduced in section 1.5.2.

## 5.4 Summary

The key characteristics for the development of phased-array weather radar systems for the application in dense networks have been presented. A first system design with LFoV array, PN-Gating method and 4x8 element subarray design was introduced. LFoV arrays are a good choice for minimizing the amount of control units for large arrays; since the combination of 4 vertical elements is not influencing the sum antenna radiation pattern for the mentioned weather radar application with narrow elevation scan range. A cost effective receiver design has been presented with reciprocal transmit and receive path. Further cost savings due to expected accurate calibration results based on the novel PN-Gating method from the TerraSAR-X instrument are possible. The subarray PCB with chip-based TRMs and control FPGA is practical and can be exchanged in case of malfunctions. The small number of 50 I/Q data channels allow the use of COTS Ethernet devices.

## Chapter 6

# Understanding and optimizing microstrip patch antenna cross polarization radiation on element level for PAWR applications

The antenna cross polarization suppression (CPS), defined in section 3.2, is of significant importance for the accurate calculation of polarimetric weather radar moments. State-ofthe-art reflector antennas fulfill these requirements, but phased-array antennas are changing their CPS during the main beam shift, off-boresight direction. Since the cross polarization (x-pol) of the array pattern is affected by the x-pol element factor, the single antenna element should be designed for maximum CPS, not only at boresight, but also for the complete angular electronic scan (e-scan) range of the phased-array antenna main beam positions. Different methods for reducing the x-pol radiation from microstrip patch antenna elements, available from literature sources, are discussed and summarized. The potential x-pol sources from probe-feed microstrip patch antennas are investigated. Due to the lack of literature references, circular and square shaped X-Band radiators are compared in their x-pol performance and the microstrip patch antenna size variation was analyzed for improved x-pol pattern. Furthermore, the most promising technique for the reduction of x-pol radiation, namely "differential feeding with two RF signals 180° out of phase", is compared to single-feed patch antennas and thoroughly investigated for phased-array applications with simulation results from CST MWS. A new explanation for the excellent port isolation of dual linear polarized and differential feed patch antennas is given graphically. The antenna radiation pattern from single-feed and differential feed microstrip patch antennas are analyzed and the shapes of the x-pol patterns are discussed with the wellknown cavity model. Moreover, two new visual based electromagnetic approaches for the explanation of the x-pol generation will be given: First, the field line approach and secondly the surface current distribution approach provide new insight in understanding the generation of x-pol components in microstrip patch antenna radiation patterns.

### 6.1 Introduction

Dual polarized phased-array antennas for weather radar application in dense radar networks are currently under discussion in reference [115]. Such antennas promise even faster three dimensional volume scanning compared to state-of-the-art high power radar systems with reflector antennas and their twin axis mechanical drives. The change from parabolic reflector antennas with fixed beamwidth and gain values to phased-array antennas with inherent scan angle dependent co/x-pol patterns is highly challenging.

Weather radar systems with dual polarization capability observe echoes backscattered by hydrometeors from illuminated volumes to classify the precipitation, primarily with horizontally and vertically polarized electromagnetic waves. For accurate polarimetric echo measurements and their interpretation, the antenna CPS performances for both polarization planes are of significant importance. Depending on the CPS, the estimation of polarimetric observables can significantly be biased. The biases for the measured polarimetric observables should be less then 1 dB, 0.1 dB and 0.005, for the Reflectivity Z, the Differential Reflectivity ( $Z_{DR}$ ) and the copolar correlation coefficient  $\rho_{co}$ , as calculated in the references [105], [106], [107]. "For example, a 1-dB bias (e.g., due to an error in calibration) in estimating Z results in about a 15% fractional rain-rate bias if the Marshall–Palmer Z-R relation is used" [106]. The interested reader can find the derivations of all state-of-the-art polarimetric weather radar observables in section 1.5.2.

High-quality reflector antennas provide CPS values of up to -30 dB in S-, C-, and X-Band, within the half power beamwidth. A new phased-array weather radar antenna should provide the same CPS on boresight, and even more challenging the same CPS over the complete e-scan range. The e-scan travelling ranges stated in [115] are 120° azimuth and 30° elevation for one planar phased-array antenna panel. The 3-D volume radar scanner presented in chapter 5, [115] would be equipped with three of such planar phased-array antennas to achieve 360° azimuth volume scanning.

From phased-array antenna theory the co- and x-pol antenna radiation pattern can be calculated with the multiplication law that gives the overall antenna pattern as product of the element pattern (EP) and the array factor (AF). Consequently special attention should be paid to the design of the single antenna element and its EP in order to avoid unwanted x-pol radiation right from the very beginning.

Antenna manufacturers typically provide only E- and H-Cut radiation patterns. For phased-array weather radar applications this amount of information is inadequate. If the phased-array main lobe is pointed off-boresight-axis, the CPS will be degraded. As a consequence, all antennas for phased-array weather applications should be analyzed also in the  $45^{\circ}/135^{\circ}$  cutting planes, since the highest x-pol radiation may be expected in this region. A detailed x-pol investigation can only be performed by the 3-D analysis of the complete upper hemisphere of the microstrip patch element pattern.

Dual polarized microstrip patch antennas are suitable candidates for phased-array weather radar applications. These antennas are fabricated easily at low cost and have known radiation characteristics. On single antenna element level, the different x-pol reduction methods and their performances are now investigated and discussed. Finally new visual based electromagnetic approaches for the explanation of the x-pol generation are induced.

## 6.2 X-pol suppression techniques on element level, known from literature

Only a few suppression techniques on antenna element level have been published. The authors in [112], [109], [116] use differential feed excitation with two signals, 180° out of phase. This method will be explained in detail by the antenna prototype in section 6.4 and promises to be a viable solution for phased-array weather radar antennas. The defective ground plane solution published in [111] is useful for single element applications without complex feeding networks and dual polarization capabilities. The radiation from the defective ground area induces amplitude taper disturbances to the array feeding network and would degrade the overall antenna performance. The authors in [114] have been presented a printed thin dielectric substrate with strip grating in front of the radiating antennas for suppressing the x-pol radiation. But strip grating solutions are only useful for single polarization applications.

Recently a new investigation to explain x-pol radiation from microstrip antennas was published in [104]. Here the x-pol for differential feeding (180° out of phase) and rotational feeding (mirrored antenna elements inside antenna array) are discussed by analyzing the near-field radiation behavior. The major intention by the authors in [104] is to provide a new understanding of the x-pol radiation generation by observing the near field disturbances. A comparison of x-pol performances of circular and rectangular/square microstrip radiators for dual linear polarization applications was surprisingly not found in available literature. Additionally, only one capable literature reference could be found where the size variation of a single polarized patch antenna was analyzed for improved x-pol patterns [107]. Consequently, the circular and rectangular shape types and the antenna size variation in dual-pol patch antennas are investigated and compared in sections 6.4.4 and 6.4.6.

## 6.3 Feeding methods for low x-pol radiation in microstrip array design

There are numerous feeding mechanisms available for microstrip patch antenna elements. An overview of the state-of-the-art feeding mechanisms is given in section 3.3.5. The layer set-ups of the different antenna architectures are shown in figure 3.12. Well-known feeding techniques are aperture-coupling, probe-feeding, proximity-coupling and insertfeeding. Aperture-coupled patch antennas are often used to enhance the bandwidth with the radiating slots underneath the patch radiator. To further enhance the bandwidth, a



Figure 6.1: Layer set-up of squared microstrip patch antenna design. Left: Single probefeed patch. Center: constructed patches. Right: Differential probe-feed patch

second patch separated with foam material from the first one and with slightly different dimensions and corresponding resonance frequency is implemented. The second patch has also the advantage of reducing the x-pol radiation, since the x-pol radiation generated by the lower patch and the slots are shadowed. The patch antenna design from [112] shows excellent CPS performances for horizontal and vertical ports with -30 to -35 dB, respectively. But due to the aperture-coupled radiating slots and the back radiation to the feeding network, the mutual coupling aspect becomes critical for array applications. Further disadvantages are the sensitivity against height tolerances of the foam material and the generation of surface waves due to the radiating slots and the cavities between the foam layers. Moreover, the design presented in [112] is working with the reflector ground plane technique, which is not useful for array operation with multiple elements and feeding networks between.

Proximity coupled patches have similar disadvantages for array configurations as aperturecoupled antennas. The back radiation close to the feeding networks for two polarization planes is undesired in array configurations and the port isolation would become insufficient. Insert feed microstrip patches have their feeding networks on the same layer and unwanted x-pol radiation is generated. In keeping with these observations, insert feed and proximity coupled patch antennas are not suitable for phased arrays with high x-pol requirements.

Probe-feed microstrip patch antennas are suitable candidates for the phased-array weather radar application with high x-pol requirements. The possibility to drive the single patch antenna element with 180° out of phase and the low back radiation due to the small feed via holes through the shielding ground plane generates only small x-pol contribution.

## 6.4 Thorough analysis of the differential feeding technique for phased-array weather radar applications

One valuable technique for the reduction of x-pol radiation, namely the "differential feeding technique", has been presented in the literature sources [112], [109]. Differential feeding can be established by driving the patch antenna with two RF drive signals exactly 180° out of

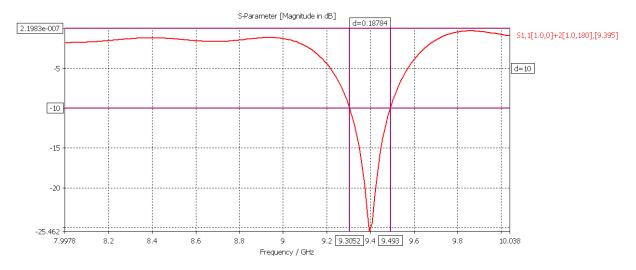


Figure 6.2: S11 resonating at 9.395 GHz with VSWR 1 : 2 Bandwidth of 188 MHz.

phase. To demonstrate and to analyze the advantages of differentially fed microstrip patch antennas for phased-array weather radar applications two probe-feed antenna designs with single and differential phase feeding are compared. It will be further explained with these antenna prototypes how the x-pol radiation is generated from surface currents and field line distributions.

The squared probe-feed microstrip patch antennas were designed and simulated with CST MWS. The patch antennas are consisting of two RO6002 substrates (dark green in figure 6.1) with  $\varepsilon_r = 2.94$ , 508 $\mu$ m height and excellent dissipation factor tan  $\delta = 0.0012$  for adequate antenna efficiency performances. The grey layers represented in figure 6.1 are the RO4403 prepress with  $\varepsilon_r = 3.17$  and 100 $\mu$ m height. This RO4403 prepress is used to combine the two RO6002 laminates during the compression process. For suppressing unwanted surface currents or propagation channels within the substrate right from the design beginning, this prepred shows only small  $\varepsilon_r$  differences compared to RO6002. The copper has a thickness of  $35\mu$ m and the diameter of the isolation circle inside the shielding ground for the probe-feed transition is 0.91 mm. The radiating square patches with 10.55 mm edge length, pin-via diameter of 0.4 and 0.416 mm pin-via to edge-distance are designed for a resonance frequency of 9.395 GHz (see figure 6.2). Both antennas from figure 6.1 are sharing the almost same design parameters. The only differences are the additional port in figure 6.1 (right) for 180° out of phase excitation and the width and length of the matching circuit (arrow geometry in copper structure) located close to the feed. The Rosenberger 3-D connector model was completely integrated in the CST MWS full wave simulation and impedance matched with GND vias and microstrip impedance transformer to the 50 $\Omega$  line impedance. The microstrip stubs in parallel to the probe-feed are used for matching the impedance of the patch antenna. In the center of figure 6.1 the constructed patches are visualized. Figure 6.2 shows the S11 of the matched connector port with patch antenna. The VSWR 1 : 2 bandwidth of 188 MHz could be established by CST MWS antenna model.

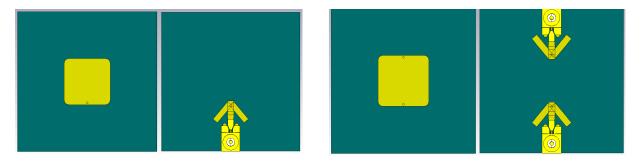


Figure 6.3: Front and back view of microstrip antennas under test. Left: Single probe-feed patch. Right: Differential probe-feed patch

The figures 6.4 and 6.5 can now be used to compare the co-pol pattern with and without the differential feeding technique. The radiation patterns are plotted with Ludwig's third definition of x-pol [113]. Note that the reference parameter "realized gain" in dBi also takes the impedance mismatch losses into account for the gain calculation. The single probe-feed patch antenna radiation patterns shows a co-pol "realized gain" of 5.85 dBi. The differential probe-feed patch antenna with 180° out of phase feeding provides a co-pol "realized gain" of 5.93 dBi.

The x-pol pattern in figure 6.6 shows two maxima and one null in the E-Cut. The radiating edge close to the feed contributes the highest x-pol radiation. The opposite to feed located radiating edge adds much lower x-pol radiation. By further analyzing the x-pol pattern it is obvious that the E-Cut( $\Phi = 90^\circ$ ) and H-Cut ( $\Phi = 0^\circ$ ), typically provided by antenna manufacturer, would not show the maximum x-pol radiation intensities from the upper far field hemisphere. The E-Cut CPS would show almost perfect results and the H-Cut would exhibit a high, but still unrealistic x-pol contribution from the 3-D antenna radiation pattern. Only the dedicated 45°-Cut would show the real antenna performance in CPS. For this reason, it is recommended to use 45°-Cuts in any CPS discussions for patch antennas. In the following discussions figure 6.10 is used for the comparison of the single and differential probe-feed patch antenna CPS performance using the recommended  $45^{\circ}$ -Cuts. The differences in CPS performances are clearly visible by the generated cuts in figure 6.10. The co- and x-pol plots from figure 6.10 are generated by the  $\Phi = 45^{\circ}$ Cuts from figures 6.4, 6.5, 6.6 and 6.7, respectively. Typically, phased-array antennas are providing azimuth e-scan ranges from  $+60^{\circ}$  to  $-60^{\circ}$ . Within this angular scan range the CPS should be as low as possible. An CPS of 14.2 dB for differential feed patch antennas can be achieved at  $\pm 60^{\circ}$  AZ position, compared to only 6.6 dB at  $-60^{\circ}$  for the single-feed patch antenna. The 3 dB half power beamwidth highlighted with the ellipse on the center top of figure 6.10 shows another advantage of the differential feed antenna for phased-array applications: The beamwidth is quiet symmetric and the phased-array scan gain loss with respect to the element pattern would also be symmetric for positive and negative scan angles.

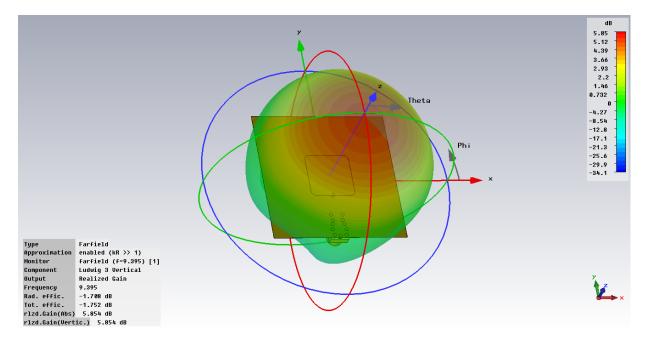


Figure 6.4: Co-pol 3D far field pattern of single probe-feed patch antenna

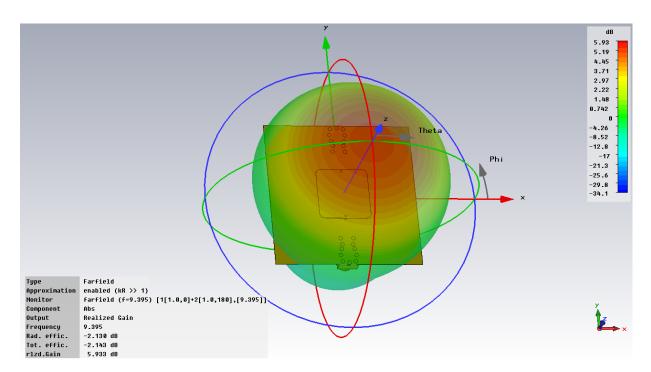


Figure 6.5: Co-pol 3D far field pattern of differential probe-feed patch antenna

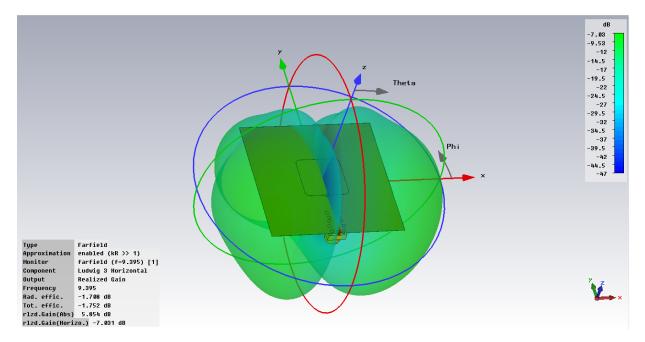


Figure 6.6: X-pol 3D far field pattern of single probe-feed patch antenna

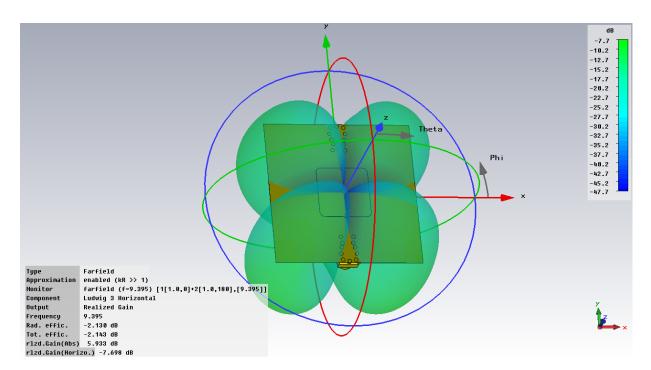


Figure 6.7: X-pol 3D far field pattern of differential probe-feed patch antenna

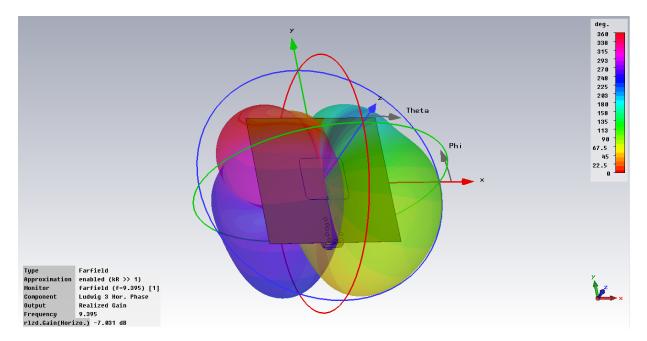


Figure 6.8: X-pol 3D phase plot of single probe-feed patch antenna

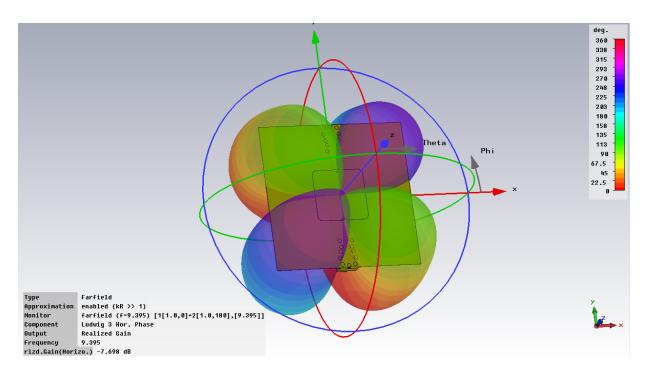


Figure 6.9: X-pol 3D phase plot of differential probe-feed patch antenna

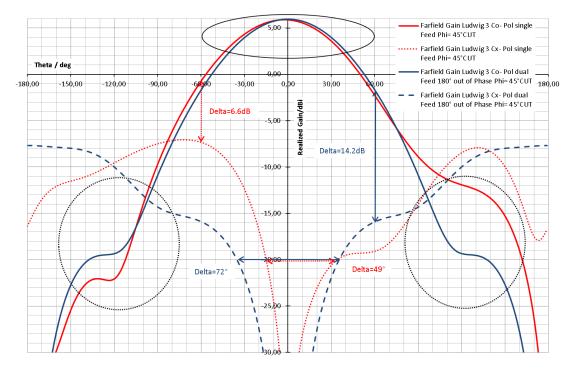


Figure 6.10: Comparison of single (red) and differential (blue) feed patch antenna CPS performances at 45°-Cut. The dashed curves are representing the gain plots of the x-pol radiation patterns.

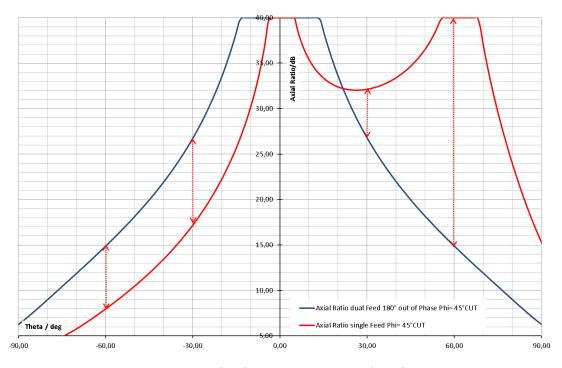


Figure 6.11: Comparison of single (red) and differential (blue) feed patch antenna axial rations at 45°-Cut.

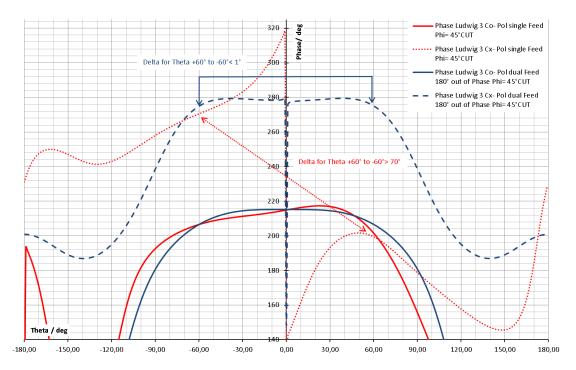


Figure 6.12: Comparison of co- and x-pol Phase plots from single (red) and differential (blue) feed patch antennas. The dashed curves are representing the phase plots of the x-pol radiation patterns.

The single-feed antenna shows a slight shift of the beam maximum in negative  $\Theta$  direction and an asymmetric beam shape. This can be associated to the single-feed configuration and the fact that stronger electromagnetic fields are radiated from the radiating edge located close to the feed point. The black circles at  $\Theta = \pm 120^{\circ}$  indicate back radiated energy and here again the differential feed antenna back radiation is symmetric and would induce the same amount of energy in both backward directions. The mutual coupling would be equal to the neighboring elements compared to the asymmetric back radiation from single-feed antennas. Furthermore, the x-pol free area below the main beam at -20 dBi is much broader for differential feeds with 72° azimuth range in contrast to only 49° azimuth range for the single-feed configuration.

Figure 6.11 compares the antenna axial ratios of the antennas. CST MWS is following the IEEE-Standard for the calculation of the axial ratio. The axial ratio is the ratio of the major axis to the minor axis of the polarization ellipse.  $\vec{E}_1$  represents the horizontal polarized field vector and  $\vec{E}_2$  the vertical polarized field vector. It is calculated as follows:

$$AR = \sqrt{\frac{\left|\vec{E}_{1}^{2}\right| + \left|\vec{E}_{2}^{2}\right| + \left|\vec{E}_{1}^{2} + \vec{E}_{2}^{2}\right|}{\left|\vec{E}_{1}^{2}\right| + \left|\vec{E}_{2}^{2}\right| - \left|\vec{E}_{1}^{2} + \vec{E}_{2}^{2}\right|}}.$$
(6.1)

The axial ratio for the differential feed patch is again symmetric and shows better results for negative and positive scan angles of up to  $\Theta = 25^{\circ}$ . For negative angles the differential

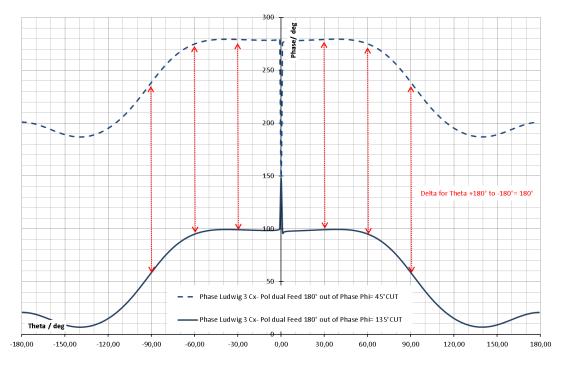


Figure 6.13: Phase difference of  $180^{\circ}$  for  $\Phi = 45^{\circ}$ -Cut (dashed) compared to  $\Phi = 135^{\circ}$ -Cut, established by differential feeding technique. The  $180^{\circ}$  phase difference is very useful in antenna array configurations for canceling out the x-pol components in far field from neighboring elements.

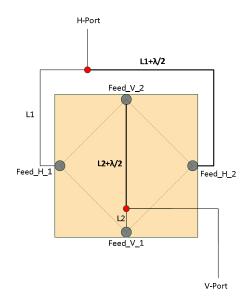


Figure 6.14: Graphical description for excellent isolation functionality of dual polarized patch antenna with differential feeding.

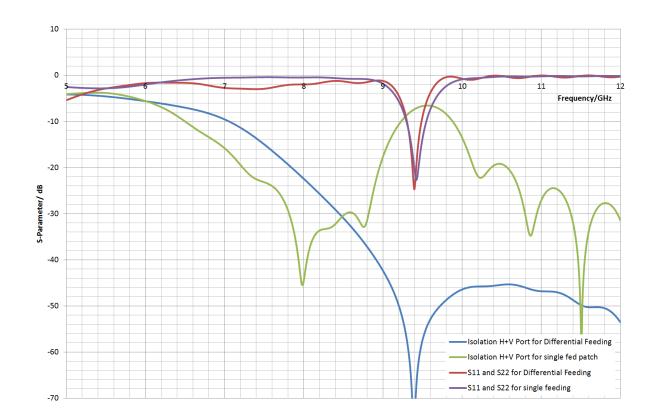


Figure 6.15: Comparison of port isolation characteristics from differential and single feed patch antennas.

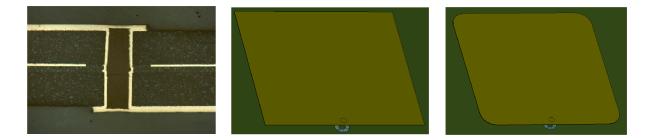


Figure 6.16: Left: Via filled with fossil resin and closed with cooper. Center: Square patch without edge bending. Right: Square patch with edge bending.

feed shows a better axial ratio with smaller decay per degree. The single-feed antenna shows for  $\Theta > +25^{\circ}$  better results than the differential feed antenna, but when considering all other disadvantages mentioned before this fact is negligible. It should also be noted here that an asymmetric axial ratio induces non-consistent scan angle biases for polarimetric phased-array weather radar observations. Of course only, if the non-constency is not considered in the radar calibration.

The x-pol phases from figure 6.12 are generated from the  $\Phi = 45^{\circ}$ -Cuts of figure 6.8 and figure 6.9, respectively. The co-pol phase plots are not visualized in 3-D. It can be recognized that the co- and x-pol phase of the differential feed antenna is very symmetrical distributed, especially in the desired scan range of  $\pm 60^{\circ}$ . The phase is identical over diagonal plane (see figure 6.9). The co- and x-pol phases of the single feed antenna are asymmetric and the maxima of x-pol phase on diagonal planes vary more than 70°. By analyzing the  $\Phi = 135^{\circ}$  and  $\Phi = 45^{\circ}$ -Cuts from figure 6.13, a phase difference of exactly 180° can be observed for the complete  $\Theta$  range of interest. Each point is exactly 180° out of phase by comparing both diagonal planes. This predictable diagonal phase distribution can be used for array configurations where the neighboring elements x-pol contributions cancel each other in far field.

For the next discussion, the two designs from figure 6.3 are redesigned with CST MWS for dual polarization capability, in order to compare the polarimetric port isolation characteristic. State-of-the-art weather radars are working in pulse alternating or simultaneously transmitting dual polarization modes. For these dual polarization modes the single-feed antenna will be equipped with two feeds; one for horizontal and one for vertical polarization. The differential feed patch antenna accommodates four feeds for dual polarization mode; two probe-feeds 180° out of phase for horizontal polarization and two probe-feeds 180° out of phase for vertical polarization. The differential feed patch antenna in dual polarization design is graphed in figure 6.14. The isolation and S11 results from CST MWS 3-D full wave simulations are visualized in figure 6.15. The differential feed dual polarized patch antenna provides maximum port isolation at the desired center frequency of 9.395 GHz. The polarimetric isolation performance of the single-feed dual polarized antenna is comparable poor. The excellent isolation characteristic of the differential feed dual polarized patch antenna can be explained with the graph in figure 6.14. By assuming a RF input signal at the vertical port in figure 6.14, the signal travels through the T-Junction power divider (red point in figure 6.14) and excites the Feed V 1 and subsequently the  $Feed_V_2$  with 180° phase shift. Both signals exciting the patch antenna to radiate, but small signal components (dashed lines in figure 6.14) are received by the horizontal ports  $Feed_H_1$  and  $Feed_H_2$ . The imperentation of current probes at the feed positions of CST MWS antenna model has shown that the two signals received by  $Feed_H_1$  and  $Feed_H_2$  are in-phase at the probe-feeds and cancel each other out at the T-Junction splitter in front of the horizontal splitter due to the length difference of  $\lambda/2$ . It turns out, that the differential feed patch antennas with  $180^{\circ}$  out of phase excitation are suitable candidates for phased-array weather radar applications. These antennas have valuable advantages compared to single-feed patch antennas.

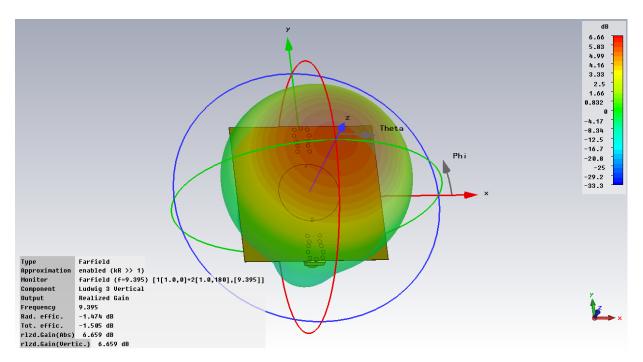


Figure 6.17: Co-pol pattern pattern of circular shaped X-Band patch antenna.

## 6.4.1 Analysis of potential x-pol sources in microstrip patch antenna design

Open via holes, rectangular patch edges and the position of connector and matching circuits below the shielding ground are investigated and verified as potential x-pol sources in this section. Additionally, circular and square patch geometries are compared and variations of the patch sizes are analyzed in their x-pol performances.

## 6.4.2 Probe-feed microstrip patches with plugged via holes

In figure 6.16 the cross section of the hole-plugged probe-feed is visualized. After drilling the via holes into the multilayer substrate the walls of the holes are galvanized with copper to connect the upper and lower RF layer. The holes are plugged using the following two-step process: First, the via hole is filled with cured resin to generate a plane surface on both sides and secondly an galvanization step takes place to close the via hole and to establish a plane surface for the radiation patch antenna element and the microstrip line. From the hole plugging process one would assume that the probe-feed produces lower x-pol radiation because of plane patch antenna surface and lower resistance in the area of the feed. CST MWS simulations have shown that the CPS is exactly (within  $\pm 0.01$  dB) the same compared to patches with conventional probe-feeds. It was verified that hole plugging does not improve the CPS of microstrip patch antennas and the expenses for the

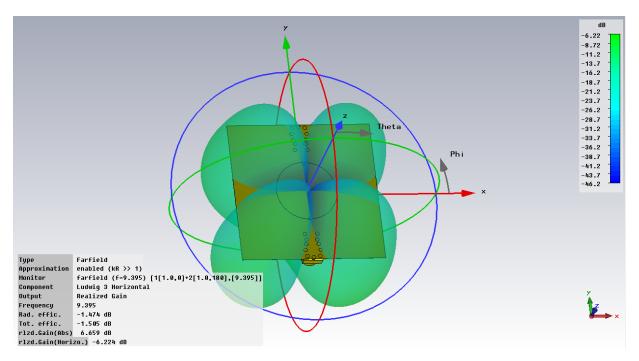


Figure 6.18: X-pol pattern pattern of circular shaped X-Band patch antenna.

additional plugging process can be saved.

## 6.4.3 Bended square patch antenna edges

By analyzing the x-pol radiation patterns in figure 6.6 and figure 6.7, two (for single-feed), respectively four (for differential-feed) maxima above the patch edges are observable. In the following test, this x-pol radiation contributions are assumed to be generated by the four 90° angles from the patch edges. Performed CST MWS simulations have evidenced that the patch antenna edge bending does not reduce the x-pol radiation. Only the resonance frequency will be shifted due to the change in absolute length of the radiating edge. After

| Patch  | Via  | GND   | Stub  | Stub   | Via-             | CPS              | Gain | GND            |
|--------|------|-------|-------|--------|------------------|------------------|------|----------------|
| Length | Dia. | Isol. | Width | length | Edge             | at $\Theta =$    |      | Size           |
|        |      | Dia.  |       |        | $\mathbf{Dist.}$ | $\pm 60^{\circ}$ |      |                |
| mm     | mm   | mm    | mm    | mm     | mm               | dB               | dBi  | mm             |
| 10.32  | 0.2  | 0.91  | 1.47  | 4.78   | 0.42             | 13.20            | 6.00 | $30 \times 30$ |
| 10.55  | 0.4  | 0.91  | 1.31  | 5.13   | 0.42             | 14.20            | 5.95 | $30 \times 30$ |
| 10.66  | 0.5  | 1.2   | 1.42  | 5.19   | 0.42             | 14.75            | 5.94 | $30 \times 30$ |
| 10.80  | 0.7  | 1.5   | 1.49  | 5.39   | 0.50             | 15.50            | 5.90 | $30 \times 30$ |
| 10.66  | 0.7  | 1.2   | 1.42  | 5.19   | 0.42             | 18.34            | 5.31 | $40 \times 40$ |

Table 6.1: Design parameter and CPS results for variable patch sizes.

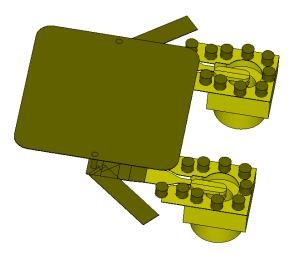


Figure 6.19: Connectors and matching stubs below the patch and shielding ground with  $90^{\circ}$  rotated.

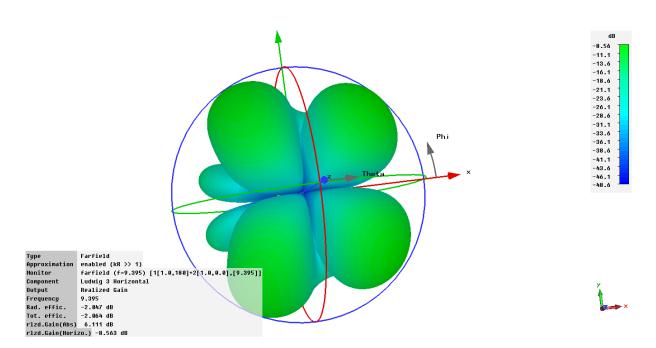


Figure 6.20: Degraded x-pol pattern due to the connector and matching stub rotation of  $90^{\circ}$ , as shown in figure 6.19

impedance re-matching of the bended patch antenna element almost the same x-pol values with the difference of only 0.04 dB was observed. Consequently, it can be stated that edge bending does not improve the CPS. The four patch edges are not contributing significant x-pol radiation.

# 6.4.4 CPS comparison of circular and square shaped microstrip patch antenna elements

An intensive literature search did not reveal any adequate reference comparing the CPS of circular and square shaped microstrip patch radiators. Therefore, a comparison of the two patch antenna shapes with respect to their x-pol performances is provided next. The comparison is based on the same resonance frequency, same layer configuration, slightly different parallel stub configuration due to the different patch impedances and the same differential feeding technique.

The circular patch radiator has a diameter of 12.67 mm, the probe via diameter is 0.4 mm and the probe via to edge distance is 0.5 mm. The diameter of the isolation circle inside the shielding ground for the probe-feed transition is again 0.91 mm. The resonance frequency is located at 9.395 GHz with a VSWR 1 : 2 bandwidth of 152 MHz. In figure 6.17 the "realized gain" of 6.66 dBi can be recognized. The x-pol pattern of the circular patch from figure 6.18 shows comparable results to the squared patch x-pol pattern in figure 6.7b-3 by featuring four maxima. The four maxima are generated due to the differential feeding technique for both radiator shapes. The realized gain is higher compared to the square patch but only due to the larger antenna patch area. The CPS of 14 dB for differentialfeed circular patch antennas was established at  $\pm 60^{\circ}$  azimuth position, which is almost equal to the 14.2 dB for differential-feed square patch antennas analized in figure 6.10. By applying longer optimization iterations for impedance matching, the same CPS for square and circular patch antenna geometries can be expected. It should be noted here that the value of 14 dB anyhow reflects the theoretical maximum of CPS at  $\pm 60^{\circ}$  for differential-feed microstrip patch antennas.

### 6.4.5 Analysis of probe-feed and its matching network position below the shielding GND of the patch antenna

For impedance matching of patch antennas the probe-feed positions is typically changed along the y axis. The maximum impedance is determined by the position of the probe-feed located at the edge of the patch, as already induced in figure 3.11 in section 3.3.4. The minimum available impedance is zero and is located at the center of the patch antenna element. For phased-array application with high x-pol requirements the differential feeding design from section 6.4 can be applied. Consequently, only edge feeding can be realized to inject two separated signals with 180° out of phase, especially for dual polarization applications. Straight connections of the edge probe-feeds are seldom possible due to the limited space for feeding networks, especially for dual polarization capabilities. In the following analysis the direction of the probe-feeds and their matching network below the shielding ground is rotated with  $90^{\circ}$  as shown in figure 6.19. As a consequence, the degradation of CPS becomes visible in figure 6.20.

For the differential-feed square-patch with 90° rotated connectors an CPS of only 6.2 dB was observed at  $\pm 60^{\circ}$  azimuth scan ranges and the 45°-Cuts of figure 6.20. This result is no longer comparable to the 14.2 dB from the previously designed differential-feed square patch antennas analyzed in figure 6.10. There the probe-feeds are straightly oriented and all mirror symmetries are maintained. From the not shown co-pol plot, an undesired main beam drift can also be recognized. The reason for the x-pol degradation is probably related to the asymmetric current distribution on the shielding ground below the patch. The asymmetric current distribution on the shielding ground is generated by the matching stub positions and the current disturbances during excitation process of the antenna. This source of x-pol radiation should be considered by every antenna designer when antennas with low x-pol contribution are required.

#### 6.4.6 Analysis of antenna patch size

Surprisingly, no capable reference could be found in literature where the patch antenna size was analyzed for improved x-pol pattern. For this reason the differential-feed patch antenna design from figure 6.1c was investigated in this regard. Figure 6.21 shows graphically the results of the co- and x-pol pattern for variable patch sizes from 10.32 to 10.80 mm. Table 6.1 summarizes all important design parameters, the results of realized gain at boresight direction and the CPS at  $\Theta = \pm 60^{\circ}$ .

The design example shows CPS of up to 15.50 dB at  $\Theta = \pm 60^{\circ}$ . On the other hand the realized gain stays almost constant between 5.9 dBi and 6.0 dBi. In figure 6.21 the impact on the x-pol pattern for increased patch sizes becomes visible. Inside the dashed circles the CPS will be improved. Furthermore, the dashed ellipses in upper right and left corner are showing CPS degradation. This redistribution is desirable, since the CPS at invisible space behind the antenna is not transmitted in the direction of interest. However, it must be further analyzed if the back radiation of the x-polar fields can degrade the CPS in boresight direction. The antennas simulated in this chapter are assumed to be in free space, whitout any metalic body behind the antenna. In reality, the antennas are mounted on support structures, which are typically produced by metal. The improvement of the CPS by increasing the microstrip antenna patch size is significant and can be identified as valuable tool for antenna designers to reduce the cross polarization of microstrip patch antennas in the angular reagion of interest. The x-pol radiation is moved from the pattern center area to the backside of the antenna radiation pattern. Especially for phased-array applications the x-pol improvement for intended scan ranges between  $-60^{\circ}$  and  $+60^{\circ}$  is remarkable.

In a separate experiment the GND layer of the 10.66 mm patch design was extended from  $30 \times 30$  to  $40 \times 40$  mm. The realized gain in boresight direction dropped to 5.3 dBi but

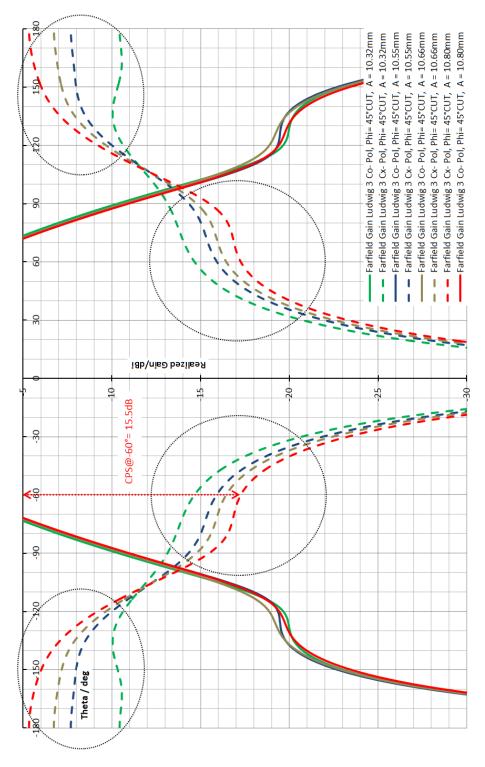


Figure 6.21: Analysis of co- and x-pol radiation pattern for differential-feed patch antennas with variable patch length. The patch length varies from 10.32 to 10.80 mm. A valuable CPS improvement can be recognized in the circles between  $\Theta = 90^{\circ}$  and  $30^{\circ}$ . The ellipses between 180° and 120° show a degradation in CPS, which is acceptable since the CPS at invisible space behind the antenna is not that important.

the CPS at  $\Theta = \pm 60^{\circ}$  became 18.34 dB. This astonishing result is interesting for single antenna applications and their designers but is not less important for phased-array applications where the GND layer and the patch to patch distance can mostly not be extended due to the occurrence of entering grating lobes.

From the results in Table 6.1 an empirical equation can be constructed for the length  $L_{\text{CPS}}^{\text{opt}}$  of a quadratic patch antenna element with optimized x-pol performance:

$$L_{\rm CPS}^{\rm opt} = K \frac{\lambda}{2\sqrt{\varepsilon_r^{\rm eff}}} = 1.12 \frac{\lambda}{2\sqrt{\frac{\varepsilon_r + 1}{2} + \frac{\varepsilon_r - 1}{2} \left[\frac{1}{1 + \sqrt{1 + \frac{12h}{W}}}\right]}}.$$
(6.2)

For patch antennas working at the dominant TM010, the edge-to-edge distance is typically  $\frac{\lambda}{2}$ . The x-pol pattern will be optimized if the patch size L is slightly enlarged with K = 1.12. The effective permittivity  $\varepsilon_r^{\text{eff}}$  for microstrip lines where the conductor width is larger than the substrate height (w > h) was found in (Hartley, 2014) and represents the part below the square root in equation 6.2.

## 6.5 Understanding the generation patch antenna xpol radiation by using the new visual based field line and surface current distribution approach

#### 6.5.1 Discussion on patch antenna cavity model

In several antenna literature references as [103] and [110], the microstrip patch antenna radiation process is explained by the well-known cavity model. The interested reader can find the detailed cavity model concept in section 3.3.3. The field distribution below the patch as illustrated in figure 3.7 generates the co- and x-pol pattern by assuming two radiating slots with distance L. The uniform field distribution over the width W and the cosine distribution over the length L for the dominant TM010 mode can be recognized. The current and charge distribution of microstrip patch antennas is presented in figure 3.6. Fringing fields from the cosine distribution along the length L are not considered by the cavity model, due to the assumption of perfect magnetic walls surrounding the volume. As a consequence, this is one source of x-pol radiation only visible in 3-D full wave analysis.

In [104] it was stated that the x-pol pattern from the cavity model does not agree with the x-pol pattern from measurements or 3-D full wave simulations. Their simulation and measurement results from single-feed antennas have only shown a single null in E-Cut and the cavity model predict nulls in E- and H-Cut.

In this section another interpretation is proposed: If the field vectors from figure 3.7 are exactly the same in intensity and 180° out of phase at the two radiating edges, the E and H-Cut can be established with two nulls like predicted from cavity model. Accordingly, the electrical field vectors are showing the same amplitude and 180° phase difference, indicated

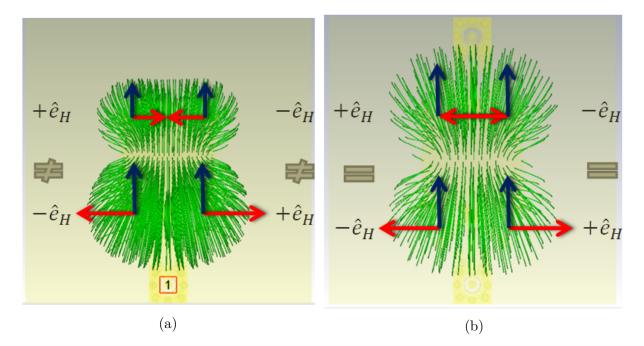


Figure 6.22: Field-line distributions: (a) Single probe-feed. (b) Differential probe-feed patch.

by the up and down direction of the electrical field vectors from figure 3.7. On the contrary, if a patch antenna will be fed by a single probe-feed like in figure 6.4, the field intensities across the length L are non-identical (see also figure 6.23). Accordingly, a x-pol pattern with only one null in the E-Cut as illustrated in figure 6.6 will be generated. From both figures it is visible that the x-pol contribution is much higher on the radiating edge side, where the probe-feed is located. This effect will now be analyzed and discussed in detail by the field line and surface current distribution approach in the sections 6.5.2 and 6.5.3.

### 6.5.2 Visual based field line distribution approach for x-pol explanation

The field line approach analyzes the field line generation process in CST MWS 3-D full wave simulation. The figures 6.23 and 6.24 are illustrating the field line distributions for single probe-feed excitation and differential excitation with two signals 180° out of phase, respectively. As mentioned before, the field intensities below the patch, across the length L is non-identical for single excitation (figure 6.23) and equal for the differential excitation (figure 6.24). The insertion loss of the path from the single probe-feed to radiating edge on the opposite side is very low and the difference in field intensity is not explained herewith. A time delay causes the field intensity differences for a given point of time. As a consequence, the field line development process on the probe-feed side is at advanced stage, with respect to the opposite side radiating edge without the feed probe. The difference in field line

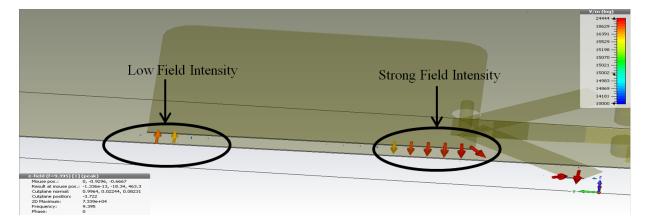


Figure 6.23: Field distribution below the patch element is different in strength and phase for single-feed patch antennas.

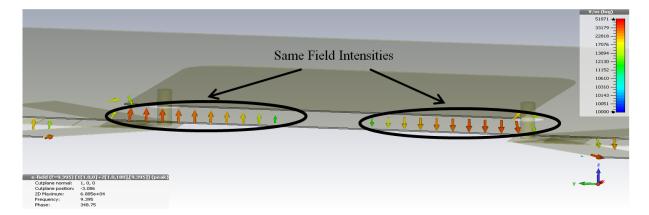


Figure 6.24: Field distribution below the patch element is equal in strength and exactly  $180^{\circ}$  out of phase for differential-feed patch antennas.

strength between the upper and lower half of the patch at a given point of time generates the higher x-pol pattern and no null in H-Cut will be produced in far field. If the x-pol contribution (generated by the field lines which are not exactly vertical (co-pol) oriented for the example in figure 6.22b of the electrical field vectors on upper and lower half of the patch) are equal in strength and  $180^{\circ}$  out of phase, the cancellation in far field takes place and the null in H-Cut will be generated. From figure 6.22b one can observe a very symmetrical and time synchronized field line development process. 3-D animations of the field line development process over a complete RF phase cycle have been shown that the opposite 180° out of phase field lines are always synchronized in time and of the same intensity. By further observing figure 6.22a and figure 6.22b, the two and four typical x-pol maxima visible in 45° and 135°-Cuts can be derived. Figure 6.22b shows the field lines with the strongest horizontal electrical vector contribution (x-pol contribution) located exactly above the 4 patch corners. Correspondingly, the very symmetric x-pol pattern with the typical four x-pol maxima over 45°-Cut and 135°-Cut will be generated as highlighted in the figures 6.7 and 6.9. The visualization of the field vectors helps to understand that the opposite x-pol vectors  $\vec{e}_{\rm H}$  (in red) must be the same of strength and exactly 180° out of phase to cancel each other out in the antenna phase center of the H-Cut. This is certainly only the case for the differential-feed antenna in figure 6.22b.

### 6.5.3 Visual based surface current distribution approach for xpol explanation

Another approach for understanding the generation process of x-pol is the observation of surface currents from microstrip patch antennas. For this approach every single current vector in the figures 6.25a to 6.25c can be interpreted as an elementary electric dipole (Hertzian Dipole) located on the patch antenna surface. By applying the right hand law, small dipole patterns are generated which add in the far field. As already discovered by the analysis of the field line approach, the mirror symmetry of field vectors is of significant importance for the reduction of x-pol radiation. The same is true for the distribution of the currents on the patch surface. Figure 6.25a shows the surface current distribution of the single-feed microstrip patch antenna. Figure 6.25b shows the current distribution on the differential-feed microstrip patch antenna, excited with two signals 180° out of phase. By thoroughly investigating the current vector directions from figure 6.25a, the different vector orientations close to the two radiating edges are unambiguous. The patch surface at the feed side shows much stronger horizontally oriented E-field vectors (x-pol). This explains the stronger x-pol radiation pattern values from figure 6.6 and the stronger field lines in figure 6.22a. Furthermore, the current distribution on the surface of the patch is not symmetrical, so that no perfect cancellation in far field can be reached for the singlefeed case. On the contrary, the current vectors from figure 6.25b and 6.25c are antipodal in direction in the region close to the two opposite probe-feeds and occur with exactly the same current strength. Because of the mirror symmetry of the current distributions at the feed areas, the radiated x-polarized electrical fields (here with horizontal content)

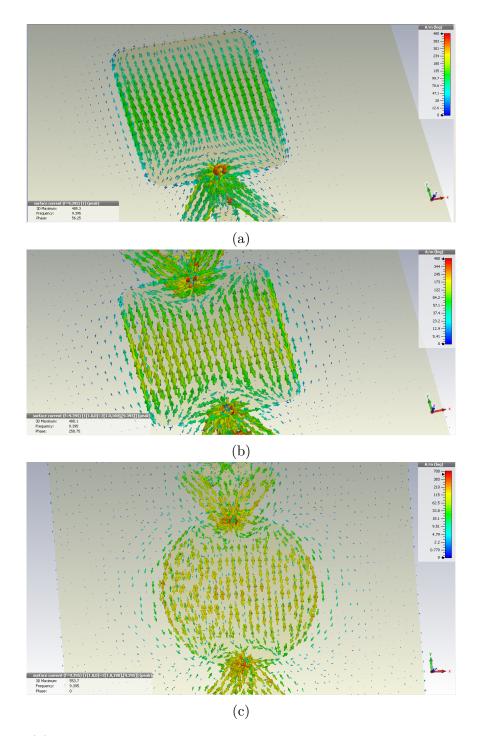


Figure 6.25: (a)Surface current distribution on single-feed, square patch antenna. (b) Surface current distribution on differential-feed, square shaped patch with two signals 180° out of phase. (c) Surface current distribution on differential-feed, circular square shaped patch with two signals 180° out of phase.

with 180° phase difference cancel each other in the far field. This explains the x-pol radiation pattern from figure 6.7 and the symmetric field line distribution in figure 6.22b. It should be stated here, that the current distribution for circular and square patches are different. Interestingly, the different surface current distributions from circular and square patch generate almost the same CPS in far field. Both current distributions are mirror symmetrical on the patch surfaces and the x-pol contributions cancel in the far field.

### 6.6 Summary of observations

The differential feeding method was verified as a valuable x-pol reduction solution from literature research for phased-array weather radar applications. Numerous feeding methods have been discussed for phased-array applications. The most beneficial feeding method is the probe-feed antenna with its relatively small ground plane via hole transition to the radiating patches. The analysis of the geometric shape of the x-pol pattern revealed that only  $45^{\circ}/135^{\circ}$ -Cuts are able to provide sufficient information for accurate cross polarization suppression measurements, since the x-pol maxima are located on the diagonal planes. The differential feeding method was verified and compared to single probe-feeding by two CST MWS modeled X-Band patch antennas. Several advantages from differential probe-feed patch antennas for phased-array applications were documented; the co-pol main beam becomes symmetric and the CPS of 14.2 dB compared to only 6.2 dB at  $\Theta = \pm 60^{\circ}$  was discovered. Furthermore, the x-pol pattern with its four maxima and exactly 180° phase difference of the two diagonal planes is advisable in order to reach reasonable x-pol far field cancellations in antenna array configurations. The analysis of potential x-pol sources in patch antenna element design has shown that resin filled, copper plated probe-feed vias and the bending of patch edges do not improve the x-pol radiation pattern. For the first time, circular and square shaped patch geometries were investigated and qualified as almost equal in CPS performance. The thorough investigation of the position of the probe-feed and its matching network below the shielding ground of the patch has shown significant x-pol degradation due to shielding ground current disturbances during the patch antenna radiation process. The improvement of the CPS by increasing the microstrip antenna patch size was identified as valuable tool for antenna designers to reduce the cross polarization of microstrip patch antennas. The x-pol radiation is moved from the center to the backside of the antenna. Especially for phased-array applications the discovered x-pol improvements for intended scan ranges stated in [115] is remarkable.

Starting from the discussion of the cavity model, two new visual based approaches with field line and surface current distributions were developed as a contribution for better understanding of the generation process of x-pol radiation from microstrip patch antennas. Finally, the reason for two and four maxima in the x-pol radiation pattern is explained with the new visual based approaches for single and differential probe-feed microstrip patch antennas.

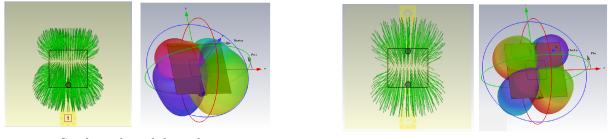
# Chapter 7

# Optimum phase excitation in limited field of view antenna arrays to reduce cross polarization radiation

From antenna theory it is known that the x-pol pattern of the antenna array is also affected by the x-pol array factor. Interestingly, the x-pol antenna array factor can be optimized by 180° out of phase excitation and mirroring the single-feed antenna radiators inside the antenna array. In consequence the optimum phase excitation distribution for the LFoV antenna arrays is investigated in this chapter for maximum CPS, not only at boresight, but also for the complete angular e-scan range.

The subarrays from the phased-array weather radar system design in chapter 5 are ordered in 4x8 lattice and are accomplished as Limited Field of View (LFoV) arrays to minimize the amount of amplitude and phased control units. The LFoV array consists of four single patch antenna elements fed with the same phase. The excitation of 4 antenna elements with the same phase is only possible because of the specified narrow elevation scan range of  $\pm 15^{\circ}$ , also called LFoV of  $\pm 15^{\circ}$ . The azimuth scan range will not be limited by the vertical combination of four patch antenna elements, so that  $\pm 60^{\circ}$  e-scan is established.

In detail, diverse phase excitation distributions, for reducing the x-pol radiation from microstrip patch antenna arrays, available from literature sources are reviewed and summarized. In section 6.4 it is shown that the patch antenna element factor can be improved in CPS by the well-known "differential feeding technique". This differential feeding technique will now be further analyzed in array configurations and compared to diverse phase excitation distributions for single-feed antenna arrays. With 3D full wave simulation results from CST MICROWAVE STUDIO (CST MWS), 1x4 and 2x4 linear antenna arrays are compared and the optimum phase excitation distribution for single-feed antenna arrays is identified. Finally the best phase excitation distribution for single-feed antennas will be applied for a 4x8 antenna subarray and compared to a differential-feed 4x8 antenna subarray. Over the e-scan azimuth range of  $\pm 60^{\circ}$ , common phase excitation distributions for single-feed antenna arrays are establishing only very poor CPS. With clever phase exci-



Single probe- fed patch

Differential probe- fed patch

Figure 7.1: Field line distribution and 3D x-pol phase pattern for single- and differential-feed patch antenna, simulated with CST MWS

tation distributions the CPS of single-feed antennas can be improved significantly. Rather providing arrays with differential-feed radiators most promising results for phased-array antennas with high CPS requirements.

### 7.1 Introduction

Microstrip patch antennas are suitable candidates for phased-array weather radar applications. These antennas are fabricated easily at low cost and known in their radiation characteristics. The array configurations in this chapter are established with probe-feed microstrip patch antennas. They are either differential or single probe-feed. In figure 7.1 the contrasting field line distribution and the x-pol radiation patterns for single and differential-feed microstrip patch antennas are visualized. Most of the x-pol contribution from the symmetric field lines of the differential-feed antenna element cancels each other in the phase center of the antenna, so that only 4 maxima of x-pol radiation appear in the area of the patch corners. Furthermore the 4 maxima are exactly  $180^{\circ}$  out of phase from one to the other diagonal axis, so that this fact can be used in array configurations to cancel the x-pol radiation of neighbored elements. Rather provides the single-feed patch antenna only poor CPS, mainly due to the x-pol radiation contributed from the probe sided edge. By comparing the 3D x-pol radiation pattern from figure 7.1 it is clear that the differential-feed antenna element seems to be the best choice for antenna array applications with high CPS requirements. But differential-feed antennas are very complicated to design. The feeding network occupies a lot of space behind the shielding ground, so that the microstrip lines must be designed very narrow and the space for mounting connectors is limited. Additionally the impedance matching of such array antennas is very complex. For implementing the TRMs on the subarray in tile structure, the feeding and the antenna matching network must be designed in stripline technology between two ground layers. The limited space in this multilayer configuration generates mutual coupling so that the amplitude and phase distribution of the antenna array would be corrupted.

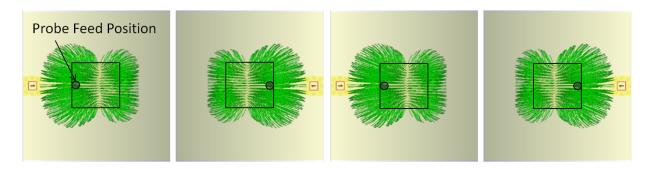


Figure 7.2: Example for phase excitation distribution for mirrored radiators in 1x4 antenna arrays. By exciting the patches at mirrored feed probe positions and/or 180° out of phase, altered x-pol sum pattern can be expected from the illustrated field lines.

For these reasons it must be investigated if mirroring of single-feed patch antenna radiators and the excitation with differential phases can be used to retrieve comparable CPS results to antenna arrays with differential feeding.

The single-feed patch antenna shows an asymmetric field line distribution. The stronger field lines and consequently stronger x-pol radiation can be observed at the radiating edge side of the probe-feed. If the probe position and the phase excitation ( $0^{\circ}$  or  $180^{\circ}$ ) are mirrored within an array, the x-pol array factor changes too. This fact can now be used to optimize the x-pol antenna array factor for adequate CPS.

Figure 7.2 shows exemplarily a 1x4 antenna array with single-feed patch antennas. From the field line distributions of these patches, altered x-pol sum patterns for different geometrical positions of the mirrored patches inside the antenna array can be expected. The squared probe-feed microstrip patch antenna designs from section 6.4 are used here for the analysis of different phase excitations from mirrored patch antenna elements in antenna arrays. The antenna design from figure 7.3 is realized with CST MWS and the element radiation patterns are simulated in 3D full wave. With the CST MWS array function the array sum pattern of the differential-feed array is calculated. All other arrays are simulated in 3D full wave.

## 7.2 Literature research about radiator configurations in array antennas to reduce x-pol radiation

A few designs of antenna arrays with different phase excitations and mirrored antenna elements have been reported in literature for optimizing the CPS. (Huayan Jin et al., 2014) presenting a differential-feed 2x2 antenna array design at Ku-Band and analyze different feeding network designs to decrease the complexity of feeding structures by constant CPS.

The authors in [120] are comparing a common single-feed 2x2 antenna array to a single-feed 2x2 antenna array with mirrored antenna elements which are excited 180° out of phase.

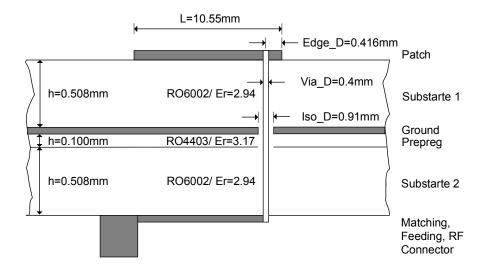


Figure 7.3: Layer set-up of squared and single-feed microstrip patch antenna design. The differential-feed antenna incorporates the same design parameters but two probe-feeds, excited  $180^{\circ}$  out of phase.

From the calculated antenna radiation pattern a significant x-pol improvement could be recognized for E- and H-Cut. 45° Cuts are not investigated. In [118] four different phase excitation distributions in dual polarized 2x2 antenna arrays are compared in order to reach optimum CPS. The best phase distribution was further applied to multiple groups of 2x2 arrays in the complete antenna array.

An antenna array demonstrator for weather radar application is published by [122], [123]. The frequency scanning antenna array design was chosen as an alternative for phased-array antennas with phase shifters. The beam steering is realized by changing the operating frequency. Two 10 element arrays are analyzed in their CPS performances and it was shown with simulation and measurement results that the CPS can again be optimized by mirroring and exciting the arrays with 180° out of phase. Unfortunately only one x-pol cut was analyzed in this publication and it is not clear if the maximum x-pol contribution can be expected in this cut. Especially in a dense network of small weather radars, frequency spectrum management becomes necessary so that frequency scanning antennas with high occupied bandwidths are not the best choice.

The authors from in [104] analyzed differential feeding on antenna element level and a 1x2 array with rotating feeding (mirroring and exciting the arrays with  $180^{\circ}$  out phase) to explain the cancellation of cross polar radiation by new near field approach.

Due to the specific LFoV design of 1x4 antenna arrays for the weather radar application published in [115], no adequate literature reference for optimum phase configurations of mirrored radiators in such arrays (1x4, 2x4 or 4x8) could be obtained. Additionally, no suitable literature reference was found in the available literature for the comparison of CPS performance of differential- and single-feed antenna arrays.

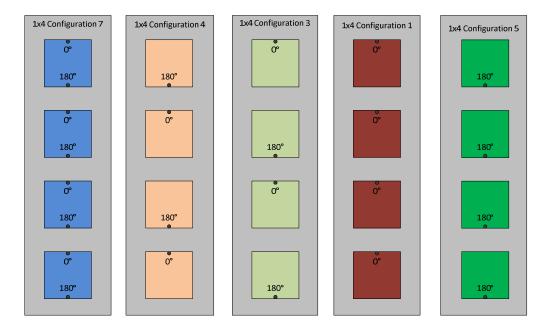


Figure 7.4: Different phase excitation distributions for mirrored elements in 1x4 antenna arrays. In blue Configuration 7 with differential-feed patch antenna elements. Orange with Configuration 4, light green with Configuration 3, red with Configuration 1 and green with Configuration 5

## 7.3 Analysis of x-pol radiation patterns for different phase excitation distributions of mirrored radiators in 1x4 antenna arrays

In figure 7.4 the five possible phase excitation distributions for 1x4 LFOV arrays are visualized. The radiators are designed as visualized in figure 7.3 and the elements are ordered with  $\frac{\lambda_0}{2}$  spacing (16mm for 9.395GHz). A single antenna establishes a realized gain in vertical polarization (co-pol) of approximately 6dBi. Only Configuration 7 (in blue) incorporates differential-feed patch antenna elements. These elements are excited simultaneously with two probe-feeds of equal input powers and 180° phase difference. Meanwhile use Configuration 4 (orange) and 3 (light green) mirrored single probe-feed patches on different mirrored positions which are excited partially 180° out of phase. In the single-feed arrays from Configuration 1 (red) and 5 (green) the elements are excited with the same phase, either all four with 0° or 180°. The 1x4 array configurations from figure 7.4 are showing different x-pol and almost equal co-pol radiation pattern in figure 7.5. The stronger develop of the nulls in the radiation pattern plots of the differential-feed array (Configuration

| Configuration   | Broadside | Max.                       | Max.                        | Max.                       | Min.               |
|-----------------|-----------|----------------------------|-----------------------------|----------------------------|--------------------|
| for 1x4 Array   | Gain      | x-pol ra-                  | x-pol ra-                   | x-pol ra-                  | CPS for            |
|                 |           | diation                    | diation                     | diation                    | $\pm 60^\circ$ az- |
|                 |           | ${f for}$ $\pm 60^{\circ}$ | ${ m for}$ $\pm 60^{\circ}$ | ${f for}$ $\pm 60^{\circ}$ | imuth              |
|                 |           | azimuth                    | azimuth                     | azimuth                    | scan               |
|                 |           | scan                       | scan                        | scan                       | range              |
|                 |           | range in                   | range in                    | range in                   |                    |
|                 |           | H-Cut                      | E-Cut                       | $45^{\circ}$ -Cut          |                    |
| Configuration 1 | 11.4dBi   | -6.8dBi                    | < -50dBi                    | -13.9dBi                   | 18.2dB             |
| Configuration 3 | 11.5dBi   | < -50dBi                   | < -50dBi                    | -19.4dBi                   | 30.9dB             |
| Configuration 4 | 11.5dBi   | < -50dBi                   | < -50dBi                    | -13.7dBi                   | 25.2dB             |
| Configuration 7 | 10.5dBi   | < -50dBi                   | < -50dBi                    | -25.4dBi                   | 35.9dB             |

Table 7.1: Broadband Gain, Max. x-pol radiation for  $\pm 60^{\circ}$  azimuth scan range in H-, E-,  $45^{\circ}$ Cut and Min. CPS for  $\pm 60^{\circ}$  azimuth scan range results retrieved from figure 7.5

7) are caused by the array calculator function of CST MWS. The differential-feed array patterns are the only ones which are calculated from single antenna element and the array factor. Consequently this array patterns are generated without considering the mutual coupling aspects. The other 1x4 array patterns are computed in 3D full wave. The results from Configuration 1 and 5 are similar by rotating their 3D results with 180°, so that only Configuration 1 will be considered for the comparison here. Configuration 5 will be later used for pattern synthesis of 2x4 arrays. From the four 3D x-pol patterns in figure 7.5 it can be recognized that the x-pol radiation is differently distributed over the upper hemisphere of the antenna array. Every array configuration provides a null in the E-Cut, meanwhile providing the H- and 45° cuts significantly different results. Configuration 1 shows a very strong x-pol radiation over the complete H-cut ( $\Phi=0^{\circ}$ ). All other configuration providing below -50 dBi x-pol radiation for the H-Cut. The best CPS can be expected from the differential-feed antenna array in Configuration 7. The CPS is below 35.9dB over the complete  $\pm 60^{\circ}$  azimuth e-scan range for the E-, H- and  $45^{\circ}$ -Cut. But also Configuration 3 shows promising results with 30.9 dB over the complete  $\pm 60^{\circ}$  azimuth e-scan range for the E-, H- and 45°-Cut. With this analysis the two most promising configurations 3 and 7 are identified and highlighted in their CPS performance in table 7.1. The boresight gain differs also for differential-feed and single-feed 1x4 arrays. The reason for this is the lower antenna efficiency of the differential-feed array, caused by the specific design. It should be noted here, that this effect is not mandatory for differential-feed antennas. The comparison of the 45° Cuts from Configuration 3 and 4 are leading to the assumption that the best CPS can be expected in the angular antenna area, where two probe-feeds are mirrored and excited with 180° phase difference. As shown in figure 7.4, Configuration 4 is mirroring the probe-feeds twice on the outside of the 1x4 array meanwhile mirrors Configuration 3 in the center of the array. Consequently Configuration 3 provides better CPS in the area of interest between  $\pm 60^{\circ}$  azimuth angles.

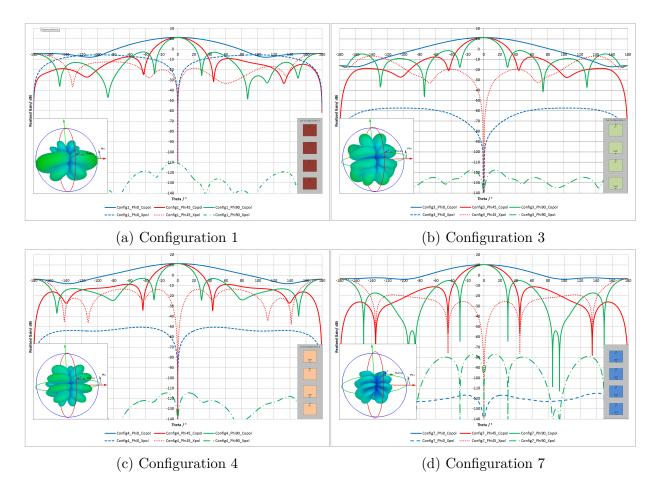


Figure 7.5: In solid lines the co-pol and in dashed lines the x-pol radiation patterns of the 1x4 arrays are shown. The blue curves are representing the H-cuts ( $\Phi=0^{\circ}$ ) and the green curves the E-Cuts ( $\Phi=90^{\circ}$ ). The red curves are expressing the diagonal cuts at  $\Phi=45^{\circ}$ . Additionally the 3D x-pol radiation patterns of the upper hemisphere of the specific arrays are visualized in the lower left corners. The specific configurations are inserted in the lower right corners. Configuration 3 shows most promising results for single-feed arrays, meanwhile provides Configuration 7 with its differential-feed array the best CPS with 35.9dB.

| Configuration    | Broadside | Max.   | Max.                        | Max.                        | Min.                 |
|------------------|-----------|--|-----------------------------|-----------------------------|----------------------|
| for 2x4 Array    | Gain      | x-pol ra-  | x-pol ra-                   | x-pol ra-                   | CPS for              |
|                  |           | diation  | diation                     | diation                     | $\pm 60^{\circ}$ az- |
|                  |           | $egin{array}{ccc} { m for} & \pm 60^{\circ} \end{array}$ | ${ m for}$ $\pm 60^{\circ}$ | ${ m for}$ $\pm 60^{\circ}$ | imuth                |
|                  |           | azimuth  | azimuth                     | azimuth                     | scan                 |
|                  |           | scan   | scan                        | scan                        | range                |
|                  |           | range in   | range in                    | range in                    |                      |
|                  |           | H-Cut  | E-Cut                       | $45^{\circ}$ -Cut           |                      |
| Configuration 11 | 13.8dBi   | -10.9dBi   | < -50dBi                    | -16.5dBi                    | 24.7dB               |
| Configuration 44 | 13.8dBi   | < -50dBi   | < -50dBi                    | -12.4dBi                    | 26.2dB               |
| Configuration 15 | 13.6dBi   | -5.4dBi  | -19.9dBi                    | -16.4dBi                    | 19.0dB               |
| Configuration 43 | 13.7dBi   | < -50dBi   | -21.2dBi                    | -17.5dBi                    | 31.2dB               |
| Configuration 33 | 13.5dBi   | < -50dBi   | < -50dBi                    | -19.6dBi                    | 33.1dB               |
| Configuration 77 | 12.5dBi   | < -50dBi   | < -50dBi                    | -24.2dBi                    | 36.7dB               |

Table 7.2: Results from 2x4 antenna array pattern from figure 7.6

# 7.4 Analysis of x-pol radiation patterns for different phase excitation distributions of mirrored radiators in 2x4 antenna arrays

In this antenna synthesis the influence of neighbored linear arrays with different configurations is investigated. The configurations from figure 7.4 are combined to six new configurations. The new configuration number indicates the combination and the antenna radiation patterns of the new combined 2x4 arrays are shown in figure 7.6. The co-pol patterns are again almost equal meanwhile are showing the 2D and 3D x-pol patterns diverging results. The combination of Configuration 1 and Configuration 5 to Configuration 15 doesn't improve the x-pol radiation compared to Configuration 11. The Configuration 43 instead improves the x-pol radiation compared to configuration 44. The Configuration 33 and 77 promising to be the best choice with results of -19.6 dBi and -24.2 dBi respectively, over the complete  $\pm 60^{\circ}$  azimuth e-scan range for the E-, H- and  $45^{\circ}$ -Cut. Furthermore it can be recognized from table 7.2 that the CPS performance of Configuration 33 is approaching those of Configuration 77. Due to the lower gain of the differential-feed array the CPS established for configuration 77 is 36.7dB. Configuration 33 provides CPS of 33.1dB. The CPS performance difference from the 1x4 array analysis was remarkable with 5dB, meanwhile provides the 2x4 array from Configuration 33 only a 3.6dB lower CPS compared to Configuration 77.

| Configuration    | Broadside | Max.   | Max.                        | Max.                        | Min.               |
|------------------|-----------|--|-----------------------------|-----------------------------|--------------------|
| for 4x8 Array    | Gain      | x-pol ra-  | x-pol ra-                   | x-pol ra-                   | CPS for            |
|                  |           | diation  | diation                     | diation                     | $\pm 60^\circ$ az- |
|                  |           | $egin{array}{ccc} { m for} & \pm 60^{\circ} \end{array}$ | ${ m for}$ $\pm 60^{\circ}$ | ${ m for}$ $\pm 60^{\circ}$ | imuth              |
|                  |           | azimuth  | azimuth                     | azimuth                     | scan               |
|                  |           | scan   | scan                        | scan                        | range              |
|                  |           | range in   | range in                    | range in                    |                    |
|                  |           | H-Cut  | E-Cut                       | $45^{\circ}$ -Cut           |                    |
| Configuration 3- | 19.1dBi   | < -50dBi   | < -50dBi                    | -26.0dBi                    | 45.1dB             |
| 4x8              |           |  |                             |                             |                    |
| Configuration 7- | 18.2dBi   | < -50dBi   | < -50dBi                    | -30.2dBi                    | 48.4dB             |
| 4x8              |           |  |                             |                             |                    |

Table 7.3: Results from 4x8 antenna array pattern in figure 7.7 for single and differential feeding configuration

# 7.5 Comparison in x-pol performance of 4x8 antenna arrays with single- and differential feeding

In the final analysis the most promising Configuration 3 and 7 are extended to 4x8 antenna arrays. As mentioned before Configuration 3 is a single-feed antenna and has shown the best CPS results for the 1x4 and 2x4 antenna array analysis. In spite of the inherent higher x-pol radiation of the single-feed radiators in Configuration 3-4x8, a remarkable CPS of 45.1dB can be established. In addition, the CPS performance compared to Configuration 7-4x8 has been shrunken to only 3.3dB. The differential-feed 4x8 antenna array from Configuration 7-4x8 provides excellent CPS results with 48.4dB. All results of this comparison are summarized in table 7.3.

# 7.6 Design considerations for single and differentialfeed 4x8 antenna arrays with dual polarization capability

The analysis of all array configurations with their phase excitations and mirrored elements for single- and differential-feed antenna arrays is a good theoretical approach to retrieve optimum CPS. For the 3D analysis from CST MWS, the feed ports are excited with phase values of exactly 0° or 180°. Commonly the feeding networks of real antennas are taking control of these phase differences between the ports by the length of striplines or microstrip lines. Significant CPS degradation and co-pol array factor changes can occur if the feeding network is not establishing the exact phases.

#### 194 CHAPTER 7. PHASE EXCITATION IN LFOV ARRAYS TO REDUCE X-POL

Especially for complex feeding networks in **dual polarized** and **differential-feed arrays**, this fact needs to be considered by every antenna designer.

Dual polarized and differential-feed arrays incorporate patch antenna radiators with 4 probe-feeds, so that the feeding network for both polarization channels becomes very complex. Such designs have to deal with limited spacing on PCB and constrains in channel isolation. Consequently, single-feed arrays are more practical and easier to design. However, the insight analysis of this publication has shown that the differential-feed arrays are the best choice for antenna with high CPS requirements.

In the phased-array weather radar application from chapter 5 the antenna subarrays of 4x8 radiators are equipped with 8 TRMs in tile structure, so that the feeding networks of a dual polarized and differential-feed arrays (like Configuration 7) must be designed in stripline technology at very limited space. Finally a very challenging multilayer antenna must be designed, where the channel isolation of both polarization paths must be optimized by constant CPS. The single-feed array in Configuration 3-4x8 is a real design alternative, since the CPS results are converging to those of the differential-feed array in Configuration 7-4x8.

### 7.7 Summary of observations

With 3D full wave simulation results from CST MWS, 1x4, 2x4, 4x8 antenna arrays are compared and the optimum phase excitation distribution of mirrored radiators in singlefeed antenna arrays was identified. The most beneficial Configuration 3 was extended to an antenna array of 4x8 radiating elements and compared to a fully differential-feed array. It was shown that mirroring single-feed patch antenna radiators and the excitation with differential phases can be used to retrieve comparable cross polarization suppression (CPS) results to antenna arrays with differential feeding. By analyzing the 3D and 2D x-pol radiation plots of the single-feed arrays, the maximum CPS could be measured on the angular positions where two probe-feeds are mirrored and excited with 180° phase difference. Antenna designers should consider the patch element mirroring in the angular area of interest for their final applications. As assumed from the very beginning, the differential-feed 4x8 array (Configuration 7-4x8) provides the best CPS results. Excellent 48.4dB CPS over the complete  $\pm 60^{\circ}$  azimuth e-scan range for the E-, H- and  $45^{\circ}$ -Cut was established. But also the single-feed patch antenna array from Configuration 3-4x8 shows remarkable CPS of 45.1dB for the same e-scan range. Furthermore it was recognized that the CPS performance difference between single and differential-feed arrays had been shrunken from 5dB for 1x4 arrays to 3.6dB for 2x4 arrays and to only 3.3 dB in 4x8 antenna arrays. Consequently, it can be expected that the CPS for single-feed arrays are further improved in larger arrays, so that comparable CPS performance to differential-feed arrays can be established.

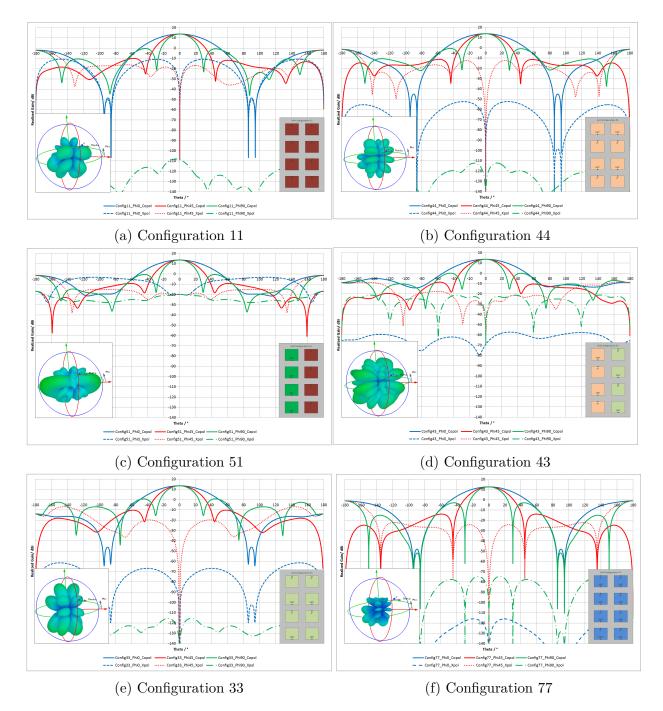
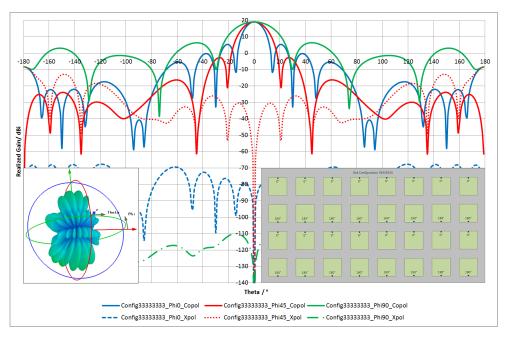
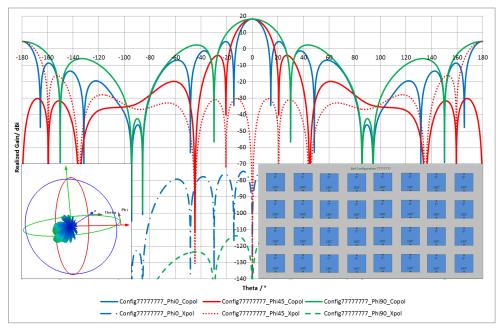


Figure 7.6: Analyzing x-pol performance for six different 2x4 antenna arrays. In solid lines the co-pol and in dashed lines the x-pol radiation patterns of the 2x4 arrays are shown. The blue curves are representing the H-cuts ( $\Phi=0^{\circ}$ ) and the green curves the E-Cuts ( $\Phi=90^{\circ}$ ). The red curves are expressing the diagonal cuts at  $\Phi=45^{\circ}$ . Additionally the 3D x-pol radiation patterns of the upper hemisphere of the specific arrays are visualized in the lower left corners. The specific configurations are inserted in the lower right corners



(a) Configuration 3-4x8



(b) Configuration 7-4x8

Figure 7.7: Antenna pattern synthesis of single-feed 4x8 antenna array with its optimum phase distribution and mirrored elements compared to a differential-feed 4x8 antenna array. In solid lines the co-pol and in dashed lines the x-pol radiation patterns of the 4x8 arrays are shown. The blue curves are representing the H-cuts ( $\Phi=0^{\circ}$ ) and the green curves the E-Cuts ( $\Phi=90^{\circ}$ ). The red curves are expressing the diagonal cuts at  $\Phi=45^{\circ}$ . Additionally the 3D x-pol radiation patterns of the upper hemisphere of the specific arrays are visualized in the lower left corners. The specific configurations are inserted in the lower right corners.

# Chapter 8

# Development, design and verification of dual polarized antennas with optimized cross polarization pattern for phased-array weather radar applications

### 8.1 Introduction

This chapter utilizes all theoretical and practical design considerations of microstrip antennas discovered in the previous chapters in order to built-up an antenna array with high polarization purity for phased-array weather radar applications.

Two types (the single- and differential-feed arrays) of antenna designs are developed, designed and characterized in this chapter. The antenna radiation patterns have been measured at the RWTH Aachen compact antenna test range (CATR). Due to the very low x-pol of the antennas the CATR has been evaluated in its performance previously. Consequently, details about the quiet zone verification, the CATR accuracy and the AUT system for active phased-array antenna measurements are given in section 8.2.

During the first design step, a single radiator made by a mircostrip patch antenna has been developed with single- and differential feeding. These single radiators are basically single polarized and finally equipped with dual polarization capability.

Subsequently, an optimum phase excited single-feed antenna array and a differential-feed antenna array have been developed and compared in their x-pol performances. Both antenna types are built as multilayer PCB in a 4x8 radiator matrix. The antenna radiation patterns are measured in active phased-array mode in the CATR. Finally, the radiation performances are investigated for boresight, but also during beam steering for up to four beam positions.

## 8.2 Antenna verification at RWTH Aachen Compact Antenna Test Range

The performance of the microstrip patch antenna prototypes has been verified at the Compact Antenna Test Range (CATR) facility of the RWTH Aachen.

Generally, a compact range is used to measure the antenna characteristics at very short distances between AUT and the feed antenna. As induced in figure 3.3 the minimum far field measurement distance is defined by  $\frac{2D^2}{\lambda}$ . The CATR is not limited by this definition. The CATR converts a spherical wave to plane wave in order to establish very accurate antenna measurements in an isolated anechoic chamber at very short distances. Typically, the feed antenna illuminates one or two reflectors to establish a plane wave front in the measurement quiet zone. A picture of the RWTH Aachen CATR is shown in figure 8.1. The RWTH Aachen CATR uses one reflector to convert a spherical wave to a plane wave. The reflector is produced with maximum surface accuracy to avoid unwanted x-polar radiation and phase- and amplitude ripple inside the measurement quiet zone. Additionally, the edges of the reflector are equipped with serrations to avoid measurement errors induced by wave diffraction. The quiet zone is the area in which the AUT will be characterized and measured. The inner walls of the CATR are covered with absorbing materials to avoid multipath radiation and reflections. All antenna measurements in this work are carried out by spherical rotation of the AUT in the quiet zone area to fulfill Ludwig's third definition of polarization [113]. The technical specifications of the RWTH Aachen CATR derived from [127] are listed next.

#### Technical specification of the RWTH Aachen CATR:

#### **Frequency Range:**

- Compact antenna test range: 2 75 GHz
- Spherical near field range: 800 MHz 12 GHz
- Radar cross section test facility: 2 GHz 18 GHz

#### Quiet Zone:

- Cylindircal, 1.2m diameter, 1.2 m long
- Amplitude ripple:  $\leq \pm 0.4$  dB at 10 GHz
- Phase ripple:  $\leq \pm 2^{\circ}$
- Cross-polar level:  $\leq \pm$  -35 dB at 10 GHz. Depending on antenna dimension!

#### AUT Positioner:

- Axis: Roll-over-Azimuth plus elevation squint and pick-up,
- Accuracy:  $\leq \pm 0.03^{\circ}$ ,
- Max. AUT mass: 100 kg

#### 8.2. ANTENNA VERIFICATION AT RWTH AACHEN CATR

- Cross-range slide: 1.2 m travel for classical AUT-positioner in azimuth
- Optional: Dielectric tower for low-gain antennas up to 12 kg

#### **RF** Instrumentation:

- Rohde&Schwarz ZVA24 VNA as LO source and receiver
- Rohde&Schwarz SMF100A as RF source at feed antenna
- Agilent 85309A LO/IF Distribution Unit and 85320 series mixers.

#### Measurement Dynamic Range:

• 100 dB (at 10 GHz)

#### Shielded Anechoic Room:

• 5 m x 5 m x 9 m

#### Control and Post-processing Software:

• Active Cell 4 by Orbit/FR Europe

#### 8.2.1 Quiet zone investigation

Due to the limited surface accuracy of the reflector, the x-polar contribution of the illuminating feed, the reflections at the walls and all other objects in the anechoic chamber the quiet zone characteristics must be verified before the antenna measurement campaign takes place. Fortunately, the quiet zone was already investigated at the center frequency of 10 GHz for horizontal polarization state by the measurement experts from RWTH. The results of this investigation are exposed in figure 8.2. The x-pol amplitude inside the quiet zone of 40 cm x 40 cm is presented in figure 8.2a. The maximum dimension of the antenna prototypes within this work is of 15 cm x 15 cm. As a consequence, the quiet zone window can be reduced to these dimensions to evaluate the x-pol contribution for the antenna measurement campaign. As shown in the inner (white) window of figure 8.2a a x-pol contribution of approximately -45 dB can be expected at 10 GHz. This value defines the minimum x-polar level at the center frequency of 10 GHz, which can be measured in this CATR. The co-polar (horizontal polarization state) amplitude measurement accuracy of  $\pm 0.2$  dB and the phase accuracy of  $\pm 2^{\circ}$  can be expected in the quiet zone window of 15 cm x 15 cm.

The operating frequency (9395 MHz) of the antenna prototypes is very close to the observation frequency of 10 GHz, so that comparable results for the x-polar contribution and the amplitude- and phase ripple can be expected. However, the quiet zone was also qualified for the center frequency of 9395 MHz with a standard gain horn with low x-polar suppression of approximately -44 dB at the center of the main lobe. In the figures 8.3a

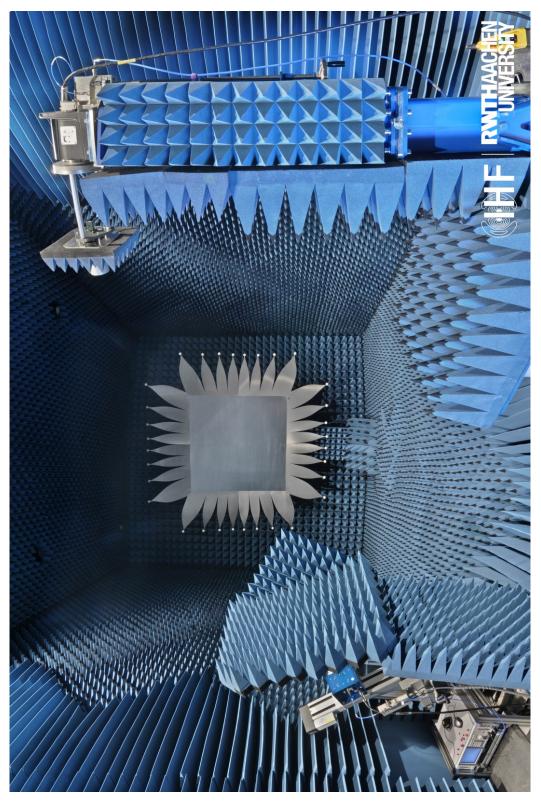


Figure 8.1: RWTH Compact range measurement overview [127]

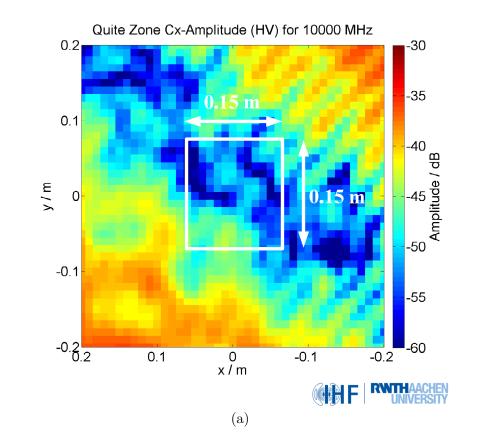
and 8.3b the results of this evaluation tests are presented. Figure 8.3b shows the radiation patterns of measured antenna horn with its E,H, 45°- and 135°- Cuts. The absolut values of the x-pol fields have been measured with -44dB for the  $\phi = 45^{\circ}$ ,  $\phi = 90^{\circ}$  and  $\phi = 135^{\circ}$ -Cut. Only the  $\phi = 0^{\circ}$ -Cut shows a lower values of approximately -47.7 dB. The absolute value of the CATR x-pol contribution was unfortunately not determined by this evaluation test, since the CATR contributes less x-pol radiation than the tested horn antenna with -44dB. Consequently, it can only be stated that the x-pol contribution of the RWTH Aachen CATR is below -44dB for the center frequency of 9.395 GHz in the quiet zone area of 15 cm x 15 cm. Results of x-polar measurements below this value of -44dB should be interpreted with care. As shown in figure 8.3b a measurement accuracy of  $\pm$  2.5 dB can be expected for the determination of the x-polar fields in the quiet zone area of 15 cm x 15 cm.

Especially during the first two days of the five days measurement campaign a lot of attention has been paid on the reproducibility of the measurements. A very meaningful compact range test (internally called "flip test") is the rotation of the AUT by 90° and a repetition of the angular scan after a period of time. In this case, the flip test was carried out with a time gap of 20 minutes. The test has shown that the co-polar measurements are perfectly matched with an accuracy below  $\pm 0.1$  dB over the complete scan range. The consecutive x-polar measurements are showing the nulls at different angular positions so that the absolute values should not be compared directly. Furthermore, it is reasonable to compare the CPS over a defined angular range from the two consecutive measurement. The reproducibility measurement of the CPS for the scan range of  $\pm$  90° was evaluated with approximately  $\pm$  1.5 dB. With this easy test the reproducibility over time and the stability condition of the quiet zone and the complete CATR was determined.

#### 8.2.2 CATR set-up for phased-array antenna operation

The measurement set-up of the active phased-array antenna system inside the CATR is presented in figure 8.4a. A picture and a technical drawing of the active phased-array antenna system is shown separately in figure 8.4b. The active phased-array antenna system under test has been installed on the roll- and azimuth positioner. The active phased-array antenna system under test was fed by the output signal of a VNA, i.e. the AUT was operated in transmit mode and used to illuminate the parabolic reflector of the CATR. The feed horn (located at the right side of figure 8.4a) was used as receiving antenna. The output signal of the receiving antenna was connected to the other port of the VNA to perform a transmission measurement in continuous-wave mode. The sample bandwidth of the VNA was selected with 100 Hz to establish an adequate signal to noise ratio (SNR) of 20 dB for x-polar measurements.

The active phased-array antenna system consists of a phase- and amplitude RF distribution network, RF absorbers, cables and a holding structure created by ROHACELL 31HF. A detailed description of the phase- and amplitude distribution network is given in appendix A1, [128] and [129]. The phase- and amplitude distribution network provides 8 amplitude



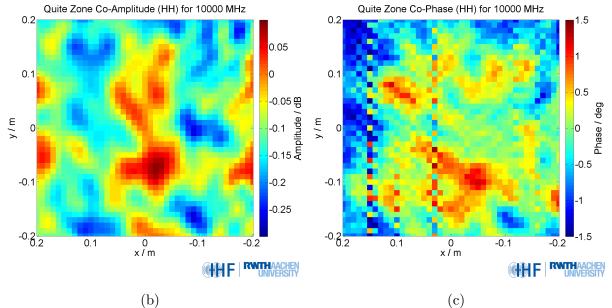


Figure 8.2: Quiet Zone characteristics of RWTH Aachen compact range provided by [127]: (a) Compact range x-pol contribution for horizontal polarization state in the quiet zone area at 10 GHz. (b) Co-polar amplitude ripple for horizontal polarization state in the quiet zone area at 10 GHz. (c) Phase variation for horizontal polarization state in the quiet zone area at 10 GHz.

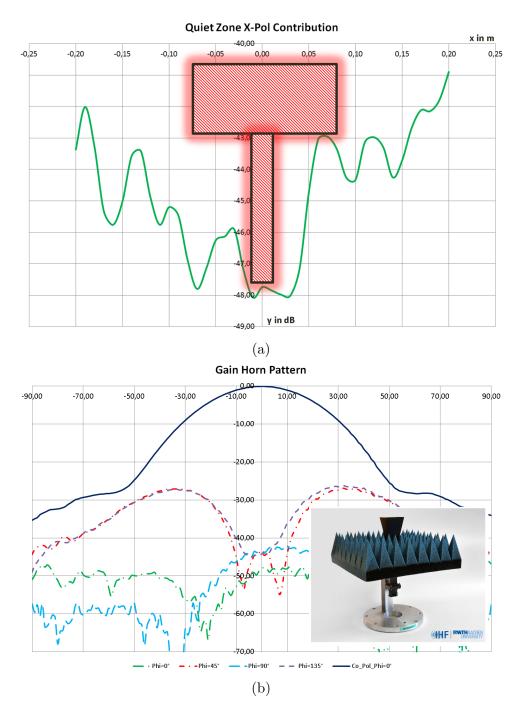


Figure 8.3: (a)Quiet zone x-pol contribution for  $\pm 25$  cm x-axis scan at 9.395 GHz. The measurement was performed with a standard gain horn. (b) E-, H-, 45°- and 135°-Cut of the standard gain horn pattern, measured in the compact range at 9.395 GHz. In the right lower corner a picture of the standard gain horn is given. Approximately -44dB to -48dB x-polar level has been measured.

and phase-variable RF signals at the operating frequency of 9395 MHz. Since most of the antenna test ranges are not able to provide multiple RF signals with variable amplitudes and phases, this unit has been developed. The pyramidal RF absorbers with reflectivity values of -45 dB have been implemented on a metal plate in order to shadow the cables and the phase- and amplitude distribution network during the antenna measurements. This action was necessary to reduce the backscattered energy by metallic units behind the antenna structure. The boundary condition in CST MWS assumes vacuum permittivity in the close environment of the antenna structure. Consequently, the different antenna prototypes have been implemented in a ROHACELL 31 HF adapter. The adapter was produced by a milling machine, which is typically used to mill metal. A manufacturing tolerance of approximately  $\pm 0.2$  mm has been established for this adapter. The dielectric constant of  $\epsilon_r = 1.0046$  has been selected to establish an equivalent RF environment as assumed by the boundary conditions in the CST MWS simulations. In order to retrieve comparable results for electromagnetic field simulations and CATR measurements, any metallic holding structures in the area of the antenna structure has been avoided. The cables are centered behind the antenna array in an acrylic glass cylinder to mitigate electromagnetic disturbances. Additionally, this cylinder was equipped with flat RF absorber material. The 8 RF cables are fed by the amplitude and phase distribution network and connected to the separate antenna rows of the 4x8 antenna arrays.

### 8.3 Discussion on antenna specification

Table 8.1 gives the specification values of the phased-array antenna concept developed in chapter 5. The most challenging goal for the antenna development is the low x-pol contribution of the microstrip patch antenna array for the scan travelling range of 120° azimuth and 30° elevation. In the references [69], the minimum CPS of -40dB for weather radars is stated. But also other specifications like beam travelling range, bandwidth, sidelobe suppression should be met.

In section 3.4.5 the polarization aspects for dual polarized planar phased-array antennas are addressed by a literature research. By recalling the most important statements of this research, in [64] it is stated the observation of polarimetric variables with electronically steered antenna can cause measurement biases that are comparable or even larger than the intrinsic polarimetric characteristics of hydrometeors. In the references [69] it was calculated that the channel imbalances (complex gain and phase imbalances between H and V channel) should be below 0.05 dB and the channel isolation (cross-coupling between H and V channel) over 40 dB, to establish a ZDR bias below 0.1 dB.

### 8.4 The phased-array antenna design process

Figure 8.5 shows the antenna development chart for the antenna arrays developed in this chapter. The development chart also highlights the low x-pol contribution for weather

#### 8.4. THE PHASED-ARRAY ANTENNA DESIGN PROCESS

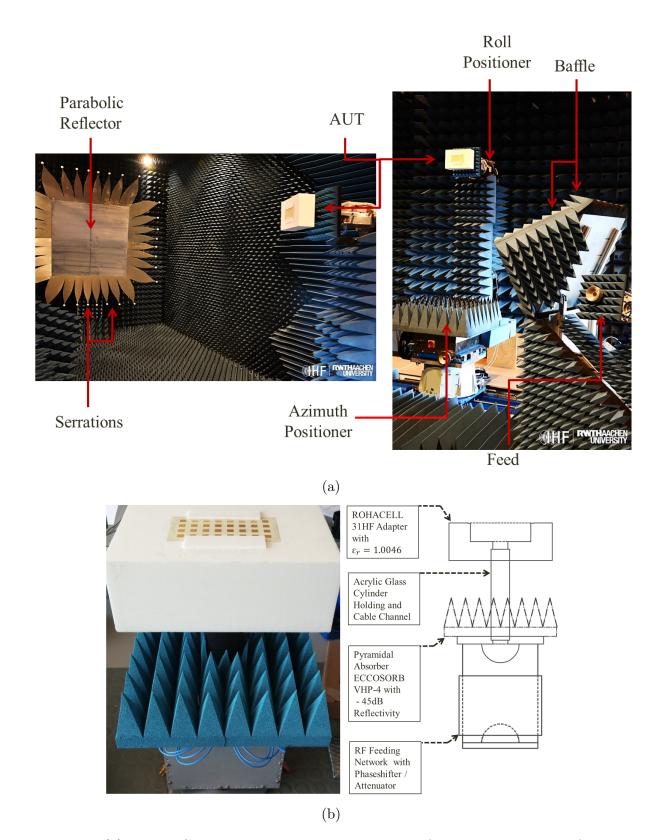


Figure 8.4: (a) RWTH Compact range measurement set-up for the measurement of phasedarray antenna radiation pattern. (b) Set-up of the antenna system under test.

| Attribute                                      | Value                                  | Status               |
|--|--|----------------------|
| Tuning Bandwidth:                              | 200 MHz (9.3 to 9.5 GHz)               | defined with [6]     |
| Demonstrator frequency:                        | $9.395 \text{ GHz} \pm 15 \text{ MHz}$ | defined with [6]     |
| Architecture:                                  | 2D Phased-Array with TRMs              | Defined              |
| Subarray concept:                              | 1:4 LFoV                               | Defined in 5         |
| Number of elements in one                      | 25600                                  | calculated           |
| planar antenna array:                          |  | in 5.2               |
| Number of elements located<br>on one Subarray: | 32                                     | Defined in 5.2       |
| Number of Subarrays:                           | 800                                    | calculated<br>in 5.2 |
| Patch element shape:                           | Squared                                | Defined in $5.2$     |
| Patch element feed:                            | Probe-feed                             | Defined in $6.3$     |
| Substrate Dielectric $\epsilon_r$ :            | 3.66                                   | Defined              |
| Subarray grid form:                            | Rectangular                            | Defined              |
| Polarization mode:                             | ATAR                                   | Defined 5.2          |
| On axis CPS:                                   | 40 dB min.                             | Defined in<br>[69]   |
| CPS at $\Theta_0 = \pm 60^\circ$ :             | 40 dB min.                             | Defined in<br>[69]   |
| Max. Antenna Element In-<br>put Power:         | 560 mW                                 | calculated<br>in 5.2 |
| TRM output power:                              | 2.5 W                                  | calculated<br>in 5.2 |
| Broadside Antenna Gain:                        | 45.8 dBi                               | using eq. $5.1$      |
| Antenna Gain at $\pm$ 60°:                     | 42.6 dBi                               | using eq. 5.1        |
| Broadside Beamwidth:                           | 1°                                     | using eqn 3.72       |
| Beamwidth at $\pm$ 60°:                        | $2^{\circ}$                            | defined in $5.2$     |
| Azimuth Travelling Range                       | 120°                                   | defined in $5.2$     |
| for 2D planar antenna:                         |  |                      |
| Elevation Travelling Range                     | 30°                                    | defined in $5.2$     |
| for 2D planar antenna:                         |  | Simulated            |
|  |  | in 5.3               |
| Sidelobe Suppression:                          | <-32dB                                 | defined in $5.2$     |
| Antenna Dimensions:                            | 2.7 m x 2.7 m                          | using eq. $3.71$     |

Table 8.1: Antenna Specification Parameter

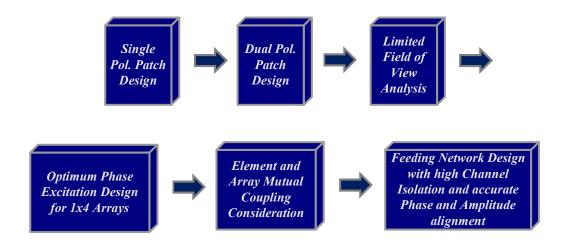


Figure 8.5: Development chart from phased-array antennas in weather radar applications with dual polarization capability, limited field of view approach and a very low x-pol contribution.

radar application in dense networks and the limited field of view configuration, due to the limited scan range in elevation.

At the very beginning of the design process a simple microstrip patch antenna has been designed with CST MWS. The antenna prototype is single polarized and the shape of the radiator is chosen to be squared. A probe-feed is selected to reduce x-pol contribution from the via- feed, as thoroughly investigated and detailed in section 6.3. Furthermore, a second ground layer is implemented between the patch and the feeding network layer to further reduce the influence of current distortion below the resonating patch area, as narrated in section 6.4.5.

After impedance- and x-pol pattern matching obtained from several optimization runs (performed by CST MWS transient solver), the single polarized patch has been adapted to a dual polarized patch antenna. This design step is easy to establish for the single-feed microstrip patch antenna; but was more challenging for the antenna counterpart with differential feeding. The differential-feed patch antenna has been equipped with four probe-feeds, in order to provide two RF- signals, which are 180° out of phase for horizontal and vertical polarization channel. The 180° phase difference between the adjacent probe-feeds is established by the differences in electrical lengths of the micostrip lines. In order to provide optimum CPS, as narrated in section 6.5, the same amplitude weights must be provided at the adjacent feeding ports. For this reason, a T-Junction power divider has been implemented on the feeding network layer of the PCB. To evaluate the single and the differential-feed stand-alone patch antenna design, the feeding network layers are equipped with  $\frac{\lambda}{4}$ - transformer and very small (4 mm x 4mm) SMP connectors.

The 3D model of the SMP connector was also implemented in the 3D field simulation from CST MWS in order to match the simulation model with the real antenna design set-up.

In the next design step the limited field of view analysis should be performed. The LFoV analysis is performed in chapter 5 for the phased-array weather radar application in a dense network of multiple small X-Band radars. As detailed in chapter 5 it is reasonable to combine a number of radiating elements to a subarray, if the scan travelling range of the phased-array antenna main beam can be limited (also called, Limited Field of View). In this way, the number of control units (phase shifters or complete TRMs) and the costs of the antenna arrays can be decreased. For the phased-array weather radar system concept, developed in chapter 5, the main beam travelling range is limited to 30° in elevation. Consequently, four vertically oriented radiating elements can be combined (fed with the same phase), in order to generate a new subarray pattern (also called subarray pattern) where 30° beam steering can still be performed.

The dual polarized patch antennas (the single-feeds with 2 feeds per polarization and the differential-feeds with 4 feeds per polarization)) are extended to 1x4 antenna arrays. All four antenna elements are fed with the same phase. For the single-feed antenna array the optimum phase distribution and the optimum positions of the mirrored antenna feeds inside the 1x4 and 4x8 antenna grids are identified. The detailed investigation about optimum phase excitation of mirrored elements is given in chapter 7. The best performing configuration 3 from figure 7.4 was selected for the design treated in this chapter.

During the development and the design process of the 1x4 single-feeds and differential-feeds antenna arrays, the mutual coupling effect of the neighboring elements could be recognized. Depending on the geometrical position of the single radiator inside the 1x4 antenna array, two groups of elements are identified for the impedance- and mutual coupling matching. The two edge-located elements inside the 1x4 antenna array are showing almost the same resonance behavior as the stand-alone antenna design, but the inner ones are showing significant resonance drifts. As a consequence, the inner patches have been matched in the new environmental conditions, with neighboring elements.

Another mutual coupling effect has been noticed when the 1x4 array was extended to the 4x8 antenna array. Here, four different groups of patches and two different groups of 1x4 arrays have been identified for the impedance- and mutual coupling matching. All of them are matched by using the optimization run function of CST MWS. The CST MWS optimization run function allows defining a set of variables. Consequently, the matching of patch elements at different positions could be performed simultaneously and the simulation time could be used efficiently.

The final step of the antenna development process is the design of the feeding network. In particular, the limited spacing on the PCB layer must be considered. In order to save space, the antenna ports are matched to  $100\Omega$  wave impedance. In this way, the width of the microstrip lines could be kept small. Another action to save space on the PCB layer

was the proper routing of the 1:8 corporate feeding networks. Here, the neighboring feeding networks are designed differently, in order to provide sufficient spacing and consequently high isolation between the polarization channels. This is especially challenging for the differential-feed antenna arrays. The feeding networks for the differential-feed arrays are separated by drilled copper walls. In order to maintain equal phases at the reference ports, every feeding network was simulated at the final geometrical position on the PCB. If the phases are not maintained, the x-pol performance will be decreased.

## 8.5 Development and design of a single probe-feed dual polarized microstrip patch antenna

# 8.5.1 Design overview of the single probe-feed dual polarized microstrip patch antenna

The dual polarized, squared and probe-feed microstrip patch antenna was designed and simulated with CST MWS. The antenna set-up and the constructed dual polarized microstrip patch antenna prototype are shown in figure 8.6a.

The patch antenna consists of two RO4350B substrates (dark blue in figure 8.6a) with  $\varepsilon_r = 3.66, 750 \ \mu\text{m}$  and 254  $\mu\text{m}$  heights and a good dissipation factor tan  $\delta = 0.004$  for adequate antenna efficiency performances. The upper layer is selected with 750  $\mu\text{m}$  to provide the required bandwidth of approximately 250 MHz. The center layer in figure 8.6a represents the RO4450F prepreg with  $\varepsilon_r = 3.52$  and 200 $\mu$ m height. This RO4450F prepreg is used to combine the two RO4350 laminates during the compression process. For suppressing unwanted surface currents or propagation channels within the substrate right from the design beginning, the RO4450F prepreg, with only small  $\varepsilon_r$  difference compared to RO4350 substrate, was choosen. The copper has a thickness of 42  $\mu$ m and the diameter of the isolation circle inside the shielding ground for the probe-feed transition is 1.2 mm.

The radiating square patches with 8.50 mm edge length, probe-via diameter of 0.5 mm and 0.55 mm probe-via-to-edge-distance are designed for a resonance frequency of 9.395 GHz. The investigation of x-pol sources in chapter 6 has shown significant degradation of CPS performance when the signal routing of the feeding network is established directly below the patch. As a consequence, two ground planes are implemented in the new patch antenna design. The second ground plane provides additional isolation between the feeding network and the resonance structure of the patch antenna. The Rosenberger 3-D connector model was completely integrated in the CST MWS full wave simulation and impedance matched with GND vias to the 50 $\Omega$  line impedance. The patch antennas impedance reference point in front of the probe-feed is matched to 100 $\Omega$ , which is necessary for the complex feeding network design in array configurations as detailed in the sections 8.7 and 8.8. For single patch antenna operation the 100 $\Omega$  patch antenna wave impedance is matched by a quarter wavelength impedance transformer to the 50 $\Omega$  line impedance in front of the Rosenberger connector.

Ground vias are implemented around the probe-feed. In this way the maximum RF power is passed to the surface of the patch and unwanted surface waves on the lower RO4350 layer are mitigated and the total antenna efficiency could be increased. Furthermore, mutual coupling between neighboring elements in array configurations are avoided.

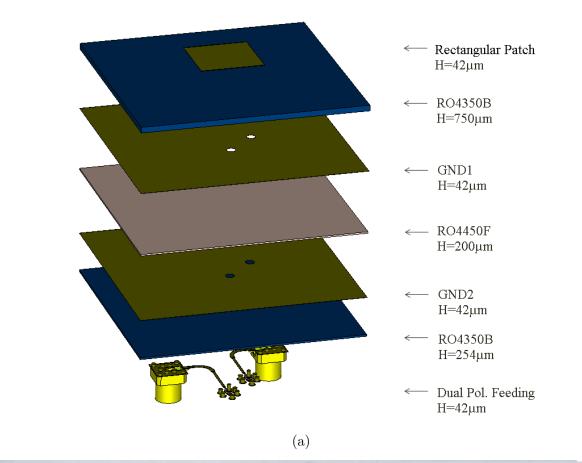
Typically, the patch antenna impedance is matched by the variation of the probe-feed position along the resonating structure of the patch or by quarter wavelength stub located close the probe-feed. But both approaches are not suitable for the design of dual polarized patch antennas with low x-pol contributions and high channel isolation. For this reason, the patch antenna was matched by a short circuit very close the probe-feed. The short circuit reflects all RF energy to the surface of the patch antenna so that unwanted radiation and surface waves at the lower substrate layer can be avoided.

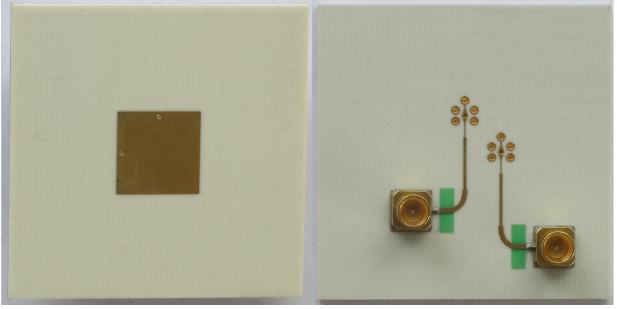
The picture of the constructed patch is given in figure 8.6b. The two antenna feeds and the two implemented sub-miniature push-on (SMP) Rosenberger connectors for dual polarization capability are also shown in figure 8.6b. To protect the multilayer PCB surface against corrosion the copper structures are plated with 5 micros of gold-nickel (Au/Ni). The rectangular areas in green color are solder resist, necessary for the installation of the SMP connectors. The solder pad of the connector occupies only 4 mm x 4 mm. The small size of these connectors is important for array applications with dense feeding networks.

#### 8.5.2 Discussion of the results

The simulated (dashed lines) and measured (solid lines) S-Parameters of the dual polarized patch antenna of figure 8.6 are both given in figure 8.7. The simulated and measured S-Parameters are very well correlated. Even the frequency response between 9 GHz and 10 GHz of the S21 has been measured and found to be in perfect agreement. The measured isolation of the two polarization channels is insufficient with approximately 12 dB for the phased-array weather radar application. But later it will be shown, how the isolation of single-feed antennas can significantly be increased by a proper design of the feeding network. However, the simulated and measured S11 values for both polarization channels are in very good agreement. The S22 of the vertical channel differs with only 20 MHz, which corresponds to a design accuracy of 99.78 %.

The CST MWS simulated 3D antenna radiation patterns are visualized in figure 8.8. The co-polar patterns are showing realized gain values of 5.65 dBi for the horizontal and 5.80 dBi for the vertical polarization planes. The radiation efficiency of this antenna is approximately 82 % for both polarizations. The total antenna efficiency is only 74 %, due to the lacking polarization purity of the single-feed antenna and the mismatch losses. The x-pol patterns are showing no nulls in the E- or in the H- cut as expected from the theoretical observations in section 6.4. The main reason for the missing nulls is the inadequate isolation of approximately 12 dB between the H- and V- channel. Due to the poor isolation the x-pol radiation has been increased significantly.





(b)

Figure 8.6: (a) Antenna set-up established with CST MWS.(b) Constructed dual polarized microstrip patch antenna element with conventional probe-feeding.

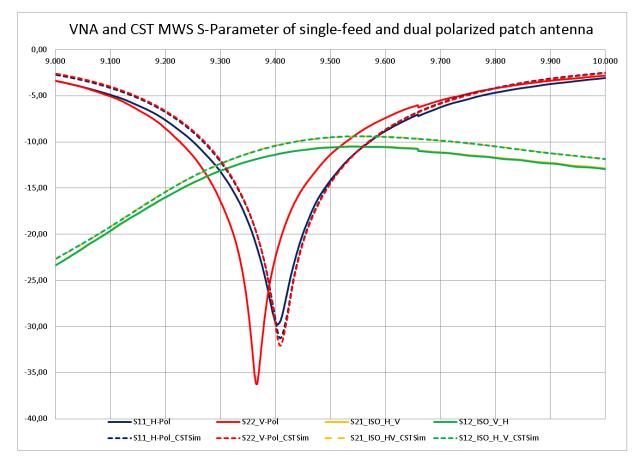


Figure 8.7: VNA measured (solid lines) and CST MWS simulated (dashed lines) S-Parameter.

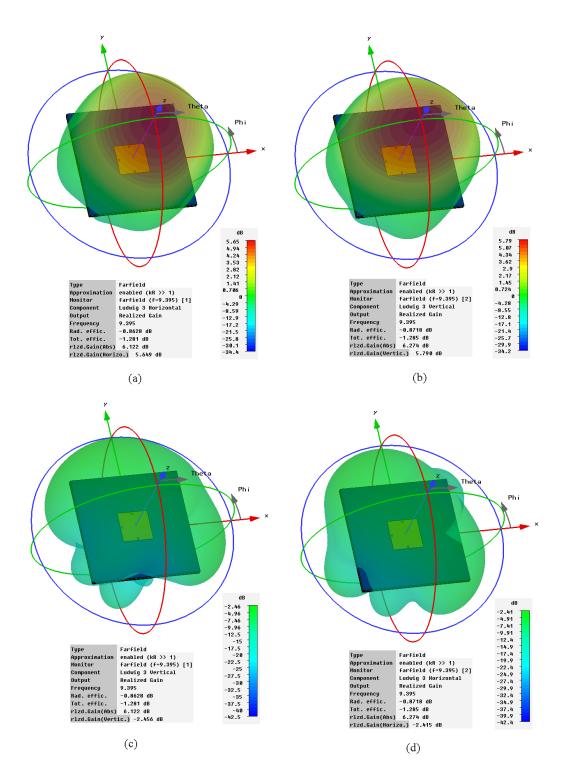


Figure 8.8: CST MWS simulated 3D antenna radiation pattern for horizontal and vertical polarization. (a) Co-polar plot for horizontal polarization. (b) Co-polar plot for vertical polarization. (c) X-polar plot for horizontal polarization. (d) X-polar plot for vertical polarization.

The detailed comparison of the measured and simulated antenna radiation pattern can be performed with figure 8.9 and figure 8.10. In figure 8.9a the Compact range and in figure 8.9b CST MWS results for the horizontal polarization are shown. In figure figure 8.10a the Compact range and in figure 8.10b) CST MWS results for the vertical polarization are shown. The agreement between CST MWS simulations and CATR measurements is very good. The graphs of the measured and simulated co-polar element patterns are perfectly matched. As expected, from previous investigations in chapter 6, the x-pol maximum is located near the probe-feed position. A very poor CPS at boresight of only 12 dB has been measured for this single-feed patch antenna element. But, as detailed in chapter 7, this single-feed antenna element will be used with optimum phase excitation and mirrored elements in a subarray of 32 elements to decrease the x-polar radiation.

Interestingly, the VNA measured channel isolation of S21=12 dB is in perfect agreement to the measured CPS at boresight direction with 12 dB. The VNA measurement can be used to get a very good estimate about the x-pol performance of an antenna at boresight direction. In this way, the costs for complex x-pol measurements at antenna measurement facilities can be saved for the first antenna verification. Furthermore, every small patch antenna can be evaluated simply via VNA measurements. Also the simulated S21 and the simulated CPS at antenna boresight are showing conformity with 10 dB. As a consequence, it can be stated that two separated evaluation methods (simulation and measurement) are showing a consistent correlation between S21 and boresight CPS performance.

## 8.6 Development and design of a differential-feed and dual polarized microstrip patch antenna

### 8.6.1 Design overview of the single differential-feed dual polarized microstrip patch antenna

The dual-polarized, differential-feed and squared microstrip patch antenna has been designed and simulated with CST MWS. The CST MWS antenna set-up and the constructed dual polarized microstrip patch antenna prototype are shown in figure 8.11a and figure 8.11b, respectively.

The single-feed antenna detailed in section 8.5 was used as a template for the design of the differential-feed antenna in this section. In order to give the interested reader the complete information of the antenna set-up and the performed design steps, some of the information content from section 8.5 must be recalled/repeated.

The patch antenna consists of two RO4350B substrates (dark blue in figure 8.11a) with  $\varepsilon_r = 3.66, 750 \ \mu\text{m}$  and 254  $\mu\text{m}$  heights and a good dissipation factor tan  $\delta = 0.004$  for adequate antenna efficiency performances. The upper layer is selected with 750  $\mu\text{m}$  to provide the required bandwidth of approximately 250 MHz. The centered layer in figure 8.11a represents the RO4450F prepreg with  $\varepsilon_r = 3.52$  and 200 $\mu$ m height. This RO4450F prepreg is

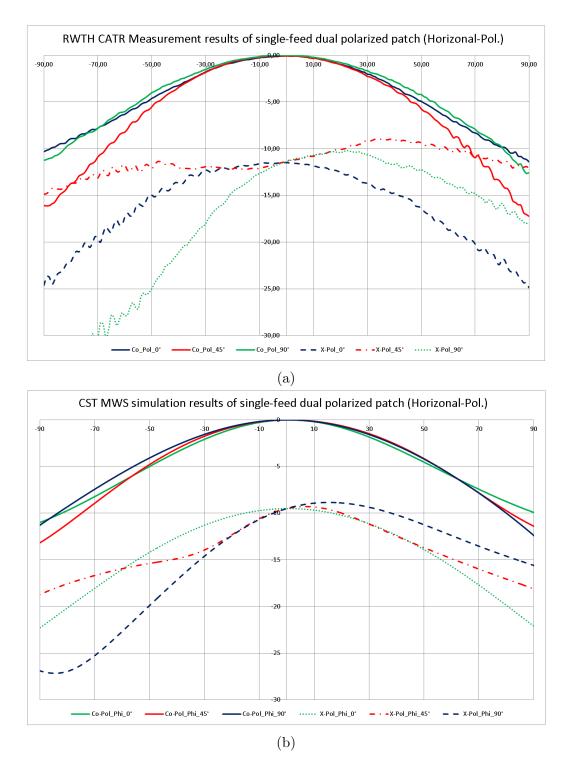


Figure 8.9: (a) Compact range and (b) CST MWS results for horizontal polarization. The copolar (solid lines) and x-polar (dashed lines) antenna radiation pattern Cuts for  $\phi=0^{\circ}$  in green,  $\phi=-45^{\circ}$  in red and  $\phi=90^{\circ}$  in blue are shown.

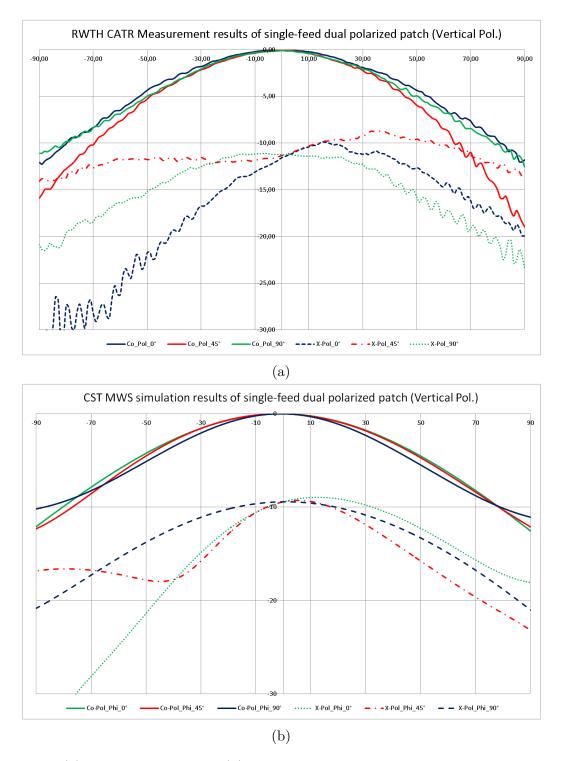


Figure 8.10: (a) Compact range and (b) CST MWS results for **vertical polarization**. The copolar (solid lines) and x-polar (dashed lines) antenna radiation pattern Cuts for  $\phi=0^{\circ}$  in green,  $\phi=-45^{\circ}$  in red and  $\phi=90^{\circ}$  in blue are shoon.

used to combine the two RO4350 laminates during the compression process. For suppressing unwanted surface currents or propagation channels within the substrate right from the design beginning, this prepreg shows only small  $\varepsilon_r$  difference compared to the RO4350B substrate.

The copper has a thickness of  $42\mu$ m and the diameter of the isolation circle inside the shielding ground for the probe-feed transition is 1.0 mm. The radiating square patches with 8.9 mm edge length, probe-via diameter of 0.2 mm and 0.346 mm probe-via to edgedistance are designed for a resonance frequency of 9.395 GHz. The investigation of x-pol sources in chapter 6 has shown significant degradation of CPS performance when the signal routing of the feeding network is established directly below the patch. As a consequence, two ground planes are implemented in the new patch antenna design. The second ground plane provides additional isolation between the feeding network and the resonance structure of the patch antenna. The Rosenberger 3-D connector model was completely integrated in the CST MWS full wave simulation and impedance matched with GND vias to the 50 $\Omega$ line impedance. The patch antennas impedance reference point in front of the probe-feed is matched to 100 $\Omega$ , which is necessary for the complex feeding network design in array configurations as detailed in the sections 8.7 and 8.8. For single patch antenna operation the 100 $\Omega$  patch antenna wave impedance is matched by a quarter wavelength impedance transformer to the 50 $\Omega$  line impedance in front of the Rosenberger connector.

The even more limited space on the network feeding layer, below the patch, has to be used very economically for the dual polarized patch with differential-feeding and the four probe-feeds. The differential feeding method can only be established by 180° phase difference between the oppositely placed feeding points. As a consequence, the new design of the microstrip line routing in figure 8.11b was developed to provide the signal distribution for the four probe-feeds.

For both polarization channels the 180° phase difference was established by the differential length of the microstrip lines. The exact power splitting was realized by the T-Junction power dividers. The innovative microstrip feeding structure in figure 8.11b was designed in order to provide maximum isolation between the two polarization channels. The via-fences around the feeding points are another reason of the high isolation between the polarization channels. As discovered during the design process of the amplitude- and phase distribution network (detailed in Appendix A1), the isolation between neighboring signal routing lines can be increased when the grounded coplanar waveguide microstrip line technology is used.

For the stand-alone patch antenna operation, the  $100\Omega$  patch antenna wave impedance has been matched by a quarter wavelength impedance transformer to the  $50\Omega$  line impedance in front of the Rosenberger connector. Additionally, ground vias are implemented around the probe-feed. In this way the maximum RF power is passed to the surface of the patch and unwanted surface waves on the lower RO4350 layer are mitigated and the total antenna efficiency could be increased. Furthermore, mutual coupling between neighboring elements in array configurations are avoided. Typically, the patch antenna impedance is matched by the variation of the probe-feed position along the resonating structure of the patch or by quarter wavelength stub located close the probe-feed. But both approaches are not suitable for the design of dual polarized patch antennas with low x-pol contribution and high channel isolation. For this reason, the patch antenna was matched by a short circuit very close to the probe-feed. The short circuit reflects all RF energy to the surface of the patch antenna so that unwanted radiation at the lower substrate layer can be avoided.

The picture of the constructed patch is given in figure 8.11b. The four antenna feeds and two implemented sub-miniature push-on (SMP) Rosenberger connectors for dual polarization capability are shown. To protect the multilayer PCB surface against corrosion the copper structures are plated with 5 microns of gold-nickel (Au/Ni). The rectangular areas in green color are solder resist, necessary for the installation of the SMP connectors. The solder pad of the connector occupies only 4 mm x 4 mm. The small size of these connectors is important for array applications with dense feeding networks.

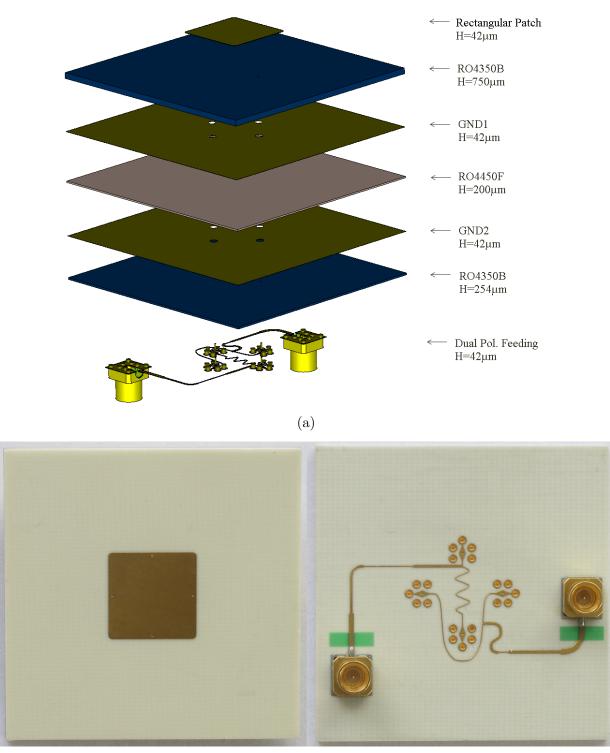
### 8.6.2 Discussion of the results

In figure 8.14a, the simulated (dashed lines) and measured (solid lines) S-Parameters of the differential-feed and dual polarized patch antenna of figure 8.11 are given. The simulated and measured S11-Parameters are very well correlated. The resonance behavior could be established exactly at the design frequency of 9.395 GHz. The simulated and the measured S11 values for both polarization channels are also in very good agreement. Furthermore, the required impedance bandwidth of 250 MHz has been established.

The measured values of S21 and S12 show approximately 33 dB of channel isolation. As narrated in the previous section 8.5, the boresight CPS can also expected to be in this region.

The difference between simulated and measured S21, S12 is 15 dB at the resonance frequency. This difference is probably related to an improper 180° phase difference alignment or an non-identical amplitude distribution of the constructed and opposite sided probefeeds. It is also possible that the phase alignment has been violated by the inhomogeneous dielectric constant distribution of the real substrate used for the production. CST MWS assumes a homogeneous dielectric constant distribution within the substrate layer, so that the differences between simulation and VNA measurements can be explained. Additionally, the frequency response between 9 GHz and 10 GHz of the measured and simulated curves of S21, S12 are diverging. The measured S21,S12 values are showing an increasing isolation for higher frequencies. For instance, at 10 GHz a perfect channel isolation of 50dB could be established. According to this observation, it can be assumed that the phase relations between oppositely placed probe-feeds are different for the simulation model and the produced prototype antenna.

In figure 8.13 the CST MWS simulated 3D antenna radiation patterns are visualized. The co-polar patterns are showing realized gain values of 6.5 dBi for the horizontal and 6.4 dBi for the vertical polarization. In order to evaluate the theoretical antenna efficiency, the graph from figure 3.15b in section 3.3.8 can be used. Here, a theoretical antenna efficiency



(b)

Figure 8.11: (a) Antenna set-up established with CST MWS.(b) Constructed dual polarized microstrip patch antenna element with differential feeding technique. Four probe-feeds are implemented. Two opposite sided feeds are used for the generation of one polarization channel. The probe-feeds are fed with 180° phase difference, induced by the wave molding microstrip line.

of approximately 86 % for the design value of  $\frac{H}{\lambda_{\epsilon_r}} = 0.046$  can be expected. The simulated antenna radiation efficiency is approximately 79 % for both polarizations and matches very well with the theoretical antenna efficiency value retrieved from figure 3.15b. The total antenna efficiency provided by CST MWS is almost equal to the radiation efficiency. The main reason for this fact is the very low x-pol contribution. Due to the differential feeding method the x-pol patterns are showing nulls in the E- or in the H- cut, as expected from the theoretical observations in section 6.4. The measured S21 values have shown adequate isolation values of approximately 33 dB between the H- and V- channel. Consequently, the CPS at boresight direction can also expect to be in this region.

The detailed comparison of the measured and simulated antenna radiation pattern for both polarization planes can be performed with figure 8.14 and figure 8.15. In figure 8.14a the CATR and in figure 8.14b the CST MWS results for the horizontal polarization are shown. In figure figure 8.15a the compact antenna test range and in figure 8.14b the CST MWS results for the vertical polarization are shown. The agreement between CST MWS simulations and CATR measurements are very good. The graphs of the measured and simulated co-polar element patterns are perfectly matched. As expected, from previous investigations in chapter 6, the x-pol minimum is located in the center of the patch and the four maxima are located across the diagonal planes. A very good CPS at boresight of approximately 33.3 dB for both polarization channels has been measured for this differential-feed and dual polarized microstrip patch antenna element. The simulated CPS of approximately 37dB at boresight could not be reached. As discussed early, the measured S-Parameter are showing only 33dB channel isolation compared to the simulated isolation of approximately 46dB.

The state-of-the-art CPS for microstrip patch antennas with 30dB to 35dB CPS from reference [112] could be established. The CPS can further be optimized by investigating a set of slightly different antenna prototypes. To overcome the differences between CST MWS simulation model and the real antenna prototype for future works, a set of single patch antennas with diverging path length in the feeding network should be produced and measured with VNA. Finally, the best performing antenna on the real substrate can be selected.

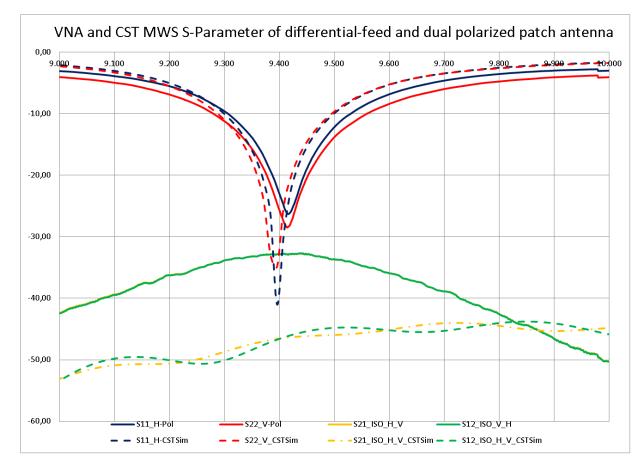


Figure 8.12: VNA measured and CST MWS simulated S-Parameter of the differential-feed microstrip patch antenna. Note that s21 - ISO - H - V and S12 - ISO - V - H are perfectly superimposed.

# 8.7 Development and design of a dual polarized microstrip patch antenna array with optimum phase excitation

### 8.7.1 Design overview of a dual polarized microstrip patch antenna array with optimum phase excitation

The single-feed patch antenna from section 8.5 has been used to create the 4x8 patch antenna array, which will be discussed now. Furthermore, the results from the analysis of the optimum phase excitation of mirrored elements in chapter 7 are also adapted to develop an antenna array with very low x-pol contribution. The most promising configuration 3 from figure 7.4 has been used to create the 4x8 array. The analysis in section 7.5 promises a CPS of 45.1 dB for the 3-4x8 array configuration, as shown in figure 7.7a. The antenna design here differs from the design template in chapter 7. Consequently, the simulated

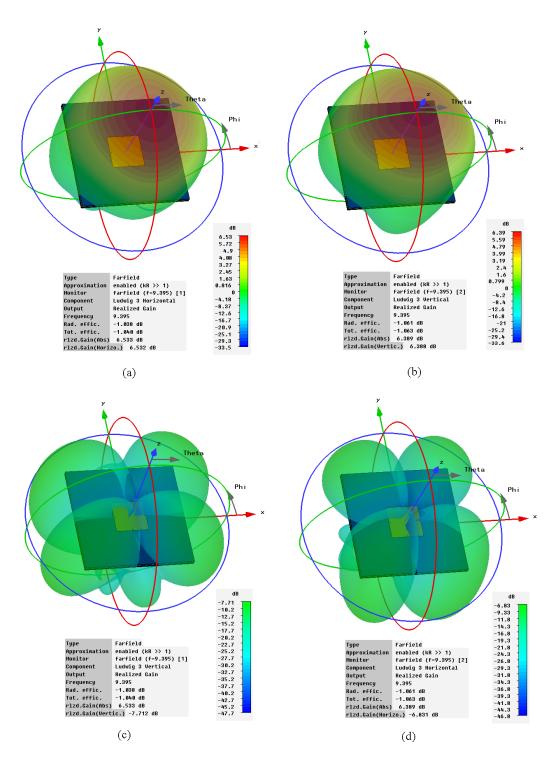
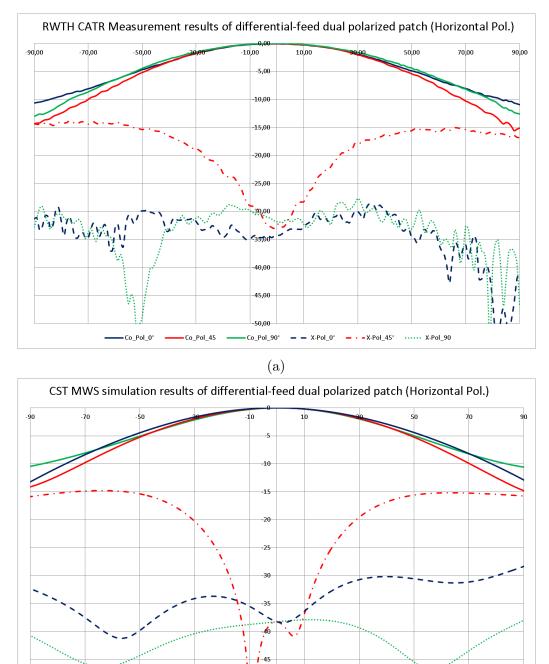


Figure 8.13: CST MWS simulated 3D antenna radiation pattern of the differential-feed patch antenna. (a) Co-polar plot for horizontal polarization. (b) Co-polar plot for vertical polarization. (c) X-polar plot for horizontal polarization. (d) X-polar plot for vertical polarization.



 $c_{0}-Pol_Phi_0^{\circ} - c_{0}-Pol_Phi_45^{\circ} - c_{0}-Pol_Phi_90^{\circ} - \cdots + X-Pol_Phi_45^{\circ} - X-Pol_Phi_90^{\circ}$ (b)

Figure 8.14: (a) Compact range and (b) CST MWS results for **horizontal polarization**. The co-polar (solid lines) and x-polar (dashed lines) antenna radiation pattern Cuts for  $\phi=0^{\circ}$  in green,  $\phi=-45^{\circ}$  in red and  $\phi=90^{\circ}$  in blue are shown.

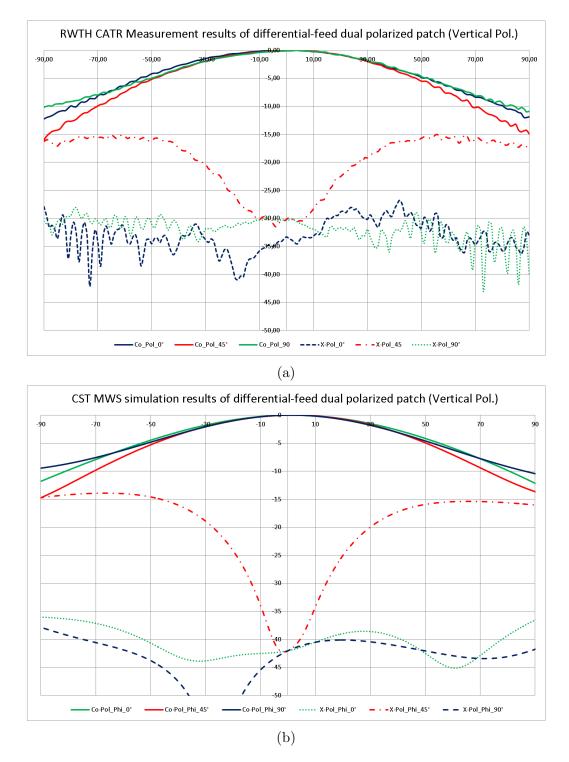


Figure 8.15: (a) Compact range and (b) CST MWS results for **vertical polarization**. The copolar (solid lines) and x-polar (dashed lines) antenna radiation pattern Cuts for  $\phi=0^{\circ}$  in green,  $\phi=-45^{\circ}$  in red and  $\phi=90^{\circ}$  in blue are shoon.

CPS results from chapter 7 can only be used as a first order reference value.

Figure 8.16 gives the 3D CST MWS model of the developed 4x8 antenna array. The array has exactly the same layer set-up as the single-feed patch antenna from section 8.5. The feeding network, with its SMP connectors for both polarization channels, is located on the bottom layer. The patches are located on the upper layer. The realized configuration 3 from the analysis in chapter 7 is applied to the new array, as shown in figure 8.17b. The configuration 3 can be recognized in horizontally (frame in blue dashed lines) and in vertically (frame in red dashed lines). The main differences to the theoretical investigation from chapter 7 is the antenna set-up and the dual polarization capability. The analysis in chapter 7 was done only for single polarization operation.

In figure 8.17b the rear side of the constructed antenna prototype is shown. Here, the dual polarization feeding network, the SMP connectors and the matched thru vias (antenna feeds) to the patch surface are apparent. In order to provide wide angle azimuth- and elevation- scanning without the appearance of grating lobes in the visible scan range, the element-to-element distance has been chosen with  $\frac{\lambda}{2}$  for the horizontal and the vertical grid of the patch antenna array. Four radiating elements are combined vertically to a LFoV subarray to decrease the number of control elements (TRMs), as detailed in the phased-array weather radar system design of chapter 5. This is only possible due to the specific weather radar application with LFoV in elevation scanning.

The feeding points for the specific phase excitations of the mirrored elements for horizontal and vertical polarization are highlighted in blue and red, respectively. The excitation phase is either 0° or 180°. Consequently, the feeding points are labeled with  $H_0^{\circ}$ ,  $H_1^{80^{\circ}}$ ,  $V_0^{\circ}$  and  $V_1^{80^{\circ}}$ . The 1:8 feeding network is designed with a number of T-junction power dividers for maximum isolation between the two polarization channels. The antenna impedance of every individual radiator is a function of its geometrical position inside the complete antenna array. For this reason, four groups of patch radiators (highlighted in yellow, light-blue, green and red in figure 8.18a) have been identified to be matched as embedded elements. After the impedance matching of the four individual embedded elements, two different groups (see the two arrays in figure 8.18a with the dashed blue lines) of subarrays for subarray matching are considered in the CST MWS simulations.

Parts of the antenna feeding network, the probe-feed via structure with surrounded ground vias and the 3D model of the SMP connector are given in figure 8.18b. The probe-feed via is surrounded by ground vias to increase the antenna efficiency and to increase the isolation between the polarization channels. As already mentioned in the previous sections, the surface waves are avoided by this configuration. The short circuit for impedance matching is also shown as enlarged picture of the CST MWS model. By length variation of this short circuit the radiating element impedances at individual geometrical positions inside the array are matched. The subarray matching was performed by the width variation of the microstrip line connecting the SMP connector. Here, the wave impedance was slightly changed to match the wave impedance at the entrance of the SMP connector to  $50\Omega$ .

The 1:8 T-junction feeding network with its equivalent circuit diagram is given in figure 8.19. The different impedance points are highlighted in the picture of the produced circuit board in order to localize these points in the equivalent circuit diagram. The microstrip lines have been selected with 100 $\Omega$  wave impedance. In this manner, the isolation between neighbored microstrip lines could be maximized and the maximum line extension could be limited to the extension for 50 $\Omega$  wave impedance at the connector entrance. The antenna ports are also matched to 100 $\Omega$  wave impedance, so that the first T-Junction power divider at the point P5 sees two 100 $\Omega$  lines in parallel, which corresponds to 50 $\Omega$ wave impedance. The 50 $\Omega$  wave impedance at point P5 is then transformed by a quarter wave transformer to 100 $\Omega$ . The quarter wave transformer was set to 70,7 $\Omega$  wave impedance. At point P7, again two 100 $\Omega$  wave impedances are in parallel. Consequently, no further impedance transformation must be established to reach the 50 $\Omega$  wave impedance at the entrance of the SMP connector.

As narrated in section 8.5 the isolation between the two polarization channels is a function of the x-pol suppression. Therefore, the 1:4 subarray was characterized separately in 3D full wave simulations to evaluate the isolation by surface current analysis. The surface currents analysis has shown that a point of wave cancellation can be identified in the opposed polarization channel of one subarray. The point of wave cancellation is given in figure 8.20. For instance, by excitation of the horizontal port the injected EM- wave travels thru the patch and will be radiated. But parts are also injected into the feeding network of the vertical channel. Due to the 180° phase difference inside the feeding network the two signal parts are cancelled at the point shown in figure 8.20. As a consequence, the isolation between horizontal and vertical channel of the 1x4 LFoV Array will significantly be increased by the so developed feeding and excitation method compared to the stand-alone isolation performance of the microstrip patch antenna from section 8.5.

#### 8.7.2 Discussion of the results

Figure 8.21 gives the simulated (dashed lines) and measured (solid lines) S-Parameters of the dual polarized microstrip patch antenna array with optimum phase excitation from the pictures in figure 8.17b. More precisely, the reported isolation with S21 and S12 and the S11 for the separate rows of the 1x4 subarrays embedded in the 4x8 array are given. The antenna array utilizes eight 1x4 subarrays for every polarization channel. To keep the overview, only the S11 values of the vertical polarization channel are visualized. The resonance frequency was perfectly met with 99.77% design accuracy. Also the VSWR 2:1 bandwidth of 250 MHz could be established. The channel isolation depends on the position of the 1x4 subarray in the 4x8 array. The measured channel isolation varies from 35 dB to 42 dB. The CST MWS simulated channel isolation is 45 dB to 55 dB. It can also be recognized that the depth of the measured and simulated S11 resonance curves are different. The main reason for this is the non-identical impedance matching of the patches and two 1x4 subarrays at different geometrical positions inside the complete antenna array.

The simulated 3D antenna radiation pattern for both polarization planes are given in fig-

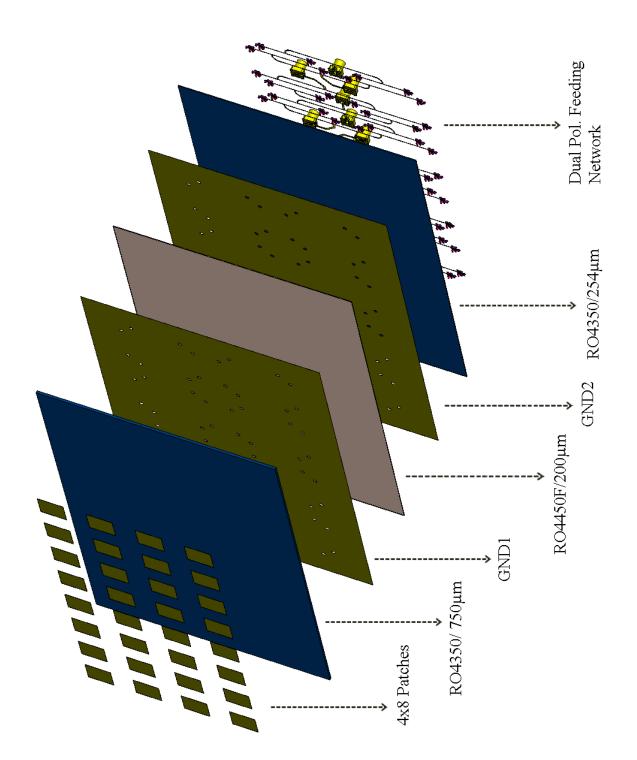


Figure 8.16: CST MWS Design of dual polarized array with 32 radiators.

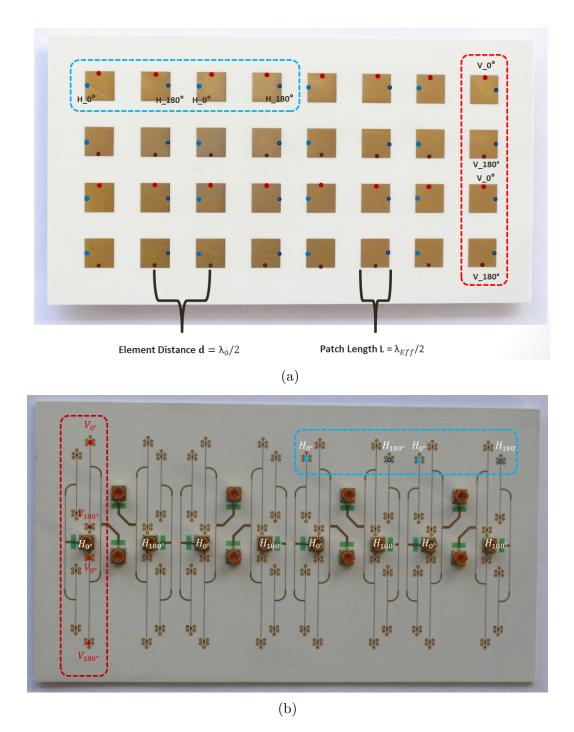


Figure 8.17: (a) Front view (b) Rear view of the constructed dual polarized phased-array antenna with optimized phase excitation. The feeding points for horizontal (blue) and vertical (red) polarization are given. The excitation is performed by two types of RF signals which are either in phase  $(0^{\circ})$  or  $180^{\circ}$  out of phase. The optimum phase excitation configuration 3 from chapter 7 is highlighted by the red and blue frames in dashed lines, respectively for horizontal and vertical polarization.

229

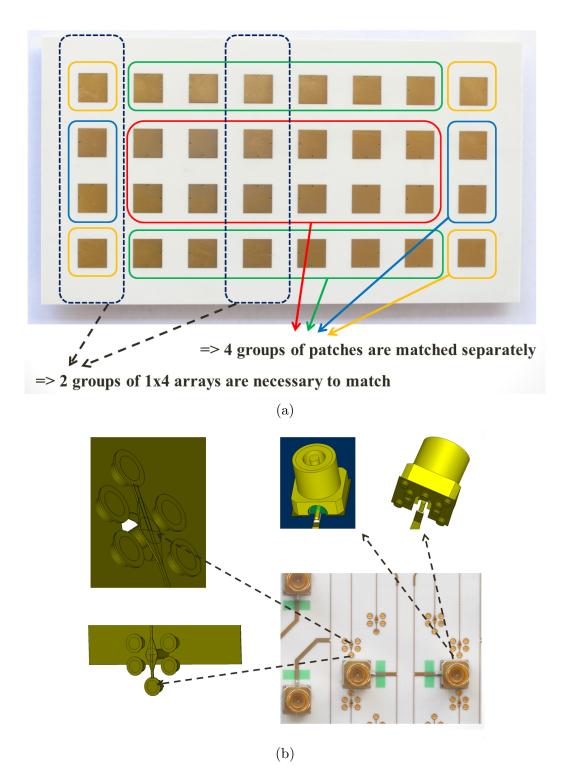


Figure 8.18: (a) Patch and subarray impedance matching, depending on the position inside the 4x8 antenna array. (b) Length variation of short circuit has been performed for impedance matching. Furthermore, the implemented 3D-model of a connector is shown.

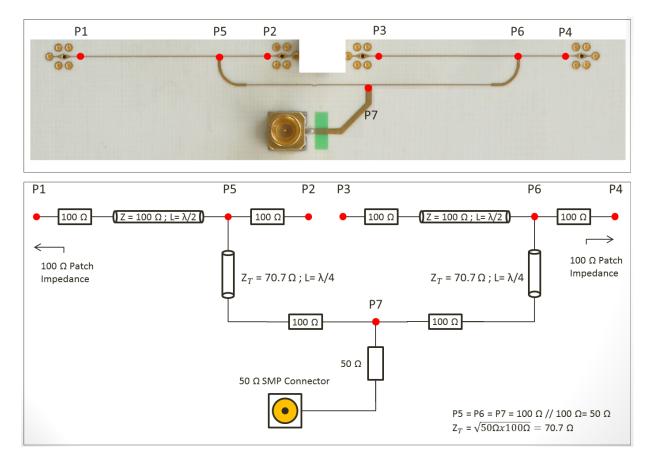


Figure 8.19: 1:8 corporate feeding network design with its equivalent circuit diagram.

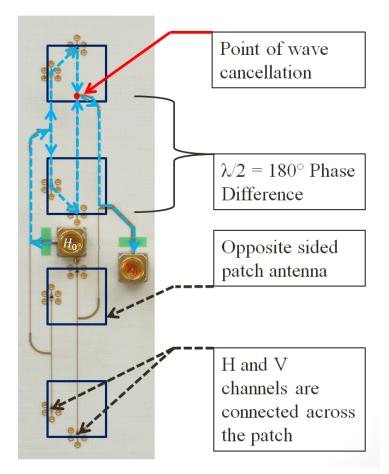


Figure 8.20: Feeding network design for maximum isolation between H and V polarization channel.

ure 8.22. The co-pol patterns are shown in figure figure 8.22a and figure 8.22b and the x-pol radiation patterns are shown in figure 8.22c and figure 8.22d. The realized gain values of 19.4 dBi are established for both polarization planes. The antenna radiation patterns have been generated by 3D full wave solution of a 4x4 antenna array and the CST MWS array factor function to provide the pattern of the 4x8 antenna array. The full wave simulation of the 4x4 array has already occupied 70 Mio mesh cells, which represents the maximum number of mesh cells for the simulation environment with GPU computing. One could propose to decrease the number of mesh cells to 35 Mio. mesh cells, in order to simulate the 4x8 array with 70 Mio. mesh cells. But this solution would lead to significant loss of accuracy for the simulation of such complex three dimensional feeding and antenna structures. Furthermore, parts of the microstrip lines and matching circuits between 77  $\mu$ m and 100  $\mu$ m wouldn't be considered accurately, if the grid spacing of the mesh would be enlarged.

The CATR measured 3D antenna radiation pattern for both polarization planes are given in figure 8.23. The co-pol patterns are shown in figure 8.23a and figure 8.23b and the x-pol radiation patterns are shown in figure 8.23c and figure 8.23d. The 3D visualization has been generated with the Orbit software used by the RWTH Aachen scientists. The coand x-pol measurements haven been performed with 5° steps of  $\Phi$  for the complete upper hemisphere of antenna array. In order to properly visualize the 3D antenna radiation pattern the CATR effects are filtered out. Furthermore, the dataset has been interpolated between the 5° steps of  $\Phi$ . The filtering and the interpolation has been carried out by the RWTH PhD Student Mr. Rasmus Cornelius. The measured 3D co-polar and the x-polar pattern from figure 8.23 are showing excellent correlation with the simulated 3D patterns in figure 8.22. Even the x-polar pattern with its unique geometry (multiple beams of weak x-polar radiation) is unambiguously observable.

For the detailed 2D comparison, the CATR measured and CST MWS simulated antenna radiation patterns for horizontal and vertical polarization are shown in figure 8.24 and figure 8.25, respectively. The correlation between the simulated and the measured co-pol antenna radiation pattern are perfectly met. But also the measured and simulated x-pol patterns are in very good agreement. By analyzing the horizontal polarization plots, the two peaks of the 45° Cut are visible in simulation and measurement. The vertical polarization plots (figure 8.25a and figure 8.25b) are showing both the peak of the 45° cut at approximately  $+12^{\circ}$  azimuth. The impressive agreement between the x-pol plots proves also the high measurement performance of the CATR from RWTH Aachen. Furthermore, it can be recognized that the effort was worthwhile to implement the antenna array in the low-permittivity ROHACELL holding structure (see the picture in figure 8.4), as part of the antenna under test. In choosing this solution, the array sum pattern was not influenced by any electromagnetic interaction with objects in the nearby environment of the antenna.

In figure 8.26 the impressive results for the CPS are given. Figure 8.26a and 8.26b show a large magnification of the x-pol patterns in figure 8.24a and 8.25a between  $+5^{\circ}$  and  $-5^{\circ}$  below the co-polar main lobe. Excellent CPS values of -46.83 dB and -50.4 dB have been

established for horizontal and vertical channel, respectively. Since the center of the main beam is used as the reference, the arithmetic mean of the three x-pol values is used for the determination of the CPS.

In order to thoroughly compare the simulated and measured antenna characteristics, table 8.2 should be used. Here, the most important antenna parameters, like the 3dB beamwidth, the x-pol suppression (CPS) and the first sidelobe suppression are contrasted for both polarization planes. All measured and simulated antenna parameter are in very good agreement.

In figure 8.27 the antenna array with optimized phased excitation was used as a phasedarray antenna. The complete system set-up of the phased-array measurements in the CATR is given in figure 8.4. Five different scan angles have been generated by the amplitude- and phase distribution network (see Appendix A1) to investigate the scan loss as a function of the single element pattern and the CPS performance during beam steering. The scan loss of the phased-array antenna main beam is dominated by the element pattern of a single radiator. Consequently, the isolated single element pattern (dashed orange line) from section 8.5 is implemented here to show the relation between array factor and element factor. Both phased-array patterns (horizontal and vertical) are following the element pattern of the single radiator very accurately during the beam steering process. As already suggested by equation 3.72 in section 3.4.3 the 3dB beamwidth will be increased by pointing the main beam of the phased-array antenna off-boresight direction. This effect is clearly visible in figure 8.27. It can also be recognized that no grating lobe is entering the visible space due to the  $\frac{\lambda}{2}$  spacing of the single radiators. Even for the  $\pm 60^{\circ}$  azimuth scan angle no grating lobe becomes visible. The scan loss at  $\pm 60^{\circ}$  is 5 dB to 6 dB, which fits very well to the theoretical scan loss evaluated for the LFoV investigation from figure 5.4c in section 5.3.

The CPS performance of the antenna array is given in figure 8.28a for horizontal polarization and in figure 8.28b for the vertical polarization plane. By recalling the definition of the CPS in section 3.2, the CPS is determined by computing the difference between the co-polar main beam value and the value of the x-pol pattern at the same angle. As thoroughly discussed in section 3.4.5, the polarization purity will be decreased by steering the main beam off the phased-array antenna boresight direction. Consequently, the best CPS can be reached for the boresight direction. Here the impressive CPS values of 47dB (H-Pol) and 50dB (V-Pol) could be realized. But also for the complete azimuth scan range of 120° the CPS could be kept below 27dB for the horizontal and below 33dB for the vertical channel. Unfortunately, the x-pol level rises at other angular positions, when the co-polar main beam is steered. For instance, if the scan is steered to  $+30^{\circ}$  in figure 8.28a, the x-pol pattern shows a maximum at  $-30^{\circ}$ . This improper x-pol performance can be explained by the violation of the optimum phase excitation, which is only valid in boresight direction. As thoroughly discussed with equation 3.62, a phase offset between neighboring radiators must be applied to perform beam steering. Consequently, the optimum phase relation noted in chapter 7 and applied for the array design here is violated. The x-pol performance is degraded if the beam is pointed off-boresight direction. The horizontal channel is even more strongly violated in CPS compared to the vertical channel. As shown in figure 8.17b the horizontal polarized LFoV subarrays must be fed with 180° phase difference between the input ports to reach maximum CPS in boresight direction. The vertical polarized LFoV arrays are already providing the optimum phase excitation on their own feeding network, so that no additional 180° phase difference between the neighboring LFoV arrays must be applied. As a consequence, the x-pol performance of the vertical polarized subarray of 32 antenna elements is more effective, even during beam steering.

In figure 8.29 the CPS performance was analyzed for 3 different taper distributions. The amplitude taper has been generated by the amplitude and phase distribution network detailed in Appendix A1. As already addressed in table 3.4 of section 3.4.3, the beamwidth is broaden when an amplitude taper is applied to the array. But also the sidelobe suppression will be increase, which is typically desirable. However, the x-pol suppression is the main focus for this experiment. The results in figure 8.29 are showing that the CPS will be optimized, when a stronger decay of the taper function is applied. The uniform amplitude distribution provides already 51 dB CPS. The first taper function 53 dB CPS and the most intensive taper function 2 provides an excellent CPS value of 55 dB. For this reason, it can be stated that the CPS of an antenna array can be further optimized by the choice of proficient amplitude taper. This observation, to the best of the authors' knowledge, is unique.

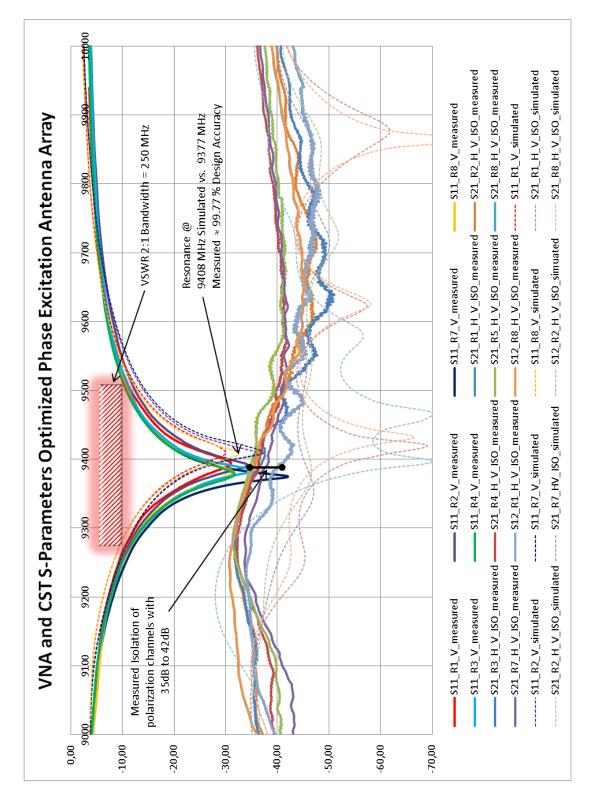


Figure 8.21: Comparison of simulated (CST MWS-dashed lines) and measured (VNA-solid lines) S-Parameters.

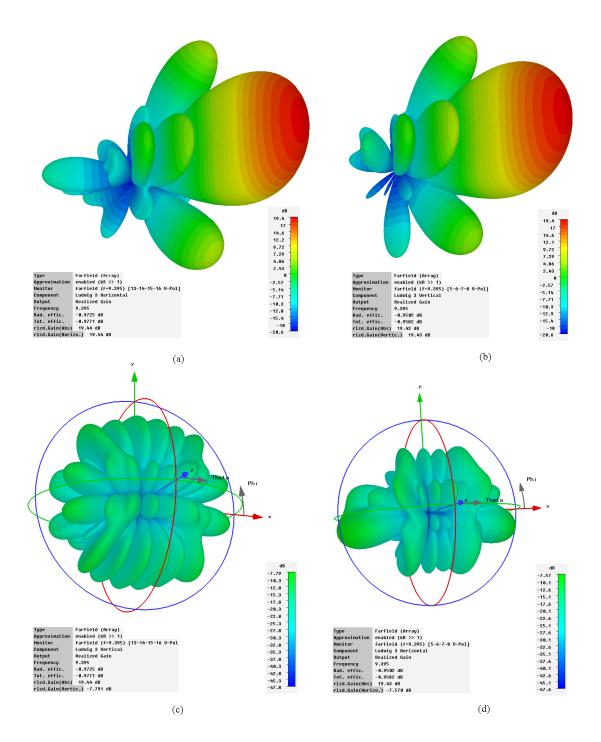


Figure 8.22: CST MWS simulated 3D antenna radiation pattern for horizontal and vertical polarization. (a) Co-polar plot for horizontal polarization. (b) Co-polar plot for vertical polarization. (c) X-polar plot for horizontal polarization. (d) X-polar plot for vertical polarization.

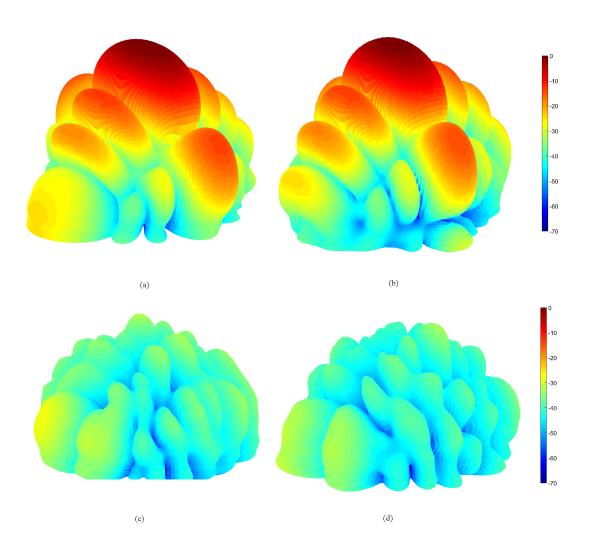
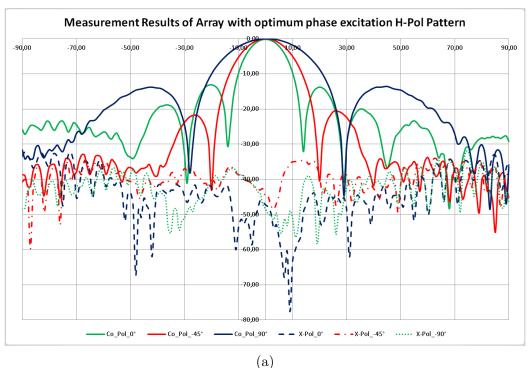


Figure 8.23: RWTH CATR measured 3D antenna radiation pattern of the optimum phase excitation array for horizontal and vertical polarization. The 3D cuts are generated by the Orbit software. The measurement was performed with 5° steps of  $\Phi$  for the complete upper hemisphere of the antenna array. The CATR effects are filtered out and an interpolation between the 5° steps of  $\Phi$  is performed. (a) Co-polar plot for horizontal polarization. (b) Co-polar plot for vertical polarization. (c) X-polar plot for horizontal polarization. (d) X-polar plot for vertical polarization.



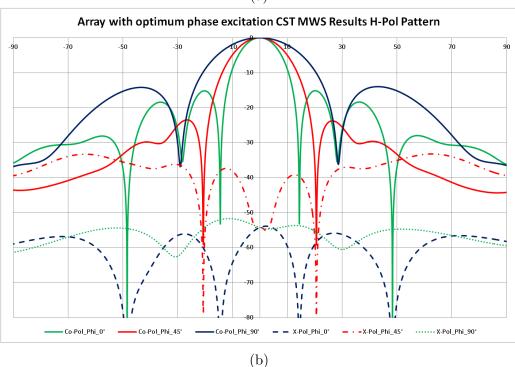
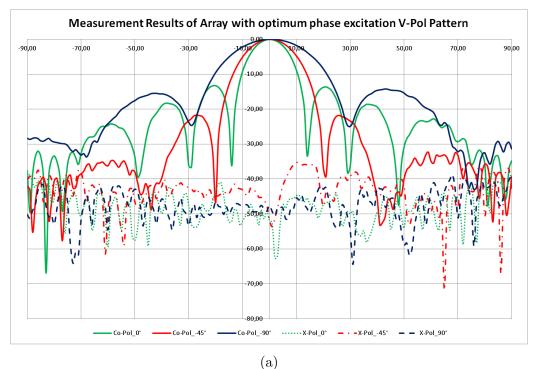


Figure 8.24: Compact range measurement results compared to CST MWS simulation results for **horizontal polarization**: (a) The co-polar (solid lines) and x-polar (dashed lines) antenna radiation pattern Cuts for  $\phi=0^{\circ}$  in green,  $\phi=-45^{\circ}$  in red and  $\phi=90^{\circ}$  in blue, measured at compact range RWTH Aachen. (b) The co-polar (solid lines) and x-polar (dashed lines) antenna radiation pattern Cuts for  $\phi=0^{\circ}$  in green,  $\phi=-45^{\circ}$  in red and  $\phi=90^{\circ}$  in blue, simulated with CST MWS.



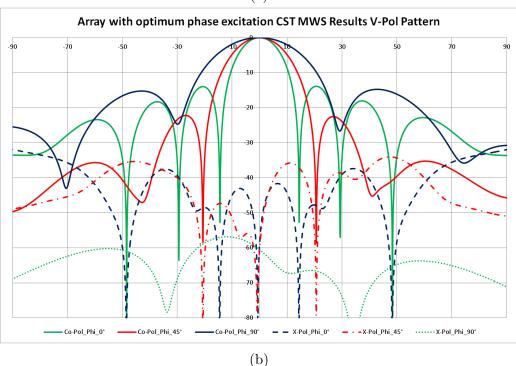
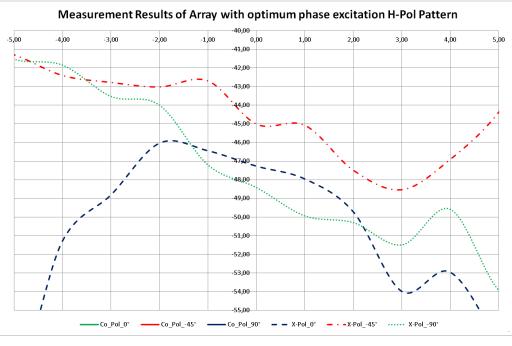


Figure 8.25: Compact range measurement results compared to CST MWS simulation results for **vertical polarization**: (a) The co-polar (solid lines) and x-polar (dashed lines) antenna radiation pattern Cuts for  $\phi=0^{\circ}$  in green,  $\phi=-45^{\circ}$  in red and  $\phi=90^{\circ}$  in blue, measured at compact range RWTH Aachen. (b) The co-polar (solid lines) and x-polar (dashed lines) antenna radiation pattern Cuts for  $\phi=0^{\circ}$  in green,  $\phi=-45^{\circ}$  in red and  $\phi=90^{\circ}$  in blue, simulated with CST MWS.





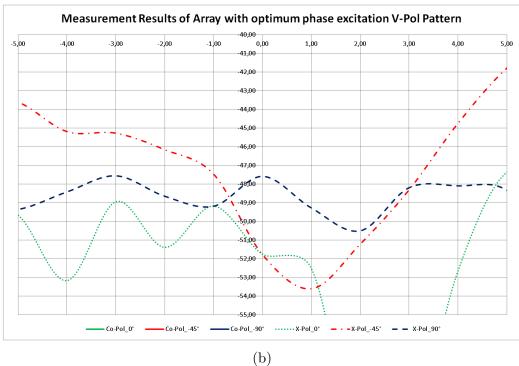


Figure 8.26: Magnification of the figures 8.25b and 8.25b at boresight direction in order to evaluate the CPS at  $\theta=0^{\circ}$ . The three CPS values at  $\phi=0^{\circ}$ ,  $\phi=-45^{\circ}$  and  $\phi=90^{\circ}$  are used to calculate the arithmetical mean of the CPS for the horizontal and vertical channel. Excellent CPS values of -46.83 dB and -50.4 dB can be evaluated for horizontal and vertical channel, respectively.

| Parameter                     | CST MWS        | CST MWS    | Compact    | Compact    |
|-------------------------------|----------------|------------|------------|------------|
|                               | Simulation     | Simulation | Range Mea- | Range Mea- |
|                               | V-Pol          | H-Pol      | surement   | surement   |
|                               |                |            | V-Pol      | H-Pol      |
| 3 dB Beamwidth                | 12.4°          | 12.4°      | 12.4°      | 12.2°      |
| at $\phi = 0^{\circ}$         |                |            |            |            |
| 3 dB Beamwidth                | 16.0°          | 15.8°      | 15.8°      | 15.5°      |
| at $\phi = -45^{\circ}$       |                |            |            |            |
| 3 dB Beamwidth                | $24.5^{\circ}$ | 24.3°      | 24.4°      | 24.1°      |
| at $\phi=90^{\circ}$          |                |            |            |            |
| CPS at $\theta = 0^{\circ}$ , | -60.4dB        | -54.3dB    | -51.8dB    | -48.3dB    |
| $\phi = 0^{\circ}$            |                |            |            |            |
| CPS at $\theta = 0^{\circ}$ , | -60.4dB        | -54.3dB    | -51.8dB    | -45.0dB    |
| $\phi = -45^{\circ}$          |                |            |            |            |
| CPS at $\theta = 0^{\circ}$ , | -60.4dB        | -54.3dB    | -47.5dB    | -47.2dB    |
| $\phi = 90^{\circ}$           |                |            |            |            |
| Suppression of                | -14.0dB        | -15.0dB    | -13.3dB    | -13.1dB    |
| first sidelobe at             |                |            |            |            |
| $\phi = 0^{\circ}$            |                |            |            |            |
| Suppression of                | -22.3dB        | -23.6dB    | -22.0dB    | -23.6dB    |
| first sidelobe at             |                |            |            |            |
| $\phi = -45^{\circ}$          |                |            |            |            |
| Suppression of                | -15.0dB        | -14.2dB    | -14.2dB    | -13.6dB    |
| first sidelobe at             |                |            |            |            |
| $\phi = 90^{\circ}$           |                |            |            |            |

Table 8.2: Comparison of simulated and measured antenna radiation pattern results.

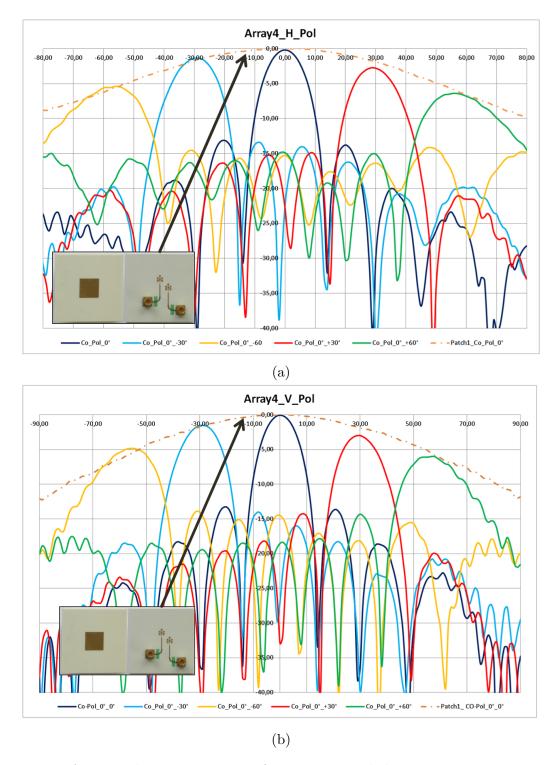
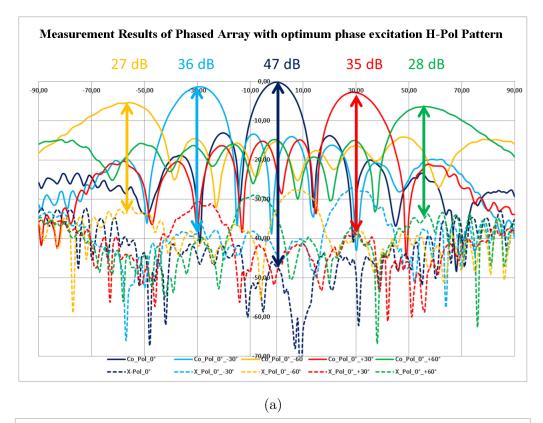


Figure 8.27: Antenna beam steering performance recorded at compact range measurements. The scan loss as the function of the single element antenna pattern can be recognized. The single element pattern was measured separately for an isolated patch element.



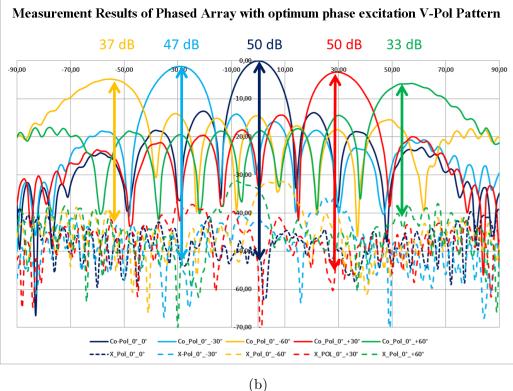
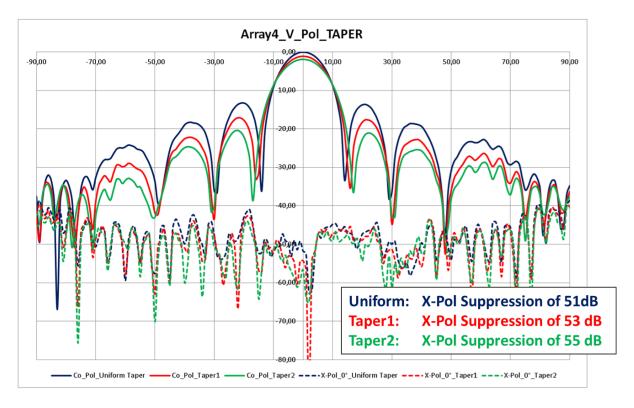


Figure 8.28: X-pol suppression during beam steering, recorded from compact range measurements. As expected, the CPS will be degraded when the main lobe is pointed off-boresight direction.



**Taper 1:** -3 dB ; -1.5 dB; -0.5 dB ; 0 dB; 0 dB; -0.5dB; -1.5 dB; -3 dB **Taper 2:** -5 dB; -2.5 dB; -1 dB; 0 dB; 0 dB; -1 dB; -2.5 dB; -5 dB

Figure 8.29: X-pol performance as a function of amplitude tapering. Additionally, the amplitude taper functions 1 and 2 are shown. The center elements of the 8 amplitude weights are used as reference with 0 dB. The other amplitudes are attenuated by the phase- and amplitude distribution network.

## 8.8 Development and design of a differential-feed and dual-polarized microstrip patch antenna array

## 8.8.1 Design overview of a dual polarized microstrip patch antenna array with differential-feeding

The differential-feed patch antenna from section 8.6 has been used to create the 4x8 patch antenna array, which will be discussed now. The array 3D model from CST MWS is given in figure 8.30 and shows exactly the same layer-configuration as the differential-feed patch antenna from section 8.6. The complex feeding network, with its SMP connectors for both polarization channels, is located on the bottom layer. The patches are located on the upper layer, as shown in 8.31a.

In figure 8.31b the rear side of the constructed antenna prototype is shown. Here, the dual polarization feeding network, the SMP connectors and the matched thru vias (4 antenna feeds per patch, 2 feeds per polarization) to the patch surface are apparent. In order to provide wide angle azimuth- and elevation- scanning without the appearance of grating lobes in the visible scan range, the element-to-element distance has been chosen with  $\frac{\lambda}{2}$  for the horizontal and the vertical grid of the patch antenna array. Four radiating elements are combined vertically to a LFoV subarray (frame in blue dashed lines for horizontal polarization and frame in red dashed lines for vertical polarization) to decrease the number of control elements (TRMs), as detailed in the phased-array weather radar system design of chapter 5. This is made possible due to the specific weather radar application with LFoV in elevation scanning.

The feeding points for the 0° and 180° phase excitations of the individual radiating elements for horizontal and vertical polarization are highlighted with blue and red points in figure 8.31b, respectively. Consequently, the feeding points are labeled with  $H_0^{\circ}$ ,  $H_1^{\circ}80^{\circ}$ ,  $V_0^{\circ}^{\circ}$  and  $V_1^{\circ}80^{\circ}$ . The phase difference is maintained by the unique stand-alone microstrip patch antenna feeding network. This feeding network provides high polarization channel isolation with minimum space below the patch.

The 1:8 corporate feeding networks for the subarrays are designed with a number of Tjunction power dividers for maximum isolation between the two polarization channels. The antenna impedance of every individual radiator is a function of its geometrical position inside the complete antenna array. For this reason, four groups of patch radiators (same procedure as already discussed with figure 8.18) have been identified to be matched as embedded elements. After the impedance matching of the four individual embedded elements, two different groups (see the two arrays in figure 8.18a with the dashed blue lines) of subarrays are considered for matching in the CST MWS simulations. All probe-feed vias are surrounded by ground vias to increase the antenna efficiency and to increase the isolation between the polarization channels. As already mentioned in the previous sections, the surface waves are avoided by this configuration. In order to provide proper patch antenna impedance matching a short circuit close to the probe-feed is used. By length variation of this short circuit the radiating element impedances at individual geometrical positions inside the array are matched (see figure 8.18b). The subarray matching was performed by the width variation of the microstrip line connecting the SMP connector. Here, the wave impedance was slightly altered to match the wave impedance of the SMP connector to  $50\Omega$ .

The 1:8 corporate T-junction feeding network with its equivalent circuit diagram is given in figure 8.32. The different impedance points are highlighted in the picture of the produced circuit board in order to localize these points in the equivalent circuit diagram. The microstrip lines have been selected with  $100\Omega$  wave impedance. In this manner, the isolation between neighboring microstrip lines could be maximized and the maximum line extension could be limited to the extension for  $50\Omega$  wave impedance at the connector entrance. The antenna ports (for instance, the point P5L and P4L) are also matched to  $100\Omega$  wave impedance, so that the first T-Junction power divider at the point P3L sees two 100 $\Omega$  lines in parallel, which corresponds to 50 $\Omega$  wave impedance at P3L. The 50 $\Omega$ wave impedance at point P3L is then transformed by a quarter wave transformer to  $100\Omega$ again. The quarter wave transformer was set to  $70,7\Omega$  wave impedance, as defined with equation 3.30. At point P2L, two  $100\Omega$  wave impedances with  $360^{\circ}$  phase difference are in parallel, which corresponds to  $50\Omega$  impedance. The  $50\Omega$  wave impedance at point P2L is then transformed by a quarter wave transformer to  $100\Omega$ . By considering the right and the left part of the feeding network, two 100 $\Omega$  wave impedances are given in parallel at P1, so that  $50\Omega$  wave impedance is established at this point. Consequently, no further impedance transformation must be used to reach the  $50\Omega$  wave impedance at the entrance of the SMP connector. The width of the quarter wave transformer closest to the SMP connector and connecting the right part of the feeding network is of course different in the design with respect to the one on the left. The path length and also the additional attenuation have been considered during the design- and simulation process in CST MWS. This action took place to provide the same amplitude- and phase- relation to all of the 8 feeding points (2 points per patch, 8 points per subarray feeding network in one polarization subarray channel).

As narrated in section 8.6, the boresight x-pol suppression is a function of the isolation between the two polarization channels. Therefore, the 1:4 subarray was characterized separately in 3D full wave simulation to evaluate the isolation by surface current analysis. The surface currents analysis has shown that three points of wave cancellation can be identified in the opposed polarization channel of one subarray. These points of wave cancellation are given in figure 8.33. For instance, by excitation of the vertical port, the injected EMwave travels thru the patch and will be radiated. But signal parts are also injected into the feeding network of the horizontal channel. Due to the differential feeding of the vertical channel, two signals with 180° phase difference are generated at the entrance of the horizontal feeding points. These two signals are cancelled in point P1, as shown in figure 8.33. The same is true for point P2. Another cancelation takes place at point P3, due to the 180° phase difference of the differential feeding network of the horizontal channel. As a consequence, the isolation between horizontal and vertical channel will significantly be increased. Due to the three points of wave cancellation observed here, an even more effective channel isolation and CPS can be expected, as compared to feeding networks without differential feeding.

#### 8.8.2 Discussion of the results

Figure 8.34 gives the simulated (dashed lines) and measured (solid lines) S-Parameters of the dual polarized microstrip patch antenna array with differential-feeding from the pictures in figure 8.31. More precisely, reported are the isolation with S21 and S12 and the S11 for the separate columns of the 1x4 subarrays embedded in the 4x8 array. The antenna array utilizes eight 1x4 subarrays for every polarization channel. Here, the S11 values of the vertical and horizontal polarization channels are visualized. The resonance frequency was perfectly met with approximately 99.50% design accuracy. A VSWR 2:1 bandwidth of approximately 180 MHz could be realized. The fluctuation of the channel isolation depends on the position of the 1x4 subarray inside the 4x8 array. The measured channel isolation varies from 43 dB to 57 dB. The CST MWS simulated channel isolation is 50 dB to 60 dB. Consequently, very good CPS values at the phased-array antenna boresight direction can be expected.

It can also be recognized that the depth of the measured and simulated S11 resonance curves are different. The main reason for this phenomenon is the non-identical impedance matching of the patches and the 1x4 subarrays at different geometrical positions inside the complete antenna array. The S11 parameters of the horizontal channels are slightly shifted to a lower resonance frequency, but still below -20 dB at the resonance center frequency of 9.395 GHz. The S11 of the R1 (column number one of the vertical channel) is not perfectly impedance matched. Even the simulation of the S11 values from column one shows imperfections. Consequently, the edge located antenna columns should be optimized for future works.

The simulated 3D antenna radiation pattern for both polarization planes are given in figure 8.35. The co-pol patterns are shown in figure 8.35a and figure 8.35b and the x-pol radiation patterns are shown in figure 8.35c and figure 8.35d. The realized gain values of 19.3 dBi and 19.4dBi are established for horizontal and vertical polarization, respectively. The antenna radiation patterns have been generated by 3D full wave solution of a 4x4 antenna array and the CST MWS array factor function to provide the pattern of the 4x8 antenna array. The full wave simulation of the 4x4 array has already occupied 70 Mio mesh cells, which represents the maximum number of mesh cells for the simulation environment with GPU computing. One could propose to decrease the number of mesh cells to 35 Mio. mesh cells, in order to simulate the 4x8 array with 70 Mio. mesh cells. But this solution would lead to significant loss of accuracy for the simulation of such complex three dimensional feeding and antenna structures. Furthermore, parts of the microstrip lines and matching circuits between 77  $\mu$ m and 100  $\mu$ m wouldn't be considered accurately, if the grid spacing of the mesh would be enlarged.

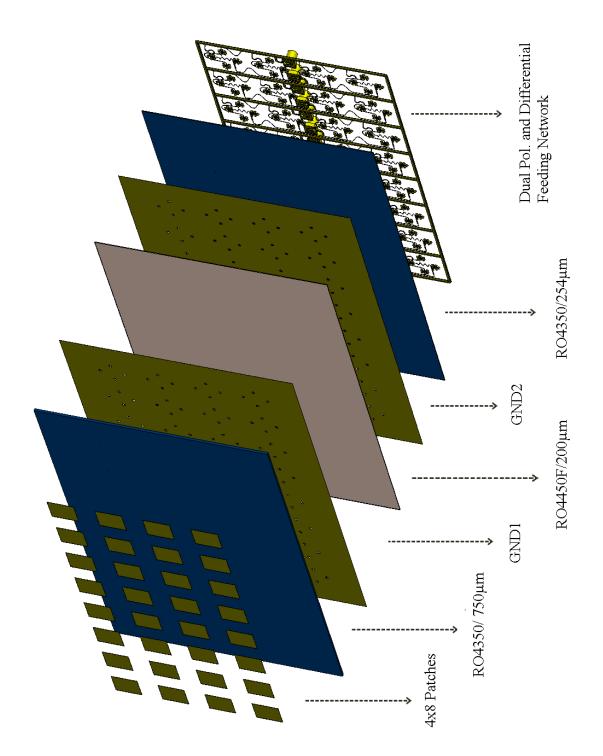


Figure 8.30: CST MWS Design of dual polarized array with 32 radiators. This design incorporates differential feeding.

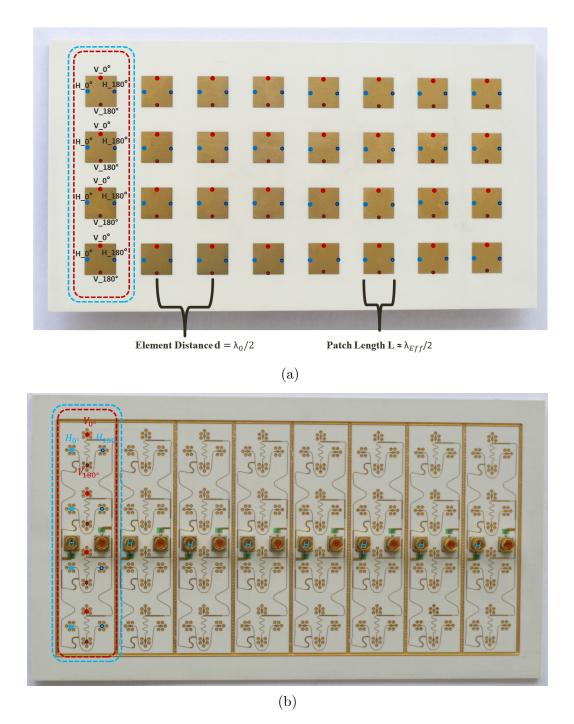


Figure 8.31: (a) Front view (b) Rear view of the constructed dual polarized phased-array antenna with differential feeding. The feeding points for horizontal (blue) and vertical (red) polarization are given. The 1x4 subarray is highlighted by the red and blue frames in dashed lines.

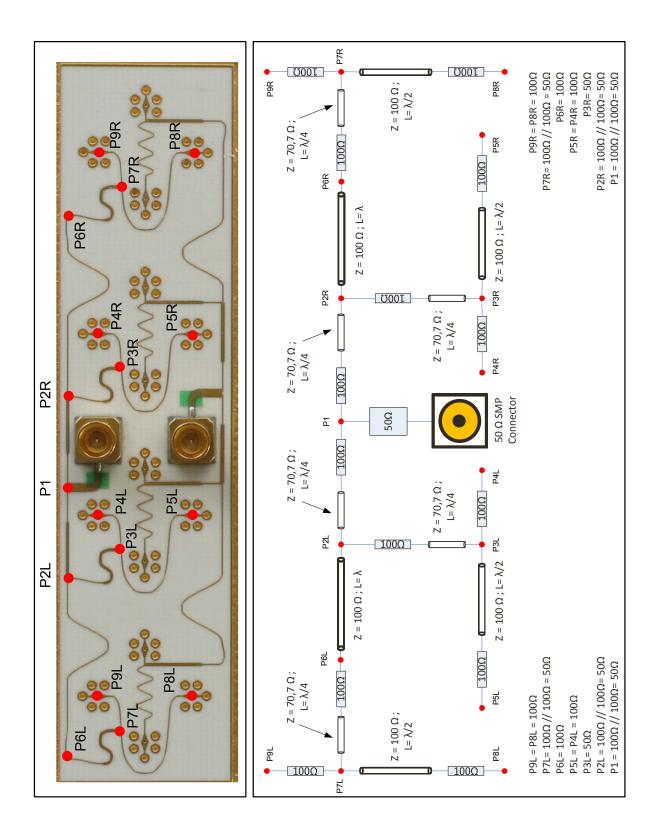


Figure 8.32: 1:8 corporate feeding network design of the dual polarized differential-feed antenna array with its equivalent circuit diagram.

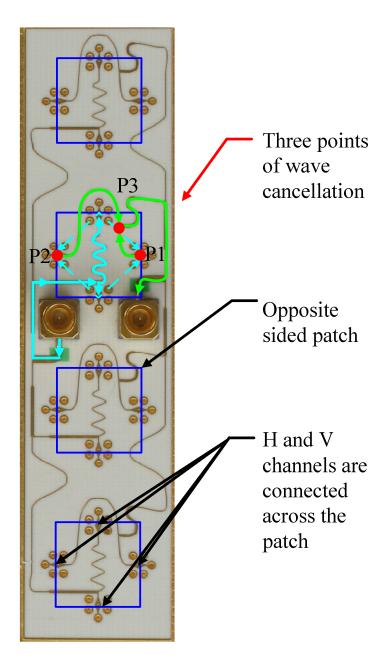


Figure 8.33: Description of the cancellation points in a feeding network with differential-feed antennas. Three cancellation points are responsible for the excellent isolation characteristics of dual-polarized differential-feed antennas.

The CATR measured 3D antenna radiation pattern for both polarization planes are given in figure 8.36. The co-pol patterns are shown in figure 8.36a and figure 8.36b and the x-pol radiation patterns are shown in figure 8.36c and figure 8.36d. The 3D visualization has been generated with the Orbit software used by the RWTH Aachen scientists. The coand x-pol measurements have been performed with 5° steps of  $\Phi$  for the complete upper hemisphere of antenna array. In order to properly visualize the 3D antenna radiation pattern the CATR effects are filtered out. Furthermore, the dataset has been interpolated between the 5° steps of  $\Phi$ . The filtering and the interpolation have been carried out by the RWTH Ph.D. Student Mr. Rasmus Cornelius. The measured 3D co-polar and the x-polar pattern from figure 8.36 are showing excellent correlation with the simulated 3D patterns in figure 8.35. Even the x-polar pattern with its unique geometry (multiple beams of weak x-polar radiation and small x-pol peak at boresight) is unambiguously observable. For the detailed 2D comparison, the CATR measured and CST MWS simulated antenna radiation patterns for horizontal and vertical polarization are shown in figure 8.37 and figure 8.38, respectively. The graphs of the simulated and the measured co-pol antenna radiation pattern are perfectly correlated. But also the measured and simulated x-pol patterns are in excellent agreement. The impressive agreement between the x-pol plots proves also the high measurement performance of the CATR from RWTH Aachen. Furthermore, it can be recognized that the effort was worthwhile to implement the antenna array in the lowpermittivity ROHACELL holding structure (see the picture in figure 8.4b), as part of the antenna under test. In choosing this solution, the array sum pattern was not influenced by any electromagnetic interaction with objects in the nearby environment of the antenna.

Excellent CPS values of -36 dB and -44 dB along boresight direction have been established for horizontal and vertical channel, respectively. Since the center of the main beam is used as the reference, the arithmetic mean of the three x-pol values has been selected for the determination of the CPS.

Is the x-polar pattern further analyzed, it can be recognized that the x-pol antenna radiation patterns are a high attenuated version of the co-polar patterns. The x-pol contribution is dominated by the channel isolation of the vertical and horizontal channel and not significantly disturbed by the x-pol contribution of the differential-feed antennas with their intrinsic low x-pol behavior. Consequently, it can be stated that an attenuated version of the co-polar antenna radiation pattern becomes visible in the x-pol antenna radiation pattern when the x-pol contribution of the antenna itself is lower than the channel isolation. The maximum level at boresight direction should then correspond to the S-Parameter value of the channel isolation. This observation is, to the authors' knowledge, first time documented for array antennas.

In order to thoroughly compare the simulated and measured antenna characteristics, table 8.3 should be used. Here, the most important antenna parameters, like the 3dB beamwidth, the x-pol suppression (CPS) and the first sidelobe suppression are contrasted for both polarization planes. All measured and simulated antenna parameter are in very good agreement. In figure 8.39 the antenna array with differential feeding was used and evaluated as a phased-array antenna. The complete system set-up of the phased-array measurements in the CATR is given in figure 8.4. Five different scan angles have been generated by the amplitude- and phase distribution network (see Appendix A1) to investigate the scan loss as a function of the single element pattern and the CPS performance during beam steering. The scan loss of the phased-array antenna main beam is dominated by the element pattern of a single radiator. Consequently, the isolated single element pattern (dashed orange line) from section 8.6 is implemented here to show the relation between array factor and element factor for the differential-feed antenna case. Both phased-array patterns (horizontal and vertical polarization) are following the element pattern of the single radiator very accurately during the beam steering process. As already suggested by equation 3.72in section 3.4.3, the 3dB beamwidth will be increased by pointing the main beam of the phased-array antenna off-boresight direction. This effect is clearly visible in figure 8.39.It can also be recognized that no grating lobe is entering the visible space due to the  $\frac{\lambda}{2}$  spacing of the single radiators. Even for the  $\pm 60^{\circ}$  azimuth scan angle, hardly no grating lobe becomes visible. The scan loss at  $\pm 60^{\circ}$  is 5 dB to 6.5 dB, which fits very well with the theoretical scan loss evaluated for the LFoV investigation from figure 5.4c in section 5.3.

The CPS performance of the antenna array during beam steering is given in figure 8.40a for horizontal polarization and in figure 8.40b for the vertical polarization plane. By recalling the definition of the CPS in section 3.2, the CPS is determined by computing the difference between the co-polar main beam value and the value of the x-pol pattern at the same angle. As thoroughly discussed in section 3.4.5, the polarization purity is typically decreased by steering the main beam off the phased-array antenna boresight direction. Consequently, the best CPS can be expected for the boresight direction. Here the very good CPS values of 36 dB (H-Pol) and 45 dB (V-Pol) could be realized. But also for the complete azimuth scan range of 120° the CPS could be kept below 36 dB for the horizontal and below 38 dB for the vertical channel, which is approximately 10 dB better that the optimized antenna array from section 8.7. Interestingly, the x-pol level does not rise at other angular positions, when the co-polar main beam is steered off-boresight direction, as for instance narrated for the optimum phase distributed antenna array in section 8.7. Due to the inherently good x-pol suppression of every individual differential-feed patch antenna, the phased-array antenna x-pol suppression during beam steering is kept below 36 dB (H-Pol) and 38dB (V-Pol). This observation, to the best of the authors' knowledge, is unique and reported for the first time.

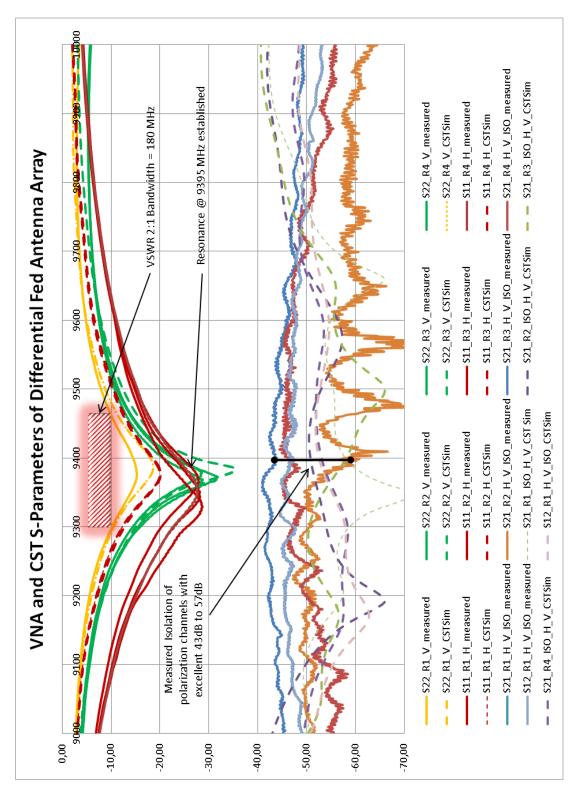


Figure 8.34: Comparison of simulated (CST MWS-dashed lines) and measured (VNA-solid lines) S-Parameters.

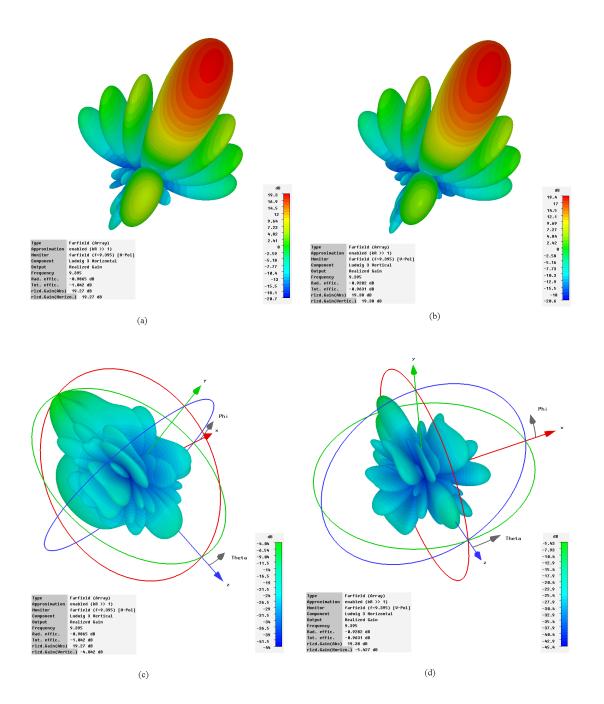


Figure 8.35: CST MWS simulated 3D antenna radiation pattern for horizontal and vertical polarization. (a) Co-polar plot for horizontal polarization. (b) Co-polar plot for vertical polarization. (c) X-polar plot for horizontal polarization. (d) X-polar plot for vertical polarization.

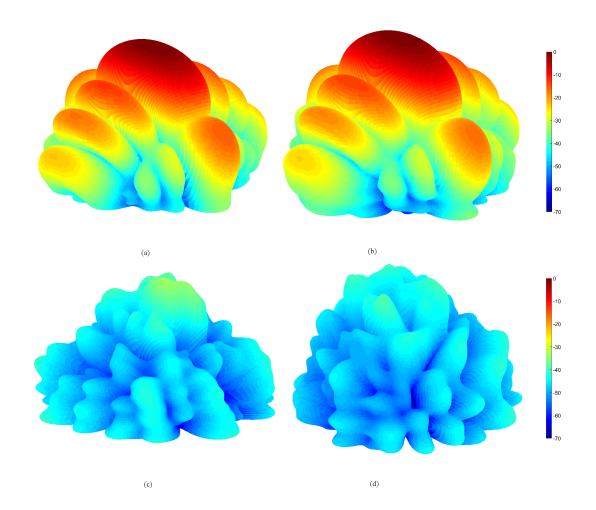
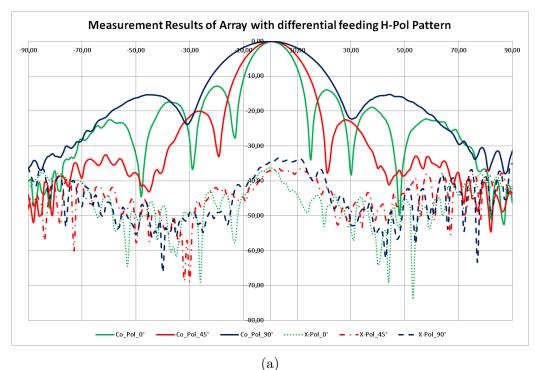


Figure 8.36: RWTH CATR measured 3D antenna radiation pattern of the differential-feed array for horizontal and vertical polarization. The 3D cuts are generated by the Orbit software. The measurement was performed with 5° steps of  $\Phi$  for the complete upper hemisphere of the antenna array. The CATR effects are filtered out and an interpolation between the 5° steps of  $\Phi$  is performed. (a) Co-polar plot for horizontal polarization. (b) Co-polar plot for vertical polarization. (c) X-polar plot for horizontal polarization. (d) X-polar plot for vertical polarization.



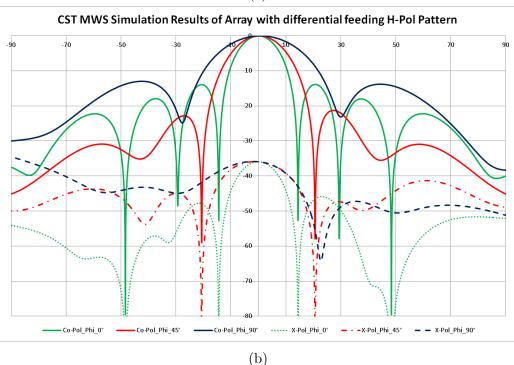
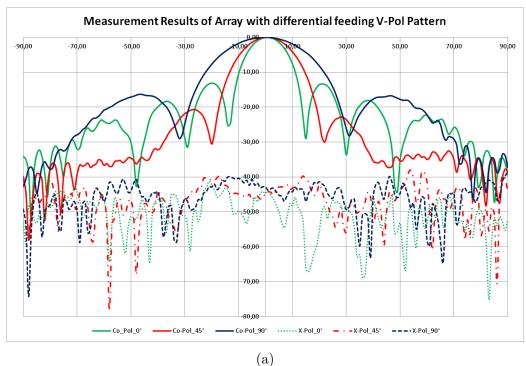


Figure 8.37: Compact range measurement results compared to CST MWS simulation results for **horizontal polarization** channel of the differential-feed antenna array: (a) The co-polar (solid lines) and x-polar (dashed lines) antenna radiation pattern Cuts for  $\phi=0^{\circ}$  in green,  $\phi=-45^{\circ}$  in red and  $\phi=90^{\circ}$  in blue, measured at compact range RWTH Aachen. (b) The copolar (solid lines) and x-polar (dashed lines) antenna radiation pattern Cuts for  $\phi=0^{\circ}$  in green,  $\phi=-45^{\circ}$  in red and  $\phi=90^{\circ}$  in blue, measured at compact range RWTH Cuts for  $\phi=0^{\circ}$  in green,  $\phi=-45^{\circ}$  in red and  $\phi=90^{\circ}$  in blue, simulated with CST MWS.



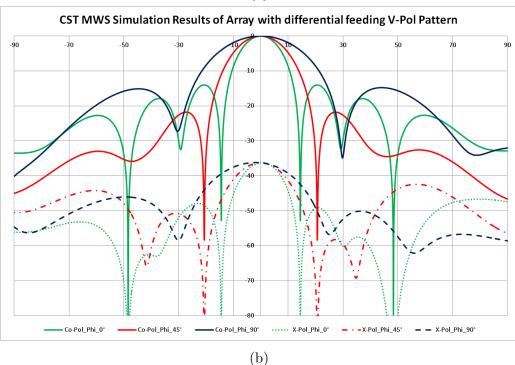
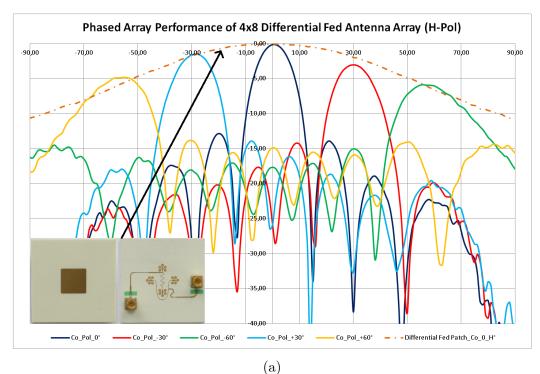


Figure 8.38: Compact range measurement results compared to CST MWS simulation results for **vertical polarization** channel of the differential-feed antenna array: (a) The co-polar (solid lines) and x-polar (dashed lines) antenna radiation pattern Cuts for  $\phi=0^{\circ}$ in green,  $\phi=-45^{\circ}$  in red and  $\phi=90^{\circ}$  in blue, measured at compact range RWTH Aachen. (b) The co-polar (solid lines) and x-polar (dashed lines) antenna radiation pattern Cuts for  $\phi=0^{\circ}$  in green,  $\phi=-45^{\circ}$  in red and  $\phi=90^{\circ}$  in blue, simulated with CST MWS.



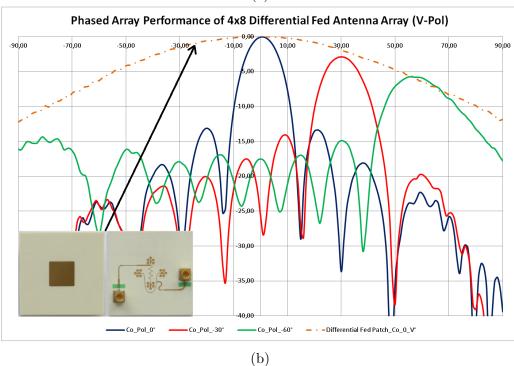
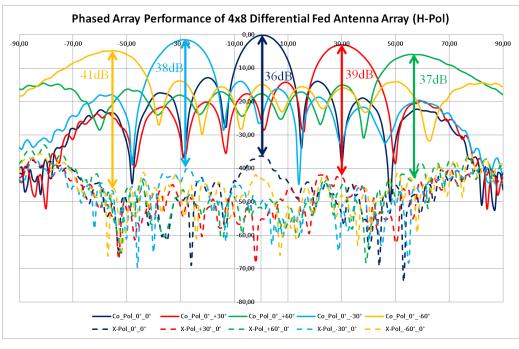


Figure 8.39: Antenna beam steering performance of differential-feed antenna array of 4x8 elements recorded at compact range measurements. The scan loss as the function of the single element antenna pattern can be recognized. The single element pattern was measured separately for an isolated patch element with differential feeding.



(a)

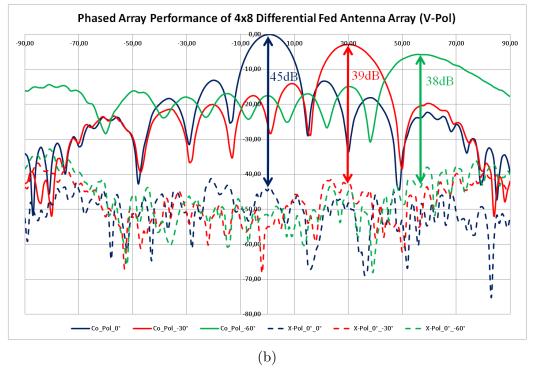


Figure 8.40: X-pol suppression of the differentially fed antenna array of 4x8 elements during beam steering, recorded at compact range. The steady CPS can be recognized when the main lobe is pointed off-boresight direction.

| Parameter  | CST MWS<br>Simulation | CST MWS<br>Simulation | Compact<br>Range Mea- | Compact<br>Range Mea- |
|--|-----------------------|-----------------------|-----------------------|-----------------------|
|  | V-Pol                 | H-Pol                 | surement<br>V-Pol     | surement<br>H-Pol     |
| $ \begin{array}{c} 3 \text{ dB Beamwidth} \\ \text{at } \phi = 0^{\circ} \end{array} $ | 12.5°                 | 12.5°                 | 12.3°                 | 12.1°                 |
| $\begin{array}{c} 3 \text{ dB Beamwidth} \\ \text{at } \phi = -45^{\circ} \end{array}$ | 16.0°                 | 15.9°                 | 16.0°                 | 15.7°                 |
| $\begin{array}{c} 3 \text{ dB Beamwidth} \\ \text{at } \phi = 90^{\circ} \end{array}$  | 24.8°                 | 24.3°                 | 25.3°                 | 25.1°                 |
| $\begin{array}{ccc} CPS & at & \theta = 0^{\circ}, \\ \phi = 0^{\circ} & \end{array}$  | -36.2dB               | -35.9dB               | -44.4dB               | -36.4dB               |
| $\begin{array}{ c c c c c c c c c c c c c c c c c c c$                                 | -36.2dB               | -35.9dB               | -44.5dB               | -37.0dB               |
| $\begin{array}{ c c c c c c c c c c c c c c c c c c c$                                 | -36.2dB               | -35.9dB               | -42.9dB               | -34.5dB               |
| Suppression of<br>first sidelobe at $\phi=0^{\circ}$                                   |                       | -14.0dB               | -13.5dB               | -13.5dB               |
| Suppression of<br>first sidelobe at $\phi=-45^{\circ}$                                 |                       | -22.0dB               | -22.3dB               | -21.0dB               |
| Suppressionoffirstsidelobeat $\phi = 90^{\circ}$ $\phi$                                | -15.0dB               | -13.5dB               | -16.6dB               | -15.3dB               |

Table 8.3: Comparison of simulated and measured antenna radiation pattern characteristics of the differential-feed antenna array.

#### 8.9 Summary of observations

The CATR was verified in its performance to prove the capability of low x-pol detection down to -50 dB. All necessary technical specifications of the CATR from RWTH Aachen are given and the quiet zone was qualified for amplitude and phase errors for measurements at 10 GHz and for the antenna design frequency of 9.395 GHz. The compact range measurement test set-up for the phased-array antenna measurements is explained in details. Furthermore, a flow chart for the design of dual-polarized microstrip patch antenna arrays with very low x-pol contribution is given in section 8.4. It was worthwhile to invest a fair level of effort in the design of the test set-up with the ROHACELL 31 HF antenna holding structure and different absorber materials. In this way, unwanted electromagnetic disturbance in the near field of the antenna under test could be avoided and very good agreements between the CST MWS simulations and the RWTH CATR measurements had been established. It can be stated that all measurement results (S-Parameter with VNA, co-polar and x-polar measurement from CATR) are in very good agreement with the CST MWS simulations.

The design of the single-feed and differential-feed stand-alone antennas is detailed in the sections 8.5 and 8.6. The stand-alone dual polarized antennas show 12 dB and 33.3 dB CPS in boresight direction, respectively, for the cases of single- and differential-feed. These values are very well correlated to the VNA measured S-Parameter of the channel isolation with values of 12 dB and 33.3 dB. For the stand-alone operation of patch antennas with low x-pol requirements the differential-feed antenna is the better choice. The performance of the differential-feed dual polarized microstrip patch antenna. Providing the production- and substrate inaccuracies are effectively considered (e.g. by the production of several test samples with different path and patch length) the x-pol performance of the differential-feed antenna can be extended to approximately 42 dB CPS at boradside direction, as shown by simulations.

In section 8.7 the 4x8 dual-polarized microstrip patch antenna array design with optimized phase excitation of mirrored elements is detailed. **Remarkable CPS values of 46.83 dB and 50.4 dB at boresight direction, respectively for the horizontal and vertical polarization planes have been measured.** During beam steering in the range of 120° azimuth the CPS could be kept below 27 dB (H-Pol) and 33 dB (V-Pol). Unfortunately, it was also noted that the x-pol levels arise on specific angular regions, oppositely placed, when the main beam is pointed off-boresight direction. Furthermore, x-pol suppression performance of phased-array antennas with optimum phase excitation distribution of mirrored elements is significantly degraded when the beam pointing angle will be increased. In case of the weather radar applications, the radiation of x-pol fields to specific angular regions, oppositely placed to the main beam, is very undesired. For instance, target-reflections from other angular directions would be received. However, it is a very effective way to optimize the x-pol performance of array antennas by the phase excitation distributions of mirrored elements, as discovered in chapter 7. **But these antennas should be used** 

only as array antennas and not as phased-array antennas, when very high x-pol suppression is required. The 4x8 antenna array design with optimized phase excitation of mirrored elements was further used for the investigation of x-pol radiation for different array taper functions. In this manner it could be established that the overall array CPS could be optimized when a stronger decay of the taper function is applied. With an edge decay of 3dB, the CPS could be increased from 51 dB to 53 dB. If the edge decay is defined with 5 dB, the CPS was further optimized to 55 dB.

In section 8.8, the 4x8 dual-polarized microstrip patch antenna array design with differentialfeeding is detailed. The CPS values of 36 dB and 44 dB at boresight direction, respectively for the horizontal and vertical polarization planes have been measured. During beam steering in the range of 120° azimuth the CPS could be kept below 36 dB (H-Pol) and 38 dB (V-Pol). The CPS values during the beam steering process are almost 10 dB better than the values of the phase optimized array from section 8.7. Furthermore, the x-pol levels are not increased in other (off-boresight) angular regions and maintained for the complete angular range of 120°. These observations are extraordinary and first time documented, to the best authors' knowledge.

The antenna radiation patterns of the 4x8 dual-polarized microstrip patch antenna array design with differential-feeding was further used for observing new information about the source of x-pol radiation. In this manner, it could be recognized that the shape of the array antenna x-polar pattern can provide information about the dominating source of x-polar radiation. An attenuated version of the co-polar antenna radiation pattern is visible in the x-pol antenna radiation pattern when the x-pol contribution of the antenna itself is lower than the channel isolation. This observation is unique and reported for the first time, to the best authors' knowledge. This fact is true for the antenna in section 8.8. Consequently, the CPS can be further optimized when the isolation between the two polarization ports are increased. To achieve this goal, the stand-alone antenna should be optimized in channel isolation, as previously explained.

## **Summary and Conclusions**

In this dissertation a substantial number of new observations and results have been documented and verified by measurements. The results promote the construction of costefficient and technically stable phased-array and dual-polarized weather radars. In particular, the results from the differential-feed antenna array can be applied to high-frequency applications which place very high requirements on the polarization purity of phased-array and dual-polarized antennas.

All the aspects and results of the weather radar system technology and the polarimetric antenna technology developed in this thesis are summarized in chapters as follows:

**Chapter 1:** The radar basics are made available to the reader. The principle functions of a pulsed Doppler radar, the point-target radar equation, the weather radar equation of a volume target along with the derivation of the radar equation for pulse compression weather radars using planar and phased array antennas are provided. After the introduction of the dual-polarized weather radar system, the basic dual-polarized weather radar parameters based on the scattering matrix and the covariance matrix are explained. The mathematical formulation of the implementation of pulse pair processing of I/Q- signals is detailed. Noise is a crucial topic in the weather radar domain. All the basic foundations are also made available to the reader in Chapter 1, which concludes with the bandwidth analysis of different radar types. Chapter 1 also provides the reader with the cascade noise theory of the receiving components in weather radars. Noise signals are very suitable for monitoring the system performance of radars. Consequently, first noise measurements from the swiss weather service were used to illustrate that the noise signal detected by the radar receiver increases as it rains above the weather radar. This increased noise could be used to calculate the additional loss of the radome and to match the weather radar equation for such events. It also highlights which internal (noise diode) and external (the sun) sources of calibration are used in today's weather radar systems. Careful attention has been paid to the bandwidth parameter of the phased-array antennas which use different types of feeding networks for signal distribution.

**Chapter 2:** In Chapter 2, the reader was appropriately prepared for a detailed discussion of polarimetric antennas and polarimetric weather radar systems so that the polarization state of electromagnetic waves can be accurately represented. Different depiction tools for the polarization of an EM-wave were provided: "The Jones vector, the polarization ellipse

and the Poincaré sphere". Maxwell's equations have also been introduced to describe the propagation of electromagnetic waves in vacuum (for example, for calculating an antenna radiation pattern) or in a medium (for example, for describing electromagnetic waves in substrates of a microstrip patch antennas). Subsequently, the polarization state of EM waves was illustrated with the help of the Jones vector, the polarization ellipse and the Poincaré sphere.

**Chapter 3:** Chapter 3 provides an overview of the relevant theoretical antenna basics the foundation for the antenna developments in the following chapters. All antennas and their design parameters from Chapters 6, 7 and 8 were derived from these basics. Additionally, the basic concepts of the phased-array antennas have been described and the relationship between the element factor of the individual radiators and the array factor is explained in full detail. Measurement definitions such as the far-field have also been considered, these definitions play an important role in chapter 8 for verifying the dual-polarized antennas in the far-field. In order to interpret polarimetric antenna radiation patterns, all the required definitions from the literature survey were presented to the reader. Particular attention was paid to the theoretical definition, which deals with the x-pol contributions of polarimetric antennas. After the introduction of the basic antenna principles, the architecture, the function (using the cavity model), the polarization control, the bandwidth definition and the feeding network design of microstrip antennas are discussed in detail. In order to design antenna arrays on printed circuit boards (PCBs), equations were provided, which were the basis for the calculation of phase constants, group velocity and wave impedances on different dielectric substrates. Different types of substrates and their characteristic influences on the antenna parameters are also considered. In the last part of the third chapter, linear and planar phased-array antennas are considered. Illustrated further is how "Mutual Coupling" affects the function of phased-array antennas and which polarization effects are to be expected when the beam direction of the main lobe is varied and when is it useful to group individual radiators into subarrays.

**Chapter 4:** CST MWS Studio suite was chosen to design and simulate the dual-polarized multilayer antennas. This chapter explained the basic functionalities of the CST MWS program and graphically explained is the FIT (Finite Integration Technology) concept, the numerical calculation method. The "Time Domain Solver", which provided all the simulation results in this dissertation was also discussed. The hardware environment and the duration of single radiator and antenna array simulations are also presented. The simulation times depended strongly on the selected "Mesh" cells, i.e. the discretization of the 3D model and consequently, the mesh settings were also introduced. At the end of the fourth chapter, the optimization function of CST MWS was shown which addressed the S-Parameters and polarimetric antenna measurement values. For very fast estimation of the key antenna parameters of large array antennas with thousands of individual elements, the function of the "Far-Field Plot Monitor" was introduced and explained with an application example.

#### SUMMARY AND CONCLUSIONS

**Chapter 5:** In Chapter 5, a system concept of a dual-polarized phased-array weather radar was developed. The reasons that justify the development of phased-array weather radar systems in a dense network against the alternative of using high-power weather radar systems were highlighted. The new phased-array weather radar system serves as a principle concept for the antenna development and particularly for this purpose, suitable dual-polarized antenna arrays were designed in Chapters 7 and 8. On the basis of the weather radar equations from Chapter 1, the required key parameters for the new PAWR were calculated so that the antenna design could be established. The PAWR was constructed with 800 subarrays, 2.7m x 2.7m edge length, and a subarray configuration of 4x8 radiators. To ensure cost-effective PCB production, a subarray with 8 chip-based TRMs and a control FPGA was implemented. Without pulsed compression functionality, the PAWR provides 14.3 kW of transmission power, which corresponds to an approximate range of 50 km. The TRM output power amounts to about 2.5 watts. Given the application, the elevation scan range is limited to  $30^{\circ}$ , with an azimuthal scan of  $120^{\circ}$  such features allow 3 planar antenna units to achieve a  $360^{\circ}$  azimuthal coverage. Due to the application of specific limit set on the elevation scan, the number of TRMs could be reduced by a factor of four. CST MWS investigations were carried out with appropriate LFOV (limited field of view) antenna configurations for the weather radar application of an X-band radar with a limited elevation range of  $30^{\circ}$ . In this spirit, the antenna radiation patterns of single radiators, together with 1x2 array, 1x4 array, and a 1x8 array were compared. It could be shown that the 1x4 array configuration is best suited for this application. The system block diagram also describes the configuration of a large array antenna with a complete analogue and digital transmission and reception paths. Solution concepts for highly accurate phase and amplitude calibrations of such a complex, phase-controlled radar system have been provided from the literature survey. By means of PN-gating (pseudo noise gating), each TRM can be evaluated in phase and amplitude, so that the excitation coefficients of the antenna elements are available at any time. Given the small number of 50 I/Q- data channels, standard network components can be used by this system concept.

**Chapter 6:** Chapter 6 gives a summary of references used in the reduction methods of x-pol radiation in single radiators. In this context, different feeding mechanisms for microstrip antennas were analyzed and evaluated. The probe-feed antennas have been identified as suitable candidates for use within phase-array weather radar systems with high polarization purity. For the first time, circular and square microstrip antennas were investigated and compared with respect to their cross polarization behavior. It was shown that the cross polar suppression is not significantly different for circular and square microstrip antennas and it has also been observed that design changes such as filled and encapsulated via feeds or the rounding off of patch antenna edges do not cause any substantial improvement in the cross-polar suppression. Subsequently the effect of increasing the antenna area, on the x-polar reduction was observed and it was evaluated by means of radiation pattern synthesis. It could be shown that the cross polar contributions in the outer angular range of the antenna pattern can be relocated when the antenna surface is enlarged. The cross-polar contributions, generated by the antenna distribution network,

are usually minimized by an insulating "GND layer". In this thesis it could be shown that asymmetries below the "GND Layer" also increase the cross polarization values. Also the direction with which the incident EM-wave enters the feed has an influence on the cross-polarization suppression. The most promising technology i.e. the differential feeding of microstrip antennas for the reduction of x-polar radiation has been investigated in great detail. The co-polar and x-polar antenna radiation patterns of the differentiallyfed microstrip patch antennas were compared with those of the separately fed antennas (single-feed), such that the advantages and disadvantages of utilizing the antennas within phased-array weather radar could be identified. The main advantages of differentially-fed antennas are the symmetric co-polar radiation pattern, the symmetrical main lobe, the symmetric array factor, and the reduced x-polar radiation, which are in the form of four maxima in the x-polar pattern. In order to study the formation of x-polar radiation of all microstrip antennas, two new graphical approaches: the field line distribution below the patch and the current distribution on the patch, together with the theoretical cavity model of microstrip antennas were developed. In this regard, the relevant reasons for the generation of cross-polar radiation components of microstrip antennas have been identified. The cross polar components in microstrip antennas are generated by the radiation mechanism of the antenna itself. Due to the differential excitation of the patch antenna (excitation of the antenna by two signals which are 180° out of phase but equal amplitude), the field line distributions above and below, as well as the surface currents of the antenna have reflection symmetry. Consequently, a minimum in the E and H cut of the cross-polar pattern is generated and the 4 cross-polar maxima occur. If the mirror symmetry around the center of the radiating surface is not maintained, increased cross-polar components are produced. Graphical analyses were used to provide evidence in Chapter 6.

**Chapter 7:** Chapter 7 summarizes the literature references used in the reduction methods of cross-polar radiation in antenna arrays. The literature research proves that the x-polar radiation is reduced by suitable phase selection of the individual radiators in antenna arrays. Given these facts, different phase distributions of 1x4 antenna arrays were simulated with CST MWS and then compared to a differential-feed 1x4 antenna array. The purpose of this study was to determine whether arrays with optimized phase distributions provide comparable CPS (cross polar suppressions) to differential-feed antenna arrays, because the design of the differential-feed antenna arrays is very complicated and the single-feed antenna elements would greatly simplify the design process of a microstrip antenna and its distribution network. The 1x4 array configuration was chosen, given the system design in chapter 5. Using the 3D field simulation program CST MWS, antenna arrays with 1x4 and 2x4 elements and optimized phase distributions are designed and qualified. According to the detailed x-pol radiation pattern synthesis, the most promising phase distribution (configuration 3) was applied to a 4x8 antenna array (configuration 3-4x8) and compared to a differential-feed 4x8 array (configuration 7-4x8). The results show that the best CPS occurs in the angular region when the mirrored individual elements are excited with  $180^{\circ}$ phase shift. Antenna engineers can use this new information to move the maximum CPS to the desired angular region. The differential-feed 7-4x8 array configuration provides the best performance, with an excellent cross-polar suppression of 48.4dB over the entire azimuthal range of  $\pm 60^{\circ}$  for the E, H, and  $45^{\circ}$  cuts of the x-pol radiation patterns. However, the 3-4x8 array configuration with optimized phase distribution of the single radiators also yields very good CPS with  $45.3 \, dB$ . In addition, it was observed that the difference in the CPS values for single- and differentially-excited antennas decreased as the array is enlarged. The difference in the CPS for the 1x4 array configuration was still 5 dB while this difference in the CPS result for the 2x4 arrays was already reduced to 3.6 dB and that for the 4x8 arrays to 3.3 dB. The investigations of chapter 7 ascertained that antenna arrays with optimized phase distribution provide comparable CPS values as the complex designed antenna arrays with differential feeding.

**Chapter 8:** In chapter 8, all theoretical and practical experiences obtained from the previous chapters are used to design pure- and dual-polarized antenna arrays suitable for a weather radar application. Two different type of antennas (first, 4x8 antenna array with optimized phase distribution and the second, a differential-feed 4x8 antenna array) are designed for this purpose by means of CST MWS simulation and are verified at the CATR (Compact Antenna Test Range) of the University of RWTH Aachen.

Given the very low x-polar radiation contributions of the antennas developed in this chapter, the CATR of the RWTH Aachen University is initially validated in its measuring accuracies (phase and amplitude) within the "QuietZone" for the co-polar and x-polar polarization patterns.

The CATR is able to detect the x-polar fields up to -50dB within the "Quiet Zone" region of 15cm x 15cm. The measurement accuracies are  $\pm 0.1$  dB for the co-polar measurements and  $\pm 1.5$  dB for the x-polar measurements. The measurement accuracy of the phase is approximately  $\pm 2^{\circ}$ . The AUT in phased array operation was supported by ROHACELL 31HF material, with the metal housing of the amplitude and phase distribution network being isolated by pyramidal absorbers at the back of the antenna. These measures have been implemented to ensure an unaffected near-field environment of the antenna within the "QuietZone" and to provide very good agreements between the CST MWS simulations and the RWTH CATR measurements.

The development process of the antennas in this dissertation has been described in great detail with reference to a flowchart. Here, the sequence of the different analyses and developments were explained to the reader in order to finally obtain an antenna array with high cross-polar suppression for use within a phased-array weather radar. As shown in the development process, four antenna developments have been carried out.

Initially, two types (single-feed and differential-feed) of dual-polarized single radiators were developed. The CST MWS simulated S11-Parameters of the single-feed and dual-polarized antenna match impressively (99.78%) with those of the VNA measurements. Also the simulated and measured antenna patterns for both polarizations are in an excellent agreement. As expected, the single-feed and dual-polarized microstrip patch antenna yields an insufficient CPS of about 12 dB. The reason for this is the low isolation of 12 dB between the two

polarization channels. Interestingly, the VNA measured channel isolation S21 of 12 dB is in perfect agreement to the measured CPS at boresight direction. The VNA measurement can be used to get a very good estimate about the x-pol performance of an antenna at boresight direction. In this way, the costs for complex x-pol measurements at antenna measurement facilities can be saved for the first antenna verification. Furthermore, every small patch antenna can be evaluated simply via VNA measurements. Also the simulated S21 and the simulated CPS at antenna boresight show conformity within 10 dB. As a consequence, it can be stated that two separated evaluation methods (simulation and measurement) are showing a consistent correlation between S21 and boresight CPS performance.

The differential-feed, dual-polarized antenna also shows an excellent agreement between CST MWS simulation and the real VNA and CATR measurements. The measured S11-Parameters match 99.83% to that of the simulation. A CPS of about 33.3 dB could be provided for the dual-polarized antenna and as expected, 4 maxima have been observed in the cross-polar antenna radiation pattern. However, the S21-Parameters of the simulation differ from those of the measurement, which indicates that the CST MWS simulation model differs to that of the produced antenna prototype. The real substrate inhomogeneity and the phase and amplitude changes that occur could be the likely reasons for this discrepancy, which are not taken into account in the CST MWS model. The simulation results prove that if the production inaccuracies are effectively taken into account, a CPS of 42 dB can be achieved by the differential-feed antenna element.

The single-feed, dual-polarized patch antenna element was used to generate a 4x8 antenna array with optimized phase distribution of mirrored radiators. The simulated S11-Parameters of the dual-polarized array antennas correspond within an impressive 99.77%to those of the VNA measurements. The antenna radiation patterns for both polarizations are in excellent agreement with that of the CST MWS simulation. Impressive CPS values of 46.83 dB and 50.4 dB in the main beam direction have been measured for the horizontal and vertical polarization channels of the dual-polarized antenna array. In phased array mode within the scan range of 120°, the CPS value was held below 27 dB (H-pol) and below 33 dB (V-pol) respectively. However, it has been demonstrated by these measurements that x-pol components on the opposite angular positions increase as the main beam is steered. This fact restricts the usage of phase optimized antenna arrays in weather radar applications, as the x-pol radiation in other angular directions is very undesirable and generates target-reflections that could lead to erroneous weather radar measurements. Nevertheless, the results obtained in this dissertation are very helpful for the development of array antennas without phased-array operation. The phase-optimized, mirrored and dual-polarized antenna arrays are ideal candidates for applications with high CPS requirements. In addition, the influence of taper functions on the cross-polar contributions was investigated using the phase-optimized antenna array.

# It could be demonstrated that the array CPS could be optimized when a stronger decay of the taper function is applied. An amplitude taper with 3dB edge-decay has improved the CPS from 51 dB to 53 dB. Whereas, amplitude taper with 5 dB edge-decay optimizes the CPS further to 55 dB.

The differential-feed dual-polarized patch antenna element was used to generate a 4x8 antenna array. The CST MWS simulated S11-Parameters of the dual-polarized array antenna correspond with an impressive 99.50% to those of the VNA measurements. Also the simulated and measured antenna patterns for both polarizations are in very good agreement. For the horizontal and vertical polarization channel of the dual-polarized antenna array, impressive CPS values of 36 dB and 44 dB in the boresight direction have been demonstrated. In phased array mode within the scan range of 120°, the CPS value could be held below 36 dB (H-pol) and below 38 dB (V-pol), respectively. This result is about 10 dB better than the phase-optimized 4x8 antenna array. In addition, it could be verified by measurements that the x-pol components do not change at other angular positions within the scanning range of 120°, when the main lobe is steered. Given this reason, the differentially-feed antenna array is identified as the perfect candidate for phased array weather radar applications.

The antenna radiation patterns of the differential-feed 4x8 antenna array were also used to investigate the dominant source of the x-polar radiation in antenna arrays. The shape of the array antenna x-polar pattern can provide information about the dominating source of x-polar radiation. If the x-polar patterns are highly attenuated versions of the co-polar patterns, then the x-pol patterns are dominated by the finite channel isolations between the polarization ports. An attenuated version of the co-polar antenna radiation pattern is visible in the x-pol antenna radiation pattern when the x-pol contribution of the antenna itself is lower than the channel isolation. With the help of this newly acquired information, antenna designers can **target-optimize** the CPS of antenna arrays or indeed other antenna types or configurations.

The amplitude and phase distribution network was explained in detail in **Appendix A**. This device was created under the author's supervision during his bachelor's thesis and was used to measure the antenna arrays in phased-array mode at the University of RWTH Aachen. An excellent phase accuracy of  $\pm 1.25^{\circ}$  and an adequate amplitude accuracy of  $\pm 0.25$  dB was achieved by this instrument. The distribution network was developed to investigate the x-pol antenna characteristics in phased-array mode. Furthermore, it enabled the investigations of different antenna excitation coefficients on the x-polar radiation patterns.

The dissertation closes with this *summary and the conclusions*, and also with a detailed discussion of possible *future research topics* in the fields of antenna and radar system technology.

## Zusammenfassung und Schlussfolgerungen

In der vorliegenden Dissertation wurden eine Vielzahl von neuen Beobachtungen und Ergebnissen dokumentiert und messtechnisch verifiziert. Die Ergebnisse erlauben es, ein kosteneffizientes und technisch herausragendes dual-polarimetrisches und phasengesteuertes Wetterradar aufzubauen. Besonders die Ergebnisse der differentiell gespeisten Gruppenantennen werden in Hochfrequenzapplikationen Anwendung finden, die sehr hohe Ansprüche an die Polarisationsreinheit von phasengesteuerten und dual-polarimetrischen Gruppenantennen stellen.

Alle in dieser Dissertation ausgearbeiteten Ergebnisse und Aspekte aus der Wetterradarsystemtechnik und polarimetrischen Antennentechnik werden kapitelweise wie folgt zusammengefasst:

Kapitel 1: Die Radargrundlagen wurden dem Leser zur Verfügung gestellt. Die Funktion eines gepulsten Dopplerradars, die Radargleichung für ein Punktziel, die Wetterradargleichung eines Volumenziels sowie die Herleitung der Radargleichung für ein pulskomprimiertes Wetterradar mit planarer- und phasengesteuerter Antenne wurden bereitgestellt. Nach Einführung des Prinzips eines polarimetrischen Wetterradarsystems wurden die grundlegenden polarimetrischen Wetterradarmessgrößen auf Basis der Streumatrix und Kovarianzmatrix diskutiert. Die mathematische Implementierung im Wetterradarempfänger geschieht durch Puls-Paar-Prozessierung von I/Q-Signalen, welche detailliert betrachtet wurden. Auch die Rauschtheorie in einer Kaskade von Empfangskomponenten eines Wetterradarsystems wurde in Kapitel 1 dem Leser zur Verfügung gestellt. Rauschsignale sind sehr gut geeignet, um die Systemperformanz eines Radars zu kontrollieren. Hierbei wurden erste Rauschmessungen und Niederschlagsmessungen von Meteo Schweiz genutzt, um zu zeigen, dass das vom Radarempfänger detektierte Rauschsignal ansteigt, wenn es über dem Wetterradar regnet. Dieser Rauschanstieg könnte genutzt werden, um die Wetterradargleichung zu korrigieren. Ebenfalls wurde gezeigt, welche internen (Rauschdiode) und externen (die Sonne) Kalibrationsquellen in heutigen Wetterradarsystemen genutzt werden. Das Kapitel 1 schließt mit der Bandbreitenbetrachtung für unterschiedliche Radarsystemvarianten ab. Besonders wurde auf die Bandbreite von phasengesteuerten Gruppenantennen eingegangen, die unterschiedlichste Speisenetzwerke zur Signalverteilung nutzen.

Kapitel 2: In Kapitel 2 wurde der Leser für eine detaillierte Diskussion von polarimetrischen Antennen und Wetterradarsystemen vorbereitet, sodass der Polarisationszustand von elektromagentischen Wellen genau dargestellt werden kann. Hierzu wurden unterschiedliche Darstellungsmöglichkeiten zur Polarisation einer EM-Welle bereitgestellt: "Der Jones Vektor, die Polarisationsellipse und die Poincaré Kugel". Es wurden die Maxwell'schen Gleichungen eingeführt, welche die Ausbreitung von elektromagnetischen Wellen im Vakuum (z. B. zur Berechnung eines Antennenrichtdiagramms) oder in einem Medium (z. B. zur Beschreibung von elektromagnetischen Wellen in Substraten einer Mikrostreifenleiterantenne) beschreibt.

Kapitel 3: Kapitel 3 liefert einen Überblick zu den relevanten theoretischen Antennengrundlagen der Mikrowellentechnik als Fundament für die Antennenentwicklungen in den Folgekapiteln. Alle Antennen und deren Designparameter aus den Kapiteln 6, 7 und 8 wurden von diesen Grundlagen abgeleitet. Zusätzlich wurden die Grundlagen zu phasengesteuerten Antennen beschrieben und der Zusammenhang zwischen Elementfaktor von Einzelradiatoren und Arrayfaktor von Antennengruppen beleuchtet. Auch Messdefinitionen wie die Fernfelddefinition wurden beschrieben, welche in Kapitel 8 zur Verifikation der dual-polarisierten Antennen im Fernfeld, eine große Rolle spielt. Zum Deuten von polarimetrischen Antennenrichtcharakteristiken wurden alle relevanten Definitionen aus der Literatur zusammengefügt dem Leser dargestellt. Besonders wurde auf die theoretische Definition eingegangen, welche sich mit den kreuzpolaren Anteil der Antenne beschäftigt. Nach Einführung der allgemein gültigen Grundlagen für alle Antennen wurde sehr detailliert auf den Aufbau, die Funktion (mittels Kavitäten -Modell), die Architektur, die Polarisationsteuerung, die Bandbreitendefinition und die Speisenetzwerke von Mikrostreifenantennen eingegangen. Um Antennenarrays auf Leiterplatten (PCBs) entwerfen zu können, wurden Gleichungen bereitgestellt, welche die Grundlage zur Berechnung von Phasenkonstanten, Phasengruppengeschwindigkeit und Wellenimpedanzen auf und in unterschiedlichen dielektrischen Substraten sind. Auch eine Reihe von unterschiedlichen Substratarten und der Einfluss von Substratkenngrößen auf die Antennenparameter wurden diskutiert. Im letzten Teil des dritten Kapitels wurden lineare und planare phasengesteuerte Antennenarrays betrachtet. Es wurde erklärt, warum "Mutual Coupling" die Funktion von phasengesteuerten Antennen beeinflusst und mit welchen Depolarisationseffekten zu rechnen ist, wenn die Strahlrichtung der Hauptkeule variiert wird. Schlussendlich wurde erklärt, wann es sinnvoll ist Einzelradiatoren zu Gruppen (Subarrays) zusammenzuschalten.

Kapitel 4: CST MWS wurde ausgewählt, um die polarimetrischen Multilagenantennen zu entwerfen und elektromagnetisch zu simulieren. In diesem Kapitel wurden die Grundfunktionalitäten des Programms CST MWS erklärt und die numerische Berechnungsmethode FIT (Finite Integration Technik) grafisch beschrieben. Besonders wurde auf den "Time Domain Solver" eingegangen, welcher alle Simulationsergebnisse innerhalb der vorliegenden Dissertation geliefert hat. Auch die Hardwareumgebung und die Simulationszeiten von Einzelradiatoren und Gruppenantennen wurden präsentiert. Die Simulationszeiten sind stark abhängig vom ausgewählten "Mesh", also der Diskretisierung des 3D Modells. Alle zu berücksichtigen Einstellungen zu einem Mesh werden demzufolge ebenfalls erklärt. Am Ende des vierten Kapitels wurde die Optimierungsfunktion von CST MWS unter Berücksichtigung von S-Parameter Werten und auch Antennenmessgrößen gezeigt. Um Antennenschlüsselparameter von sehr großen Arrayantennen mit vielen Tausend Einzelelementen schnell abschätzen zu können, wurde die Funktion des "Far-Field-Plot-Monitors" eingeführt und anhand eines Applikationsbeispiels erklärt.

Kapitel 5: In Kapitel 5 wurde ein Systemkonzept eines phasengesteuerten Wetterradars entwickelt. Es wurden die Gründe benannt, die eine Entwicklung von phasengesteuerten Wetterradarsystemen in einem dichten Netzwerk, anstatt der Verwendung von Hochleistungswetterradarsystemen, rechtfertigen. Das neue Systemkonzept dient als Vorlagekonzept für die Antennenentwicklung. In den Kapiteln 7 und 8 wurden geeignete polarimetrische Antennenarrays für genau dieses Systemkonzept entworfen. Anhand der Wetterradargleichungen aus Kapitel 1 wurden die benötigten Schlüsselparameter für das neue PAWR berechnet, sodass die Antennenauslegung stattfinden konnte. Das entwickelte PA-WR wurde mit 800 Subarrays, 2.7m x 2.7m Kantenlänge und einer Subarraykonfiguration von 4x8 Radiatoren ausgelegt. Eine Subarrayplatine wird mit 8 chipbasierten TRMs und einem Kontroll-FPGA realisiert, um eine kostengünstige Produktion der Leiterplatten zu gewährleisten. Wird ohne Pulskompression gearbeitet, stellt das PAWR 14.3 kW Sendeleistung zur Verfügung, was einer Reichweite von etwa 50 km entspricht. Die TRM Ausgangsleistung beläuft sich dabei auf etwa 2.5 Watt. Der Elevationsscanbereich ist aufgrund der Applikation eingeschränkt auf 30°, wobei in Azimutaler Richtung mit 120° gescannt werden kann. Für eine 360° Azimutalabdeckung würden 3 planare Antenneneinheiten verwendet werden. Aufgrund der applikationsbedingten Einschränkung des Elevationsscans konnte die TRM- Anzahl um den Faktor 4 minimiert werden. Mittels CST MWS fanden diesbezüglich Untersuchungen statt, welche sich mit geeigneter LFOV (Limited Field of View) Antennenkonfiguration für die Wetterradarapplikation eines X-Band Radars mit eingeschränktem Elevationsbereich von 30° befassen. Hierzu wurden die Antennenrichtcharakteristiken für Einzelradiatoren, 1x2 Array, 1x4 Array und einem 1x8 Array verglichen. Es konnte gezeigt werden, dass die 1x4 Arraykonfiguration für diese Anwendung am besten geeignet ist. Das System-Blockdiagramm beschreibt zudem die Konfiguration einer großen Array Antenne mit komplettem analogen und digitalen Sende- und Empfangspfad. Lösungskonzepte für hochgenaue Phasen- und Amplitudenkalibrationen eines solch komplexen, phasengesteuerten Radarsystems wurden aus der Literatur bereitgestellt. Mittels PN-Gating (Pseudo Noise Gating) kann jedes TRM in Phase und Amplitude ausgewertet werden, sodass die Anregungskoeffizienten der Antenne zu jeder Zeit zur Verfügung stehen. Aufgrund der geringen Anzahl von 50 I/Q- Datenkanälen können Standard Netzwerkkomponenten verwendet werden.

Kapitel 6: Das Kapitel 6 gibt zu Beginn eine Zusammenfassung von Literaturquellen zu Reduktionsmethoden von x-pol Strahlung bei Einzelradiatoren. In diesem Zusammenhang wurden unterschiedliche Speisemechanismen für Mikrostreifenantennen analysiert und ausgewertet. Die Probe-Feed Antennen wurden als geeignete Kandidaten für die Nutzung innerhalb von phasengesteuerten Wetterradarsystemen mit hoher Polarisationsreinheit identifiziert. Zum ersten Mal wurden kreisförmige und quadratische Mikrostreifenantennen in ihrem Kreuzpolarisationsverhalten verglichen. Es konnte gezeigt werden, dass sich die Kreuzpolarisationsunterdrückung nicht signifikant für kreisförmige und quadratische Mikrostreifenantennen unterscheidet. Ebenfalls wurde nachgewiesen, dass Designänderungen wie gefüllte und gekapselte Via-Feeds oder das Abrunden von Patchantennenkanten keine nennenswerte Verbesserung der Kreuzpolarisationsunterdrückung hervorrufen. Darauffolgend wurde der Effekt der x-polaren Reduktion durch Vergrößerung der Antennenfläche betrachtet und anhand von Antennenrichtcharakteristiken ausgewertet. Es konnte gezeigt werden, dass sich die Kreuzpolarisationsanteile in den Außenwinkelbereich des Antennenpatterns verschieben lässt, wenn die Antennenfläche vergrößert wird. Die Kreuzpolarisationsanteile, hervorgerufen durch das Antennenverteilernetzwerk, werden üblicherweise durch einen isolierenden "GND Layer" minimiert. In diesem Kapitel wurde nachgewiesen, dass auch Asymmetrien unterhalb der "GND Layer" die Kreuzpolarisationsanteile erhöhen. Auch die Richtung, mit der die einfallende Welle auf das Feed trifft, hat Einfluss auf die Kreuzpolarisationsunterdrückung. Die vielversprechendste Technologie zur Reduktion von x-polarer Strahlung, die differentielle Speisung von Mikrostreifenantennen, wurde genauestens erforscht. Die co-polaren und x-polaren Richtcharakteristiken der differentiell gespeisten Mikrostreifenantennen wurden mit denen der separat gespeisten Antennen (single-feed) verglichen, sodass die Vor- und Nachteile für die Nutzung der Antennen innerhalb eines phasengesteuerten Antennenarrays für ein Wetterradar identifiziert werden konnten. Die Hauptvorteile von differentiell gespeisten Antennen sind die symmetrischen co-polaren Richtcharakteristiken, die symmetrische Hauptkeule, der symmetrische Arrayfaktor und die geringen x-polaren Anteile, die sich in Form von vier Maxima in der x-polaren Richtcharakteristik zeigen. Um die Entstehung von x-polarer Strahlung aller Mikrostreifenleiterantenne zu erforschen, wurden zwei neue grafische Ansätze, die Feldlinienverteilung unterhalb des Patches und die Stromverteilung auf dem Patch zusammen mit dem theoretischen Kavitätsmodel von Mikrostreifenantennen, entwickelt. Bei dieser Betrachtung konnten die maßgeblichen Gründe für die Entstehung von kreuzpolaren Strahlungsanteilen von Mikrostreifenantennen identifiziert werden. Die Kreuzpolarisationsanteile bei Mikrostreifenantennen entstehen durch den Abstrahlmechanismus der Antenne selbst. Durch differentielle Anregung der Patchantenne (Anregung der Antenne durch zwei Signale, die 180° Phasenversatz und gleiche Amplitude aufweisen) sind die Feldlinienverteilungen ober- und unterhalb sowie die Oberflächenströme der Antenne spiegelsymmetrisch. Dadurch ergeben sich ausgeprägte Minima im E- und H- Schnitt des kreuzpolaren Patterns und 4 kreuzpolare Maxima entstehen. Wird die Spiegelsymmetrie um den Mittelpunkt der Strahlerfläche bei der Anregung der Antenne nicht gewährleistet, entstehen erhöhte kreuzpolare Anteile. Durch grafische Analyseansätze wurden in Kapitel 6 dafür Belege geliefert.

**Kapitel 7:** In Kapitel 7 wird zu Beginn eine Zusammenfassung von Literaturquellen zu Reduktionsmethoden von x-pol Strahlung bei Antennengruppen bereitgestellt. Die Literaturrecherche belegt, dass durch geeignete Phasenansteuerung der Einzelradiatoren in Antennengruppen, die x-polare Strahlung herabgesetzt wird. Aufgrund dessen wurden in Kapitel 7 unterschiedliche Phasenverteilungen für 1x4 Antennenarrays mit CST MWS simuliert und mit einem differentiell gespeisten 1x4 Antennenarray verglichen. Ziel dieser

Untersuchung war es, herauszufinden, ob Arrays mit ausgewählten Phasenverteilungen eine vergleichbare CPS liefern wie differentiell gespeiste Antennenarrays. Das Design des Speisenetzwerkes von differentiell gespeisten Antennenarrays für die Anwendung in einem Radar mit phasengesteuerter Antenne ist sehr kompliziert. Daher würden einzelangeregte Antennenelemente den Designprozess einer Mikrostreifenleiterantenne erheblich vereinfachen. Die 1x4 Arraykonfiguration wurde aufgrund des System Designs in Kapitel 5 gewählt. Mittels CST MWS wurden Antennenarrays mit 1x4 und 2x4 Elementanordnung und optimierter Phasenverteilung designt und qualifiziert. Nach detaillierter Richtdiagrammsynthese wurde die vielversprechendste Phasenverteilung (Konfiguration 3) auf ein 4x8 Antennenarray (Konfiguration 3-4x8) angewendet und mit einem differentiell gespeisten 4x8 Array (Konfiguration 7-4x8) verglichen. Die Resultate zeigen, dass die beste CPS im Winkelbereich auftritt, wo die gespiegelten Einzelelemente mit 180° Phasenversatz angeregt werden. Antenneningenieure können diese neugewonnene Information nutzen, um die maximale CPS auf den gewünschten Winkelbereich zu verlegen. Das differentiell gespeiste Array in Konfiguration 7-4x8 liefert die beste Performanz, mit einer exzellenten Kreuzpolarisationsunterdrückung von 48.4dB über den gesamten azimutalen Winkelbereich von  $\pm 60^{\circ}$  für den E-, H- und 45° Schnitt der Richtcharakteristik. Aber auch das Antennenarray in Konfiguration 3-4x8 mit geeigneter Phasenansteuerung der Einzelradiatoren liefert sehr gute CPS mit 45.3 dB. Zusätzlich konnte festgestellt werden, dass die Differenz der CPS Werte für einzel- und differentiell angeregte Antennen bei Vergrößerung des Arrays abnimmt. Beim 1x4 Arrayvergleich lag der Unterschied der CPS noch bei 5 dB, wobei die Differenz im CPS Ergebnis bei den 2x4 Arrays schon auf 3.6 dB und bei den 4x8 Arrays auf 3.3 dB minimiert wurde. Durch die Untersuchungen in Kapitel 7 konnte nachgewiesen werden, dass Antennenarrays mit geeigneter Phasenansteuerung der Einzelradiatoren vergleichbare CPS Werte liefern wie komplex designte Antennenarrays mit differentieller Speisung.

**Kapitel 8:** In Kapitel 8 wurden alle theoretisch und praktisch erlangten Erfahrungen aus den Untersuchungen und Analysen der vorherigen Kapiteln angewandt, um polarisationsreine, dual-polarimetrische Antennenarrays zu entwerfen, welche für eine Wetterradarapplikation mit phasengesteuerter Antenne geeignet sind. Zwei unterschiedliche Antennentypen (erstens, ein 4x8 Antennenarray mit optimierter Phasenverteilung und zweites ein differentiell gespeistes 4x8 Antennenarray, beide dual-polarisiert) wurden zu diesem Zwecke entwickelt, mittels CST MWS simuliert und messtechnisch in der CATR (Compact Antenna Test Range) der RWTH Aachen verifiziert.

Aufgrund der sehr geringen x-polaren Strahlungseigenschaften der in diesem Kapitel entwickelten Antennen, wurde die CATR der RWTH Aachen in ihren Messeigenschaften bei der Nutzfrequenz von 9.395 GHz qualifiziert und die Messgenauigkeiten innerhalb der "Quiet Zone" für die co-polaren und x-polaren Messungen angegeben. Die CATR ist in der Lage, innerhalb der "Quiet Zone" von 15cm x 15cm, x-polare Leistungen bis -50dB zu detektieren. Die Messgenauigkeiten belaufen sich dabei auf  $\pm 0.1$  dB für die co-polaren Messungen und  $\pm 1.5$  dB für die x-polaren Messungen. Die Messgenauigkeit der Phase liegt etwa bei  $\pm 2^{\circ}$ . Die AUT wurde getragen durch ROHACELL 31HF Material, wobei das Metallgehäuse des Amplituden- und Phasenverteilungsnetzwerkes für den Phased-Array-Betrieb durch pyramidenförmige Absorber im hinteren Teil der Antenne isoliert wurde. Diese Maßnahmen wurden durchgeführt, um eine unbeeinflusste Nahfeldumgebung der Antenne innerhalb der "Quiet Zone" zu gewährleisten und sehr gute Übereinstimmungen von Simulation und realen Antennenmessungen bereitzustellen.

Der Entwicklungsprozess der in dieser Arbeit entwickelten Antennen wurde anhand eines Ablaufdiagramms detailliert beschrieben. Hierbei wurde die Reihenfolge der unterschiedlichen Analysen und Entwicklungen dem Leser erklärt, um schließlich ein Antennenarray mit hoher Kreuzpolarisationsunterdrückung für die Nutzung innerhalb eines phasengesteuerten Wetterradars zu erhalten. Wie im Entwicklungsprozess dargestellt, sind vier Antennenentwicklungen durchgeführt worden. Zunächst wurden zwei Typen von dual-polarisierten Einzelradiatoren entwickelt, welche einfach und differentiell gespeist sind. Die S11 Werte der einfach gespeisten dual-polarimetrischen Antenne stimmen beeindruckenden 99,78% mit denen der VNA- Messung überein. Auch die Antennenpattern für beide Polarisationen stimmen exzellent mit denen der CST MWS Simulation überein. Wie erwartet, liefert die einfach gespeiste dual-polarimetrische Antenne nur eine sehr unzureichende CPS von etwa 12 dB. Der Grund dafür ist die geringe Isolation, von ebenfalls 12 dB, zwischen den beiden Polarisationskanälen. In diesem Zusammenhang konnte nachgewiesen werden, dass relativ einfach von VNA Messungen auf die CPS in Hauptstrahlrichtung von Patchantennen geschlossen werden kann. Teure Antennenmesskampagnen könnten demzufolge bei einfachen (Stand-Alone) Antennen eingespart werden.

Die differentiell gespeiste und dual-polarisierte Antenne zeigt ebenfalls exzellente Übereinstimmungen zwischen CST MWS Simulation und den echten VNA- und CATR-Messungen. Die S11-Paramter stimmen mit einer Designgenauigkeit von 99,83% mit denen der Simulation überein. Eine CPS von etwa 33.3 dB konnte für die dual-polarimetrische Antenne bereitgestellt werden. Wie erwartet sind 4 Maxima im kreuzpolaren Antennendiagramm gesichtet worden. Die S21- Parameter der Simulation weichen allerdings von denen der Messung ab, was darauf hinweist, dass sich CST MWS Simulationsmodel und der produzierte Antennenprototyp unterscheiden. Die Gründe liegen mit hoher Wahrscheinlichkeit bei der Inhomogenität des realen Substrates und dem damit eingehenden Phasen- und Amplitudenänderungen, welche in CST MWS nicht berücksichtigt werden. Werden die Produktionsungenauigkeiten effektiv berücksichtigt, so kann eine CPS von 42 dB durch das differentiell gespeiste Antennenelement zur Verfügung gestellt werden, wie die Simulationsergebnisse beweisen.

Das einfach gespeiste und dual-polarisierte Patchantennenelement wurde verwendet, um ein 4x8 Antennenarray mit optimierter Phasenansteuerung von gespiegelten Radiatoren zu erzeugen. Die S11-Parameter der dual-polarimetrischen Arrayantenne stimmen mit beeindruckenden 99,77% mit denen der VNA- Messung überein. Auch die Antennendiagramme für beide Polarisationen stimmen exzellent mit denen der CST MWS Simulation überein. Erstaunliche CPS Werte von 46.83 dB und 50.4 dB in Hautstrahlrichtung sind für den horizontalen und vertikalen Polarisationskanal des dual-polarisierten Antennenarrays messtechnisch nachgewiesen worden. Im Phased-Array-Betrieb innerhalb des Scanbereiches von 120° konnte die CPS unter 27 dB (H-Pol) beziehungsweise unter 33 dB (V-Pol) gehalten werden. Jedoch wurde messtechnisch nachgewiesen, dass x-pol Anteile an gegenüberliegenden Winkelpositionen ansteigen, wenn die Hauptkeule geschwenkt wird. Diese Tatsache schränkt den Nutzen von phasenoptimierten Antennenarrays für Wetterradarapplikationen ein, da eine Abstrahlung von x-pol Anteilen in andere Winkelrichtungen sehr unerwünscht ist und Reflektionen generieren, die zu Radarfehlmessungen führen könnten. Dennoch sind die in dieser Dissertation erzielten Ergebnisse sehr Hilfreich für die Entwicklung von Arrayantennen **ohne** Phased-Array-Betrieb. Die phasenoptimierten, gespiegelten und dual-polarisierten Antennenarrays sind ideale Kandidaten für Anwendungen mit hohen CPS Anforderungen. Zusätzlich wurde anhand des phasenoptimierten Antennenarrays der Einfluss von Taperfunktionen auf die Kreuzpolarisationseigenschaften untersucht. Es konnte messtechnisch nachgewiesen werden, dass ein intensiver abfallender Amplitudentaper die abgestrahlten x-polaren Feldanteile eines Antennenarrays minimiert. Ein Amplitudentaper mit 3dB Kantenabfall hat die CPS von 51 dB auf 53 dB verbessert. Wohingegen ein Amplitudentaper mit 5 dB Kantenabfall die CPS weiter auf 55 dB optimierte.

Das differentiell gespeiste und dual-polarisierte Patchantennenelement wurde verwendet, um ein 4x8 Antennenarray mit differentieller Speisung aller Elemente zu erzeugen. Die S11-Parameter der dual-polarimetrischen Arrayantenne stimmen mit beeindruckenden 99,50% mit denen der VNA- Messung überein. Auch die Antennendiagramme für beide Polarisationen stimmen exzellent mit denen der CST MWS Simulation überein. Sehr gute CPS Werte von 36 dB und 44 dB in Hautstrahlrichtung wurden für den horizontalen und vertikalen Polarisationskanal des dual-polarisierten Antennenarrays messtechnisch nachgewiesen. Im Phased-Array-Betrieb innerhalb des Scanbereiches von 120° konnte die CPS unter 36 dB (H-Pol) beziehungsweise unter 38 dB (V-Pol) gehalten werden. Dieses Resultat ist etwa 10 dB besser als das vom phasenoptimierten 4x8 Antennenarray. Zusätzlich konnte messtechnisch nachgewiesen werden, dass die x-pol Anteile **nicht** an anderen Winkelpositionen innerhalb des Scanbereiches von 120° ansteigen, wenn die Hauptkeule geschwenkt wird. Aus diesem Grund ist das differentiell gespeiste Antennenarray der perfekte Kandidat für eine Phased-Array-Wetterradarapplikation. Die Antennenrichtdiagramme des differentiell gespeisten 4x8 Antennenarrays wurden desweiteren dazu verwendet, um die dominante Quelle der x-polaren Strahlung des Antennenarrays zu identifizieren. Wird ein gedämpftes co-polares Antennenrichtdiagramm im x-polaren Antennenrichtdiagramm gesichtet, kann davon ausgegangen werden, dass der dominierende x-polare Beitrag von der Kanalisolation der beiden Polarisationskanäle hervorgerufen wird. In so einem Fall sind die intrinsischen x-polaren Feldanteile kleiner als die Isolation der Polarisationskanäle. Mit Hilfe dieser neu gewonnenen Information kann ein Antennenentwickler gezielt die CPS von Antennenarrays optimieren.

In **Anhang A** wird das Amplituden- und Phasenschiebernetzwerk beschrieben, welches während einer vom Autor geleiteten Bachelorarbeit entstanden ist. Das im X-Band betriebene Amplituden- und Phasenschiebernetzwerk wurde zur Verifikation der in dieser Dissertation entwickelten Antennen verwendet. Das Instrument stellt eine Phasengenauigkeit von  $\pm 1.25^{\circ}$  und eine Amplitudengenauigkeit von  $\pm 0.25$  dB zur Verfügung. Das Amplituden- und Phasenschiebernetzwerk ermöglichte es, Arrayantennen als phasengesteuerte Antennenarrays zu betreiben und die Einflüsse der Anregungskoeffizienten auf das x-polare Antennendiagramm zu erforschen.

## **Future Outlook and Suggestions**

The generation and the causes of x-pol radiation has been thoroughly investigated in chapter 6. Investigations, starting with an analysis of possible x-pol sources in stand-alone patch antenna designs together with techniques for the reduction of x-pol radiation in antenna arrays were carried out. Appropriately future work in this field could be an investigation of 3D geometries of patch antennas. The state-of-the-art 3D printer technology already allows the production of patch antennas in 3D geometries with adequate production accuracy even at X-Band frequencies. Different types of 3D antennas could be evaluated to increase the cross polarization suppression of microstrip patch antennas. Additionally, different copper structures (electric band gap EBG- structures), acting as metamaterials implemented in and around the resonance cavity of patch antennas, should be investigated to further reduce the x-pol radiation. As a consequence, the current distribution of the patch antenna surface would be modeled to produce low x-pol fields. In this manner, the performance of single-feed patch antennas can probably be aligned for achieving x-pol radiation performance of differential feed antennas or even better. Consequently, the feeding network and multilayer antenna designs can be simplified to single-feed antennas with excellent x-pol performances.

Another innovative approach would be the step-by-step x-pol optimization by deleting small copper parts of the patch antenna surface (any shape) and using the optimizer function (for instance the genetic algorithm of CST MWS optimizer) of the 3D full wave simulators. In this way, new patch antenna shapes are derived with optimized x-pol performance. Again, the surface current distribution would be modeled for optimum CPS.

In section 8.6 the results of the simulated and measured S-parameters are given (figure 8.12). The simulated and measured S21 isolation values differ by approximately 13 dB. The different results are probably related to the incomplete simulation model of CST MWS. The CST MWS model considers the substrate as a homogeneous medium. But in reality, the dielectric constant and also the dissipation factor of the substrate are not homogeneously distributed. Consequently, the electrical length and the attenuation for 3D field simulations and real VNA measurements differ. To overcome this difference, a set of single patch antennas with slightly varying path length in the feeding network can be produced and measured with VNA. Finally, the best performing antenna can be selected (also useful for the array design). A strong correlation between the measured S21 and the measured boresight CPS could be demonstrated in the sections 8.5 and 8.6. For this reason, it can be expected that the CPS will significantly be optimized by maintaining excellent S21 isolation values.

Two kinds of phased-array antennas have been developed within this dissertation. Namely, the differential-feed and the single-feed antennas with 32 microstrip patch elements. The best performing phased-array antenna is evidentially the differential-feed patch antenna array with its excellent polarization purity. But also the single-feed array from section 8.7 with optimized phase excitation has shown very good x-pol values for small scan angles. The printed circuit boards of the multilayer antennas use microstip feeding networks. These feeding networks tend to contribute unwanted electromagnetic fields. Consequently, an additional GND-layer has been implemented to reduce the effect of unwanted radiation. The final phased-array weather radar system concept in chapter 5 is using multiple subarrays with eight TRMs for each subarray with 32 patch antenna elements. The phased-array antenna works with a limited angular scan range in elevation, also called "limited field of view". The optimum position of these TRMs is the backplane of the multilayer PCB, so that the TRMs are surface mountable. Consequently, the feeding network of the antennas developed in this work should be redesigned with stripline technology. The new stripline feeding network should be implemented between the patch antenna layer and the TRM layer. To keep the production costs low, the RO4350 material should also be used for the TRM layer. This substrate was also used for the other layers and has shown excellent RF performances at approximately 10 GHz. The mechanical stability of the thin RO4350 substrate is however, insufficient for the implementation of the TRM chips on the backplane of the antenna. For this reason, an additional FR4 substrate layer, also for the DC supply, should be installed for the final multilayer antenna configuration as required in the system concept from chapter 5.

To further enhance the efficiency of the antenna subarray and to reduce the system noise temperature, the losses in front of the LNA (the LNA is part of the TRM) should be reduced. To meet this goal, the LoPro 4350 substrate from Rogers should be selected for the final subarray design. This substrate provides a smooth copper structure below the microstrip line or stripline and consequently provides lower attenuation values as the typical RO4350 substrate by maintaining the same design parameters. In the bachelor thesis by Andre Eisengarten [131] down- converter, up- converter and RF-filter PCBs have been developed. It was the author's responsibility to guide this project and to define the work for the student during this period. Here we investigated different finishing methods for the PCBs. Finally, we discovered that gold/nickel finishing induces significant attenuation. As a consequence, the multilayer subarray with integrated antenna and TRM should be covered only with solder mask to provide protection against corrosion and simultaneously minimize the RF path losses. The dielectric constant of the solder mask must be implemented in the EM simulations to retrieve conformance between EM- simulations and real RF measurements. In section 8.7, the subarray requires special matching for the single patch radiators at different geometrical positions inside the array. Furthermore, the 1x4 LFoV arrays are also matched for their position inside the 4x8 array. This was indeed necessary to verify the performance of the subarray in the compact antenna test range as a stand-alone subarray antenna. To simplify the antenna design process of subarrays for the final subarray design of a demonstrator antenna it is effective to create (simulate and design) only one embedded patch antenna with EM simulation tools like CST MWS. The embedded patch element is then simulated with surrounded radiators of the same design. The truncation errors at the edges of the complete phased-array antenna (for instance the 2.7 m x 2.7 m antenna array from chapter 5) could be equipped with 2 additional rows of dummy radiator elements (radiators not fed by the TRMs). In this way, the antenna gain will slightly be increased and the truncation and matching errors are minimized.

The system concept developed in chapter 5 incorporates a 2.7 m x 2.7 m antenna with 800 subarrays to fulfill the requirements established in table 5.1. This number of subarrays and TRMs is very expensive to establish for the first phased-array weather radar demonstrator. For this reason, the proof of concept should be established with a lower number of subarrays. A 1.2 m x 1.2 m phased-array antenna with 128 subarrays provides already an adequate beamwidth of approximately  $2.5^{\circ}$  in boresight direction and  $3.5^{\circ}$  beamwidth at the maximum azimuth angle of  $\pm 60^{\circ}$ . The antenna gain values are ranging, as a function of scan angle, between 37 dBi and 35 dBi. The demonstrator cost can be significantly reduced by restricting the electronic scan capability to one plane. For instance, if the azimuth scanning is performed mechanically, the feeding network can be changed and the number of control elements (TRMs) can be reduced significantly. However, the main advantage of non-rotating elements in the context of lifetime and maintenance will be lost. The agility and the speed of the scan would also be limited to the rotational speed of the azimuth drives. If the system design is driven by cost issues, the hybrid phased-array design (AZ scanning mechanically and EL scanning electronically) is probably the best choice. The LFoV configuration of 1x4 elements can then also be changed to provide higher degree of freedom for the electronic scan range in elevation. The LFoV concept with 4 vertically grouped antenna radiators can be changed to 2x 16 elements. A combination of 2 vertically grouped radiators limits the elevation scanning only very slightly, as simulated in figure 5.4b. A horizontal combination of 16 elements does not have any effect on the elevation scan range. It would only have an effect on the electronic azimuth scanning. However, if the azimuth scanning is performed mechanically, this fact can be neglected. The 2x16 configuration is also chosen to reach a minimum transmitted power of 300 W. To reach this goal the number of TRMs must be chosen adequately for the antenna array grid. The minimum transmitted power value of 300 W becomes reasonable by considering its application with pulse compression and an observation range of approximately 30 km. If azimuth and elevation scanning for phased-array weather radars in a dense radar network is required, the 1x4 LFoV configuration from figure 5.4c should be kept. In chapter 5, Pseudo-Noise-Gating has been identified to be a suitable candidate for calibrating dual polarized phased-array weather radars. In this regard, different PN-Gating correlation algorithms should be thoroughly investigated in order to identify an individual TRM in an array of thousands of TRMs. Furthermore, a suitable and fast evaluation of amplitude- and phase coefficients of multiple TRM output signals (up to 6400 signals) should be established.

## Appendix A

### A.1 X-Band phase- and amplitude distribution network for phased-array antenna measurements

The measurement- and test device explained next, has been developed and build during a bachelor thesis at Selex-ES GmbH by Gereon Michalek. It was the author's responsibility to guide this project and to define the work for the student during this period. All technical details are published in German language in the bachelor thesis [128]. The measurement system set-up induced next and parts of the measured antenna radiation patterns from chapter 8 are published in reference [129].

The design and the performance of an X-Band mixed signal PCB with adjustable phases and amplitudes for phased-array antenna measurements with up to 32 antenna elements is presented in this section. The implementation of the 6 Bit RF phase- shifters and 5 Bit attenuators within a feeding network will be shown and the digital control functions of FPGA are explained. The phase- and amplitude calibration of the distribution network was calibrated with by a vector network analyzer and has shown an excellent phase accuracy of  $\pm 1.25^{\circ}$  and adequate amplitude accuracy of  $\pm 0.25$  dB. The distribution network was developed to investigate the x-pol antenna characteristics during beam steering in anechoic chambers.

#### A.1.1 Introduction

Most laboratories with their near- and compact field ranges are not able to provide multiple RF signal sources with adjustable amplitudes and phases for studying phased-array antenna pattern measurements. Consequently, the presented distribution network here, with adjustable amplitudes and phased becomes necessary for analyzing and measuring the phased-array antenna radiation pattern performances from suitable antenna array cases. With this new device, the analysis of suitable amplitude- and phase- tapers is made possible in order to investigate the reduction of sidelobes, the subarrays half-power beamwidth and the optimization of x-pol patterns. Furthermore, it can be measured how the phase- or amplitude deviations (mostly induced by antenna feeding network) degrades the array antenna performance. The control sequences for X-Band phase- and amplitude distribution network for phased-array antenna measurements is very similar to the control functions

of TRMs. The PCB design requirements are also very similar for both cases. As a consequence, the experience gained with this mixed signal PCB development project will be further used for future TRM designs with programmable RF chip-sets.

#### A.1.2 System set-up of phase- and amplitude distribution network to measure the antenna performance

The RF-, DC, and Communication flow-chart of the operational measurement system setup is illustrated in Figure 8.41. The amplitudes and phases of the eight output signals are set via graphical user interface (GUI) from the control computer. The GUI was developed with "LabView" and establishes the desired beam position angle and to generate the phase shifter offset angles in binary format. This binary format will be sent via RS232 to the DC Supply and Distribution Board and combined with DC- voltages for one-signal cable, which transfer all data and voltages to the RF board. The data strings from RS232 are received by the "Field Programmable Gate Array" (FPGA), which is located on the RFboard. The FPGA calculates the phase- and/or attenuation values for each corresponding phase shifter or attenuator inside the antenna array, depending on the position of the linear subarray inside the complete antenna array.

## A.1.3 Labview- graphical user interface for amplitude and phase control

Due to the minimum phase step size of 5.6°, only a limited number of possible beam position angles are available. The "LabView- GUI" compares the user desired phase value with a look-up table of all adjustable beam position angles (6-bit- combinations). The beam position angle with smallest deviation from user defined angle will be automatically selected and the phase shifter offset angle is transferred via RS232 to the FPGA. To determine the discretization error of the beam position angle, the realized and the desired beam position angles are compared and the deviation is made visible for the user as shown in figure 8.42a. The beam position error calculation is performed for both the azimuth and elevation scan angle. The Bit configuration for the phase-shifter-offset-angle for Azimuth and Elevation is also shown in figure 8.42a. The operating frequency and the patch antenna element distance can be inserted for different antenna designs. The operating frequency and the element distance will be used for calculating adequate phases for the desired beam position. The required relation between beam pointing angle and phase-difference of adjacent patch elements was already induced in equation 3.62. By recalling figure 3.16 in chapter 3.4, the generation of linear phased-array antenna pattern can be explained.

The "LabView- GUI" provides also a selection of amplitude tapers, as shown in figure 8.42b. Furthermore, the absolute amplitude calibration can be supported by separate attenuator offsets. Every phase shifter is manually selectable for the purpose of absolute phase calibration. The subarray position inside the array is read by configurable jumper cascade.

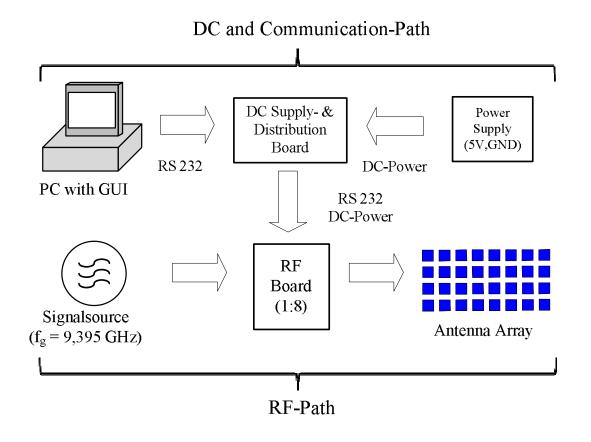


Figure 8.41: System Set-Up for Phased-Array Antenna Measurements

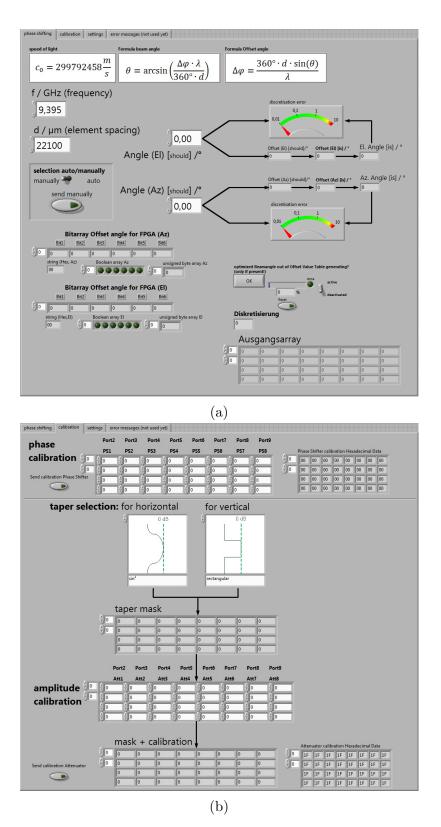


Figure 8.42: (a) GUI main page with used equations, discretization error AZ and EL and the desired beam position angle. (b) calibration page for phase and amplitude corrections.

# A.1.4 Design overview of the phase- and amplitude distribution network

The block diagram and picture of the RF-board are shown in the figures 8.43a and 8.43b, respectively . The functionalities of the mixed signal PCB can be separated into two sections: The DC and digital sections are located in the center of the board covered with black solder resist mask. The RF section comprises a 1:8 power divider network with the RF chips for modulating the phase and the amplitude of the RF signals. The mixed signal PCB was developed with four different software packages. The FPGA circuit layout was designed with *EAGLE*, the lossless RF power divider network in conductor backed coplanar waveguide (CBCW) microstrip line technology was developed with ADS (Agilent-Advanced Design Systems), the FPGA was programmed with Xilinx ISE Design Suite 14.7 and the transition through the RF housing from the SMA connector to the CBCW microstrip line was simulated and impedance matched with the Transient 3D Solver from CST MWS.

The digital section in the middle of the board comprises the FPGA for providing the parallel and serial data streams to the RF chips. The Spartan-3A is relatively small, low cost and supplies 195 I/O ports. For the project realization 114 I/Os have been used: 88 I/Os for parallel bit distribution and 8 serial I/Os for the phase shifters, 12 I/Os for the subarray position identification inside the complete antenna array (realized by jumper-cascade), two I/Os for RS232 TX/RX, two I/Os for channel coding and one I/O for serial/parallel selection.

For accurate FPGA operation a stable clock reference is required. This is generated by a high-frequency crystal oscillator "SG-8002CA" from Epson. This device provides the reference clock signal at 40MHz.

The CBCW microstrip line with a width of  $305\mu$ m was designed on RO4350B with  $168\mu$ m height and a wave impedance of  $50\Omega$  at 9.395 GHz was realized. The standard copper thickness of  $17\mu$ m was extended with 25 microns plated copper because of the via hole grounding connection for CBCW design and the isolation fences between digital and RF sections. For corrosion protection a chemical Ni/Au finishing has been applied. The distance between signal- and ground layer has 200 microns. To achieve reasonable path shielding the CBCW microstrip line is fenced with via holes in order to reflect the electromagnetic wave back into the transmission line. The 1:8 power divider network is a cascade of three identically designed power dividers. The divider is used in matched forward direction only; accordingly the adjustment of the output ports was not necessary. Just like the microstrip line, the power dividers are designed in CBCW. The two  $\Lambda/4$ -transformation lines were dimensioned to  $70.7\Omega$ , which corresponds to a lossless T-Junction power divider. By implementing a  $100\Omega$  resistor between the two output ports behind the  $\Lambda/4$ -transformation lines, a "Wilkinson" power divider can be established.

For the phase- and amplitude modulation, phase shifters (6-bit digital MAPS-010166) and attenuators (5-Bit HMC941LP4E) in 4x4mm QFN package have been selected. Both chips

are fed with  $\pm 5V$  operating voltage. This chip generates phase-shifts up to 360° with stepsize of 5.6°. The maximum attenuation is 15.5 dB and can be set with 0.5 dB steps resolution.

### A.1.5 Absolute phase- and amplitude calibration using vector network analyzer

The measurement of all S- Parameters for every phase- and attenuator state was carried out and recorded with a ZVB20 vector network analyzer from Rohde&Schwarz. With activated phase shifters and attenuator chips the input port 1 shows S11=-16 dB. As absolute phase- and amplitude reference point, the output ports from one of the 8 RF cables is used, so that the induced phase differences from these cables are also calibrated out. The cables are used to connect the antenna array with the distribution network. The absolute amplitude difference can be minimized by the adjustment of the attenuators, but due to the minimum step size of 0.5 dB, absolute calibration accuracies below  $\pm 0.25$  dB become difficult. To calibrate the phase at the reference point, the phase shifters were set to minimum phase difference.

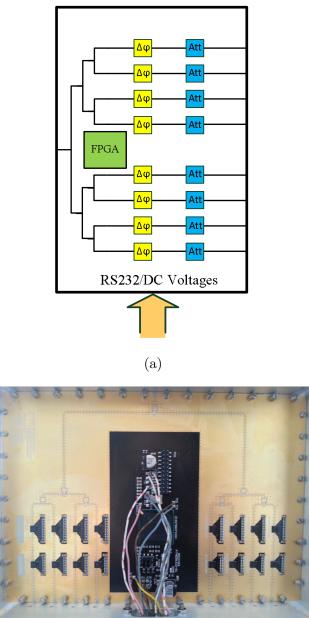
Finally a clever algorithm, implemented in LabView, extracts the optimum phase- and amplitude configurations from all recorded S-Parameter values. After calibration an excellent phase accuracy of  $\pm 1.25^{\circ}$  and an adequate amplitude accuracy of  $\pm 0.25$  dB could be established.

# A.1.6 Hardware development experience gained for future TRM design

From substrate suppliers, a new substrate with smoother copper surfaces between substrate and the lower side of the microstrip line was discovered. The copper roughness induces less attenuation and is a possible candidate for the design of the TRM, since each additional loss in front of the LNA would increase the system noise figure of the phasedarray weather radar. The recommended RO4350B LoPro shows 0.35 dB less insertion loss than the RO4350B we have chosen. A change from RO4350B to RO4350B LoPro is easily accomplished since all (excepting the cu-roughness) RF design parameters are identical.

The choice for the CBCW technology has shown the advantage of very good isolation between the channels. It has to be further analyzed whether the improved isolation justifies the additional losses. In [130] the Microstrip line and the CBCW were compared. From Figure 2 in reference [128] one can recognize an insertion loss difference of approximately 0.25 dB for 10 GHz at one inch length between traditional microstrip line technology and CBCW design.

The chosen substrate height with 168 microns has induced several disadvantages during the production process. The implementation of the FPGA with its solid grid ball arrays required too much heat for the soldering process. As a consequence, the thin substrate



RF Modul

(b)

Figure 8.43: (a) Block diagram of the RF Board. (b) RF board design with conductor backed coplanar waveguide (CBCW) microstrip line technology installed in aluminum RF housing unit, where the RS232 signals and DC voltages are connected.

was altered. Accordingly, a more robust substrate thickness is recommended. To simplify signal routing below the FPGA, the solder balls of the FPGA should be placed directly on the vias. This gains extra space for further signal routing. For a better grounding the free space of the RF-area should contain more vias between top and bottom layer.

### A.1.7 Summary

A phased-array antenna system can created from a planar antenna array and the new X-Band phase- and amplitude distribution network. The development and the function of the phase- and amplitude distribution network were explained briefly. The new measurement device establishes beam steering and amplitude tapering in order to investigate antenna radiation pattern. The proper function of the distribution network was verified and calibrated by a Vector Network Analyzer and has shown an excellent phase accuracy of  $\pm 1.25^{\circ}$  and an adequate amplitude accuracy of  $\pm 0.25$  dB in X-Band. To further analyze and demonstrate the opportunities of the phase- and amplitude distribution network, the dual polarized planar antenna from chapter 8 was measured with amplitude tapers. It could be shown that CST MWS simulated and measured antenna radiation patterns for co- and x-polarization are in very good agreement. The main reasons for the very good agreement between simulations and compact range measurements are the proper mesh and calculation of the antenna design in CST MWS, the very accurate antenna measurement environment at RWTH Aachen and the excellent performance of the X-Band phase- and amplitude distribution network for phased-array antenna measurements.

It can be stated that a very useful phase- and amplitude distribution network was developed in order to perform X-Band phased-array antenna measurements and investigating its patterns.

## List of Figures

| 1.1  | Pulse Doppler radar blockdiagram   | 51 |
|------|--|----|
| 1.2  | a) Pulsed radar transmit-receive cycle; b) Line spectrum for the explana-<br>tion of unambiguous Doppler velocity; c) Graphical description of the range<br>resolution; d) Graphical description of the unambiguous range  | 52 |
| 1.3  | Chart description of the pulse spectrum to determine pulse width PW and pulse repetition frequency PRF   | 55 |
| 1.4  | Visual explanation of the point target equation 1.15. The blue waves are representing the back propagation towards the radar.  | 57 |
| 1.5  | Pulse volume target for weather radar equation 1.27  | 59 |
| 1.6  | a) Side view of the pulse volume; b) Pulse volume homogeneously filled; c)<br>Pulse volume weighted with 3dB antenna beamwidth for improved reflectiv-<br>ity estimates, discovered by Probert Jones.  | 60 |
| 1.7  | Planar antenna array with $\alpha$ , the angle between the direction of main beam<br>and the normal (Z-axis) of the array face. $\xi$ and $\psi$ are the beam angles<br>between X-Z axis and Y-Z axis, respectively. In arbitrary direction, the<br>antenna beam generates an ellipse on the surface of a sphere [26]                            | 63 |
| 1.8  | Typical $Z_{DR}$ values of raindrops in various sizes and hail measured at S-Band. The black arrow on the hail particle represents the tumbling motions as it falls in a thunderstorm. Adapted from [50] and [51].   | 66 |
| 1.9  | Graphical description of all parameters to retrieve $\rho_{co}^{(1)}$ from equation 1.71.<br>Pulse trains in the H and V channels and pulse pairs used in the calculations<br>of the correlation functions in either channel and in both channels, adapted<br>from [60].   | 73 |
| 1.10 | Radar receiver module connected through a lossy line to antenna, adapted from [29]. The units highlighted in blue are considered for the calculation of the equivalent system temperature in equation 1.82.  | 73 |
| 1.11 | Noise output power analysis of a cascaded radar system, including the antenna, the lossy transmission line and the receiver performance [29]. The blue highlighted units are considered for the calculation of the equivalent system temperature $T_e^{SYS}$ in equation 1.85 and the cascaded out noise power $N_o^{Cascade}$ in equation 1.87. | 78 |
|      | o  |    |

| Noise signal observation for monitoring the weather radar system perfor-<br>mance. The observation of the cascaded noise output power of a dual polar-<br>ized weather radar system located in Switzerland on Albis for a 24 h time<br>interval and a rain event above the radar. The data sets are acquired at 35°<br>antenna elevation, so that the main beam is not filled with noise contributed<br>by ground. The correlation between the rain rate $R_{Rain}$ in $\frac{mm}{h}$ (right y-axis)<br>from external rain sensor, located at the radar tower and the detected noise<br>power $N_o^{Cascade}$ (left y-axis) from radar antenna system (radome + antenna),<br>receiving waveguide path losses and analog- and digital radar receiver can be<br>seen. The cascade of the receiving units are corresponding to the equivalent<br>system noise temperature $T_{SYS}$ in equation 1.84 and the cascaded output<br>noise power $N_o^{Cascade}$ from equation 1.87. | 81   |
|--|--|
| Propagation of electromagnetic plane wave, exemplary shown with a) right<br>hand circular polarized (RHCP) and b) left hand circular polarized (LHCP)  |  |
| plane wave   | 87   |
| a  | 91<br>92   |
| Grapical explanation of the antenna directivity [12]. The maximum radi-<br>ation density in the main beam direction $S_{max}(r, \theta, \phi)$ will be referred to<br>isotropic radiation $\langle S_i(r, \theta, \phi) \rangle$ . The ideal isotropic radiator is radiating the<br>same amount of field intensity in all angular directions.  | 94   |
| Equivalent beam solid angle  | 97   |
| Definition of near field, fresnel zone and far field, adapted by $[12]$<br>Microstrip transmission line geometry with substrate height H, the dielectric<br>constant $\epsilon$ of the substrate and W the width of the microstrip line. Above   | 98   |
|  | 103  |
| Electric (solid blue) and magnetic (dashed blue) field line distribution around the microstrip line. Above the microstrip line $\epsilon_r = 1$ for air is assumed.  | 104  |
| Current and charge distribution of microstrip patch antenna  | 106  |
| • •  | 108  |
|  | 100  |
| patterns, adapted by [110]   | 109  |
| Geometry of rectangular microstrip patch antenna with spherical angles $\theta$<br>and $\phi$ , the feed location at $(x_0, y_0)$ , the patch width W and length L, the<br>substrate height H and $\epsilon_r$ the relative permeability of the substrate  | 111  |
|  | mance. The observation of the cascaded noise output power of a dual polarized weather radar system located in Switzerland on Albis for a 24 h time interval and a rain event above the radar. The data sets are acquired at 35° antenna elevation, so that the main beam is not filled with noise contributed by ground. The correlation between the rain rate $R_{Rain}$ in $\frac{mm}{16}$ (right y-axis) from external rain sensor, located at the radar tower and the detected noise power $N_o^{Cascade}$ (left y-axis) from radar antenna system (radome + antenna), receiving waveguide path losses and analog- and digital radar receiver can be seen. The cascade of the receiving units are corresponding to the equivalent system noise temperature $T_{SYS}$ in equation 1.84 and the cascaded output noise power $N_o^{Cascade}$ from equation 1.87 |

| 3.10 | Basic microstrip patch antenna shapes commonly used in practice, adapted by [110]  | 112         |
|------|--|-------------|
| 3 11 | The impedance $ Z $ , voltage U and current I distribution along the patch   | ±± <b>=</b> |
| 0.11 | resonator length $L \approx \lambda_e/2$   | 113         |
| 3.12 | Patch antennas with different feeding structures with a) Coaxial feeding, b)<br>Coplanar feed, c) Aperture-coupled feeds for dual linear or circular polariza-<br>tion mode, d) Proximity (Electromagnetically) coupled microstrip feed, e)<br>probe-feed microstrip patch antenna with two feeds for dual linear or circular<br>polarization capability, f) A combination of different feeding structures are<br>given within one dual polarization microstrip patch antenna design, adapted<br>from [112]. The grey layers represent copper structures for patch microstrip<br>lines and ground, the substrate layers are indicated with blue color and the<br>green layers are spacers, made by foam material.  | 115         |
| 3.13 | and circular microstrip patch with feeding network, providing two excita-<br>tion signals 90° out of phase. After the equal power split, the 90° phase<br>difference will be established by microstrip line with $\frac{\lambda}{4}$ difference in length.<br>c) and d) are typical configurations for radiating circular polarization by<br>the excitation of only one feed. The shape geometry establishes the simul-<br>taneous radiation of two vector components, exactly 90° out of phase. The<br>square and circular patch in c) and d) are excited at the edges, crosswise. e)<br>shows the excitation of a square microstrip patch with 4 feeds. The opposite<br>sided feeds are excited with 180° phase difference to radiate either horizon-<br>tal or vertical polarization. This configuration is used for the reduction of |             |
|      | cross-polarization levels, briefly discussed in the later chapters   | 118         |
| 3.14 | Feeding networks   | 119         |
| 3.15 | (a) Antenna bandwidth characteristics as a function of $\frac{H}{\lambda\epsilon_r}$ . (b) Antenna efficiency $\eta$ characteristics as a function of $\frac{H}{\lambda\epsilon_r}$ . Both graph are adapted by [20].  | 121         |
| 3.16 | Linear antenna array geometry with equiphase wave front, generating the far field antenna radiation pattern at scan angle $\theta_0$ . The first phase shifter, on the right, defines the reference phase. The consecutive phase shifters are excited with a phase increment of $n\Delta\Phi_x$ .  | 123         |
| 3.17 | Geometry of planar phased-array antenna  | 125         |
| 3.18 | a) Illustration of sparse array concept for polarization control. A set of elements are excited with orthogonal polarization to mitigate the x-pol contribution from phased-array misprojection and the intrinsic array characteristic. b) 32x32 antenna array with thinning factor K=5%. c) 32x32 antenna array with thinning factor K=16%. All three figures are adapted by [67].  | 131         |
| 4.1  | Allocation of field components of one grid cell with the discretization of Maxwell's equations to Maxwell's Grid Equations, adapted from [87]  | 137         |

| 4.2                                       | Mesh examples of 4x4 antenna array with 68 million mesh cells. On, below<br>and above the radiating patches, a very high mesh density is selected. Also<br>the 3D connectors and the patch antenna probe-feeds (vias for exciting the<br>patch edges) are meshed with very high resolution. In these areas the field<br>concentration and gradients are very strong, so that higher mesh resolution<br>is applied.   | 139          |
|---|--|--------------|
| 4.3                                       | Selected open boundary conditions with add space, for 3D full wave simu-   | 100          |
| 4.4                                       | lations of antennas and proper calculation of the far field The CST MWS far field calculator was used to evaluate the antenna array performance. From single patch antenna element pattern, the array sum pattern will be calculated, without the consideration of mutual coupling and edge effects. In (a) the single antenna with the far field calculator is visualized. An element spacing of 16 mm is selected and corresponds to half free space wavelength at X-Band frequency. In (b) the 3D co-planar antenna | 140          |
| 4.5                                       | radiation pattern result for a 4x8 antenna array is shown  | 142<br>144   |
| 5.1                                       | Two dimensional planar phased-array antenna. The PAWR should be composed of three 2-dimensional planar antennas with $120^{\circ}$ azimuth and $30^{\circ}$  |              |
|   | elevation scanning range in order to provide 360° weather radar observation.   |              |
| 5.2                                       | PAWR System Blockdiagram with PN Gating sequence from [100], [101], [102   | 151          |
| 5.3                                       | 3D pattern of single-feed and dual-polarized patch antenna, as an example  | 159          |
| 5.4                                       | used to establish the LFoV analysis  | 152          |
|   | to the first null  | 153          |
| 6.1                                       | Layer set-up of squared microstrip patch antenna design. Left: Single probe-<br>feed patch. Center: constructed patches. Right: Differential probe-feed patch  | 162          |
| 6.2                                       | S11 resonating at $9.395\mathrm{GHz}$ with VSWR $1:2$ Bandwidth of 188 MHz   | 163          |
| 6.3                                       | Front and back view of microstrip antennas under test. Left: Single probe-<br>food patch. Differential probe food patch  | 164          |
| 6.4                                       | feed patch. Right: Differential probe-feed patch   | 164<br>165   |
| $\begin{array}{c} 0.4 \\ 6.5 \end{array}$ | Co-pol 3D far field pattern of differential probe-feed patch antenna   | $105 \\ 165$ |
| 6.6                                       | X-pol 3D far field pattern of single probe-feed patch antenna  | 166          |
| 6.7                                       | X-pol 3D far field pattern of differential probe-feed patch antenna  | 166          |
| 6.8                                       | X-pol 3D phase plot of single probe-feed patch antenna   | 167          |

#### LIST OF FIGURES

| 6.9  | X-pol 3D phase plot of differential probe-feed patch antenna  | 167 |
|------|---|-----|
| 6.10 | Comparison of single (red) and differential (blue) feed patch antenna CPS performances at 45°-Cut. The dashed curves are representing the gain plots of the x-pol radiation patterns.   | 168 |
| 6.11 | Comparison of single (red) and differential (blue) feed patch antenna axial rations at 45°-Cut.   | 168 |
| 6.12 | Comparison of co- and x-pol Phase plots from single (red) and differential (blue) feed patch antennas. The dashed curves are representing the phase plots of the x-pol radiation patterns.  | 169 |
| 6.13 | Phase difference of $180^{\circ}$ for $\Phi = 45^{\circ}$ -Cut (dashed) compared to $\Phi = 135^{\circ}$ -Cut, established by differential feeding technique. The $180^{\circ}$ phase difference is very useful in antenna array configurations for canceling out the x-pol components in far field from neighboring elements.  | 170 |
| 6.14 | Graphical description for excellent isolation functionality of dual polarized patch antenna with differential feeding.  | 170 |
| 6.15 | Comparison of port isolation characteristics from differential and single feed patch antennas.  | 171 |
| 6.16 | Left: Via filled with fossil resin and closed with cooper. Center: Square patch without edge bending. Right: Square patch with edge bending   | 171 |
| 6.17 | Co-pol pattern pattern of circular shaped X-Band patch antenna.   | 173 |
| 6.18 | X-pol pattern pattern of circular shaped X-Band patch antenna   | 174 |
| 6.19 | Connectors and matching stubs below the patch and shielding ground with $90^{\circ}$ rotated.   | 175 |
| 6.20 | Degraded x-pol pattern due to the connector and matching stub rotation of 90°, as shown in figure 6.19  | 175 |
| 6.21 | Analysis of co- and x-pol radiation pattern for differential-feed patch anten-<br>nas with variable patch length. The patch length varies from 10.32 to 10.80<br>mm. A valuable CPS improvement can be recognized in the circles between<br>$\Theta = 90^{\circ}$ and $30^{\circ}$ . The ellipses between $180^{\circ}$ and $120^{\circ}$ show a degradation<br>in CPS, which is acceptable since the CPS at invisible space behind the<br>antenna is not that important. | 178 |
| 6.22 | Field-line distributions: (a) Single probe-feed. (b) Differential probe-feed patch.   | 180 |
| 6.23 | Field distribution below the patch element is different in strength and phase for single-feed patch antennas.   | 181 |
| 6.24 | Field distribution below the patch element is equal in strength and exactly 180° out of phase for differential-feed patch antennas.   | 181 |
| 6.25 | (a)Surface current distribution on single-feed, square patch antenna. (b)<br>Surface current distribution on differential-feed, square shaped patch with<br>two signals 180° out of phase. (c) Surface current distribution on differential-  |     |
|      | feed, circular square shaped patch with two signals $180^{\circ}$ out of phase  | 183 |

| 7.1 | Field line distribution and 3D x-pol phase pattern for single- and differential-feed patch antenna, simulated with CST MWS   | 186 |
|-----|--|-----|
| 7.2 | Example for phase excitation distribution for mirrored radiators in 1x4 an-<br>tenna arrays. By exciting the patches at mirrored feed probe positions<br>and/or 180° out of phase, altered x-pol sum pattern can be expected from<br>the illustrated field lines.  | 187 |
| 7.3 | Layer set-up of squared and single-feed microstrip patch antenna design.<br>The differential-feed antenna incorporates the same design parameters but<br>two probe-feeds, excited 180° out of phase.   | 188 |
| 7.4 | Different phase excitation distributions for mirrored elements in 1x4 an-<br>tenna arrays. In blue Configuration 7 with differential-feed patch antenna<br>elements. Orange with Configuration 4, light green with Configuration 3,<br>red with Configuration 1 and green with Configuration 5   | 189 |
| 7.5 | In solid lines the co-pol and in dashed lines the x-pol radiation patterns<br>of the 1x4 arrays are shown. The blue curves are representing the H-cuts<br>$(\Phi=0^{\circ})$ and the green curves the E-Cuts $(\Phi=90^{\circ})$ . The red curves are ex-<br>pressing the diagonal cuts at $\Phi=45^{\circ}$ . Additionally the 3D x-pol radiation<br>patterns of the upper hemisphere of the specific arrays are visualized in the<br>lower left corners. The specific configurations are inserted in the lower right<br>corners. Configuration 3 shows most promising results for single-feed arrays,<br>meanwhile provides Configuration 7 with its differential-feed array the best<br>CPS with 35.9dB.        | 191 |
| 7.6 | Analyzing x-pol performance for six different 2x4 antenna arrays. In solid lines the co-pol and in dashed lines the x-pol radiation patterns of the 2x4 arrays are shown. The blue curves are representing the H-cuts ( $\Phi=0^{\circ}$ ) and the green curves the E-Cuts ( $\Phi=90^{\circ}$ ). The red curves are expressing the diagonal cuts at $\Phi=45^{\circ}$ . Additionally the 3D x-pol radiation patterns of the upper hemisphere of the specific arrays are visualized in the lower left corners. The specific configurations are inserted in the lower right corners .   | 195 |
| 7.7 | Antenna pattern synthesis of single-feed 4x8 antenna array with its optimum<br>phase distribution and mirrored elements compared to a differential-feed<br>4x8 antenna array. In solid lines the co-pol and in dashed lines the x-<br>pol radiation patterns of the 4x8 arrays are shown. The blue curves are<br>representing the H-cuts ( $\Phi=0^{\circ}$ ) and the green curves the E-Cuts ( $\Phi=90^{\circ}$ ).<br>The red curves are expressing the diagonal cuts at $\Phi=45^{\circ}$ . Additionally the<br>3D x-pol radiation patterns of the upper hemisphere of the specific arrays are<br>visualized in the lower left corners. The specific configurations are inserted<br>in the lower right corners. | 196 |
| 8.1 | RWTH Compact range measurement overview [127]  | 200 |
|     |  |     |

#### LIST OF FIGURES

| 8.2  | Quiet Zone characteristics of RWTH Aachen compact range provided by [127]: (a) Compact range x-pol contribution for horizontal polarization state in the quiet zone area at 10 GHz. (b) Co-polar amplitude ripple for horizontal polarization state in the quiet zone area at 10 GHz. (c) Phase variation for horizontal polarization state in the quiet zone area at 10 GHz.                                      | 202 |
|------|--|-----|
| 8.3  | (a)Quiet zone x-pol contribution for $\pm 25$ cm x-axis scan at 9.395 GHz. The measurement was performed with a standard gain horn. (b) E-, H-, 45°- and 135°-Cut of the standard gain horn pattern, measured in the compact range at 9.395 GHz. In the right lower corner a picture of the standard gain horn is given. Approximately -44dB to -48dB x-polar level has been measured.                             | 203 |
| 8.4  | (a) RWTH Compact range measurement set-up for the measurement of phased-array antenna radiation pattern. (b) Set-up of the antenna system under test.  | 205 |
| 8.5  | Development chart from phased-array antennas in weather radar applica-<br>tions with dual polarization capability, limited field of view approach and a<br>very low x-pol contribution.  | 207 |
| 8.6  | (a) Antenna set-up established with CST MWS.(b) Constructed dual polar-<br>ized microstrip patch antenna element with conventional probe-feeding   | 211 |
| 8.7  | VNA measured (solid lines) and CST MWS simulated (dashed lines) S-Parameter.   | 212 |
| 8.8  | CST MWS simulated 3D antenna radiation pattern for horizontal and verti-<br>cal polarization. (a) Co-polar plot for horizontal polarization. (b) Co-polar<br>plot for vertical polarization. (c) X-polar plot for horizontal polarization.<br>(d) X-polar plot for vertical polarization.  | 213 |
| 8.9  | (a) Compact range and (b) CST MWS results for <b>horizontal polariza-</b><br><b>tion</b> . The copolar (solid lines) and x-polar (dashed lines) antenna radiation<br>pattern Cuts for $\phi=0^{\circ}$ in green, $\phi=-45^{\circ}$ in red and $\phi=90^{\circ}$ in blue are shown.  |     |
| 8.10 | (a) Compact range and (b) CST MWS results for <b>vertical polarization</b> . The copolar (solid lines) and x-polar (dashed lines) antenna radiation pattern  | 216 |
| 8.11 | Cuts for $\phi=0^{\circ}$ in green, $\phi=-45^{\circ}$ in red and $\phi=90^{\circ}$ in blue are shown (a) Antenna set-up established with CST MWS.(b) Constructed dual polar-<br>ized microstrip patch antenna element with differential feeding technique.<br>Four probe-feeds are implemented. Two opposite sided feeds are used for<br>the generation of one polarization channel. The probe-feeds are fed with | 210 |
| 8.12 | 180° phase difference, induced by the wave molding microstrip line VNA measured and CST MWS simulated S-Parameter of the differential-feed microstrip patch antenna. Note that $s21 - ISO - H - V$ and $S12 - ISO - H - V$   | 219 |
| 8.13 | ISO - V - H are perfectly superimposed   | 221 |
|      | plot for vertical polarization. (c) X-polar plot for horizontal polarization.<br>(d) X-polar plot for vertical polarization.   | 222 |
|      |  |     |

| 8.14 | (a) Compact range and (b) CST MWS results for horizontal polariza-   |     |
|------|--|-----|
|      | tion. The co-polar (solid lines) and x-polar (dashed lines) antenna radiation  |     |
|      | pattern Cuts for $\phi=0^{\circ}$ in green, $\phi=-45^{\circ}$ in red and $\phi=90^{\circ}$ in blue are shown.   | 223 |
| 8.15 | (a) Compact range and (b) CST MWS results for <b>vertical polarization</b> . The   |     |
|      | copolar (solid lines) and x-polar (dashed lines) antenna radiation pattern   |     |
|      | Cuts for $\phi=0^{\circ}$ in green, $\phi=-45^{\circ}$ in red and $\phi=90^{\circ}$ in blue are shown  | 224 |
| 8.16 | CST MWS Design of dual polarized array with 32 radiators   | 227 |
| 8.17 | (a) Front view (b) Rear view of the constructed dual polarized phased-array  |     |
|      | antenna with optimized phase excitation. The feeding points for horizontal   |     |
|      | (blue) and vertical (red) polarization are given. The excitation is performed  |     |
|      | by two types of RF signals which are either in phase $(0^{\circ})$ or $180^{\circ}$ out of phase.  |     |
|      | The optimum phase excitation configuration 3 from chapter 7 is highlighted   |     |
|      | by the red and blue frames in dashed lines, respectively for horizontal and  |     |
|      | vertical polarization.   | 228 |
| 8.18 | (a) Patch and subarray impedance matching, depending on the position   |     |
|      | inside the 4x8 antenna array. (b) Length variation of short circuit has been   |     |
|      | performed for impedance matching. Furthermore, the implemented 3D-   | 000 |
| 0.10 | model of a connector is shown  | 229 |
|      | 1:8 corporate feeding network design with its equivalent circuit diagram.  | 230 |
| 8.20 | Feeding network design for maximum isolation between H and V polarization channel.   | 231 |
| 0.01 |  | 291 |
| 8.21 | Comparison of simulated (CST MWS-dashed lines) and measured (VNA-<br>solid lines) S-Parameters.  | 235 |
| 0 00 |  | 200 |
| 0.22 | CST MWS simulated 3D antenna radiation pattern for horizontal and verti-<br>cal polarization. (a) Co-polar plot for horizontal polarization. (b) Co-polar  |     |
|      | plot for vertical polarization. (c) X-polar plot for horizontal polarization.  |     |
|      | (d) X-polar plot for vertical polarization. (c) X polar plot for horizontal polarization.  | 236 |
| 8 23 | RWTH CATR measured 3D antenna radiation pattern of the optimum phase   | _00 |
| 0.20 | excitation array for horizontal and vertical polarization. The 3D cuts are   |     |
|      | generated by the Orbit software. The measurement was performed with $5^{\circ}$  |     |
|      | steps of $\Phi$ for the complete upper hemisphere of the antenna array. The  |     |
|      | CATR effects are filtered out and an interpolation between the 5° steps of   |     |
|      | $\Phi$ is performed. (a) Co-polar plot for horizontal polarization. (b) Co-polar   |     |
|      | plot for vertical polarization. (c) X-polar plot for horizontal polarization.  |     |
|      |  | 237 |
| 8.24 | Compact range measurement results compared to CST MWS simulation   |     |
|      | results for <b>horizontal polarization</b> : (a) The co-polar (solid lines) and x-   |     |
|      | polar (dashed lines) antenna radiation pattern Cuts for $\phi=0^{\circ}$ in green, $\phi=-$  |     |
|      | 45° in red and $\phi=90^{\circ}$ in blue, measured at compact range RWTH Aachen.   |     |
|      | (b) The co-polar (solid lines) and x-polar (dashed lines) antenna radiation<br>pattern Cuta for $\phi = 0^{\circ}$ in group $\phi = 45^{\circ}$ in rad and $\phi = 00^{\circ}$ in blue simulated |     |
|      | pattern Cuts for $\phi=0^{\circ}$ in green, $\phi=-45^{\circ}$ in red and $\phi=90^{\circ}$ in blue, simulated with CST MWS.   | 238 |
|      |  | 200 |

#### LIST OF FIGURES

| 8.25 | Compact range measurement results compared to CST MWS simulation<br>results for <b>vertical polarization</b> : (a) The co-polar (solid lines) and x-polar<br>(dashed lines) antenna radiation pattern Cuts for $\phi=0^{\circ}$ in green, $\phi=-45^{\circ}$ in<br>red and $\phi=90^{\circ}$ in blue, measured at compact range RWTH Aachen. (b) The<br>co-polar (solid lines) and x-polar (dashed lines) antenna radiation pattern<br>Cuts for $\phi=0^{\circ}$ in green, $\phi=-45^{\circ}$ in red and $\phi=90^{\circ}$ in blue, simulated with<br>CST MWS. | 239 |
|------|--|-----|
| 8.26 | Magnification of the figures 8.25b and 8.25b at boresight direction in order to evaluate the CPS at $\theta=0^{\circ}$ . The three CPS values at $\phi=0^{\circ}$ , $\phi=-45^{\circ}$ and $\phi=90^{\circ}$ are used to calculate the arithmetical mean of the CPS for the horizontal and vertical channel. Excellent CPS values of <b>-46.83 dB</b> and <b>-50.4 dB</b> can be evaluated for horizontal and vertical channel, respectively.  | 240 |
| 8.27 | Antenna beam steering performance recorded at compact range measure-<br>ments. The scan loss as the function of the single element antenna pattern<br>can be recognized. The single element pattern was measured separately for<br>an isolated patch element   | 242 |
| 8.28 | X-pol suppression during beam steering, recorded from compact range mea-<br>surements. As expected, the CPS will be degraded when the main lobe is<br>pointed off-boresight direction.   | 243 |
| 8.29 | X-pol performance as a function of amplitude tapering. Additionally, the amplitude taper functions 1 and 2 are shown. The center elements of the 8 amplitude weights are used as reference with 0 dB. The other amplitudes are attenuated by the phase- and amplitude distribution network   | 244 |
| 8.30 | CST MWS Design of dual polarized array with 32 radiators. This design incorporates differential feeding.   | 248 |
| 8.31 | (a) Front view (b) Rear view of the constructed dual polarized phased-array<br>antenna with differential feeding. The feeding points for horizontal (blue)<br>and vertical (red) polarization are given. The 1x4 subarray is highlighted<br>by the red and blue frames in dashed lines   | 249 |
| 8.32 | 1:8 corporate feeding network design of the dual polarized differential-feed antenna array with its equivalent circuit diagram.  | 250 |
| 8.33 | Description of the cancellation points in a feeding network with differential-<br>feed antennas. Three cancellation points are responsible for the excellent<br>isolation characteristics of dual-polarized differential-feed antennas   | 251 |
| 8.34 | Comparison of simulated (CST MWS-dashed lines) and measured (VNA-<br>solid lines) S-Parameters   | 254 |
| 8.35 | CST MWS simulated 3D antenna radiation pattern for horizontal and verti-<br>cal polarization. (a) Co-polar plot for horizontal polarization. (b) Co-polar<br>plot for vertical polarization. (c) X-polar plot for horizontal polarization.<br>(d) X-polar plot for vertical polarization.  | 255 |

| 8.36 | RWTH CATR measured 3D antenna radiation pattern of the differential-   |     |
|------|--|-----|
|      | feed array for horizontal and vertical polarization. The 3D cuts are generated                                       |     |
|      | by the Orbit software. The measurement was performed with 5° steps of $\Phi$   |     |
|      | for the complete upper hemisphere of the antenna array. The CATR effects   |     |
|      | are filtered out and an interpolation between the 5° steps of $\Phi$ is performed.                                   |     |
|      | (a) Co-polar plot for horizontal polarization. (b) Co-polar plot for vertical  |     |
|      | polarization. (c) X-polar plot for horizontal polarization. (d) X-polar plot   |     |
|      | for vertical polarization.   | 256 |
| 0 97 |  | 200 |
| 0.07 | Compact range measurement results compared to CST MWS simulation   |     |
|      | results for <b>horizontal polarization</b> channel of the differential-feed antenna                                  |     |
|      | array: (a) The co-polar (solid lines) and x-polar (dashed lines) antenna   |     |
|      | radiation pattern Cuts for $\phi = 0^{\circ}$ in green, $\phi = -45^{\circ}$ in red and $\phi = 90^{\circ}$ in blue, |     |
|      | measured at compact range RWTH Aachen. (b) The copolar (solid lines)   |     |
|      | and x-polar (dashed lines) antenna radiation pattern Cuts for $\phi=0^{\circ}$ in green,                             |     |
|      | $\phi = -45^{\circ}$ in red and $\phi = 90^{\circ}$ in blue, simulated with CST MWS                                  | 257 |
| 8.38 |  |     |
|      | results for vertical polarization channel of the differential-feed antenna   |     |
|      | array: (a) The co-polar (solid lines) and x-polar (dashed lines) antenna   |     |
|      | radiation pattern Cuts for $\phi=0^{\circ}$ in green, $\phi=-45^{\circ}$ in red and $\phi=90^{\circ}$ in blue,       |     |
|      | measured at compact range RWTH Aachen. (b) The co-polar (solid lines)  |     |
|      | and x-polar (dashed lines) antenna radiation pattern Cuts for $\phi=0^{\circ}$ in green,                             |     |
|      | $\phi$ =-45° in red and $\phi$ =90° in blue, simulated with CST MWS  | 258 |
| 8.39 | Antenna beam steering performance of differential-feed antenna array of  |     |
|      | 4x8 elements recorded at compact range measurements. The scan loss as  |     |
|      | the function of the single element antenna pattern can be recognized. The  |     |
|      | single element pattern was measured separately for an isolated patch element   |     |
|      | with differential feeding.   | 259 |
| 8.40 | X-pol suppression of the differentially fed antenna array of 4x8 elements  |     |
|      | during beam steering, recorded at compact range. The steady CPS can be   |     |
|      | recognized when the main lobe is pointed off-boresight direction.  | 260 |
| 8.41 | System Set-Up for Phased-Array Antenna Measurements  | 287 |
| 8.42 | (a) GUI main page with used equations, discretization error AZ and EL  |     |
|      | and the desired beam position angle. (b) calibration page for phase and  |     |
|      | amplitude corrections.   | 288 |
| 8.43 | (a) Block diagram of the RF Board. (b) RF board design with conductor  | -   |
|      | backed coplanar waveguide (CBCW) microstrip line technology installed in   |     |
|      | aluminum RF housing unit, where the RS232 signals and DC voltages are  |     |
|      | connected.   | 291 |

## List of Tables

| K factors for different antenna shapes and amplitude distributions [16]   | 96  |
|---|---|
| Properties for relevant microwave substrates with material cost factor (MCF),   |   |
| using RO4350 as reference. $tan(\delta)$ was measured at 10 GHz   | 105   |
| Performance parameters of rectangular, circular, equitriangular and annular-<br>ring patch antenna shapes for comparison, adapted by [15]. The parameters<br>are retrieved for $\epsilon = 2.32$ substrate height H=1.59mm and a frequency of 2 |   |
|   | 114   |
| Taper functions   | 127   |
| PAWR System Parameter   | 150   |
| Design parameter and CPS results for variable patch sizes   | 174   |
| Broadband Gain, Max. x-pol radiation for $\pm 60^{\circ}$ azimuth scan range in H-,<br>E-, 45°Cut and Min. CPS for $\pm 60^{\circ}$ azimuth scan range results retrieved  |   |
| from figure 7.5   | 190   |
| Results from 2x4 antenna array pattern from figure 7.6  | 192   |
| tial feeding configuration  | 193   |
| Antenna Specification Parameter   | 206   |
| Comparison of simulated and measured antenna radiation pattern results.   | 241   |
| Comparison of simulated and measured antenna radiation pattern charac-  |   |
| teristics of the differential-feed antenna array.   | 261   |
|   | Properties for relevant microwave substrates with material cost factor (MCF), using RO4350 as reference. $\tan(\delta)$ was measured at 10 GHz Performance parameters of rectangular, circular, equitriangular and annular-<br>ring patch antenna shapes for comparison, adapted by [15]. The parameters are retrieved for $\epsilon_r$ =2.32, substrate height H=1.59mm and a frequency of 2 GHz |

### Bibliography

- [1] Selex internal communication with marketing and sales department, 2017
- [2] Bernhard Huder: Einführung in die Radartechnik, Stuttgart, Leipzig, Teubner, 1999
- [3] Piccolo, F. and G. B. Chirico, 2005: Sampling errors in rainfall measurements by weather radar. Adv. Geosci. 2, 151-155
- [4] Maxwell, J., C.,: A treatise on Electricity and Magnetism, Dover, N.Y., 1954
- [5] SHORT- WAVELENGTH TECHNOLOGY AND THE POTENTIAL FOR DIS-TRIBUTED NETWORKS OF SMALL RADAR SYSTEMS, BAMS, David Pepyne, University of Massachusetts, April 2009
- Bundesnetzagentur: Frequenzbereichszuweisungsplanverordnung FreqBZPV, Juris GmbH, September 2004
- [7] Toomay and Hannen: Radar Principles for the Non-specialist, Third Edition, 2004
- [8] Mailloux, Robert J.: Phased Array Antenna Handbook, Second Edition, 2005
- [9] Hansen, R., C.: Phased Array Antennas, John Wiley and Sons, Inc. New York, 1998
- [10] Thomas A. Milligan: Modern Antenna Design, Second Edition, 2005
- [11] Jones, R., C. : A New Calculus for the Treatment of Optical Systems, I. Description and Discussion of the Calculus, J. Opt. Soc. Am., vol. 31, pp. 488 – 493, July 1941.
- [12] Kark, Klaus: Antennen und Strahlungsfelder, Elektromagnetische Wellen auf Leitungen, im Freiraum und ihre Abstrahlung, Friedr. Vieweg und Sohn Verlag GWV Fachverlage GmbH, 2006
- [13] Rinehart, Ronald E.: RADAR For Meteorologists, Fourth Edition, Rinehart Publications, 2004
- [14] Doviak, Zirnic: Doppler Radar and Weather Observations, Second Edition, 2006
- [15] JR James and PS Hall : Handbook of MICROSTRIP ANTENNAS, IEEE Electromagnetic Wave Series 28, 1989

- [16] Farsold, Grundlagen von Reflektorantennen, FH- München, 2007
- [17] Johnson, R. C., and H. J. Jasik, Antenna Engineering Handbook, 2nd ed., New York: McGraw-Hill, 1984
- [18] G. A. Deschamps, "Techniques for Handling Elliptically Polarized Waves with Special Reference to Antennas, Part II - Geometrical Representation of the Polarization of a Plane Electromagnetic Wave, Proc. I.R.E., vol. 39, pp. 540 – 544, May 1951
- [19] Frederiks G., Area Sales Manager, Rogers Corporation, Advanced Circuit Materials, Meeting and discussion at Selex, October 2012
- [20] Dreher, A.: Adaptive Planarantennen mit digitaler Strahlenformung, CCG Seminarunterlagen zu Intelligente Antennensysteme, 2009
- [21] Wanielik, Gerd: Skriptum Nachrichtentechnik 2, TU- Chemnitz, 2008
- [22] Rouphael Tony J.: Wireless Receiver Architectures and Design: Antennas, RF, Synthesizers, Mixed Signal, and Digital Signal Processing, Academic Press, 17.06.2014
- [23] Schreuder, Frans and Bij de Vaate, Jan Geralt: LOCALIZED LNA COOLING IN VACUUM, Nice, Côte d'Azur, France, 27-29 September 2006
- [24] H. S. Cao, R. H. Witvers, S. Vanapalli, H. J. Holland, and H. J. M. ter Brake: Cooling a low noise amplifier with a micromachined cryogenic cooler, Review of Scientific Instruments 84, 105102 (2013); doi: 10.1063/1.4823528, 2013
- [25] Skolnik, M.: RADAR HANDBOOK, Third Edition, McGRAW-HILL BOOK COM-PANY, 2008
- [26] Knorr, J. B.: Weather radar equation correction for frequency agile and phased array radars. IEEE Transactions on Aerospace and Electronic Systems, 43, 1220–1227., 2007
- [27] WU Chong and LIU Liping: Comparison of the observation capability of an X-band phased-array radar with an X-band Doppler radar and S-band operational radar, ADVANCES IN ATMOSPHERIC SCIENCES, VOL. 31, 814–824, JULY 2014
- [28] Henke, Heino: Elektromagnetische Felder, Theorie und Anwendung, 2007
- [29] Pozar, D. M.: Microwave Engineering, Third Edition, 2005
- [30] Zinke, O., Brunswig, A. V.: Lehrbuch der Hochfrequenztechnik, Band 1, Hochfrequenzfilter, Leitungen, Antennen, Vierte Auflage, 1990
- [31] Levanon, N., Mozeson, E. : Radar Signals, Wiley-IEEE Press, July 2004

- [32] Mahafza, B. R., Radar Systems Analysis and Design Using MATLAB, CHAPMAN AND HALL/CRC, 2000
- [33] Skolnik, M.I.: INTRODUCTION TO RADAR SYSTEMS, McGRAW-HILL BOOK COMPANY, 1981
- [34] Wolff, C.: Grundlagen der Radartechnik, www.radartutorial.eu/index.html, last excess July 2015
- [35] Probert-Jones, J. R.: The radar equation in meteorology. Quart. J. R. Met. SOC., 88, 485-495, 1962
- [36] Gunn, K. L. S. and East, T. W. R.: The microwave properties of precipitation particles. Q.J.R. Meteorol. Soc., 80: 522–545. doi:10.1002/qj.49708034603, 1954
- [37] J. S. Marshall and W. M. Palmer, The Distribution of Raindrops with Size, J. Meteorol., vol. 5, pp. 165 – 166, August 1948
- [38] A. C. Schroth, M. S. Chandra, and P. F. Meischner: A C-band coherent polarimetric radar for propagation and cloud physics research, Journal of Atmospheric and Oceanic Technology, vol. 5, pp. 803–822, Dec. 1988
- [39] Vollbracht, D., Gekat, F., Hilger, D., Hille. M.: Waveguide Fibre Optic Rotary Joint for Antenna Mounted Radar Receivers. 34th Conference on Radar Meteorology 5 -9 October 2009, Williamsburg, VA., Oct. 2009
- [40] Martin Hagen, Institut für Physik der Atmosphäre, DLR Oberpfaffenhofen, D-82234 Weßling: Overview of the full polarimetric weather radar POLDIRAD: www.pa.op.dlr.de/cleocd/poldirad/poldirad.htm, last excess Dec. 2015
- [41] Vollbracht D., Ridene D., Reimann J.(12), Hagen, M.(12): Receiver Upgrade for the Polarimetric C-Band Radar POLDIRAD, ERAD 2014, 8th European Conference on Radar in Meteorology and Hydrology (ERAD 2014), Garmisch-Partenkirchen, Germany, 1.-5. Sept. 2014
- [42] Urs Germann, Marco Boscacci, Marco Gabella and Maurizio Sartori: Peak Performance: Radar design for prediction in the Swiss Alps: The latest fourth-generation MeteoSwiss weather radar network called is Rad4Alp, http://www.meteoswiss.admin.ch/content/dam/meteoswiss/en/Mess-Prognosesysteme/doc/peak-performance-radar-design-for-prediction.pdf, METEO-**ROLOGICAL TECHNOLOGY INTERNATIONAL**, April 2015
- [43] Vollbracht, D., Ridene, D., Gekat, F.: Receiver over Elevation (ROEL) Weather Radar System Design and its Advantages, 12th URSI Commission F Triennial Open Symposium on Wave Propagation and Remote Sensing, Garmisch-Partenkirchen, 8
   - 11 March 2011

- [44] Vollbracht D., Gabella M.(1), Sartori M.(1): Absolute dual-polarization radar calibration: temperature dependence and stability with focus on antenna-mounted receivers and noise source generated reference signal, 8th European Conference on Radar in Meteorology and Hydrology (ERAD 2014), Garmisch-Partenkirchen, Germany, 1.-5. Sept. 2014
- [45] G. C. McCormick and A. Hendry, "Principles for the radar determination of the polarization properties of precipitation," Radio Sci., vol. 10, pp. 421 – 434, 1975
- [46] Hema Singh, H. L. Sneha, and R.M. Jha: Mutual Coupling in Phased Arrays: A Review, Hindawi Publishing Corporation International Journal of Antennas and Propagation Volume 2013, Article ID 348123, 23 pages, 2013
- [47] Jameson, A. R.: Microphysical Interpretation of Multiparameter Radar Measurements in Rain. Part III: Interpretation and Measurement of Propagation Differential Phase Shift between Orthogonal Linear Polarizations, Journal of the Atmospheric Sciences, 42, 607-614, 1985
- [48] Borgeaud M., Shin R.T. and Kong J.A.: Theoretical Models For Polarimetric Radar Clutter, Journal of Electromagnetic Waves and Applications Volume 1,pages 73-89, Issue 1, January 1987
- [49] Pruppacher, H.R. and K.V. Beard: A wind tunnel investigation of the internal circulation and shape of water drops fall at terminal velocity in air, Roy. Meteor. Soc., Vol. 96, 247-256, 1970
- [50] Wakimoto, R.M. and V.N. Bringi: Dual-polarization observations of microbursts associated with intense convection: The 20 July storm during the MIST project, Mon. Wea. Rev., vol. 116, 1521-1539, 1988
- [51] Bringi V.N., Thurai M., Hannesen R.: Dual-Polarization Weather Radar Handbook, 2nd Edition, Aug. 2005
- [52] Tragl, K. : Polarimetric radar backscattering from reciprocal random targets, Trans IEEE Geosci Remote Sens, vol. 8, 856-864, 1990
- [53] Holt, A. R.: Extraction of differential propagation phase from data from S-Band circularly polarized radars, Electron. Lett., 24, 1241–1244, 1988
- [54] Sachidananda, M. and D.S. Zrnic: ZDR measurement considerations for a fast scan capability radar, Radio Sci, vol. 20, 907-922, 1985
- [55] Balakrishnan, N. and D.S. Zrnic: Use of Polarization to Characterize Precipitation and Discriminate Large Hail. J Atmos Sci, vol. 47, 1525–1540, 1990

- [56] Illingworth, A.J. and I.J. Caylor: Correlation measurements of precipitation, Preprints 25th Int Conf Radar Meteor, American Meteor Soc, Paris, France, 650-653, 1991
- [57] Aydin K. and C. Tang: Relationships between IWC and Polarimetric Radar Measurands at 94 and 220 GHz for Hexagonal Columns and Plates, J Atmos and Oceanic Tech, vol. 14, 1055–1063, 1997
- [58] GDRX® Signal Processing User Manual from Selex ES GmbH, Document Release 4.2,Document Code: GEMA-SD-0104-0116-0042, 2015
- [59] Gölz P., Vollbracht, D., Gekat, F. (2013): Calibration of a Weather Radar Receiver with a Noise Diode, 36th AMS Conference on Radar Meteorology, Breckenridge, CO, 16 - 20 Sept. 2013
- [60] Melnikov, V. and Zrnic, D, 2007, AutoCorrelation and Cross-Correlation Estimators of Polarimetric Variables, Journal of Atmospheric and Oceanic Technology, Vol. 24, pp 1337-1350, August 2007
- [61] Holleman, Iwan, Asko Huuskonen, Mikko Kurri, Hans Beekhuis, Operational Monitoring of Weather Radar Receiving Chain Using the Sun. J. Atmos. Oceanic Technol., 27, 159–166, 2010
- [62] Gorgucci, E., G. Scarchilli, and V. Chandrasekar, A procedure to calibrate multiparameter weather radar using properties of the rain medium, IEEE Trans. Geosci. Remote Sens., 37, 269–276., 1999
- [63] Boryssenko : Polarization constraints in dual-polarized phased arrays derived from an infinite current sheet model, IEEE Antennas and Wireless Propagation Letters, vol. 8, pp. 955–958, 2009
- [64] G. Zhang, R. J. Doviak, D. S. Zrnic, J. Crain, D. Staiman, and Y. Al-Rashid, : Phased array radar polarimetry for weather sensing: A theoretical formulation for bias corrections, IEEE Transactions on Geoscience and Remote Sensing, vol. 47, no. 11, pp. 3679–3689, 2009
- [65] G. Zhang, R. J. Doviak, D. S. Zrnic, R. Palmer, L. Lei, and Y. Al-Rashid: Polarimetric phased-array radar for weather measurement: a planar or cylindrical configuration, Journal of Atmospheric and Oceanic Technology, vol. 28, no. 1, pp. 63–73, 2011
- [66] M. Simeoni, I. E. Lager, and C. I. Coman: Interleaving sparse arrays: A new way to polarization-agile array antennas?, in Proc. Antennas Propag. Soc. Symp. Dig., pp. 3145–3148., 2007

- [67] Barbetty, M. S., Jackson R. W., and Frasier S., Interleaved sparse arrays for polarization control of electronically steered phased arrays for meteorological applications, IEEE Transactions on Geoscience and Remote Sensing, vol.50, no.4, pp. 1283–1290, 2012
- [68] C. Fulton and W. Chappell: Calibration of panelized polarimetric phased array radar antennas: a case study, in Proceedings of the 4th IEEE International Symposium on Phased Array Systems and Technology (Array '10), pp. 860–867, Oct. 2010
- [69] Chen Pang, Peter Hoogeboom, François Le Chevalier, et al., : Dual-Polarized Planar Phased Array Analysis for Meteorological Applications, International Journal of Antennas and Propagation, vol. 2015, Article ID 340704, 12 pages, 2015 doi:10.1155/2015/340704, 2015
- [70] Jian Dong, Qingfu Liu, and Xuesong Wang,: New Polarization Basis for Polarimetric Phased Array Weather Radar: Theory and Polarimetric Variables Measurement, International Journal of Antennas and Propagation, vol. 2012, Article ID 193913, 15 pages, 2012. doi:10.1155/2012/193913, 2012
- [71] Bhattacharyya, Arun.: Phased Array Antennas Floquet Analysis, Synthesis, BFNs, and Active Array Systems, A Wiley-Interscience publication., ISBN-13: 978-0-471-72757-6, 2006
- [72] R. J. Mailloux, S. G. Santarelli, T. M. Roberts: Array Aperture Design Using Irregular Polyomino Subarrays, 2010 IEEE International Symposium on Phased Array Systems and Technology (ARRAY), Waltham, MA, 12-15 Oct. 2010
- [73] R. J. Mailloux, S. G. Santarelli, T. M. Roberts, and D. Luu,: Irregular Polyomino-Shaped Subarrays for Space-Based Active Arrays, International Journal of Antennas and Propagation, vol. 2009, Article ID 956524, 9 pages, doi:10.1155/2009/956524, 2009
- [74] Sergei P. Skobelev: Methods of Constructing Optimum Phased-Array Antennas for Limited Field of View, IEEE Antennas and Propagation Magazine, Vol. 40, No. 2, April 1998
- [75] P.S. Hall , C.M. Hall: Coplanar corporate feed effects on microstrip patch array design. IEE Proc. H, 3, 180 - 186, 1987
- [76] R.Bechini, V.Chandrasekar, R. Cremonini, S. Lim: Radome attenuation at X-band radar operations, ERAD, 2010
- [77] Germann, U. : Radome attenuation—a serious limiting factor for quantitative radar measurements? Meteorol. Z.,8,85–90, 1999

- [78] Thompson, R., Illingworth, A.: Improving radar estimates of rainfall by monitoring the attenuation by the wet radome, 8th European Conference on Radar in Meteorology and Hydrology (ERAD 2014), Garmisch-Partenkirchen, Germany, 1.-5. Sept. 2014
- [79] Thompson, R., Illingworth, A., Ovens, J.: Emission: a simple new technique to correct rainfall estimates from attenuation due to both the radome and heavy rainfall., Weather Radar and Hydrology (Proceedings of a symposium held in Exeter, UK) (IAHS Publ. 3XX, 2011), April 2011
- [80] Huuskonen, A.; Holleman, I. Determining weather radar antenna pointing using signals detected from the Sun at low antenna elevations. J. Atmos. Oceanic Technol., 24, 476–483., 2007
- [81] Holleman, I.; Huuskonen, A.; Kurri, M.; Beekhuis, H. Operational monitoring of weather radar receiving chain using the Sun. J. Atmos. Oceanic Technol., 27, 159–166., 2010
- [82] Holleman, I.; Huuskonen, A.; Gill, R.; Tabary, P. Operational monitoring of radar differential reflectivity using the Sun. J. Atmos. Oceanic Technol., 27, 881–887., 2010
- [83] Gabella, M., Sartori, M., Boscacci, M., and Germann, U.: Vertical and Horizontal Polarization Observations of Slowly Varying Solar Emissions from Operational Swiss Weather Radars, Atmosphere 2015, 6, 50-59; doi:10.3390/atmos6010050, 2015
- [84] Weiland, T.: A discretization method for the solution of Maxwell's equations for six-component fields: Electronics and Communication, (AEÜ), Vol. 31, pp. 116-120, 1977
- [85] Clemens, M. and Weiland, T.: Discrete electromagnetism with the finite integration technique, Progress in Electromagnetics Research, PIER 32, pp. 65-87, 2001
- [86] CST STUDIO SUITE 2013 Help Description, last access November 2015
- [87] Naishadham, K. : Finite Integration Technique (FIT) and CST Microwave Studio, Modeling and Simulation of Antennas, Georgia Tech Defence Technology Professional Education, April 2012
- [88] Yussouf, Nusrat, David J. Stensrud: Impact of Phased-Array Radar Observations over a Short Assimilation Period: Observing System Simulation Experiments Using an Ensemble Kalman Filter. Mon. Wea. Rev., 138, 517-538. 2010
- [89] Personal conversation with Meteo Swiss, KNMI, CHMI, Arpa Piermonte Italy weather services, 2006-2014
- [90] Piccolo, F. and G. B. Chirico "Sampling errors in rainfall measurements by weather radar" Adv. Geosci. 2, 151-155, 2005

- [91] V. Chandrasekar, Y. Wang, M. Maki and T. Maesaka "Urban Flood Monitoring using X-band Dual-polarization Radar Network: Program of the CASA-NIED partnership, AMS 2009, 2009
- [92] Shaya Karimkashi, University of Oklahoma, USA: Cylindrical Polarimetric Phased Array Radar: Design and Analysis of a Frequency Scanning Antenna Array, Array 2013, 2013
- [93] Redmond Kelley, University of Oklahoma, USA: Cylindrical Polarimetric Phased Array Radar:Hardware Design and Mobile Demonstrator, Array 2013, 2013
- [94] Bundesnetzagentur: Frequenzbereichszuweisungsplanverordnung FreqBZPV, Juris GmbH, September 2004
- [95] Selex ES GmbH, 41470 Specification for Neuss, Germany: "METEOR COMPACT WEATHER 60DX RADAR", HTML: http://www.gematronik.com/products/radar-systems/meteor-60dx/, last excess 2014
- [96] Robert J. Mailloux: Phased Array Antenna Handbook, Second Edition, 19-35, ARTECH HOUSE 2005
- [97] D. Fasold, University of Applied Sciences Munich: Seminar Grundlagen Reflektorantennen, 2007
- [98] Ronald E. Rinehard: RADAR For Meteorologists, Fourth Edition, 92-94, 2004
- [99] Jorge L. Salazar, Eric A. Knapp, David J. McLaughlin:" Antenna Tradeoffs for dense distributed radar network for weather sensing" CASA, 2014
- [100] Marco Schwerdt, David Hounam, Martin Stangl, German Aerospace Center, DLR "Calibration Concept for the TerraSAR-X Instrument", 2003
- [101] Benjamin Bräutigam, Marco Schwerdt, Markus Bachmann, German Aerospace Center, DLR, Martin Stangl, EADS Anstrium "Individual T/R Module Characterisation of the TerraSAR-X Active Phased Array Antenna by Calibration Pulse Sequences with Orthogonal Codes", 23-28 July 2007
- [102] Marco Schwerdt, Benjamin Bräutigam, Markus Bachmann, Björn Döring, Dirk Schrank, Jaime Hueso Gonzalez: "Final TerraSAR-X Calibration Results Based on Novel Efficient Methods", February 2010
- [103] Balanis, C. A.: Antenna Theory, Analysis and Design, 3rd Edn., 1136 pp., 2005
- [104] Bhardwaj, S. and Rahmat-Samii, Y.: Revisiting the Generation of X-pol in Rectangular Patch Antennas: A Near-Field Approach, IEEE Antenn. Propag. M., 56, 14-38, 2014

- [105] Wang Y. and Chandrasekar V.: Polarization isolation requirements for linear dualpolarization weather radar in simultaneous transmission mode of operation, IEEE Trans. on Geosc. and Rem. Sens., vol. 44, pp. 2019–2028, 2006
- [106] Zrnic D. S., Doviak R., Zhang G. and Ryzhkov A.: Bias in differential reflectivity due to cross coupling through the radiation patterns of polarimetric weather radars, Journal of Atmospheric and Oceanic Technology, vol. 27, pp. 1624–1637, 2010
- [107] Galletti M. and Zrnic D. S.: Bias in copolar correlation coefficient caused by antenna radiation patterns, IEEE Trans. on Geosc. and Rem. Sens., vol. 49, pp. 2274–2280, 2011
- [108] Abbas S., Paul S., Sen J., Gupta P., Malakar K., Chattopadhyay S. and Banerjee S.: Aspect Ratio: A Major Controlling Factor of Radiation Characteristics of Microstrip Antenna, Journal of Electromagnetic Analysis and Applications, Vol. 3 No. 11, pp. 452-457. doi: 10.4236/jemaa.2011.311072., 2011
- [109] Fulton, C. and Chappell, W.: A dual-polarized patch antenna for weather radar applications, IEEE International Conference on Microwaves, Communications, Antennas and Electronics Systems (COMCAS), Tel Aviv, Israel, 7–9 November 2011, 1–5, 2011
- [110] Garg, R., Bhartia, P., Bahl, I., and Ittipiboon, A.: Microstrip Antenna Design Handbook, ARTECH HOUSE, London, UK, Boston, USA, 2001
- [111] Guha, D., Biswas, M., and Antar, Y. M. M.: Microstrip Patch Antenna With Defected Ground Structure for X-pol Suppression, IEEE Antenn. Wirel. Pr, 4, 455-458, 2005
- [112] Liang, X.-L., Zhang, Y.-M., Zhong, S.-S., and Wang, W.: Design of Dual-Polarized Microstrip Patch Antenna With Excellent Polarization Purity, Proc. 3rd International Conference on Computational Electromagnetics and Its Applications, Beijing, China, 1–4 November 2004, 197–199, 2004
- [113] Ludwig, A. C.: The Definition of X-pol, IEEE Transactions on Antennas and Propagation, AP-21(1), 116–119, 1973
- [114] Mohanty, A. and Das, N. K.: Characteristics Of Printed Antennas And Arrays Covered With A Layer Of Printed Strip-Grating For Suppression Of X-Pol, International Symposium of Antennas and Propagation Society, Ann Arbor, MI, USA, 28 June to 2 July, 1993
- [115] Vollbracht, D.: System specification for dual polarized low power X-Band weather radars using phased array technology, TPH22, International Radar Conference, ISBN: 978-1-4799-4195-7, Lille, October 2014

- [116] Zhou, S.-G. and Chio, T.-H.: Dual Linear Polarization Patch Antenna Array with High Isolation and Low X-pol, International Symposium on Antennas and Propagation (APSURSI), Spokane, WA, USA, 3-8 July 2011, 588–590 2011
- [117] Hartley R.: RF/Microwave PC Borad Design and Layout, www.jlab.org/accel/eecad/pdf/050rfdesign.pdf, last access December 2014.
- [118] Woelders K. and Granholm J.: Cross-Polarization and Sidelobe Suppression in Dual Linear Polarization Antenna Arrays, IEEE Transactions on Antennas and Propagation (Volume: 45, Issue: 12), Pages 1727 - 1740, Dec 1997
- [119] Woelders K. and Granholm J.: Dual Polarization Stacked Microstrip Patch Antenna With Very Low Cross-Polarization, IEEE Transactions on Antennas and Propagation (Volume: 49, Issue: 10), Pages 1393 - 1402, Oct 2001
- [120] Egashira, K. , Nishiyama, E., Aikawa, M.: Microstrip array antenna for suppression of cross polarization, Computational Electromagnetics and Its Applications, 3rd International Conference on 1-4 Nov. 2004
- [121] Huayan Jin, Kuo-Sheng Chin, Wenquan Che, Chih-Chun Chang: Differential-Fed Patch Antenna Arrays With Low Cross Polarization and Wide Bandwidths, Antennas and Wireless Propagation Letters, IEEE (Volume:13) Pages 1069 - 1072, June 2014
- [122] Karimkashi S., Zhang G., Kishk A.: A Dually Polarized Frequency Scanning Microstrip Array Antenna for Weather radar Applications, 2013 7th European Conference on Antennas and Propagation (EuCAP), Pages 1795 - 1798, Gothenburg, 8-12 April 2013
- [123] Karimkashi S., Zhang G., Kishk A. Bocangel W. Kelley R., Meier J., Palmer R.: Dual Polarization Frequency Scanning Microstrip Array Antenna With Low Cross- Polarization for Weather Measurements, Antennas and Propagation, IEEE Transactions on (Volume:61, Issue: 11), Pages 5444-5452, 28 October 2013
- [124] IEEE Std. 211-1997, IEEE Standard Definitions of Terms for Radio Wave Propagation, IEEE, New York, 1997
- [125] IEEE Std. 145-1993, IEEE Standard Definitions of Terms for Antennas, IEEE, New York, 1993
- [126] D. A. Brunkow, V. N. Bringi, P. C. Kennedy, S. A. Rutledge, V. Chandrasekar, E. A. Mueller, and R. K. Bowie: A description of the CSU–CHILL national radar facility, J. Atmos. Ocean. Technol., vol. 17, no. 12, pp. 1596–1608, Dec. 2000

- [127] Institut für Hochfrequenztechnik RWTH Aachen, 52056 Aachen, Deutschland, Institutsleiter: Prof. Dr.-Ing. Dirk Heberling, HTML: http://www.ihf.rwthaachen.de/forschung/ausstattung/messkammern/fernfeld-compact-range/, last excess March 2016
- [128] Michalek, G.: Entwicklung und Aufbau eines RF-Phasenschiebernetzwerks für eine phasengesteuerte Antenne, Bachelorarbeit, Hochschule Niederrhein, Prüfer: Prof. Dr.-Ing. Christoph Degen, Dipl.-Ing. (FH) Dennis Vollbracht, Aug. 2013
- [129] Vollbracht D., Michalek, G.: X-Band Phase- And Amplitude Distribution Network for Phased Array Antenna Measurements, 10th European Conference on Antennas and Propagation, ISBN: 978-8-8907-0186-3, Davos, April 2016
- [130] Coonrod J., Rautio B.: Comparing Microstrip and CPW Performance, MI-CROWAVE JOURNAL, JULY 2012
- [131] Eisengarten, A.: Projektierung eines Up-Down-Converters für das X-Band bei einer Mittenfrequenz von 9395 MHz, Bachelorarbeit, Rheinische Fachhochschule Köln, Prüfer: Dipl.-Ing. Paul Langen, Prof. Dr. Peter Armbrüster, Betreuer: Dipl.-Ing. (FH) Dennis Vollbracht, Dec. 2015
- [132] Vollbracht D.: Optimum phase excitations and probe- feed positions inside antenna arrays for the reduction of Cross Polarization radiation in demanding phased array weather radar applications, 10th European Conference on Antennas and Propagation, ISBN: 978-8-8907-0186-3, Davos, April 2016
- [133] Vollbracht, D.: Understanding and optimizing microstrip patch antenna cross polarization radiation on element level for demanding phased array antennas in weather radar applications, Adv. Radio Sci., 13, 251-268, doi:10.5194/ars-13-251-2015, 2015.

### Lebenslauf

Herr Dennis Vollbracht wurde am 14.09.1980 in Haltern (heute, Haltern am See) geboren. Nach Realschulabschluss in Dülmen, Fachoberschulabschluss in Münster sowie der Ausübung des Zivildienstes in Senden begann Herr Vollbracht im Oktober 2001 das Studium der Elektrotechnik mit dem Studienschwerpunkt Nachrichtentechnik/Kommunikationstechnik an der Fachhochschule Münster.

Im Praxissemester des Studium sammelte Herr Vollbracht am Deutschen Zentrum für Luft- und Raumfahrt im Institut für Hochfrequenztechnik und Radarsysteme in Oberpfaffenhofen die ersten Facherfahrungen mit dem Thema: "Aufbau einer L-Band Antenne für ein fluggestütztes synthetisches Apertur Radar". Während des Hauptstudiums arbeitete Herr Vollbracht bei der Firma Lenord+Bauer in Oberhausen als Werkstudent im Bereich der Magnetfeld Sensorik und war mit Prototypentests betraut. Die Diplomarbeit, betreut durch Prof. Dr. -Ing. Fischer aus dem Hochfrequenzlabor der FH-Münster, zum Thema: "Zwei-Wege-Untersuchung eines bildgebenden, breitbandigen Sonarsystems" absolvierte er bei der Firma Altas Elektronik in Bremen mit der Note "sehr gut". Das Fachhochschulstudium beendete Herr Vollbracht im April 2006.

Seit Mai 2006 ist Herr Vollbracht als Systemingenieur und Projektleiter bei der Firma Selex ES GmbH in Neuss tätig und Herrn Dr. Gekat, dem Entwicklungsleiter, direkt unterstellt. Als Systemingenieur in der Entwicklungsabteilung ist Herr Vollbracht mit der Systementwicklung und Entwicklungsleitung von Radarneusystemen mit "Antenna Mounted Receiver "betraut. "Antenna Mounted Receiver (AMR)" bedeutet, dass der komplette analoge und digitale Empfänger an der drehenden Radarantenne positioniert wird. Um die hohe Datenrate zwischen Digitalreceiver und Signalprozessor zu gewährleisten, entwickelte Herr Vollbracht eine Hohleiter- und Glasfaserdrehkupplung sowie ein geeignetes optisches Übertragungsnetzwerk. Die innovative Hohleiter- und Glasfaserdrehkupplung wurde an namhafte Kunden wie der US-Bundesbehörde für Luft- und Raumfahrt NASA und dem Deutschen Zentrum für Luft- und Raumfahrt geliefert. Nach erfolgreicher Abnahme der AMR Prototypensysteme in Italien (Arpa Piemonte) und Deutschland (DLR POL-DIRAD am Institut für Physik der Atmosphäre) befasste sich Herr Vollbracht ab 2009 mit der Serienentwicklung der AMR Wetterradarsysteme und war für die Lieferung von fünf Wetterradarsystemen an den Kunden Meteo Schweiz zuständig. Hier war er direkter Ansprechpartner der Meteo Schweiz Wetterradargruppe in Locarno-Monti (radar, satellite and nowcasting division, MeteoSwiss) geleitet durch Herrn Dr. Urs Germann und für die Systeminstallationen und Abnahmen auf Alpinen Standorten bis 3000m ü. M. verantwortlich. Das letzte der fünf Systeme wurde im Dezember 2015 auf dem Weißfluhgipfel bei Davos abgenommen. Seit Anfang 2016 ist Herr Vollbracht für die Entwicklung der neusten S-Band Klystron Serie verantwortlich, um diese auf bis zu 33 Radarstandorte in Kanada zu installieren. Das erste Seriensystem wurde im Dezember 2017 erfolgreich in Radisson abgenommen. Zudem betreut er die Neuentwicklung eines transportablen C-Band Klystronsystems, welches Mitte 2017 nach Indien ausgeliefert wurde.

Seit 2011 promoviert Herr Vollbracht an der Technischen Universität Chemnitz nebenberuflich unter Leitung von Prof. Dr. rer. nat. Madhukar Chandra mit dem Thema: "Entwicklung und Aufbau von dual-polarimetrischen und phasengesteuerten Gruppenantennen für Wetterradarsysteme". Die Promotion ist berufsbegleitend organisiert und wurde in Kooperation mit Firma Selex ES GmbH (Gematronik Weather Radars) vereinbart. Im Rahmen der Promotionsarbeit beschäftigte sich Herr Vollbracht mit dem Entwurf, der Simulation und der Realisierung von kreuzpolarisationsarmen Einzelradiatoren und Array-Konfigurationen. Die dual-polarimetrischen Mikrostreifenantennen werden später den Einsatz in Wetterradaranwendungen finden, bei denen ein hoher Anspruch von Polarisationsreinheit gefordert ist. Die kreuzpolarisationsarmen, phasengesteuerten Antennen stellen eine nennenswerte Eigenentwicklung dar, welche auch außerhalb des Wetterradarbereiches Anwendung finden wird. Während der Promotionsphase hat Herr Vollbracht mehrere Master- und Bachelorarbeiten innerhalb der Firma Selex ES GmbH betreut. Die Resultate dieser Studienarbeiten und die Antennenentwicklung seiner Dissertation werden es ermöglichen, in naher Zukunft einen Demonstrator eines phasengesteuerten Wetterradars zu realisieren.

